Doctoral Dissertation
博士論文

Search for the neutral heavy Higgs bosons decaying to hadronic ditau in proton-proton collisions at $\sqrt{s}$ = 13 TeV

(重心系エネルギー13 TeV の陽子衝突におけるタウ粒子のハドロニック崩壊を用いた重い中性ヒッグス粒子の探索)

A Dissertation Submitted for the Degree of Doctor of Philosophy
July 2019

令和元年 7 月博士(理学)申請

Department of Physics, Graduate School of Science,
The University of Tokyo

東京大学大学院理学系研究科
物理学専攻

I-Huan Chiu
邱　奕寰

Abstract

After the discovery of the scalar Higgs boson that is predicted in the Standard Model of the particle physics (SM) with a mass of 125 GeV, the remaining issues in particle physics, such as dark matter in the universe and hierarchy problem of the Higgs boson, are to be solved by an extension of the SM. A boson-fermion symmetry, which is known as a "supersymmetry", is one of the most motivated extensions of the SM as it might address the missing of dark matter candidates, the hierarchy problem of Higgs boson mass, and realization of the grand unification, simultaneously. The supersymmetry requires the Higgs sector of the SM to be extended with at least one additional Higgs doublets, resulting in five physical Higgs states; two neutral CP-even Higgs states (h, H), one CP-odd Higgs state (A), and two charged Higgs states ($H^{\pm}$). One of the two neutral CP-even Higgs states is considered to be the discovered 125 GeV boson (h), and the other will be an additional heavy Higgs boson (H). An observation of the new heavy Higgs boson (H and A) can provide important insight into the nature of the supersymmetry. The coupling constants of the new heavy Higgs bosons are expected to depend on the ratio of the vacuum expectation values of the two Higgs doublets ($\tan\beta$), and the coupling constants to τ leptons are enhanced for a large $\tan\beta$ scenario. This thesis presents a search for the neutral heavy Higgs boson (H or A) decaying into a pair of tau leptons ($H/A \to \tau^{+}\tau^{-}$), which can provide the best sensitivity for a large $\tan\beta$ scenario of the Higgs sector extension. Hadronic decay mode of τ leptons ($\tau \to \text{hadrons} + \nu$) is considered in the identification of the tau leptons. This analysis uses 139 fb^{-1} of proton-proton collisions recorded by the energy frontier ATLAS experiment at the Large Hadron Collider with a center-of-mass energy of $\sqrt{s} = 13$ TeV. This analysis applies an optimal set of event selection criteria to enhance $H/A \to \tau^{+}\tau^{-}$ signals. Possible backgrounds remaining after the selection are estimated with data-driven techniques, exploiting control regions, and with the assistance of the simulation of the background processes. New analysis techniques have been developed to maximize the search sensitivity. An improved τ selection and categorization in the signal extraction are used in the $H/A \to \tau\tau$ search for the first time in this analysis. The result confirms no significant excess from SM prediction in the search for $H/A \to \tau^{+}\tau^{-}$. An exclusion limit in the context of the hMSSM scenario is presented, and the analysis excludes $\tan\beta > 23$ at $M_{H/A} = 1500$ GeV at 95% confidence level. This analysis allows setting the most stringent limit for the production of the heavy neutral Higgs boson.

Acknowledgment

I thank Prof. Shoji Asai at the University of Tokyo for supervising me during the four years of my Ph.D. course. I would like to express Prof. Junichi Tanaka and Associate Prof. Yasuyuki Okumura. They support throughout my thesis, provide lots of advice for the research, and give me the good opportunity to join many conferences in the ATLAS. I cannot accomplish this goal without their support.

I appreciate the staffs of the International Center for Elementary Particle Physics (ICEPP). Thanks to Associate Prof. Ryu Sawada, Dr. Koji Terashi, Dr. Yuji Enari, Dr. Tatsuya Masubuchi, Dr. Tomoyuki Saito, Dr. Takuya Nobe. They provide me lots of knowledge and advice for the detectors, analysis techniques, and way to presentation in the weekly meetings. A special thanks to Dr. Masahiro Morinaga, who is a reliable and knowledgeable collaborator in this analysis.

I would like to thank my colleagues at CERN, who make an enjoyable work environment for me. Thanks to Dr. Syunsuke Adachi, Mr. Yuji Minegishi, Dr. Masahiko Saito, Dr. Yuya Kano, Mr. Tomohiro Yamazaki, Mr. Masahiro Yamatani, Mr. Kenta Uno, Mr. Ryunosuke Iguchi, Mr. Kenta Uchidai, and Mr. Nobuo Matsuzawa, especially Mr. Yi-Lin Yang, who always accompany me to eat *kebabs* and gossip every Friday.

I am very grateful to work in a wonderful environment with my collaborators in the MSSM group in ATLAS. Thanks to Prof. Luca Fiorini, Dr. Lei Zhang, Dr. Adam Bailey, Dr. Max Maerker, Dr. Dirk Duschinger, and Mr. Lino Gerlach. They help me a lot to slove the difficult issues of this analysis.

A huge thanks to Ms. Wong Wing Lam for her kind support, that helps me to complete my Ph.D. course. Last but not the least, I would like to thank my family for being there for me.

Contents

1 Introduction

The Standard Model of the particle physics (SM) is turned out to be well-consistent with most of the experimental results. After the discovery of the scalar Higgs boson with the mass of 125 GeV at the Large Hadron Collider (LHC) at CERN, there are still a lot of questions remaining to be answered, such as unknown nature of the astrophysical dark matter, the hierarchy problem of the Higgs mass, unification of the fundamental interactions, and quantization of the gravitational interaction. Extensions of the Standard Model of the particle physics are expected to address the problems. Extensive studies to prove the beyond-the-SM (BSM) physics have been actively conducted in both theoretical and experimental methodologies.

The LHC is the energy frontier proton-proton collider running at the center-of-mass energy $\sqrt{s} =$ 13 TeV. Many questions of the incomplete SM may be addressed by an observation of a new symmetry between bosons and fermions, which is known as a "supersymmetry" or SUSY. The supersymmetry is one of the most motivated extensions of the SM as it may address the missing of dark matter candidates, the hierarchy problem of Higgs boson mass, and realization of the grand unification simultaneously. The supersymmetry requires the Higgs sector of the SM to be extended with at least one additional Higgs doublet, resulting in five physical Higgs states; two neutral CP-even Higgs states (h, H), one CP-odd Higgs state (A), and two charged Higgs states ($H^{\pm}$). One of the two neutral CP-even Higgs states is considered to be the discovered 125 GeV boson (h), and the other will be an additional heavy Higgs boson (H). An observation of the new neutral heavy Higgs boson (H and A) can provide important insight into the nature of the supersymmetry. The coupling constants of the new neutral heavy Higgs bosons are expected to depend on the ratio of the vacuum expectation values of the two Higgs doublets ($\tan\beta$), and the coupling constants to down-type fermions are enhanced for a large $\tan\beta$ scenario. Among the decay channels of the new neutral heavy Higgs boson, $\tau\bar{\tau}$ and $b\bar{b}$ channels are dominant modes with the typical branching ratios of $\sim 10\%$ and $\sim 90\%$, respectively, for the high $\tan\beta$ region.

This thesis presents a search for the neutral heavy Higgs boson (H or A) decaying into a pair of tau leptons ($H/A \to \tau^{+}\tau^{-}$), which can provide the best search sensitivity for a large $\tan\beta$ scenario of the Higgs sector extension. This thesis work uses 139 fb^{-1} of proton-proton collisions recorded by the energy frontier ATLAS experiment at the Large Hadron Collider at a center-of-mass energy of $\sqrt{s} = 13$ TeV during the 2015 and 2018 data-taking period, which is denoted as the LHC "Run2". The tau leptons will further decay in either of a hadronic decay mode ($\tau \to \text{hadrons} + \nu$) and a leptonic decay mode ($\tau \to \nu_{\tau}\ell\nu_{\ell}$). As τ leptons decay hadronically approximately 65% of the time, the hadronic decay mode of τ leptons is considered in the identification of the tau leptons in this analysis. The channel where the both tau leptons decay hadronically ($H/A \to \tau_{\text{had}}\tau_{\text{had}}$) is found to provide the best sensitivity in the high-mass region ($m_{H/A} > 600$ GeV) of all the search channels. The hadronically decaying tau leptons can be reconstructed with experimental data by the combination of the information of the calorimeter clusters and charged particle tracks (τ_{had} reconstruction and identification).

This analysis exploits an optimal set of event selection criteria, including the τ_{had} reconstruction and identification, to enhance $H/A \to \tau_{\text{had}}^{+}\tau_{\text{had}}^{-}$ signals. Considering the largest contribution of multi-jets background process with hadronic jets wrongly identified as tau leptons, the tau identification is tuned to suppress such a “fake” backgrounds effectively. Possible backgrounds remaining after the selection are estimated with a data-driven technique, exploiting control regions, and with the assistance of the simulation of the background processes. The signal extraction will be performed on the categorized data samples by $m_{\mathrm{T}}^{\mathrm{tot}}$ variable (defined as Equation 6.1), and the signal hypothesis will be tested in the context of hMSSM scenario [1].

Further, this thesis work has introduced the following two major improvements in the $H/A \to \tau_{\mathrm{had}}^{+}\tau_{\mathrm{had}}^{-}$ search in order to pursue the search sensitivity in a wide-range;

- **Improvement of the tau reconstruction with use of “2-prong” signature:** A new “2-prong tau reconstruction” has been developed to maximize the search sensitivities in the high mass regions ($M_{H/A} > 1.5$ TeV). This thesis describes that the traditional way of tau reconstruction based on signatures characterized with one charged track (1-prong) and three charged tracks (3-prong) is not fully efficient for a high p_{T} τ objects due to possible hit sharing among tracks and the contamination of additional tracks from $e^{+}e^{-}$ pair-creation associated with $\pi^{0} \to \gamma\gamma$. It is found that often the tau lepton can be associated with two charged tracks (2-prong). A new tau reconstruction technique with the 2-prong signature have been developed to maximize the signal selection efficiency in this search. The details are discussed in Section 4.6.

- **Categorization:** A new event categorization with respect to the number of tracks and the output of tau identification algorithm, which corresponds to “tau-likelihood”, is newly introduced in this analysis to maximize the search sensitivities. This new technique efficiently improve the sensitivity in particular in the low mass regions ($M_{H/A} < 600$ GeV). Given the different fraction between signals and backgrounds for the different tau identification requirements, the categorization in the final signal extraction improve statistical sensitivities. The details of categorization are discussed in Section 5.3.

With the development of two new techniques, 2% $\sim$ 10% better results have been achieved for the hypothesis of $M_{H/A} > 1500$ GeV (high mass), and 25% $\sim$ 50% better results for $M_{H/A} < 600$ GeV (low mass).

This thesis is structured as follows. The theoretical foundations of this analysis is discussed in Chapter 2. The LHC experiment and ATLAS detectors are illustrated in Chapter 3. Chapter 4 provides an overview for the reconstruction of the collision events, including reconstruction and identification of final-state objects. The dataset used in this analysis and the event selection for signal extraction optimal to select $H/A \to \tau_{\mathrm{had}}\tau_{\mathrm{had}}$ and background events are described in Chapter 5. The estimation of backgrounds are achieved via the several methods. They are discussed in Chapter 6, in particular for the data-driven estimation technique for the backgrounds with fake τ_{had}. The study of the systematic uncertainties from the sources of each analysis step and detectors are summarized in Chapter 7. Chapter 8 presents the results including the statistical methods applied to test signal hypothesis. The interpretation in the context of hMSSM, major achievements of this thesis work, and future prospect are discussed in Chapter 9. The conclusion is given in Chapter 10.

2 Theoretical Foundations

This chapter presents an overview of theoretical foundations of this search. An introduction of the Standard Model (SM) is given in Section 2.1. The remaining issues in particle physics, such as dark matter and hierarchy problem provide a strong motivation for this analysis. To solve the remaining problems in the Standard Model, one of the extensions of the Standard Model [2], Minimal Supersymmetry Standard Model (MSSM), is discussed in Section 2.2. Section 2.3 presents the phenomenology of the proton-proton collisions at the LHC. A large phase space of initial and final states in the high energy collisions are modeled by the Monte Carlo simulation, which is given in the Section 2.4.

2.1 Standard Model of Particle Physics

The SM is an established theoretical framework which describes properties of the particles and their interactions using quantum field theory with the gauge symmetry in $SU(3)_C \otimes SU(2)_L \otimes U(1)_Y$ group [3–5]. The SM explains three of the four known fundamental forces. It also provides a mechanism for elementary particles to obtain masses as a result of spontaneous garge symmetry breaking, which is known as the Higgs mechanism.

A unification of electromagnetic and weak interactions is described with $SU(2)_L \otimes U(1)_Y$ group. The four gauge bosons, $W^{\pm}$, Z and γ are associated to $SU(2)_L \otimes U(1)_Y$ group. The gauge theory was developed based on the invariance of field theory for the strong interaction and electroweak theory. The gravitational interaction is not described by SM.

The SM contains twelve fermions (quark and lepton) and five bosons with their electromagnetic charges, colors, and isospin as shown in Table 2.1. Six flavors of quarks are grouped into three generations; (up, down), (charm, strange) and (top, bottom). The lepton sector consists of three charged leptons (electron, muon and tau) with their corresponding neutrinos which are electron neutrino (ν_e), muon neutrino (ν_μ) and tau neutrino (ν_τ). Electron, muon and tau lepton are the fermions carrying electric charge -1 and colorless.

2.1.1 Problems in the Standard Model

Although the SM successfully describes experimental data of particle physics, unsolved problems, such as dark matter, still adjudicate a revise of the SM or an extension models. Theories that include an extention of the SM is called "physics beyond the Standard Model" (BSM). This section presents a brief overview of major problems of the SM that remain after Higgs discovery such as dark matter and hierarchy problem.

Dark Matter and Dark Energy

The cosmic microwave background (CMB) analysis with Wilkinson Microwave Anisotropy Probe (WMAP) [7] and the Planck Collaboration [8] have provided for a lot of information of the early Universe. The Λ-CDM

Name	Charge	Spin	Mass
	Leptons		
electron	-1	1/2	0.5 MeV
muon	-1	1/2	105.6 MeV
tau	-1	1/2	1.7 GeV
electron neutrino	0	1/2	$<$ 2.2 eV
muon neutrino	0	1/2	$<$ 1.7 eV
tau neutrino	0	1/2	$<$ 15.5 eV
	Quarks		
up	2/3	1/2	2.2 MeV
down	-1/3	1/2	4.7 MeV
charm	2/3	1/2	1.3 GeV
strange	-1/3	1/2	96 MeV
top	2/3	1/2	173.1 GeV
bottom	-1/3	1/2	4.2 GeV
	Bosons		
gloun	0	1	0
γ	0	1	0
Z	0	1	91.2 GeV
W	±1	1	80.4 GeV
Higgs	0	0	125 GeV

Table 2.1.: Table of the SM particles with the corresponding charge, spin and mass [6].

(Cold Dark Matter) model may explain phenomena of the CMB and the accelerating expansion. Based on the experimental result of the combined data from WMAP and the Planck, the dark energy density parameter is defined as Ω_Λ for cosmological constant [9, 10]. It predicts dark energy and dark matter (DM) contribute 68% and 27% of the total energy of Universe, respectively [11]. The SM does not provide a candidate particle for dark matter and an explanation for dark energy.

Hierarchy Problem in Higgs Section

Loop corrections for the particle coupling to the Higgs field includes contributions of virtual particles with the energy upto the Plank scale $\Lambda = (8\pi G_N)^{-1/2} \sim 10^{19}$ GeV where G_N is Newton's constant [12, 13]. An example is shown in Fig 2.1a which present the 1-loop process containing a Dirac fermion f with its mass m_f. The correction for the Higgs mass due to the virtual fermion loop is given as the following:

$$\Delta m_H^2 = -\frac{|\lambda_f|^2}{8\pi^2}\Lambda^2 + \mathcal{O}(log\Lambda), \tag{2.1}$$

where the Λ is in the order of the Plank scale. This quantum correction, which is used for the calculation of physical mass, to bare mass of Higgs is derived to be $\mathcal{O}(10^{38})(\text{GeV})^2$. Thus, it leads to the fine-tuning of the bare Higgs mass with the unnaturally large and precise quantum corrections to be consistent with the observed Higgs boson mass of 125 GeV. The problem is called "Hierarchy Problem" or "fine-tuning problem". It shows that the SM have to be extended to describe physics at higher energies.

Suppose that a new heavy complex scalar particle, referred to as S, is introduced with its mass m_S. Its coupling to the Higgs boson is given by a Lagrangian term $-\lambda_S|H|^2|S|^2$. The corresponding correction for the Higgs mass is given by

$$\Delta m_H^2 = \frac{\lambda_S}{16\pi^2}\Lambda^2 + \mathcal{O}(log\Lambda), \tag{2.2}$$

where the Feynman diagram is shown in Fig 2.1b.

The additional heavy particle predicted demonstrates that the quadratic terms Λ^2 can be eliminated via the regularization on the loop integral [14]. If the restrictions on the theory is accompanied with $\lambda_S = |\lambda_f|^2$, the Λ^2 term will be cancelled. The $\lambda_S = |\lambda_f|^2$ can be satisfied by a hypothetical symmetry relating the fermions and bosons. It is called "Supersymmetry" or "SUSY" [15]. This new symmetry theory includes additional Higgs bosons, which encourage the motivation of this thesis as discussed below.

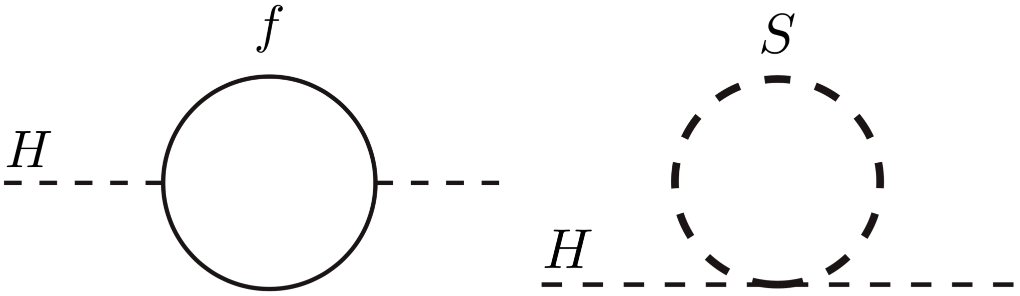

(a) Top loop. **(b)** Scalar-top loop.

Figure 2.1.: (a) and (b) are the illustration for 1-loop processes corrections to the Higgs mass by Dirac fermion f and a scalar S, respectively.

2.2 Supersymmetry and The Minimal Supersymmetric Standard Model

The major problems discussed in Sec. 2.1.1 of the SM can be addrssed by the new symmetry, called a *Supersymmetry* (SUSY). It predicts a new symmetry between bosons and fermions [16, 17]. The SUSY has to introduce new particles (sparticles), which are partners of the SM particles [18, 19]. The spin of a sparticle is 1/2 different from its SM partner [20, 21]. The supersymmetry transformation is given as:

$$\mathcal{Q}\,|\text{fermion}\rangle = |\text{boson}\rangle\,,\, \mathcal{Q}\,|\text{boson}\rangle = |\text{fermion}\rangle\,. \tag{2.3}$$

These operators are constructed according to Haag-Lopuszanski-Sohnius extension of the Coleman-Mandula theorem in the quantum field theory [22, 23].

R-parity

A new quantum number, which is referred to as "R-parity", is defined with the baryon number(B) and the lepton number (L) number as follows [24]:

$$R = (-1)^{3(B-L)+2s}\,, \tag{2.4}$$

where s stands for the spin of the particles. The R is equal to 1 (even parity) for all particles, while all sparticles have $R = -1$ (odd parity). As a consequence, R-parity conservation results in the following phenomenological features:

- The lightest supersymmetric particle (LSP) with $R = -1$ must be stable, which is a candidate of a dark matter.
- Other *sparticles* must eventually decay into stable particles that contains SM particles and odd number of LSPs.
- Each interaction vertex has even number of *sparticle* [15].

The *sparticle* search has been conducted with various experimental approach with respect to the phenomenological features.

2.2.1 The MSSM Higgs Sector

The Minimal Supersymmetric Standard Model (MSSM) is built based on several hypotheses to minimize the matter contents and freedom on the SUSY [25–29]. The MSSM requires an additional Higgs doublet, which corresponds to two-Higgs-doublet models (2HDM) [30]. The 2HDM introduces the complex Higgs doublets, H_u and H_d, for the up-type and down-type fermions. It results in the five Higgs bosons; two charged Higgs bosons ($H^{\pm}$), a CP-odd pseudoscalar Higgs (A) and two CP-even scalar Higgs (h and H).

In the unconstrained MSSM, a huge number (105) of unknown parameters with 19 parameters of the SM are introduced [25, 31]. After the assumptions for the SUSY–breaking parameters, the MSSM is constrained with only 22 input parameters [32]. It contains 13 mass parameters for sparticles, six trilinear couplings terms (so called A-parameters) and the ratio of the vacuum expectation values (VEVs) corresponding to the two–Higgs doublet superfields ($\tan\beta$) with two Higgs mass parameters. The two–Higgs doublet superfields $\hat{H}_{\mathrm{up}}$ and $\hat{H}_{\mathrm{down}}$ corresponding to the two Higgs doublets H_u and H_d have the Yukawa couplings to give masses to up-type quarks and down-type fermions, respectively (type II 2HDM [30]). The VEVs of $\hat{H}_{\mathrm{up}}$ and $\hat{H}_{\mathrm{down}}$ are defined as υ_u and υ_d. The $\sqrt{\upsilon_u^2 + \upsilon_d^2}$ is suited with 246 GeV to realize the mass of W boson. The ratio of VEVs is a parameter of MSSM, called $\tan\beta$,

$$\tan\beta = \frac{\upsilon_u}{\upsilon_d}. \tag{2.5}$$

In the MSSM, the superpotential W is introduced with the supersymmetric Lagrangian $\mathcal{L}_W$ and the superfields. The superpotential represents the Yukawa interaction and the supersymmetric version of the Higgs boson mass in the SM [15].

In the MSSM, there are three different sources with the superfields in the scalar Higgs potential V_H; Higgs interactions, superpotential and soft SUSY–breaking. [33].

$$\begin{aligned} V_H \quad &= \tfrac{g_u^2}{8}[4|H_d^\dagger \cdot H_u|^2 - 2|H_d|^2|H_u|^2 + (|H_d|^2)^2 + (|H_u|^2)^2] + \tfrac{g_d^2}{8}(|H_u|^2 - |H_d|^2)^2 && \text{Higgs interactions,} \\ &+\mu^2(|H_d|^2 + |H_u|^2) && \text{Superpotential,} \\ &+m_{H_d}^2 H_d^\dagger H_d + m_{H_u}^2 H_u^\dagger H_u + B\mu(H_u \cdot H_d + h.c.) && \text{Soft SUSY–breaking,} \end{aligned} \tag{2.6}$$

where g_u and g_d show gauge couplings of up- and down-type fermions, respectively. The μ is a parameter for the Higgs mass terms, $\mu H_u H_d$. When the potential V_H ($\partial V_H/\partial H_{u,d} = 0$) is minimized, one can obtain the relation between υ_u and υ_d:

$$\upsilon_u^2 + \upsilon_d^2 = \frac{4M_Z^2}{(g_u^2 + g_d^2)} = (246\ \mathrm{GeV})^2. \tag{2.7}$$

In order to obtain the Higgs physical fields and their masses, representation of the two doublet complex scalar fields around the vacuum in introduced as follows,

$$H_u = \begin{pmatrix} H_u^+ \\ H_u^0 \end{pmatrix} = \frac{1}{\sqrt{2}} \begin{pmatrix} H_u^+ \\ \upsilon_u + H_u^0 + iP_u^0 \end{pmatrix}. \tag{2.8}$$

$$H_d = \begin{pmatrix} H_d^0 \\ H_d^- \end{pmatrix} = \frac{1}{\sqrt{2}} \begin{pmatrix} \upsilon_d + H_d^0 + iP_d^0 \\ H_d^- \end{pmatrix}, \tag{2.9}$$

where real(imaginary) parts indicates the CP–even(CP-odd) Higgs bosons. The vacuum mass matrices

	g_{VV}	g_{uu}	$g_{dd,ll}$	$g_{\Phi AZ}/g_{\Phi H^+W^-}$
A	0	$\cos\beta$	$\tan\beta$	$\propto 0\ /\ 1$
H	$\cos(\beta-\alpha)$	$\sin\alpha/\sin\beta$	$\cos\alpha/\cos\beta$	$\propto \sin(\beta-\alpha)$
h	$\sin(\beta-\alpha)$	$\cos\alpha/\sin\beta$	$-\sin\alpha/\cos\beta$	$\propto \cos(\beta-\alpha)$

Table 2.2.: The effective coupling of the MSSM Higgs to the massive vector boson or SM ferminons. The couplings, g, with SM ferminons and bosons are depends on the β and α.

with their mixing angles for CP–even and CP–odd neutral Higgs bosons are given by:

$$\mathcal{M}_R^2 = \begin{bmatrix} -\bar{m}_3^2\tan\beta + M_Z^2\cos^2\beta & \bar{m}_3^2 - M_Z^2\sin\beta\cos\beta \\ \bar{m}_3^2 - M_Z^2\sin\beta\cos\beta & -\bar{m}_3^2\cos\beta + M_Z^2\sin^2\beta \end{bmatrix} \tag{2.10}$$

$$\mathcal{M}_I^2 = \begin{bmatrix} -\bar{m}_3^2\tan\beta & \bar{m}_3^2 \\ \bar{m}_3^2 & -\bar{m}_3^2\cot\beta \end{bmatrix}. \tag{2.11}$$

Since $\mathrm{Det}(\mathcal{M}_I^2) = 0$, the pseudoscalar Higgs mass is given as $M_A^2 = -2\bar{m}_3^2/\sin 2\beta$. The mass of CP-even Higgs bosons, the mass of the charged Higgs boson, and the rotation angle α are expressed as following:

$$M_{H^\pm}^2 = M_A^2 + M_W^2 \tag{2.12}$$

$$M_{h,H}^2 = \frac{1}{2}[M_A^2 + M_Z^2 \pm \sqrt{(M_A^2+M_Z^2)^2 - 4M_A^2M_Z^2\cos^2 2\beta}]. \tag{2.13}$$

$$\alpha = \frac{1}{2}\arctan(\tan 2\beta\frac{M_A^2+M_Z^2}{M_A^2-M_Z^2}), -\frac{\pi}{2} \leq \alpha \leq 0. \tag{2.14}$$

The role of the SM Higgs boson h in the MSSM is shared by $\hat{H}_{\mathrm{up}}$ and $\hat{H}_{\mathrm{down}}$.The neutral scalar MSSM Higgs has interactions with bosons and SM fermions. Table. 2.2 summarizes the effection coupling constracts for the MSSM Higgs.

2.3 Phenomenology of MSSM Higgs Bosons in the Proton-Proton Collisions

2.3.1 MSSM Benchmark Scenarios

A benchmark model was built, reducing the number of MSSM Higgs parameters down to two; the mass of A (M_A) and $\tan\beta$ [34–36]. In this "hMSSM" approximation, the range for the $\tan\beta$ is around $1 < \tan\beta < 60$ [37]. In the large $\tan\beta$ region, the neutral heavy Higgs bosons dominantly couple with bottom quarks and τ lepton. A high seach sensitivity for the neutral heavy Higgs bosons H/A (denoted as Φ) is expected with the final state with a pair of τ in the high $\tan\beta$ region. Since a mass of 125 GeV for SM Higgs boson cannot be obtained for the region in $\tan\beta < 3$, the low $\tan\beta$ region was excluded in the context of the hMSSM.

The mass matrix of neutral components CP–even (h and H) can be formed in the following formula, related to the M_A, M_Z and β [38]:

$$\mathcal{M}^2 = \mathcal{M}_R^2 + \begin{bmatrix} \Delta\mathcal{M}_{11}^2 & \Delta\mathcal{M}_{12}^2 \\ \Delta\mathcal{M}_{12}^2 & \Delta\mathcal{M}_{22}^2, \end{bmatrix} \tag{2.15}$$

where $\mathcal{M}_R^2$ is the same tree-level matrix described in Eq. 2.10. The $\Delta\mathcal{M}_{ij}^2$ corresponds to the radiative corrections [39]. It is used to calculate the Higgs masses and couplings. In the context of SUSY, the the average of the two stop ($\tilde{t_1}$ and $\tilde{t_2}$) masses, M_S, also plays an improtant role for the radiative corrections [34]. [1]

Three assumptions for the hMSSM approach are discussed in the items below.

- the observed Higgs boson is the light scalar h.
- only the element $\Delta\mathcal{M}^2_{22}$ has non zero value and $\Delta\mathcal{M}^2_{11}$, $\Delta\mathcal{M}^2_{12}$, and $\Delta\mathcal{M}^2_{21}$ can ne considered to be zero.
- all SUSY particles are heavy enough to escape detection at the LHC, so that search for the model is possible with experimental data.

In general, the SUSY radiative corrections are known to be very small. A basic assumption for hMSSM shows that $\Delta\mathcal{M}^2_{22}$ is to be much larger than $\Delta\mathcal{M}^2_{11}$ and $\Delta\mathcal{M}^2_{12}$ [25]. The $\Delta\mathcal{M}^2_{22}$ is derived as follows with the known mass value of $M_h = 125$ GeV:

$$\Delta\mathcal{M}^2_{22} = \frac{M_h^2(M_A^2 + M_Z^2 - M_h^2) - M_A^2 M_Z^2 \cos^2 2\beta}{M_Z^2 \cos^2\beta - M_h^2}. \tag{2.16}$$

The assumption is valid for the current experimental constraints in most of cases, such as large M_S or large $\tan\beta$ value. For instance, the maximal value of the h mass is computed as $M_h^{\max} \sim 130$ GeV in the M_S at the TeV scale.

The mass of the heavier neutral CP even Higgs particle, H, and the mixing angle α are then given as:

$$M_H^2 = \frac{(M_A^2 + M_Z^2 - M_h^2)(M_Z^2\cos^2\beta + M_A^2\sin^2\beta) - M_A^2 M_Z^2\cos^2 2\beta}{M_Z^2\cos^2\beta + M_A^2\sin^2\beta - M_h^2}. \tag{2.17}$$

$$\alpha = -\arctan\left(\frac{(M_Z^2 + M_A^2)\cos\beta\sin\beta}{M_Z^2\cos^2\beta + M_A^2\sin^2\beta - M_h^2}\right). \tag{2.18}$$

In the hMSSM approach, the mass of the charged Higgs boson is given as $M^2_{H_\pm} = M_A^2 + M_W^2$ by tree–level relation.

Production of the Neutral Heavy Higgs Bosons

The production of H/A bosons (denoted as Φ) is dominated by two main production processes; gluon-gluon fusion ($gg \to \Phi$) and bottom-annihilation (gg or $q\bar{q} \to b\bar{b}\Phi$), is known as four-flavour scheme [2]. The bottom-annihilation process also contains five-flavour scheme ($b\bar{b} \to \Phi$) in this analysis. The other production processes, such as top-quark associated production ($pp \to \Phi t\bar{t}$), has much smaller corss-section than them due to the small couplings with VV or $t\bar{t}$, and therefore not considered in this study. In the high $\tan\beta$ region, the production rates of H and A states are approximately same.

In this analysis, the $\sigma(gg \to \Phi)$ and $\sigma(bb \to \Phi)$ are computed by the code *SusHi 1.5.0* [40] using the Next-to-Next-to-Leading order (*NNLO*) in Quantum Chromodynamics (QCD) [41] perturbation theory [42] and Next-to-Leading order (*NLO*) in the $M_\Phi > 2m_Q$ [43]. [3] The top- and bottom-loop contributions at *NNLO* in QCD, NNLO-QCD top contributions and the Leading order (*LO*) electroweak contributions by light quarks are exploited for gluon-gluon fusion in the code. The b-associated production in the four-flavour scheme are calculated using Ref. [44]. In the five-flavor scheme case, the

---

[1] M_S is $\sqrt{m_{\tilde{t_1}} m_{\tilde{t_2}}}$, which can be few TeV or 100 TeV scale.

[2] b-quarks are not considered as partons.

[3] m_Q is defined as the quark mass as the pole of the propagator. For instance, m_t of 175 GeV and m_b of 5 GeV are considered for the t and b pole mass.

amplitude for the production of SM Higgs boson is re-weighted with the effective coupling g_{dd} given in Table. 2.2. Finally, the cross section of bottom-annihilation production is obtained with the combination of the five-flavor and four-flavor schemes by the "Santander matching" and overlap is removed [45]. The computed cross sections of gluon-gluon fusion and bottom-annihilation production are of the same order of magnitude. The production cross sections of the A in $(\tan\beta, M_A)$ plane for gluon-fusion and bottom-annihilation mechanism are shown in Fig.2.2.

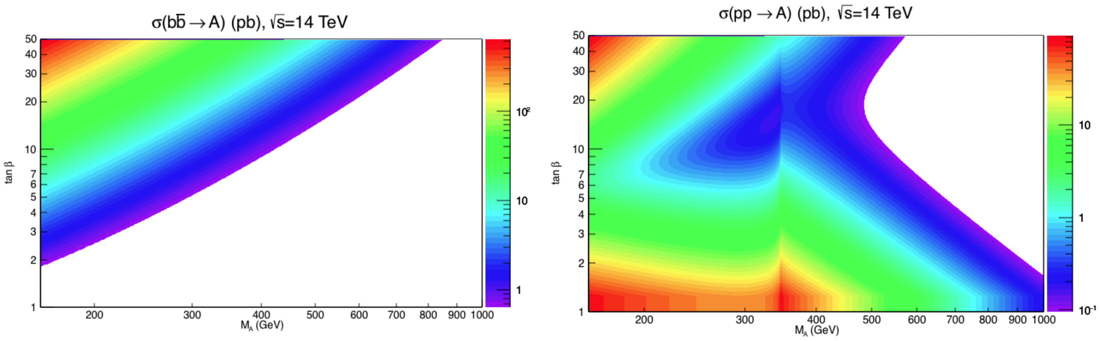

(a) bottom-annihilation production

(b) gluon-fusion

Figure 2.2.: The production cross sections of the neutral Higgs bosons A (shown as the color column in right part of the figure) in $(\tan\beta, M_A)$ plane at the hMSSM benchmark scenarios for gluon-fusion (a) and bottom-annihilation mechanism (b) [34].

Decay of the Neutral Heavy Higgs Bosons

H/A bosons strongly couple to down-type quarks and charged leptons in high $\tan\beta$ region ($\tan\beta > 10$). Among entire decay channels of Φ, the branching fraction (referred to as **BF**) of $\tau\tau$ pair is computed to be $\mathbf{BF}(\Phi \to \tau\tau) \approx m_\tau^2/(m_\tau^2 + 3m_b^2)$. [4] The τ lepton mass $m_{\mathrm{tau}} = 1.78$ GeV and bottom quark mass at the scale of the Higgs mass $m_b \approx 3$ GeV result that the branching fractions of $\tau\tau$ and $b\bar{b}$ decay channels of 10% and 90%, respectively [34]. The other decay channels of Φ states, especially to up–type quarks, are strongly suppressed at high $\tan\beta$ since the coupling to up–type fermions is inversely proportional to $\tan\beta$. In the $M_A \gg M_Z$ condition, the α shown in Eq. 2.18 is drived as:

$$\alpha \xrightarrow{M_A \gg M_Z} -\arctan(1/\tan\beta) = -(\frac{\pi}{2} - \beta). \tag{2.19}$$

The relation of the coupling in the approximation [46] for up–type quarks ($g_{u,u}$ shown in Table 2.2) can be written as:

$$g_{uu} = \frac{\sin\alpha}{\sin\beta} \xrightarrow{M_A \gg M_Z} \frac{\sin(-(\frac{\pi}{2} - \beta))}{\sin\beta} = -\frac{1}{\tan\beta}. \tag{2.20}$$

In the $\Phi \to VV$, where V stands for W or Z boson, and $\Phi \to hh$ cases, the couplings gets to be close to zero for large M_A value ($g_{VV} = \cos(\beta - \alpha) \xrightarrow{M_A \gg M_Z} 0$) [25]. Figure 2.3 shows branching ratios of Φ in $(\tan\beta, M_A)$ parameter space based on the hMSSM benchmark scenario for each decay channels.

2.3.2 Search Channels for the Neutral Heavy Higgs Boson

As a consequence of hMSSM benchmark scenarios, gluon-fusion and bottom-annihilation production are main processes for high $\tan\beta$. The other processes are negligible as they are highly suppressed at the target parameter space. Since that $\mathbf{BF}(\Phi \to \tau^+\tau^-)$ is 10% and $\mathbf{BF}(\Phi \to b\bar{b})$ is 90% for high $\tan\beta$

---

[4] The branching fraction of $b\bar{b}$ is computed by $\mathbf{BF}(\Phi \to b\bar{b}) \approx m_b^2/(m_\tau^2 + 3m_b^2)$.

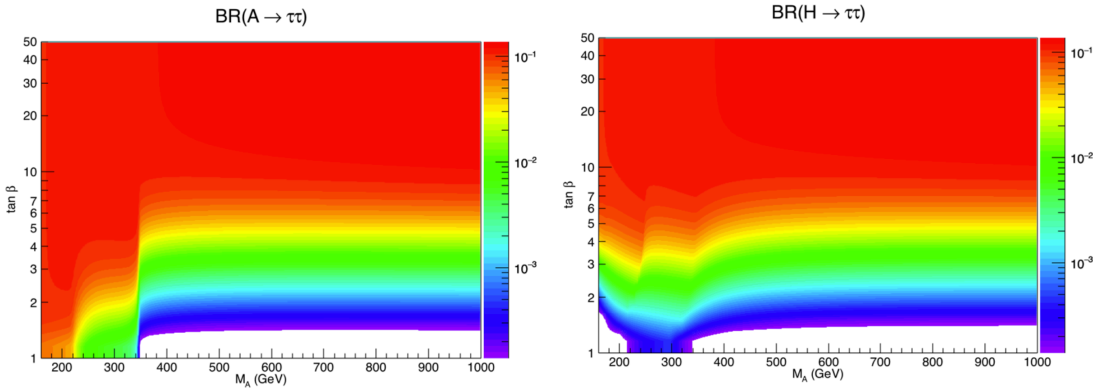

(a) $A \to \tau\tau$ **(b)** $H \to \tau\tau$

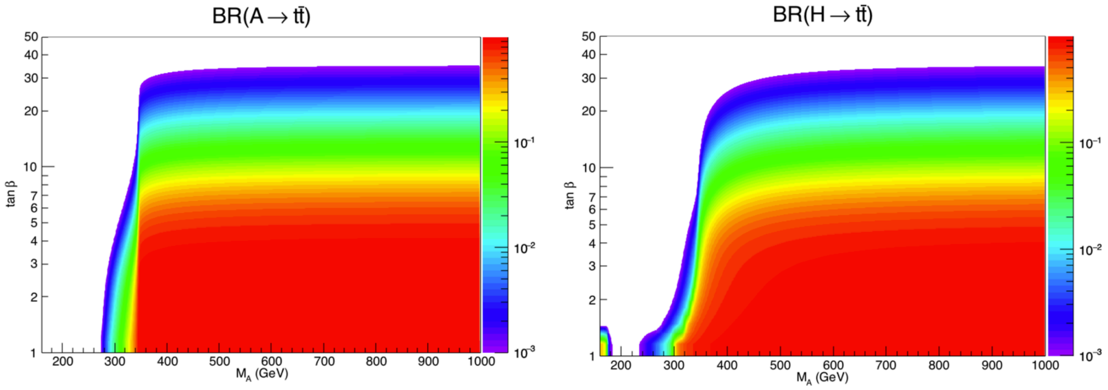

(c) $A \to t\bar{t}$ **(d)** $H \to t\bar{t}$

Figure 2.3.: The branching fractions of the neutral heavy Higgs bosons Φ in ($\tan\beta$,M_A) plane (shown as the color column in right part of the figure). (a) and (b) show the dominated decay channel for $\tau\tau$. The BF plots for the suppressed decay channels with up-type quark, top quark for instance, are shown in (c) and (d) [34].

condition, they are sensitivity in the neutral heavy Higgs search. Requiring tau lepton significance in the final state suppresses background effectively, and therefore a better sensitivity is expected in $\tau^+\tau^-$ search channels than $b\bar{b}$ channel. Three sub-channels for $\tau^+\tau^-$ decay channel are classified for A/H search based on the final state of τ lepton decay products. The H/A decay channels with leptonic decaying tau (τ_ℓ) and hadronic decaying tau (τ_{had}) are grouped as the $\tau_\ell\tau_\ell$, $\tau_\ell\tau_{\text{had}}$ and $\tau_{\text{had}}\tau_{\text{had}}$ final states. The branching fractions of each sub-channel are around 12% ($\tau_\ell\tau_\ell$), 45% ($\tau_\ell\tau_{\text{had}}$) and 40% ($\tau_{\text{had}}\tau_{\text{had}}$) as discussed in Sec. 4.5. The $\tau_\ell\tau_{\text{had}}$ channel is significant in low mass region because requirement of final state lepton suppresses large fraction of background, while the $\tau_{\text{had}}\tau_{\text{had}}$ provides the best sensitivity in high mass region due to lower contribution for QCD background. This analysis focuses on the search for the neutral heavy Higgs boson H/A in gluon-fusion and bottom-annihilation production. The $\tau_{\text{had}}\tau_{\text{had}}$ final state is chosen as best sensitivie channel in high mass region. The current experimental constraints of H/A are described in Sec. 2.5.

2.4 Simulation of Physics Process at the Proton-Proton Collisions

Monte Carlo (MC) simulation used to assist the definition for the complex signal extraction, background suppression as well as the analysis techniques [47]. Hard scattering processes is a dominant process of proton-proton collision. It is described using the parton distribution functions (PDF). A very flexible tree-level matrix-element generator (ME) is used to simulate hard scattering processes. The phenomenon occurring in the final state of proton scattering where color-charged quarks and gluon transformed into the color-neutral hadrons is called "hadronization". The low energy interactions which are QCD factorization theorems is referred to as *underlying event*. There is still no complete theory for this phenomenon. The additional interactions normally happen as a nuisance. The lowest order partons emit hard particles, which carry the colour and electric charges as the initial state radiation (ISR) and final state radiation (FSR) in parton-shower model due to the effects of QCD Bremsstrahlung [48].

2.4.1 Parton Distribution Function (PDF)

High energy proton-proton collisions in LHC are known as deep-inelastic scattering (DIS) processes. The universal Parton Distribution Function (PDF) was investigated carefully from the rates of the various proton scattering process of LHC data-taking based on the theoretical factorization scheme. In the past decades, heavy flavors with the different gluon distributions and different values of the strong coupling are imported into the PDF analysis [49–51]. A parton carries the fraction x of hadron's momentum. μ_F is the factorization scale in the parton model. The PDF $f(x, \mu_F)$ is evaluated to calculate the cross section for the processes in hadron-hadron collisions. The PDFs, which is related hard scattering processes, are studied based on all possibles DIS at the different order in QCD perturbation theory. [5] However, a higher-order correction to reduce μ_F dependence is essential. It leads to the choice of the μ_F to play an important role. In the hard-scattering cross-section calculation, the μ_F is usually chosen to be of order Q which denotes an energy scale of the hard interaction. The factorization scale is separated to short-distance physics and long-distance hadronic physics for the different phenomenon of the evolution. Figure 2.4 presents an example of *MSTW 2008* PDFs at NLO with 1-σ confidence level uncertainty bands. The corresponding uncertainties of the PDF are computed by the global fits to the experimental data. The other PDF set used in the LHC are extracted from the global data analysis such as *PDF4LHC* [52] , *NNPDF* [50] , *CT14* [53] and *MSTW* [54].

---

[5] Leading-order (LO), next-to-leading order (NLO) and next-to-next-to-leading order (NNLO)

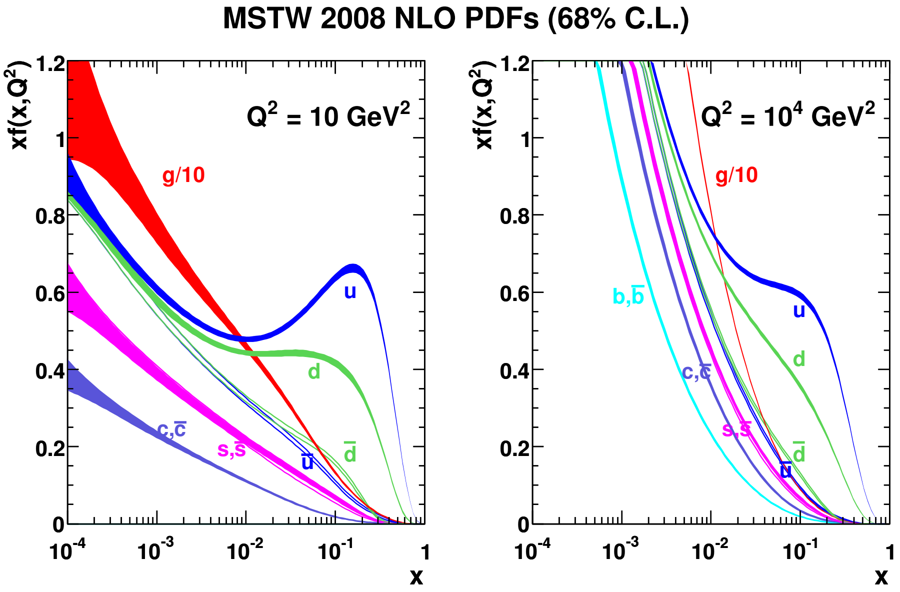

Figure 2.4.: MSTW Parton distribution functions at the interaction scale of $Q^2 = 10$ GeV^2 and $Q^2 = 10^4$ GeV^2 [55].

2.4.2 Hadronization

Hadronization is the transition process where the color quarks and gluons in a generated parton event into the hadrons [56–58]. A complex and well-known string fragmentation model are introduced based on the *Lund-String Model* [59]. The Lund string framework is implemented in the *Pythia* event generator [60]. The space-time of a Lund string is illustrated as shown in the left plot of Fig. 2.5. In a simple condition of $q\bar{q}$ two parton event, the potential energy increases when $q\bar{q}$ move away from the creation vertex z-axis. The string, which indicates strong color field, is known to break and create new $q'\bar{q}'$. The set of $q_i\bar{q}'_i$ pairs as the i-primary hadrons are created. The q' has no mass and transverse momentum and the primary hadrons of the different breaks are separated independently in space (z-axis). A constant string tension, which corresponds to the energy–momentum, is defined as $\kappa = |dE/dz|$. Furthermore, two adjacent breaks are constrained by the mass shell of the produced hadron as shown in the right plots of Fig. 2.5. The transverse mass is computed to be $m_\perp^2 = E^2 - p_z^2$. Based on the Quantum mechanics, the field energy can be transformed into the transverse mass $m_\perp^2$. In addition, the quark production must be limited in one point and tunnel out to an allowed region. The production probability for this tunnelling process is written by $\exp(-\pi m_\perp^2)/\kappa$. The computed result with the experimental data presents a high suppression value for heavy quark. It shows the fractions to generate a pair of $q\bar{q}$ with $u\bar{u} : d\bar{d} : s\bar{s} : c\bar{c} \approx 1 : 1 : 0.3 : 10^{-11}$.

2.4.3 Underlying events

The hard interactions irrelevant with the primary hard process are called “underlying events”. The number of those soft collisions with low transverse momenta is expected to be huge in the proton-proton collision at the LHC. The models based on multiple parton interactions (MPI) is used to describe the characteristic of soft QCD. It provides a rigorous and reasonable explanation for the phenomenon of several parton-parton interactions happened within a single hadron-hadron collision. The MPI for the underlying events is implemented in all *Pythia*, *Sherpa* and *Herwig++* models. However, the simulation of the additional jets is still difficult even those jets affect the total amount of scattered energy. The poorly understood part on the color reconnection related to color-space correlations also cause significant uncertainties in the MPI models. In the analysis step, these soft particles from underlying events present

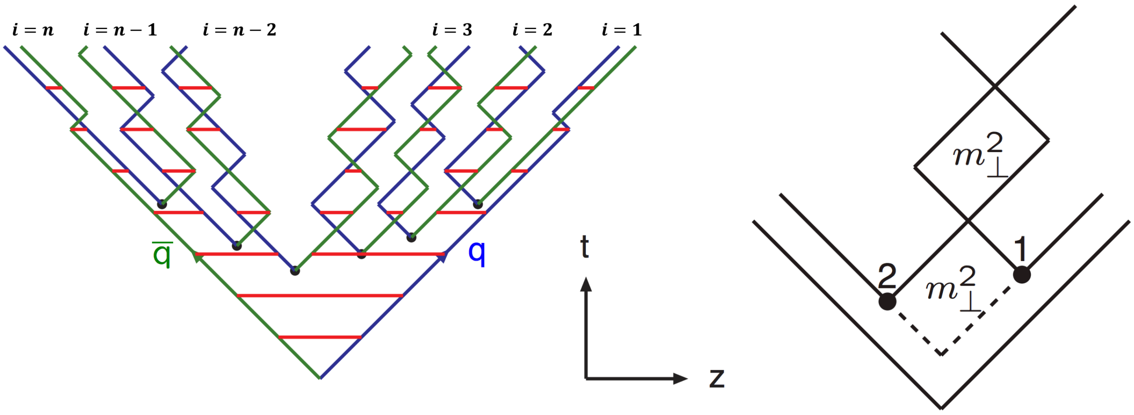

(a) Lund string system **(b)** Mass shell

Figure 2.5.: (a) shows the motion of a Lund string system with n hadrons. z-axis and t respond to space-time plane. (b) indicates the mass shell conditions on nearby string breaks [56–58].

the impacts for jet energy calibrations and performance of missing transverse momentum.

2.4.4 Pileup simulation

Multiple collisions in a single bunch crossing, which is called as "pile-up", is known as another source of the soft QCD interactions. During the high-energy run of the LHC, the average number of collisions per bunch crossing reaches up to 50 with a peak value 80. Additional collisions are generated by *Pythia8* for two dominant components of pile-up background, named as "In-time pile-up" and "Out-of-time pile-up" which are discussed in the chapter 3. Moreover, the pileup simulation is implemented in the MC step to model the mixture of both hard and soft interactions. The minimum-bias event generation for single proton-proton interactions is done with *Pythia8*, *A3 tune* [61] and *NNPDF23LO PDFs* [62] set.

2.5 Experimental Constraints of Heavy Higgs Bosons Searches

The search for heavy neutral Higgs bosons predicted by MSSM has been conducted by the experiments including the LEP, the Tevatron, and the CMS and the ATLAS at the LHC.

LEP experiments

The search for the neutral Higgs bosons was studied with the data recorded in the LEP by the four collaborations, which are the *ALEPH*, *DELPHI*, *L3*, and *OPAL*. [63] The interpretation on $(m_A, \tan\beta)$ plane is carried out based on the accepted lower bound of SM Higgs mass of 114.4 GeV at 95% confidence level in a number of benchmark models. The exclusion limit in the m_h^{max} benchmark scenario [36] is shown in Fig. 2.6. [6] The LEP experiments recorded e^+e^- collision with center-of-mass energies of 91 GeV to 209 GeV. The two main signal processes, Higgsstrahlung $e^+e^- \to HZ(orhZ)$ and pair production $e^+e^- \to AH(orAh)$, are considered. The final states of H are $b\bar{b}$ and $\tau^+\tau^-$ with Z decaying to $q\bar{q}, e^+e^-, \mu^+\mu^-, \nu^+\nu^-$ or $\tau^+\tau^-$. Finally, the combined statistical result with the several topological searches is computed based on the CL_s method.

---

[6] m_h^{max} benchmark scenario is originally made to obtain the exclusion bounds on $\tan\beta$ in LEP experiments [].

Tevatron experiments

Results of the MSSM neutral Higgs (h, H and A are marked as ϕ) searches were provided with 2.6 fb^{-1} and 5.2 fb^{-1} of data collected by the CDF and the DØ collaborations, respectively [64]. The main decay mode $\phi \to b\bar{b}$ with 90% branching fractions and the second decay mode $\phi \to \tau^-\tau^+$ were dominated due to the factor of $\tan\beta$. As the interpretation in the m_h^{max} benchmark scenario shown in Fig. 2.6, the Tevatron experiments provided a limits on neutral heavy Higgs boson. Since the coupling of neutral heavy Higgs boson is dominant to bottom quark, a useful b-jet tagging technique was developed at the Tevatron experiments. This method is also applied in the analyses at the LHC experiments.

ATLAS and CMS collaboration at the LHC experiments

The ATLAS (CMS) collaboration provided search results for H/A in $\tau^+\tau^-$ final states with proton-proton collision data at a center-of-mass energy of 13 TeV corresponding to an integrated luminosity of 36.1 (35.9) fb^{-1} at the LHC [65, 66]. Due to the higher center-of-mass energy and the huge integrated luminosity, the sensitivity was significantly improved in the high $\tan\beta$ and high m_A region compared to the Tevatron results. The $\tau^+\tau^-$ channel has a much better sensitivity, in spite of its small branching fraction, than the $b\bar{b}$ channel because of the lower background rate. Figure 2.7 shows the interpretations in the m_h^{max} benchmark scenarios at 95% confidence level. Two dominated signal processes, gluon fusion and bottom annihilation production, are exploited with the three (four) most sensitive final states of $\tau^+\tau^-$ pair. A pair of $\tau^+\tau^-$ are considered to be $e\tau_{\mathrm{had}}$, $\mu\tau_{\mathrm{had}}$ and $\tau_{\mathrm{had}}\tau_{\mathrm{had}}$ ($e\mu$, $e\tau_{\mathrm{had}}$, $\mu\tau_{\mathrm{had}}$ and $\tau_{\mathrm{had}}\tau_{\mathrm{had}}$) for the ATLAS (CMS) experiments. The other Higgs decay mode beside $\phi \to \tau^+\tau^-$ are also presented at LHC Run1 and Run2 analyses as shown in Fig. 2.8.

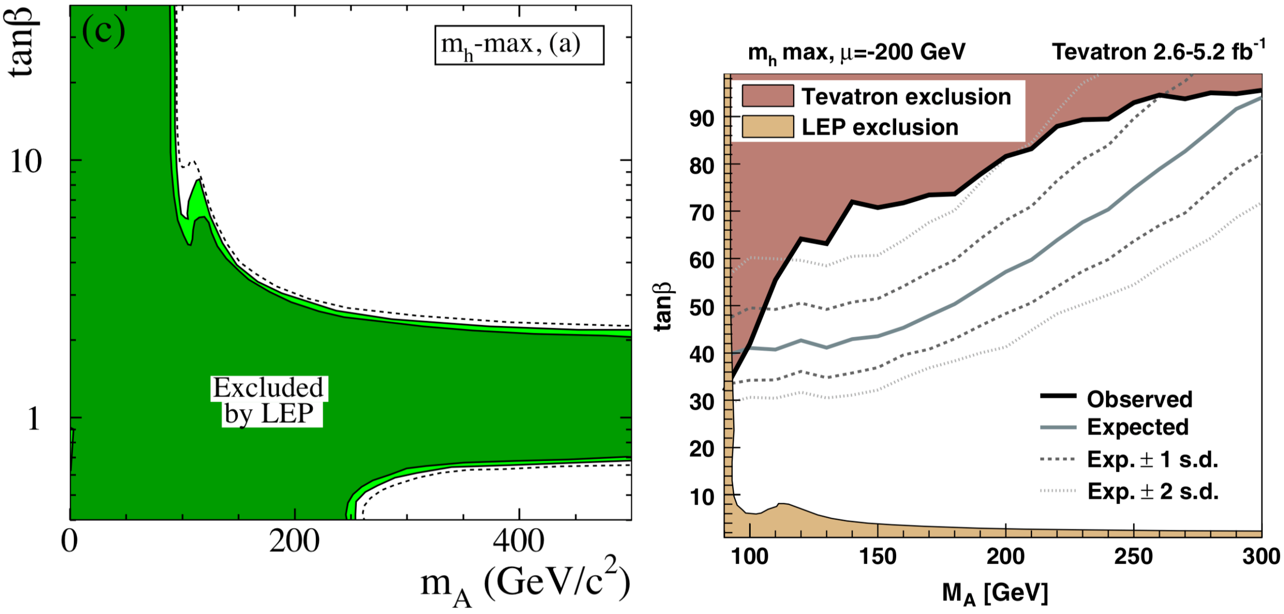

(a) LEP result

(b) Tevatron result

Figure 2.6.: Exclusion limits for MSSM Higgs searches at LEP (a) and Tevatron (b) in the m_h^{max} benchmark scenario at 95% confident level [67]. The light (dark) green area shows the limit at 95% (99.7%) confident level.

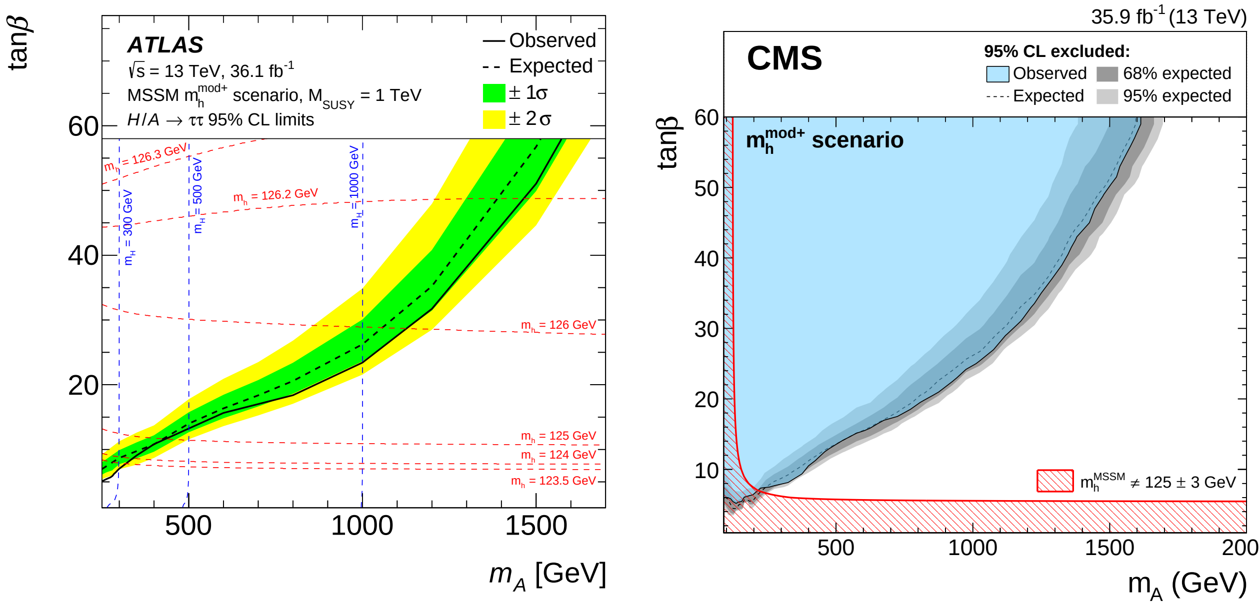

(a) ATLAS result

(b) CMS result

Figure 2.7.: The newest exclusion limits at 95% confident level by MSSM Higgs searches with $\tau^+\tau^-$ final state at ATLAS (a) [65] and CMS (b) [66] in the m_h^{mod+} benchmark scenario. The total integral luminosities of proton-proton collision data are around 36 fb^{-1} recorded during 2015 to 2016 at a center-of-mass energy of 13 TeV. In the ATLAS limit, dashed lines of constant m_h and m_H are shown in red and blue, respectively.

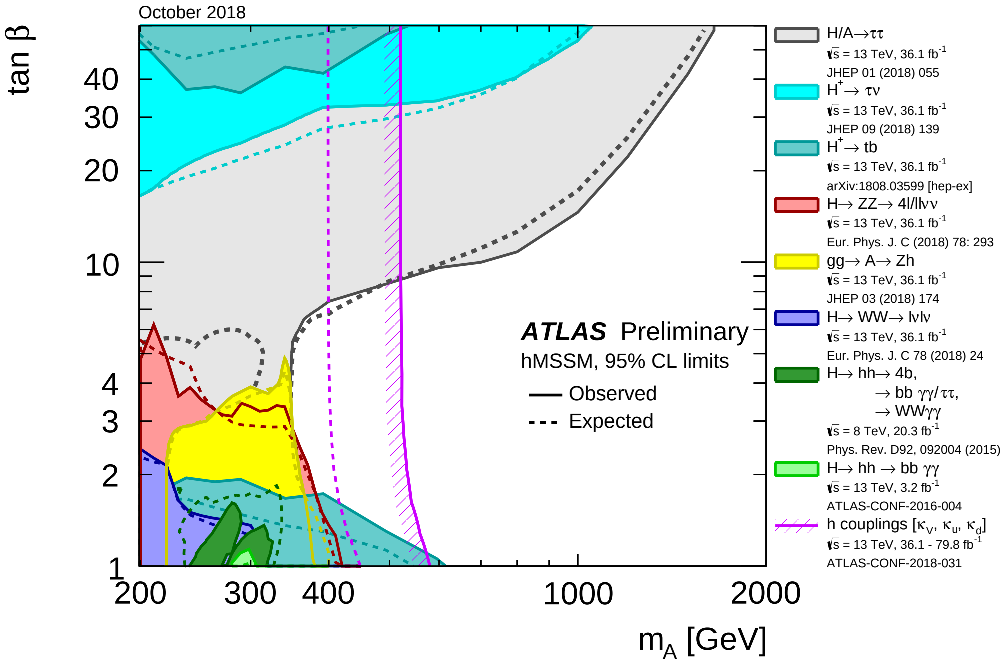

Figure 2.8.: Exclusion limits on the $(m_A, \tan\beta)$ plane for MSSM Higgs searches with the different decay modes in the hMSSM benchmark scenario at 95% confident level by the ATLAS collaboration [68].

3 The ATLAS Experiment at the LHC

3.1 The Large Hadron Collider

The LHC is a synchrotron accelerator with four interaction points for four large experiments [1] with the circumference of 27 km [70, 71]. It is re-utilizing the Large Electron Positron collider (LEP) tunnel and crosses the France-Swiss border. The LHC provides the high-energy collisions with the existing injector chain which consists of linear accelerator (LINAC2), Proton Synchrotron Booster (PSB), Proton Synchrotron (PS) and Super Proton Synchrotron (SPS). The LINAC2 is the beginning for accelerating the protons to reach the energy up to 50 MeV. The proton is accelerated up to 1.4 GeV by PSB, which receives protons from the LINAC2. The proton's energy is further increased to 26 GeV by the PS. The last pre-accelerator of LHC is the SPS. The SPS is the second largest accelerator at the European Organisation for Nuclear Research (CERN) with the circumference of 7 km. It brings the proton's energy up to 450 GeV. The proton is accelerated up to 7 TeV in LHC by oscillating radio-frequency (RF) electric fields[2]. The LHC accelerator consists of the 1232 superconducting dipole magnets, cooled by liquid helium to 1.9 K. The magnetic fields up to 8.33 T to bend the counter-rotating proton beams. Figure 3.1 shows a schematic overview of the LHC accelerator complex. Typically, a beam in LHC has 2808 bunch collisions at *Point-1*, where ATLAS detector is located with a crossing angle of 285 mrad. One bunch consists of 1.15×10^{11} protons. The obtained luminosity is given as the function of:

$$L = \frac{n_b N_b^2 f \gamma F}{4\pi\epsilon\beta^*}, \tag{3.1}$$

where n_b is the number of bunches per beam, N_b is the number of protons per bunch, f is the revolution frequency, and γ is the relativistic gamma factor. The denominator is a production of the normalized transverse beam emitting ϵ and the beta function at the collision point β^*. The geometric luminosity reduction factor F due to the crossing angle at the interaction point is given as:

$$F = (1 + (\frac{\theta\sigma_z}{2\sigma^*}))^{-1/2}, \tag{3.2}$$

which is computed based on the crossing angle at interaction point θ with σ_z, and σ^* is RMS bunch length and RMS of beam size in transverse plane, respectively. The achievement of the peak luminosity in both main experiments, ATLAS and CMS, amounts up to $L = 0.7$ - $1.4 \times 10^{34}\,\mathrm{cm^{-2}\,s^{-1}}$ in 2015 and 2016 runs, and $L \sim 2 \times 10^{34}\,\mathrm{cm^{-2}\,s^{-1}}$ for 2017 and 2018 runs for proton operation. Another collision data with the heavy ions (Pb) with an energy of 2.8 TeV with a peak luminosity $L = 10^{27}\,\mathrm{cm^{-2}\,s^{-1}}$ is

---

[1] There are ATLAS (A Toroidal LHC ApparatuS), CMS (Compact Muon Solenoid), LHCb (The Large Hadron Collider beauty), and ALICE (A Large Ion Collider Experiment) are located on the accelerator ring of the LHC for the different purposes [69].

[2] The RF is delivered to all the system not only to the accelerator apparatus but also to the detector system, so that the operation coherent to the LHC operation is achieved.

not described in this thesis.

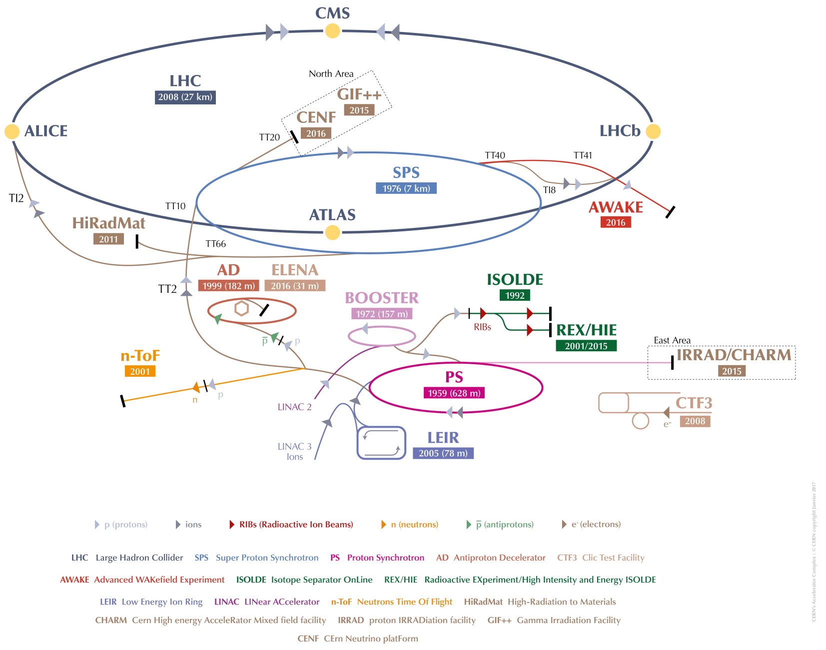

Figure 3.1.: Schematic overview of the current CERN accelerator complex, with year of first operation and circumference in parentheses [72].

3.2 The ATLAS experiment

ATLAS and CMS are two general purpose detectors to proceed with energy fronier physics programs at the LHC. Several important missions of these main detectors are like the search for SM Higgs boson, and test the SUSY model or other BSM theories.

The requirement to the ATLAS detectors are summarized in the following items:

- The ATLAS provides a capability to handle the particle fluxes, which is produced in high luminosity conditions at the LHC with overlapping events.

- The acceptance of the detectors is maximized in pseudo-rapidity. ATLAS provides a high geometrical coverage up to 4π .

- For tagging of τ lepton and b hadron jets, the high-resolution information of vertices are essential. The inner tracker of the ATLAS presents a good resolution for the charged-particle momentum and reconstruction efficiency as discussed in Sec. 4.5.

- The measurement of particle's energy and momentum is one of the most important purposes of the detector. The electromagnetic (EM) calorimetry and the hadronic calorimetry in ATLAS accurately provide the basis of the particles studies for the identification and measurement of the electron, photon, jet, and missing transverse energy.

- The muon spectrometers of the ATLAS provides the information for the muon identification and momentum measurement.

- The trigger system of ATLAS successfully collects collision data from the design bunch-crossing rate of 40 MHz. ATLAS trigger system provides an average recording rate of a few hundred Hz in high luminosity collision at the LHC [73].

An overview of the detector is shown in Fig. 3.2, which consists of inner detectors, calorimeter systems and the muon spectrometers. The origin of the coordinate system is defined as the center of the detector corresponding to the nominal interaction point of p-p collisions [74]. The beam pipe is located along the z-axis, and the x-axis points the center of the LHC ring. The y-axis is vertical to the ground. The coordinate (x, y, z) corresponds to a right-handed coordinate system, also, the polar coordinate (ϕ, θ, z) is used to describe the coordinate system of ATLAS detector. The pseudo-rapidity η defined as,

$$\eta = -\ln \tan(\theta/2), \tag{3.3}$$

is used instead of the polar angle θ as shown in Fig. 3.3. The transverse momentum $p_{\mathrm{T}} = \sqrt{p_x^2 + p_y^2}$ and the transverse energy $E_{\mathrm{T}} = \sqrt{E_x^2 + E_y^2}$ are the parameters used for describing the particles. The ΔR is used to represent for the distance between two particles i and j as $\Delta R_{ij} = \sqrt{\Delta\phi_{ij}^2 + \Delta\eta_{ij}^2}$.

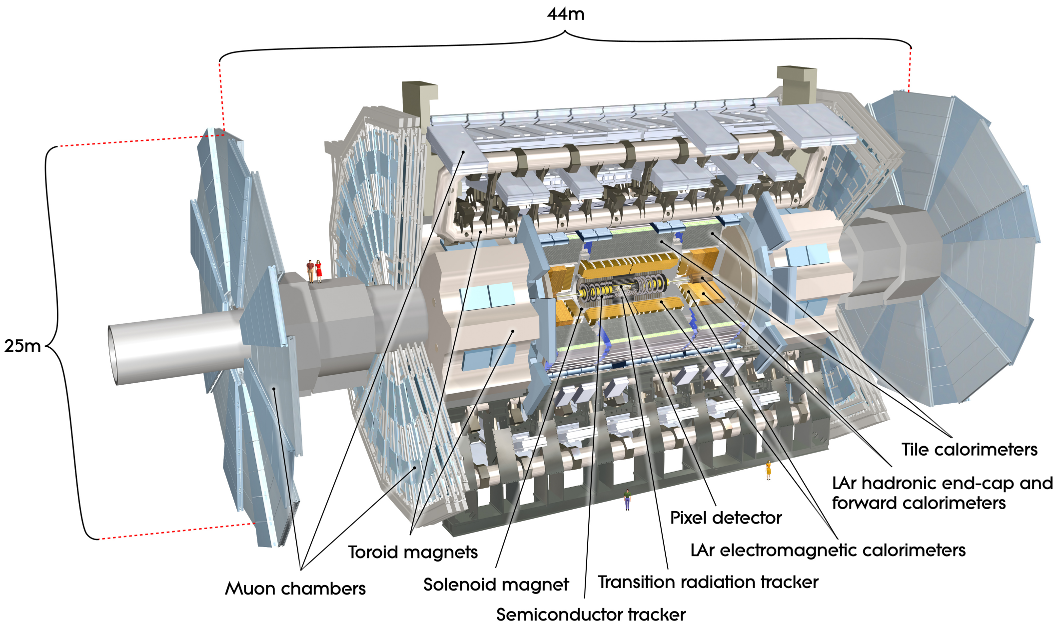

Figure 3.2.: A schematic diagram of the ATLAS detector with its subsystems. The ATLAS consists of tracking detectors, calorimeter and the muon spectrometers. [75]

3.2.1 The Inner Detector

The Inner Detector (ID) is the detector closest to the collision point with a length of about 7 m and a diameter up to 2.3 m. It was designed to measure the charged particles trajectories and vertices in around 1000 particle's emerging every 25 ns. ID is illustrated in Fig. 3.4, which is installed in a magnetic field of 2 T along the z-axis generated by the central solenoid magnet [77]. There are three subdetectors of ID; Pixel, silicon microstrip tracker (SCT), and Transition Radiation Tracker (TRT). The tracks of chraged particles are recontructed within the coverage of the ID. The coverage of Pixel deterctor and SCT is the region of $|\eta| < 2.5$, while the TRT covers $|\eta| < 2.0$.

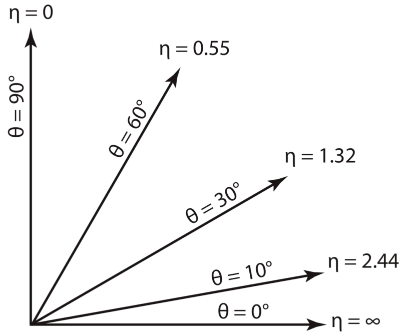

Figure 3.3.: Visualization of pseudo-rapidity η and polar angle θ [76]

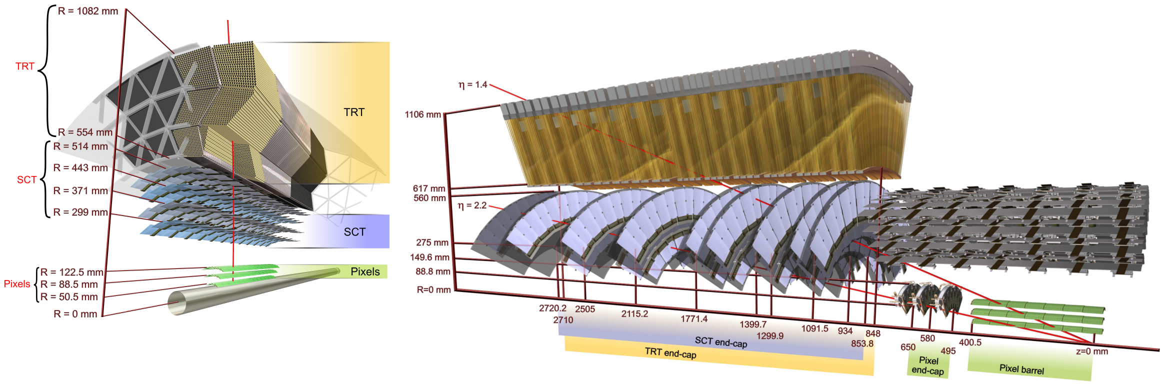

(a) **(b)**

Figure 3.4.: Schematic diagram of the Inner Detector [78].

The Pixel Detector

The silicon Pixel Detector is the innermost detector of the ATLAS located between 3.4 cm - 12.0 cm from the beam pipe. It consists of four pixel layers with a coverage of $|\eta| < 2.5$ [79]. The Insertable b-Layer (IBL), the innermost layer of Pixel Detector, was introduced during the first Long Shutdown of the LHC [3] and installed at 3.4 cm from the beam line. It directly improves the resolution of b-hardon tagging and also takes an important role for the pileup issues [80, 81]. [4] The three outer layers placed in the radii range larger 5 cm are referred B-Layer, Layer-1 and Layer-2 for a important role involved with the reconstruction of jets and τ. 1744 pixel modules with 47232 pixels on each module are building around 80 million readout channels. The operating voltages can be up to 600 V to cover detector efficiency in case of radiation damage. In addition, since the noise is very sensitive with the temperature, the operation temperature is requested to be as low as $-5\,^\circ\mathrm{C}$ to $.0\,^\circ\mathrm{C}$ in order to reduce the dark current [82].

The Silicon Microstrip Tracker (SCT)

The Silicon Microstrip Tracker is the second component of ID located in the central ID region with the radii range between 29.9 cm to 51.4 cm and a length of 14.9 cm. It is built of 4 088 modules with 6.3 million readout channels for a position measurment in two dimensions by 2 pairs of silicon p-in-n microstrip sensors and provide a coverage up to $|\eta| < 2.5$. The SCT and Pixel are often called the "Silicon Detectors", and the two detectors cover a same pseudorapidity range $|\eta| < 2.5$. They are used for precision measurement from the initial interaction point. The SCT is operated in a temperature range of $-10\,^\circ\mathrm{C}$ to $-5\,^\circ\mathrm{C}$ to reduce the noise from leeakage current [83].

Transition Radiation Tracker (TRT)

Transition Radiation Tracker is the outermost tracking system. It is a straw-tube tracker, that consists of 73 tubes in the barrel and 160 tubes in the end-cap, while the diameter of each tube is around 4 mm. The tube is filled by a gas mixture of 70 % xenon, 27 % carbon dioxide and 3 % oxygen [84]. TRT precisely measures each particle trajectory with the creation of the transition radiation, which depends on the Lorentz factor γ:

$$\gamma = \frac{1}{\sqrt{(1 - v^2/c^2)}}, \tag{3.4}$$

where v is the velocity of the particle and c is the speed of light in vacuum. Lorentz factor provides a parameter to distinguish electrons and the pions decaying to protons with the energy range 1 GeV - 200 GeV in the ATLAS detector. Electron candidates from photon conversions and Z boson decays are separated with the corresponding Lorentz factor of 10^3 - 10^4 and 10^5 respectively. While the pion candidates are selected with the criteria of a minimum of 20 TRT and four silicon hits to reject electrons and protons candidates. Additionally, the track selection for pion reduces the contamination from protons in low momentum region. Two different sets on thresholds for the TRT, low- and high-threshold. The low-threshold is used to identify electrons from the particles, while the high-threshold is used to identify a large energy transition radiation [85] [86].

3.2.2 The Calorimeter System

The Calorimeter measures energy of the particles. The Calorimeter System of ATLAS is installed around the inner track to absorb all incoming electrons, photons, and hadrons these from collision for paricle identication and energy measurment. It must prevent most of the particles from passing through

---

[3] A period of almost two years since February 2013.

[4] The quality of track recontruction and b tagging performance in high luminosity pileup environment provide a strong motivation for the IBL.

into muon detector. The calorimeter system covers a large pseudorapidity range η of 4.9. Two sub-detetor components with different technologies are employed as shown in the Fig. 3.5 which presents a composition of each calormeter sub-system. The electromagnetic calorimeter (ECAL) is designed to measure electrons and photons. The ECAL provide the precise three-dimentional position of the "electromagnetic (EM) showers" based on the $e^+ \; e^-$ pair creaion and Bremsstrahlung processes. The hadronic calorimeter (HCAL) is suited for hadrons reconstruction. The energy of the high energy hadrons is estimated by measuring the hadron showers. The HCAL is designed as a absorber for the hadron particles. Furthermore, thanks to the large η converage, the calorimeter system ensures a good missing transfer energy measurement for weakly interacting particles like neutrinos escaping detection.

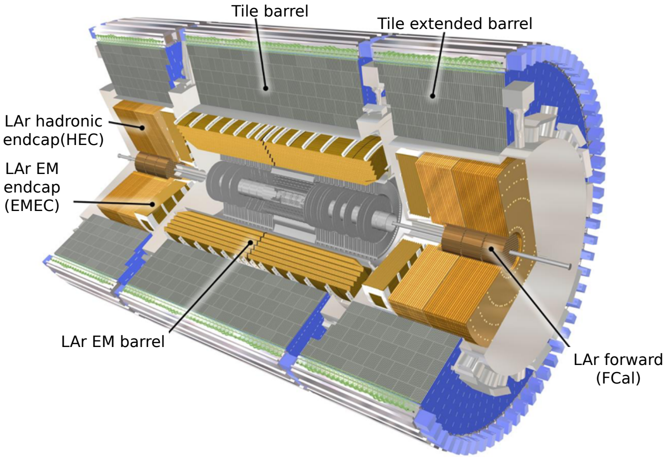

Figure 3.5.: Cut-away view of the ATLAS calorimeter system [87].

LAr Electromagnetic Calorimeter

Liquid Argon calorimeter (LAr) was chosen for the barrel and the two end-caps of the electromagnetic calorimeter (ECAL). The LAr is benefit in its intrinsic radiation-hardness, and high level resolution for the reconstruction of electron and photon objects [87, 88]. The LAr sampling calorimeter was built and interleaved with lead absorber plates and electrode. The size of gap of the electrode is 2.1 mm with a bias voltage of typically 2000 V, which correspond to the total drift time of 450 ns. The pseudorapidity converage of ECAL is divided into $|\eta| < 1.475$ for the Electromagnetic Barrel (EMB) and $1.375 < |\eta| < 3.2$ for the two Electromagnetic End-Caps (EMECs). The EMEC is further splited into two sub-calorimeters with a spacing of about 3 mm, the outer ring located in pseudorapidity range of $1.375 < |\eta| < 2.5$ and the inner ring of 2.5 to 3.2 in absolute η. The total thickness is overall 22 radiation length X_0, increasing from $22X_0$ to $33X_0$ and $24X_0$ to $38X_0$ for the EMB and the EMEC respectively. EMB and EMEC components described above are further divided in three layers based on the segmentation of cells in $\eta - \phi$ plane to present a good angular resolution. The innermost layer, is also referred to as strip layer, with a granularity of $\Delta\eta \times \Delta\phi = 0.0031 \times 0.098$ is suitable for the identification of $\pi^0 \to \gamma\gamma$ decays in the $6X_0$. The second layer with the cells of $\Delta\eta \times \Delta\phi = 0.025 \times 0.0245$ is the largest volume (16 X_0) used for providing a best resolution of enery measurment. The last layer is desiged to measure the tail of EM showers with a granularity of $\Delta\eta \times \Delta\phi = 0.05 \times 0.0245$. Futhurmore, the ECAL consist of an additional thin layer, so called presampler, located in front of three layers with coverage up to $|\eta| = 1.8$. The presampler is used to recover mainly the jet energy measuremen and The segmentation of the EMB is illustrated in Fig. 3.6. Energy resolution of ECAL is computed as $\sigma_E/E = 10\%/\sqrt{E/\text{ GeV}} \oplus 0.7\%$, which is an excellent performance on the energy resolution for the electrons and photons reconstruction.

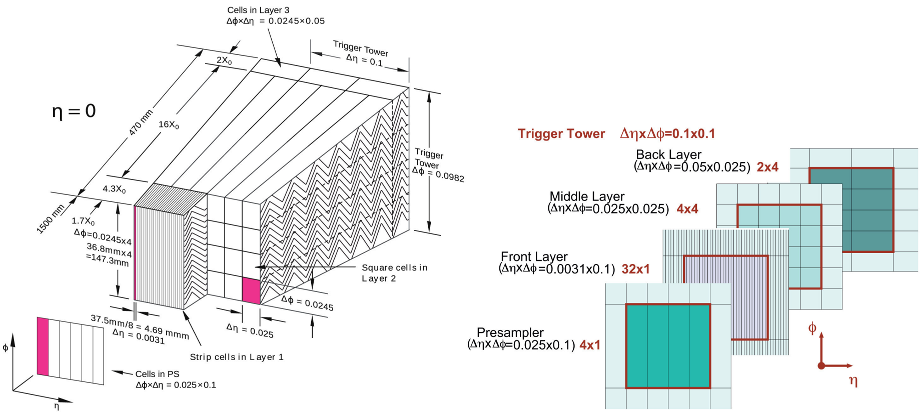

Figure 3.6.: An overview of the EM LAr calorimeter barrel module and The components of 4-layers in EMB, which are the Presampler, the fornt Layer, the middle Layer and the back Layer [87]. The front layer with a granularity of $\Delta\eta \times \Delta\phi = 0.0031 \times 0.098$ is suitable for the identification of $\pi^0 \to \gamma\gamma$ decays in the $6X_0$. The middle layer with the cells of $\Delta\eta \times \Delta\phi = 0.025 \times 0.0245$ is the largest volume (16 radiation lengths X_0) used for povideing a best resolution of enery measurment. The back layer is desiged to measure the tail of EM showers with a granularity of $\Delta\eta \times \Delta\phi = 0.05 \times 0.0245$.

Hadronic Calorimeter

The Hadronic Calorimeter (HCAL) is behind the LAr ECAL with three main components, Tile calorimeter (TileCal), LAr Hadronic End-Cap (HEC), and LAr forward calorimeter (FCAL). TileCal covers the region from $\eta < 1.7$ as a absorber and active material in the barrel parts of HCAL. The coverage for the HEC is $1.5 < \eta < 3.2$, while FCAL coverage is upto $3.1 < \eta < 4.9$. The significant overlaps between TileCal, HEC and FCAL are designed for a smooth transition with suppressing energy losses.

TileCal is a sampling calorimeter with steel layers and scintillators. It is positioned behind the EM calorimeter. It has a cylindrical structure with inner (outer) radius of 2280(4230) mm and 5 640 mm in length along the z-axis. The missing-energy, which plays a important role in many particle searches, depends on the acceptance of TileCal and its thickness. A approximately 30% of jets are captured by the TileCal. TileCal provides a good jet- and missing-energy measurement. The photo-multiplier tubes (PMTs) are used as the photon detectors.

HEC is a LAr ionization detector for the calibration accuracy on the jet energy resolution. HEC1 and HEC2 are the two wheel components of HEC. Thay are made of 32 identical wedge-shaped modeules with a small size read-out cell ($\Delta\eta \times \Delta\phi = 0.1 \times \pi/32$). It was designed with a good performance in a high radiation, high rate and low temperature environment.

Since the pseudorapidity range of FCAL is a very high, it is close to the beams axis. The three modules with electrode structures made with copper tubes and electrode rods are referred FCal1, FCal2 and FCal3. FCal1 is used for avoiding local heating to protect the liquid argon, while the roles for FCal2 and FCal3 are to have an precision measurement. It improves the resolution accuration of missing transverse energy, which is a key parameter for the much searches [89].

In term of resolution of HCAL, the overall energy resolutions, within a segmentation of $\Delta\eta \times \Delta\phi = 0.1 \times 0.1$, of the HCAL for hadronic jets are $\sigma_E/E = 53\%/\sqrt{E/\text{ GeV}} \oplus 6\%$, $\sigma_E/E = 50\%/\sqrt{E/\text{ GeV}} \oplus 3\%$, and $\sigma_E/E = 100\%/\sqrt{E/\text{ GeV}} \oplus 10\%$ for the TileCal, HEC and FCAL respectivily [90].

3.2.3 The Muon Spectrometer

The muon particle has very small interactions characteristic. It usually passes through the Electromagnetic Calorimeter or the Hadronic Calorimeter with small enregy deposit around 3 GeV. Therefore, the

Muon Spectrometer (MS) was located at the outermost part of the ATLAS detector to identify muons and measure the momentum. A large barrel magnet constructed around hadron calorimeter provide a pseudorapidity coverage range of $|\eta| < 1.4$. In the pseudorapidity range of $1.6 < |\eta| < 2.7$, the two end-cap magnet is inserted into both ends of barrel toroid. The transition interval region with pseudorapidity range of $1.4 < |\eta| < 1.6$ is covered to measure the momentum of the muons by magnetic deflection. The MS provides a overall pseudorapidity range up to $|\eta| < 2.7$ with three large toroids which generate the magnetic field. The field strength for MS is estimated from the muon trajectory given by $\int \overrightarrow{B} d\overrightarrow{s}$, where the B is the normalized field to the muon direction s. The field range are 1.5 Tm to 5.5 Tm and 1.0 Tm to 7.5 Tm in barrel and endcap magnetic toroids respectively.

The global view of the Muon Spectrometer are presented in Fig. 3.7. Monitored Drift Tubes (MDT) provides a precision measurement of the muon trajectory and the muon momentum, while Cathode Strip Chambers (CSC) occupies the forward region designed to replace MDT for the regions of high particle densities. Resistive Plate Chambers (RPC), and Thin Gap Chambers (TGC) are the trigger system of the MS used in the barrel and end-cap regions respectively [91]. The futher detail are presented in following subsection.

Monitored Drift Tubes (MDT)

MDT performes the precision measurement of muon momentum in the coverage $|\eta| < 2.7$. It consists of the aluminum tubes with 3 cm diameter and length in the range 0.9 to 6.2 m. The chambers are filled with the gas maxture of Ar-CO$_2$ (93% and 7%) in 3 bar absolute pressure. In high luminosity environment, the resolution range with multi-layers reaches approximately 40 μm. An MDT chamber is constituted by six layers of drift tubes which are arranged on the both sides of a support structure to against background and ensures a good discovery potential of signal at the TeV scale [92].

Cadcade Strip Chamners (CSC))

The four-layered CSCs are multi-wire proportional chambers with a coverage of $2.0 < |\eta| < 2.7$. Overall 16 CSCs located on each end-cap offer high rate capability and excellent spatial resolution. A gas mixture of Ar-CO$_2$ (80% and 20%) is used to fill chambers with a high voltage of 1900 V. Both cathodes are segmented; one with the strips perpendicular to the wires and the other parallel to the wires. The resolution for the muon trajectory is better than 50 μm on bending plane.

Resistive Plate Chambers (RPC)

The RPCs with 596 RPC chambers and 355000 read-out channels are used for triggering signals in the barrel region with the coverage $|\eta| < 1.05$. The low-($p_{\mathrm{T}} > 6$ GeV) and high-momentum ($p_{\mathrm{T}} > 20$ GeV) thresholds are built by three stations located near the magnetic field region and outer radius of the magnet. It provides the trigger with the good discrimination on the muon transverse momentum p_{T}. The typical spatial and timing resolution achieved by a RPC chamber are 1 cm and 2 ns, respectively.

Thin Gap Chambers (TGC)

TGC provides the Level-1 muon trigger in the end-cap with the coverage of $1.05 < |\eta| < 2.7$. The chamber uses the highly quenching gas maxture of CO$_2$ (55%) and n-pentane (45%). The anode-cathode gaps of TGSs (around 1.4 mm) is smaller than the wire spacing (1.8 mm) for the goal to obtain the best time resolution with the lowest operating voltage of 3.1 kV. Typical time resolution is around 4 ns rms for the efficiency of 98% [93].

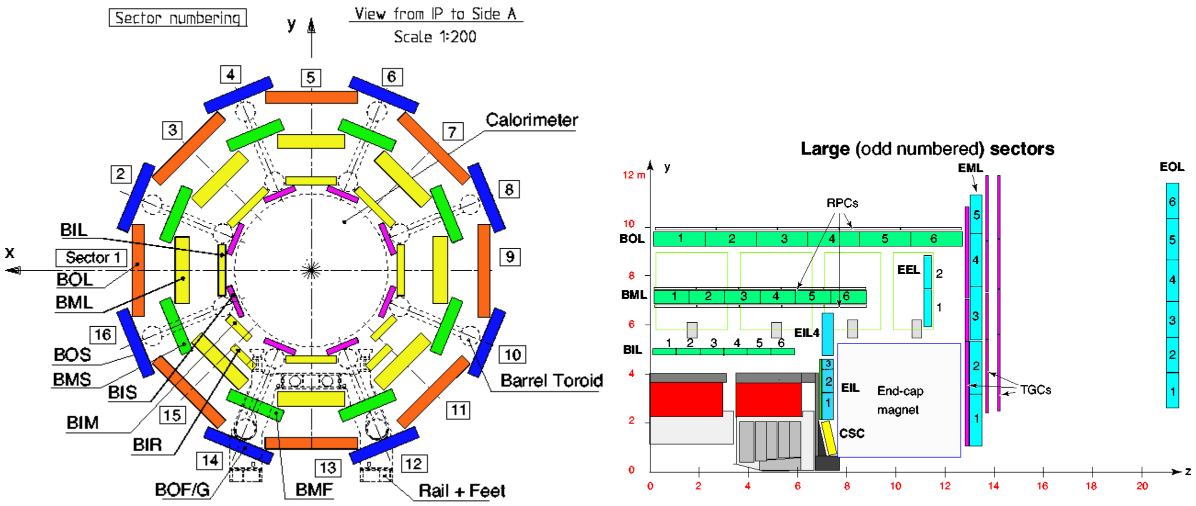

(a) (b)

Figure 3.7.: Schematic diagram of the barrel part of the muon Spectrometer (left) and the overview in y-z plane (right) [94].

3.2.4 Forward Detectors for Luminosity Measurement

The Forward Detectors consist of three small sub-detectors, LUCID[5], ZDC[6] and ALFA[7]. They cover the forward region of the ATLAS [95]. The LUCID is located at the distance of 17m from the IP for a high acceptance and time resolution for the events. It is the dedicated detector for luminosity monitoring and requested to have the good resistance to the extreme radiation of $60-70$ kGray per year [8]. The main purpose of LUCID is designed to detect proton-proton inelastic scattering in the IP. ALFA is designed to determine the elastic proton-proton scattering at very small angles. [9]

An overview of the Forward Detectors is shown in Fig. 3.8.

3.2.5 The Trigger System and Dada Acquisition System

In the LHC Run2 data taking period, the bunch spacing of protons is 25 ns. It results the collision rate at the ATLAS detector is around 40 MHz. Considering the average size for the raw data is approximate 1.6 megabytes (MByte) per event, the bandwidth of more than 50 terabytes (TByte) per second for storing them [98]. This is far away from the limitation on the bandwidth of the data storage and achievable computing resources at CERN. Furthermore, there are huge amount of inelastic scattering processes, therefore, a fast and efficient trigger system is extremely essential. The trigger and data acquisition system (TDAQ) consists of a hardware-based first-level trigger (Level-1 trigger) and a software-based high-level trigger (HLT) to select major interest events from the hard scattered collision. The data flow of the system ATLAS TDAQ in Run2 is shown in Fig. 3.9.

The Level-1 trigger is deployed to fastly reduce the collision rate from 40 MHz to 100 kHz in the first stage by the muon detectors and the calorimeter with a latency of less than 2.5 μs [99]. Regions of Interest (RoI), which is used to determine the acception of events for the adjudgment of further processing, is then collected from the 100 kHz dataset by the ATLAS Region of Interest Builder. Level-1 trigger

---

[5] LUminosity measurement using Cerenkov Integrating Detector

[6] Zero-Degree Calorimeter

[7] Absolute Luminosity For ATLAS

[8] “Gray” is a derived unit of ionizing radiation. The design for PMTs is $3-5$ kGray per year

[9] ALFA is located at the distance of approximately 240 m at both sides of the ATLAS IP. It is also related with a total proton-proton cross section based on the optical theorem given in the following function [96]. For the LHC beam, the protons at very small angles corresponds to a very small t-values ($t = 0$).

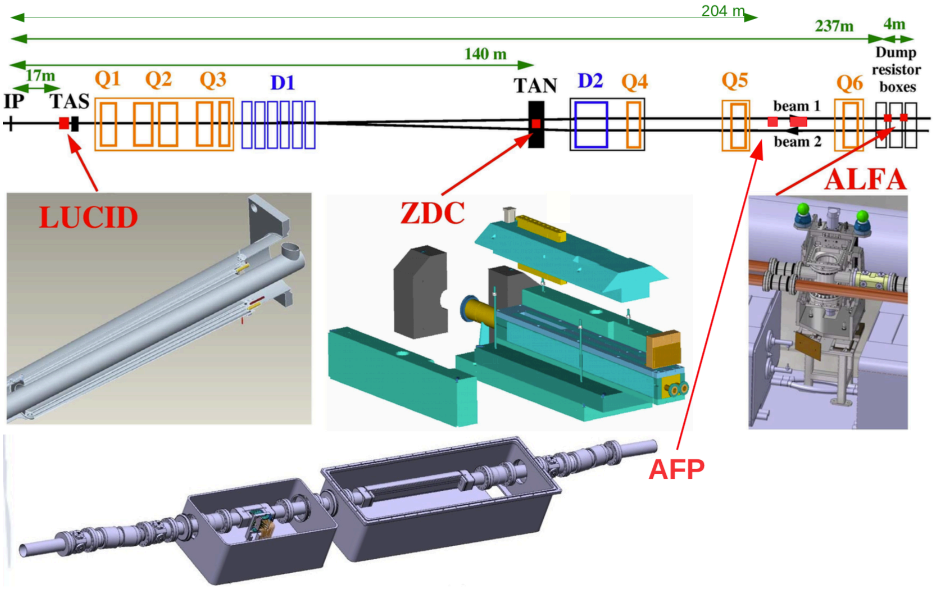

Figure 3.8.: Overview of the ATLAS Forward Detectors with the position description of four sub-detectors from IP [97].

system consists of the three main sub-trigger systems, L1 calorimeter system (L1Calo), L1 muon trigger system (L1Muon) and L1 topological trigger modules (L1Topo). L1Calo uses calorimeter information to search for high transverse-momentum electrons, photons, jets, and hadronic τ leptons, as well as large missing transverse energy. The reconstruction of the input for L1Calo is based on a segmented blocks of combined calorimeter cells called "Trigger Towers" (TT). The 7200 trigger towers are built with a granularity of 0.1×0.1 in the η-ϕ range of the electromagnetic and hadronic calorimeters. The sliding window algorithms based on TT and programmable thresholds are used to identify the electron and γ with the EM calorimeter, while the τ candidate is defined based on same TT window size with the hadronic calorimeter. L1 jets are determined with both hadronic calorimeter and EM calorimeter. "L1Muon" makes fast decisions on a muon candidate based on the signals exceeds a piece of predefined threshold information on the RPC and TGC. (see Section 3.2.3) Finally, L1 missing transverse energy trigger (L1XE) provides a missing transverse energy based on the vectorial sum of the TT energy of the full L1 candidates. L1Topo combines output from L1Calo and L1Muon objects to apply topological event selections at Level-1 [100].

The further process of TDAQ is a software-based trigger, High-Level Trigger (HLT), with a average recording rate of $\sim$ 1 kHz. The HLT applys offline reconstruction algorithms with the RoI defined at Level-1 and makes the final decision to store into data cernter [10] [101]. The trigged event is transferred to the Tier-0 computing center for the final event reconstruction. The HLT runs on a conventional computer cluster with up to approximately 40000 CPU cores and take about 200 ms on average of the processing time per an event [102].

3.3 Data Recorded of LHC Full Run 2

After the first Long Shutdown for the maintenance and the detector upgrade, LHC attempted to restart with the increasing center-of-mass energy up to a maximum collision energy $\sqrt{s} = 14\,\text{TeV}$ [11]. LHC is

---

[10] *Tier-0* is the CERN Data Centre for the raw data from the online DAQ system.

[11] ATLAS records data corresponding total integrated luminosity of 25 fb^{-1} at the centre-of-mass energy $\sqrt{s} = 7\,\text{TeV}$ and $8\,\text{TeV}$ during 2011 and 2012, so called as *Run1*, respectively.

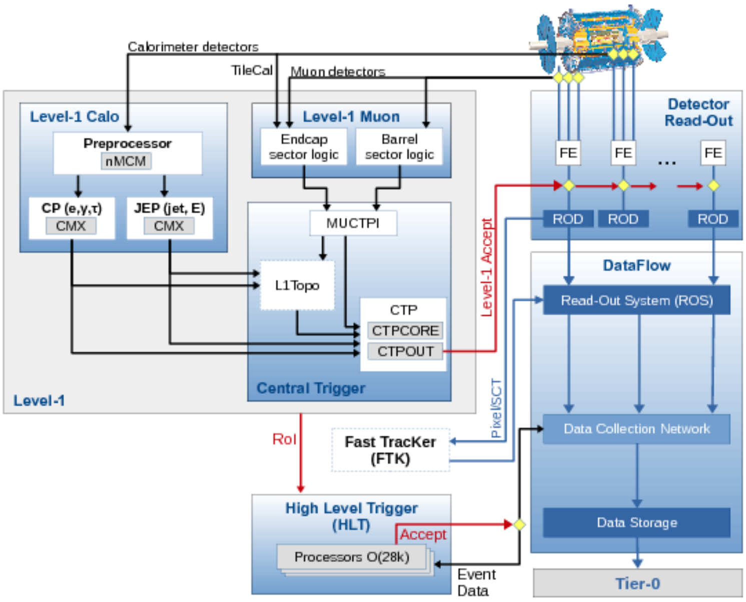

Figure 3.9.: The overview for the ATLAS trigger system in Run2, while the L1Topo (topological trigger) and FTK (Fast Tracker) in the illustration were being commissioned since 2015 and not used anymore [103].

designed initially and expected to get a better sensitivity on the discovery of the Higgs particles and the study of rare events at a high collision energy $\sqrt{s} = 14$ TeV. However, the super higher the magnetic field and electric current in the magnet's superconducting coils cause a issue that retraining to 14 TeV would take much longer time away from physics research compare with retraining to 13 TeV. Finally, taking the expected integrated luminosity reduction[12] for operation to 14 TeV into consideration, CERN decides to choose 13 TeV for getting to new results quickly [104, 105].

The LHC is designed with the specifications on the bunch spacing of 25 ns, which corresponds to an achieved peak luminosity of $1 \times 10^{34} cm^{-2} s^{-1}$. The recored data on the operation with the bunch spacing of 50 ns was employed in early 2015. They are used for the previous studies of the gradual effect reduction, such as the source from pressure rise and beam instability. An achieved peak luminosity in the study is $7.7 \times 10^{33} cm^{-2} s^{-1}$ for the bunch spacing of 50 ns results the separation technology has to be considered due to the different calibration.These data corresponding to a small integrated luminosity (about 0.1 fb^{-1}) are not considered in this analysis. Furthermore, the data recording with small luminosity (0.2 fb^{-1}) in two runs of 2015 is also not used in this analysis due to the technical problem the IBL [13] during the data taking. The bunch spacing of 25 ns is selected for 2017 and 2018 runs at $\sqrt{s}$ =13 TeV. In 2017, the LHC was operated with “8b4e” bunch train operation [14] to investigate the effect from peak luminosity and pileup [106]. This analysis only uses the dataset after good quality checking of the ATLAS. [15] An integrated luminosity of 139 fb^{-1} is measured by the LUCID-2 detector described in Sec. 3.2.4 [105] with 1.7% error given. An overview for the total integrated luminosity recorded by ATLAS from 2015 to 2018 and the one certified to be good quality data for physics is shown in Fig. 3.10(a). Table 3.1 shows an overview of the luminosities for each year, together with the LHC parameters.

The number of proton-proton interactions occurring per bunch crossing (μ), which is calculated using the following function, highly relates with the instantaneous luminosity and referred as *in-time pile-up*

---

[12] Approximately 21% to 37% compared to 13 TeV case. The study is based on the performance for 1 year before Long Shutdown 2

[13] The reason for the low data quality efficiency of 2015 data taking

[14] A pattern of eight bunches separated by 25 ns followed by a four bunch-slot gap.

[15] The good quality checking of the ATLAS is called as *Good Runs Lists* (GRL).

Parameter	2015	2016	2017	2018
Bunch spacing (ns)	25	25	25	25
Peak luminosity (10^{33} $cm^{-2}s^{-1}$)	5	13	16	19
Peak number of inelastic interactions ($\langle\mu\rangle$)	$\sim$ 16	$\sim$ 41	$\sim$ 45	$\sim$ 55
Integrated luminosity (fb^{-1})	3.2	33.9	43.8	60.1

Table 3.1.: LHC parameters for pp collisions at $\sqrt{s}$ =13 TeV in 2015–2018 The physics data delivered during 2015 with 50 ns and the 2015 data with technical problem are not listed [104].

(PU) [16].

$$\mu = \frac{L \times \sigma_{\text{inel}}}{N_b f_r}, \tag{3.5}$$

where L is the luminosity, σ_{inel} is the total inelastic cross-section, N_b is the number of colliding bunches and f_r is the frequency. The average μ is summarized in Table 3.1. The measured mean number of interaction per bunch-crossing for the recorded data 2015-2018 by ATLAS is shown in Fig. 3.10(b).

On the other hand, out-of-time PU is occurring before or after the interesting collision. It might affect the signal in the collision of interest if the detectors are sensitive. Two independent sources of PU are the significant background to the events, which impact the event reconstruction or trigger performance in the ATLAS. The corrections for the PU effect are considered in the ATLAS simulation step based on the superimposing and overlap techniques for In-time PU and Out-of-time PU, respectively [107, 108]. The uncertainty of the calibration is discussed in Sec. 7.1.

After the trigger application at the “Point 1” of CERN discussed in Sec. 3.2.5, the recorded data is stored in the ”Tier-0” center as the ATLAS *Raw* data [109]. The prompt reconstruction for each physics object is applied to the ATLAS *Raw* data and stored as Analysis object data (*AOD*). The derivation frameworks are built by *Athena* software to reduce the *AOD* datasets of petabyte size to the derivated-*AOD*, which is called as *DAOD*. The *AOD* datasets sized to *DAOD* datasets of terabyte size in the derivation steps by *skimming*, *slimming* and *thinning* [110]. The dedicated *DAOD* samples for Higgs search are used in this analysis by the *ROOT*-based analysis frameworks with calibrations and common object selections.

---

[16] In-time PU is several additional proton-proton collisions occurring in the same bunch crossing.

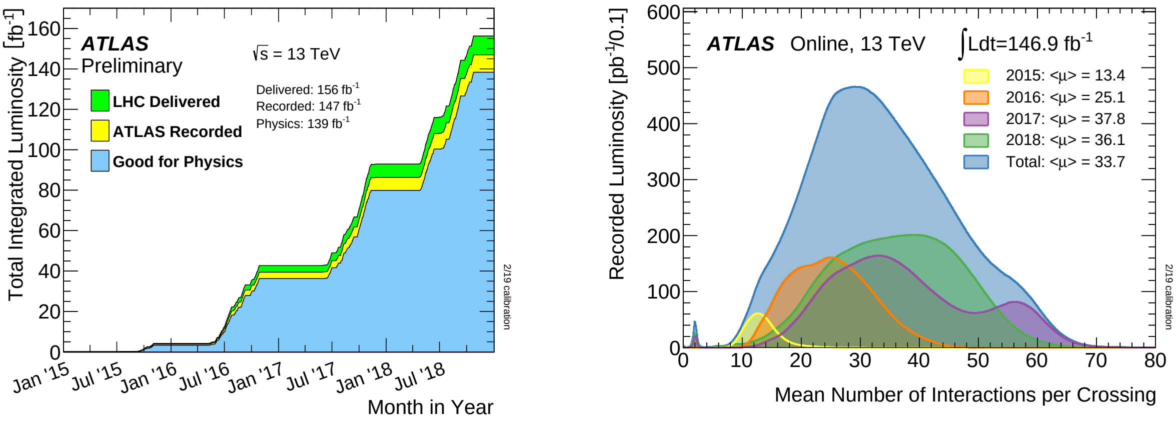

(a) **(b)**

Figure 3.10.: (a) is the cumulative luminosity versus time. The delivered data by the LHC (Green), recorded data by the ATLAS (yellow), and certified data (blue) by the ATLAS are present for pp collisions at 13 TeV during 2015-2018. (b) shows the luminosity-weighted distribution of mean number of interaction per bunch crossing for for 2015-2018 recorded data. The $\langle\mu\rangle$ for 2017-2018 data are both larger than 40, that shows the PU is obviously higher than the one for 2015 data [111].

4 Physics Object Reconstruction

The raw data information recorded by the ATLAS detector is translated into physics quantities through the sequence of reconstruction, identification and calibration. Though it is partially performed at the trigger level, the recorded events are further elaborated by the sophisticated off-line algorithms. The particles reconstructed by the off-line algorithms are referred to as “object”. Following the “online requirements” of the detectors, such as TDAQ (See Sec. 3.2.5), three important processes of reconstruction, identification and calibration (so called as “online algorithms”) define the physics objects. The off-line algorithm is built by the ATLAS dedicated software framework, so-called *Athena* framework. The main purpose of the identification algorithm is made to maximize the performance with the reduction power for mis-reconstructed objects and the identification efficiency. The calibration process is applied to correct the differences of the reconstruction and identification efficiencies.

In the $H/A \to \tau_{\text{had}}\tau_{\text{had}}$ search, the jets and hadronic τ objects play the major roles. This section overviews the procedures regarding to the object definitions. They are discussed in Sec. 4.2 and Sec. 4.5. The lower-level object like tracks or vertex are also described in Sec. 4.1. In order to suppress backgrounds, other objects, such as electrons and muons, are used in this analysis. The algorithms for electrons and muons are discussed in Sec. 4.3 and Sec. 4.4. In Sec. 4.7, the missing transverse energy (MET) is also described.

4.1 Low-Level Objects

Analysis-level objects are built in the reconstruction and identification with low-level objects, such as tracks, vertices and calorimeter clusters. The performance of the low-level object reconstruction highly depends on the resolution of the detectors. The Sec. 4.1.1 provides a description about the definition of the track reconstruction [112].The vertex candidates are defined based on the reconstruction of charged-particle tracks in the Inner Detector and presented in Sec. 4.1.2 [113]. Furthermore, the Sec. 4.1.3 shows the clustering algorithm based on the the information of electromagnetic and hadronic showers detected by ECAL and HCAL for jet and MET reconstructions.

4.1.1 Track Reconstruction

The charged track is a fundamental unit various off-line particle reconstructions. Standard tracks used in ATLAS, which are reconstructed by hits created in the inner detector (ID), are referred to as ID tracks. In the ATLAS, the inside-out track is the main sequence used for the track reconstruction of the primary charged particles to the interaction point. The inside-out algorithm is built using the hit information in the innermost layers of the Pixel detector and the outer layers of the SCT for the track candidates. The hits in a space of Pixel detector and the SCT are detected as a cluster, and the TRT provides the information at the higher radii. Hits from a particle are identified and merged using a combination of a pattern recognition technique called connected component analysis (CCA) [114, 115] and a neural network classifier (NN) [116]. More neighboring pixel hits are considered as a CCA cluster in eight cells of Pixel Detector and also provide the position information by CCA. The strategy for the optimization of track quality is based on the basic criteria of the number of associated track measured by the pixel and SCT detectors. The track quality of the χ_2 fitter also need to be satisfied to remove track duplicates and the fake tracks [117]. The clusters are assembled from the measurement of the ID and the SCT by the CCA, and then the loss of identification efficiency for the merged clusters is minimized by the NN. Based on the three-dimensional position information and the readout charge associated to each hit in the silicon detectors, spatial charge profile is constructed. The CCA and NN tools, have been introduced since Run1 studies, make a precise three-dimensional measurement of the position of charged particles possible.

For a further separations of high p_{T} jets and τ-leptons in the search for new heavy particles decaying to highly boosted objects, a dedicated environments (TIDE) [112] is used from Run2 to cope with the dense particle environment. The TIDE is a dedicated algorithm of track reconstruction for the denser particle environment and provides a significant improvement for high p_{T} track reconstruction. Figure 4.1 shows the reconstruction efficiency of tracks for τ lepton which are the important objects in this search.

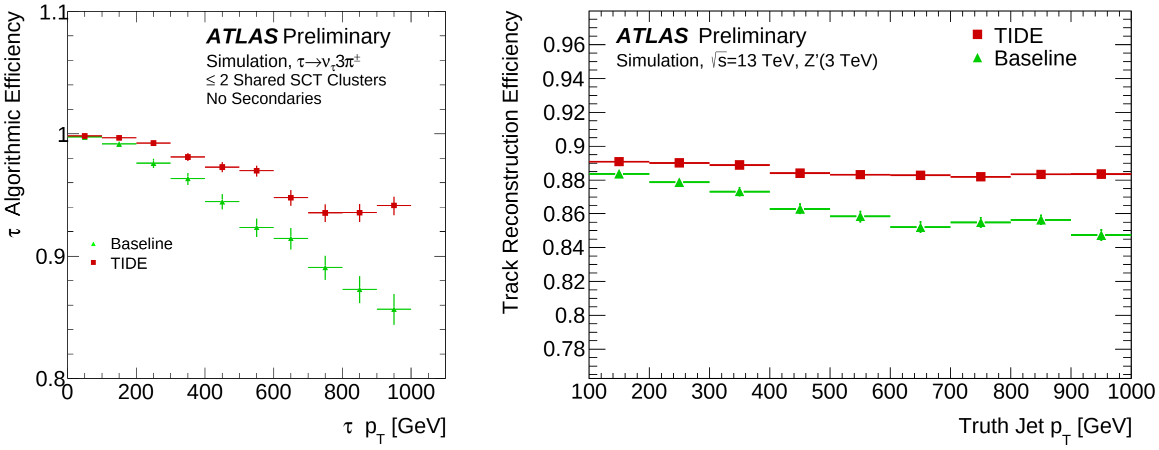

(a) (b)

Figure 4.1.: (a) is the efficiency to reconstruct all decay products of τ with three charged tracks. (b) shows the result of the average efficiency of track reconstruction and observed the significant increasing in efficiency for high p_{T} jet momenta [112].

4.1.2 Primary Vertices Reconstruction

A precise reconstruction of positions on primary vertices (PVs), which are locations of inelastic proton-proton collisions, is important. Accurate assignment of charged-particle trajectories to the correct primary vertex is essential to reconstruct a full kinematics property of an event. The reconstruction of PV is based on the reconstruction of charged tracks described in Sec. 4.1.1. There are the quality requirements in PV reconstruction for the track such as the cuts in p_{T} and the number of hits of the sub-detectors. There two steps for the PV reconstruction; vertex finding algorithm [118] and vertex fitting algorithm [119], for associating reconstructed tracks to the vertex candidates and reconstructing the vertex position with the fitting quality respectively. The best vertex position of PV is determined with selected tracks in the three-dimensional information and required to have at least two associated tracks. The PV position is also often used as the initial point of the objects in the analysis. The overall efficiency of PV reconstruction is sufficiently high as shown in Fig. 4.2.

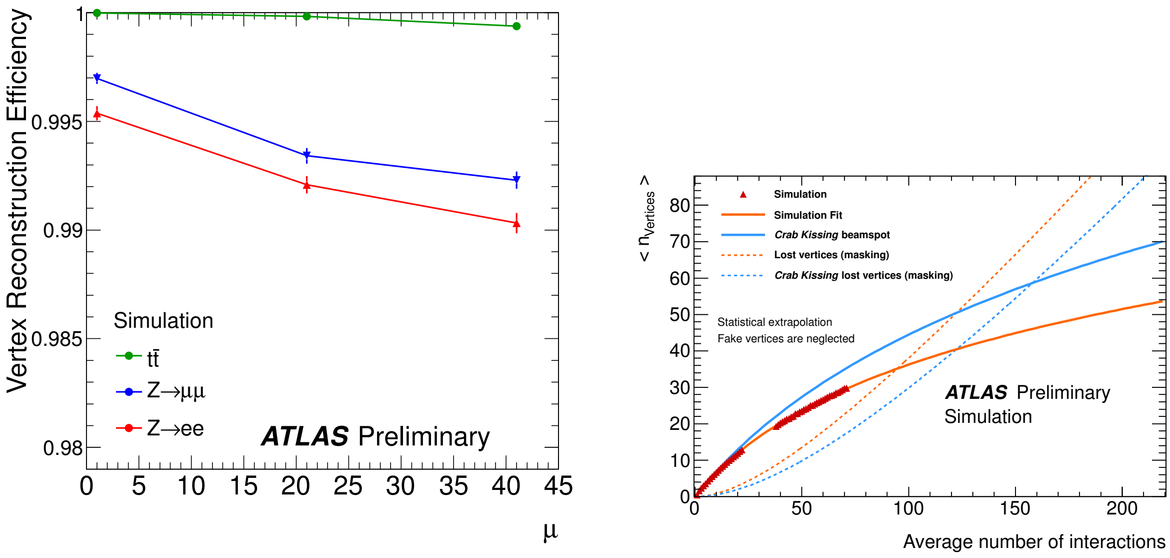

(a) **(b)**

Figure 4.2.: (a) is the efficiency to reconstruct the hard-scatter interaction vertex as a function of the number of interactions per bunch crossing per bunch crossing. (b) is the expected average number of reconstructed vertices with high-μ data taking runs in the future [120].

4.1.3 Calorimeter Clusters

In order to reconstruct the hadronically decaying τ and jet objects, a three-dimensional topological clustering (Top-Cluster or TC for short) of cell signals with a signal-significance pattern based on the shower information of ECAL and HCAL system is used. Topo-cluster is a basic unit of energy measurement in the calorimeters and used as the input for jet clustering. It is formed by three-dimensionally grouping cells with significant energy deposit. The clusters of the TC are used to connect the information of the calorimeter cells to reconstruct a final state with isolated hadrons, jets and hadronically decaying τ leptons. Therefore, the signal of the calorimeter cell can largely improve the performance for jet and missing transverse momentum reconstruction. The signal significance algorithm is made by highly granular calorimeter system (See Sec. 3.2.2) for removing the background like the electronic noise, the noise from pile-up sources and other insignificant signals which are not close enough with the significant signal cells. Figure. 4.3 shows the expected noise in the different sub-detectors with two different μ settings. The signal significance for a cell is given by the following formula:

$$\varsigma_{cell}^{EM} = \frac{E_{cell}^{EM}}{\sigma_{noise,cell}^{EM}}, \tag{4.1}$$

where the average expected noise in this cell $\sigma_{\mathrm{noise,cell}}^{EM}$, and the signal of the cell E_{cell}^{EM} are measured on the electromagnetic (EM) energy scale. Three parameters {S,N,P} with a set of default values {4,2,0} are defined as the boundary features of topo-clusters as shown below.

- $\varsigma_{\mathrm{cell}}^{EM} > \mathrm{S}$: The first and primary threshold for all the cells to select seed cells passing this threshold. The corresponding cluster is called "proto-cluster". The proto-cluster is defined to include only a core of cells with highly $\varsigma_{\mathrm{cell}}^{EM} > \mathrm{S}$.
- $\varsigma_{\mathrm{cell}}^{EM} > \mathrm{N}$: The neighbouring cells of the seed are subsequently merged to the seed if they passed this threshold.

- $\varsigma^{EM}_{\text{cell}} > \text{P}$: If a seed cell, satisfying with this threshold, is a neighbour of two proto-cluster, the two proto-clusters are merged.

The spatial signal structures of the large proto-cluster are ignored when the more than an injecting energy into the cell is identified as a single signal maximum. The proto-clusters with multi-local maximal seed cell are split to another cluster in the three dimensions. The threshold definition of local signal maximum for the splitting is $E^{\text{EM}}_{\text{cell}} > 500$ MeV. In addition, the cell with at least four neighbors and no larger signal in the neighbors are required. The proto-cluster after the splitting step corresponds to TC. The direction of TC is reconstructed as $(\eta_{\text{clus}}, \phi_{\text{clus}})$ and used for the shower axis measurement of the incoming particles. It plays an important role to build the cluster signal used to the calibrations and corrections. The precise measurement is sensitive to the calibrations of missing transverse momentum and improves the cluster energy resolution. The calibrations are related to cell signal weighting, which is called "Local Hadronic Cell Weighting" (LCW). It is built for the energy scale based on the comparison of energy distribution between data and MC. The TC with a good performance and well-modeled by simulation after all the calibrations have been introduced in [121]. In this search, TC with energy scale and LCW are used in the jets and τ lepton reconstruction described in the following section.

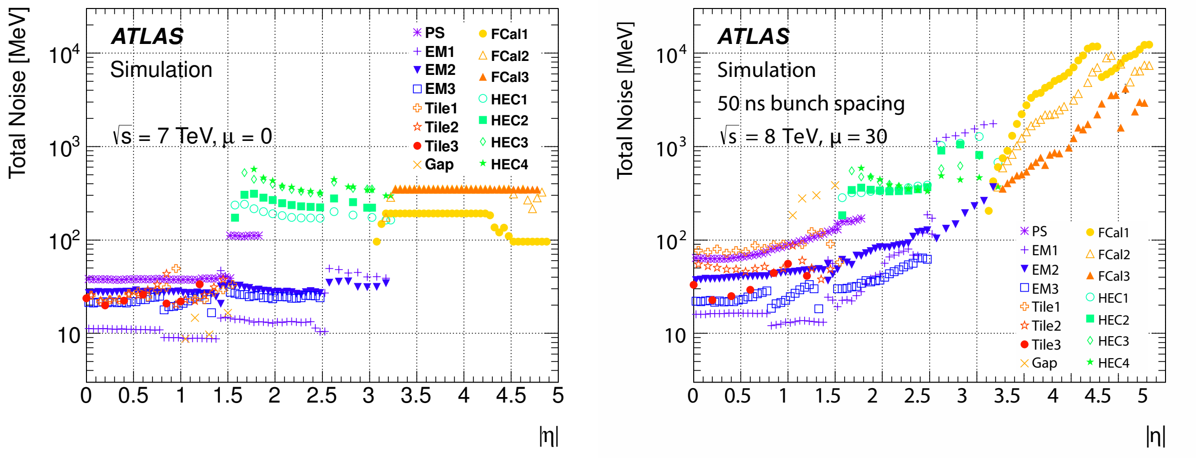

(a)

(b)

Figure 4.3.: The expected energy noise as a function of $|\eta|$ for the cell on the electromagnetic (EM) scale for each sub-detector. The one with $\mu = 0$ configuration is shown in 4.3(a), while 4.3(b) is with the configuration of $\mu = 30$ [121].

4.2 Jets

Jets are reconstructed using the topo-clusters calibrated with EM scale and LCW as described in Sec. 4.1.3. Several main components of the jets reconstruction are introduced in this section. The algorithm for the reconstruction is defined in Sec. 4.2.1. The identification of jets so-called flavor tagging is shown in Sec. 4.2.3. And, a detail of the jets calibration is described in Sec. 4.2.2.

4.2.1 Jet Reconstruction and Clustering Definition

The topo-clusters after the calibration in the previous section are used for jet reconstruction. The jet reconstruction is implemented in the FastJet software package with the anti-k_t clustering algorithm [122–124]. The anti-k_t algorithms are used for consisting the group's pairs of *proto-jets* to form a new *proto-jet*. It labels the combined *proto-jet* as a "jet" object. There is no other additional manipulation applied.

The nearby *proto-jets* in (p_{T} , η, ϕ) space are defined as a group pair of *proto-jets* shown in Eq. 4.2.

$$d_{ij} = min({p_{\mathrm{T}}}_i^{-2}, {p_{\mathrm{T}}}_j^{-2})\frac{\Delta R_{i,j}^2}{r^2}, \tag{4.2}$$

where $\Delta R_{i,j}^2$ is an angular distinace between two *proto-jets* in η-ϕ plane calculated by $\sqrt{(\Delta\eta)^2 + (\Delta\phi)^2}$. A radius parameter of the algorithm is defined as r with a default value of 0.4. If the angular distance $\Delta R_{i,j}^2$ is smaller than the distance between the *proto-jet* i and the beam (d_{iB}), the pair of *proto-jets* i, j is grouped into a new *proto-jet*. This process continues until clusters are associated with one jet.

4.2.2 Jet Calibration

As the energy of TC is calibrated in the EM scale, the clustered jet needs an additional calibration based on the hadronic interaction activity. Particle-level jet in simulated events (referred as "truth jet") are used for the reference of the truth energy. They are clustered by the same algorithm (anti-k_t with r of 0.4) using only stable and final-state particles as input. The input particles are required to have a life-time of $c\tau > 10$ mm. The muon neutrinos and particles from pile-up activity are excluded [125]. A series of dedicated calibration procedures is employed to restore the energy to that of the truth jets reconstructed at the particle-level energy scale. It proceeds as following stages.

Origin Correction

The origin correction forces the four-momentum of the jet to point to the hard-scatter primary vertex rather than to the center of the detector, while keeping the jet energy constant. Despite the default angular coordinate of TC for the energy of particles is to point at the IP position or the center of the detector, the jet direction is recalculated based on the primary vertex position that the jet is associated with. This correction significantly improves the η resolution.

Pile-up Correction

Effects of pile-up events provide an unexpected background from the low-energy particles. The contribution of the particles from pile-up jets is removed using the method of area-based density subtraction. The jet-area is a way of measuring its susceptibility to contamination from soft radiation. The "ghost" particles in jet area is defined as the infinitesimally soft particles ($p_{\mathrm{T}} = \mathcal{O}(10^{-100}$ GeV)) with four-momenta g_i and transverse momentum density ν_g within jet j. The four-momentum of jet area A_j can be written as $A_j = \frac{\mathrm{Number of ghosts}}{\nu_g}$ and provides the effect from pile-up. Pile-up contributions to the measured jet energies are accounted for by using a two step procedure. First, the effect of pile-up is corrected for in the reconstructed jet energy using the average energy density in the event and the area of the jet. Second, a residual correction is applied to remove the remaining dependence of the jet energy on the number of reconstructed primary vertexes, N_{PV}, and the expected average number of interactions per bunch crossing, μ. The pT density subtraction discussed below is applied to reduce pile-up jets:

$$p_{\mathrm{T}}^{corr.} = p_{\mathrm{T}}^{reco} - \rho \cdot A, \tag{4.3}$$

where transverse momentum before and after correction of jet are $p_{\mathrm{T}}^{corr.}$ and p_{T}^{reco}, while ρ is average p_{T} density measured in the event.

The pile-up correction on p_{T} is defined as the following function after the pile-up suppression:

$$p_{\mathrm{T}}^{corr.} = p_{\mathrm{T}}^{reco} - \rho \times A - \alpha(p_{\mathrm{T}}, \eta) \times (N_{\mathrm{PV}} - 1) - \beta(p_{\mathrm{T}}, \eta) \times \mu. \tag{4.4}$$

The pile-up correction is determined using the simulation as function of p_{T} and η and linear coefficients α and β. Figure. 4.4 shows the simulation distribution before and after corrections.

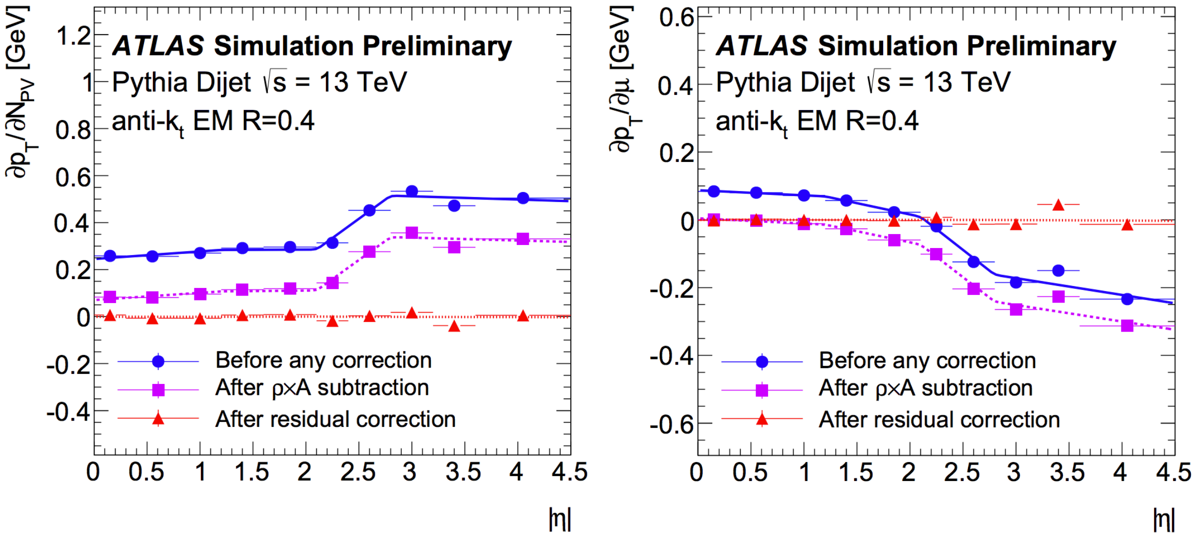

(a) (b)

Figure 4.4.: The p_{T} distributions before and after subtraction and correction. (a) shows the effect on in-time pile-up, and (b) is for the one on out-of-time pile-up as a function of jet η [125].

Jet energy scale and and η calibration

The reconstructed jet energy is corrected to the particle-level jet energy using MC simulation. In addition, a correction is applied to the reconstructed jet pseudo-rapidity to account for the biases caused by the transition between different calorimeter regions and the differences in calorimeter granularity. The calibration factor is a response with the Gaussian fitting result on E_T^{reco}/E_T^{true} distribution of jets, where E_T^{reco} and E_T^{true} are the transverse energies of reconstructed jet and truth jet, respectively. The output is binned in various p_{T} and η for correcting the reconstructed jet energy to the truth jet energy. These jet energy scale (JES) and calibration in η are employed in simulation step and the very small uncertainty [1] is considered in this search. Figure 4.5 shows the average energy response.

Global Sequential Calibration

The Global Sequential Calibration (GSC) corrects the jet four-momenta to reduce the response dependence on the flavour of the initiated-jet parton. The GCS is determined using the following information: The significant improvement of resolution of energy is expected with further information from muon spectrometer as well as the inner detector. GSC consists of the five stages for the jet response on each item in following table:

- The energy of HCAL.
- The energy of ECAL.
- The number of tracks with $p_T > 1GeV$.
- Average distance of all tracks in the $\eta - \phi$ plane from the jet.
- The number of muon track.

---

[1] Around 1% for the jet with p_{T} of 20GeV and much smaller than 1% with increasing p_{T}

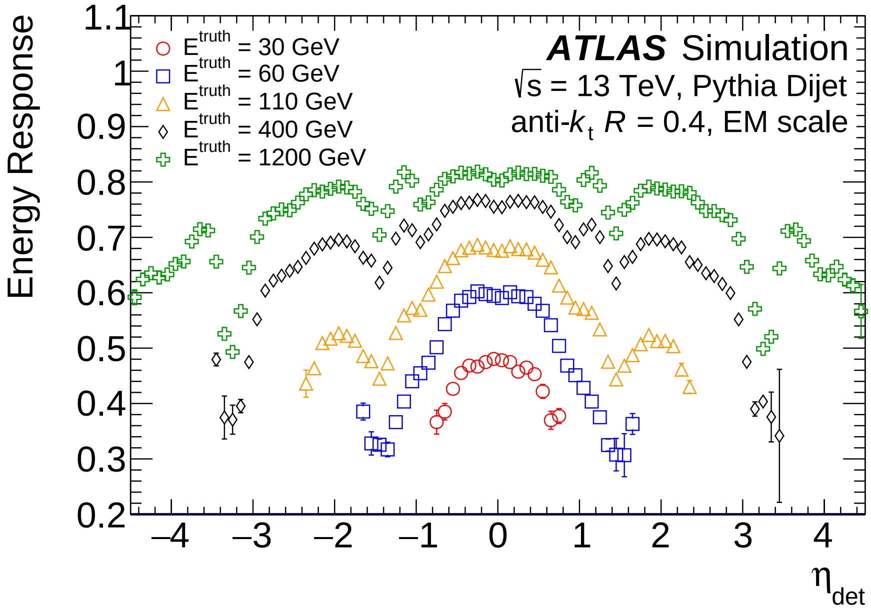

Figure 4.5.: The average energy response as a function of η for jets after applying origin correction and pile-up correction discussed in the previous items [125].

GSC is an extension of main jet calibrations like EM scale, LCW, and JES. It improves the jet performance with more information about the energy in the calorimeter and track information from the other detectors. After the full stages of GSC applied, the deviations between data and Monte Carlo [2] is within 2-4%.

In-Situ Calibration

The *In-Situ* calibration applied to data for the combined measurement of data-to-MC ratio in the jet p_T distribution is the final calibration discussed in this section. The γ/Z+jet and multijet processes corresponding with the physics objects (photons, Z bosons or jets) in the transverse plane are used for finding the correction which is applied to jets reconstructed in data [126, 127]. (See Fig. 4.6) The formula for the ratio $(\frac{R_{data}}{R_{MC}})$ is obtained to compare with data and MC. Finally, the in-situ calibration makes the jet response the same in data and MC simulation as a function of detector pseudo-rapidity using dijet events, and as a function of jet transverse momentum using well calibrated reference objects in Z/γ and multi-jet events.

4.2.3 Heavy Flavour Jet Tagging

Heavy flavor jet tagging relies on the unique properties of the b-hadrons with the largest mass and long decay length. The long lifetime ($c\tau \sim 450\mu$m) of b-hadron leads to a measurable decay length to make an identification of b-jet possible. For identifying b-jets, the three dedicated sub-algorithms are built. Impact Parameter based Algorithm (IP2D and IP3D), Secondary Vertex Finding Algorithm (SV), and Decay Chain Multi-Vertex Algorithm (JetFitter) are a set of algorithms to exploit the different properties between b-hadrons and light jet [128]. The ID system with the components of the pixel detector, SCT and TRT provides the important trajectories information for flavor tagging algorithms to reconstruct particle tracks as well as their parameter determination [129]. Furthermore, the outputs of the sub-algorithms are combined by the BDT classifier. In this heavy Higgs search, the b-tagging is used not only for extracting bottom-annihilation production signal but also to make a control region enriched $t\bar{t}$ events for background estimation.

---

[2] Both full and fast simulations

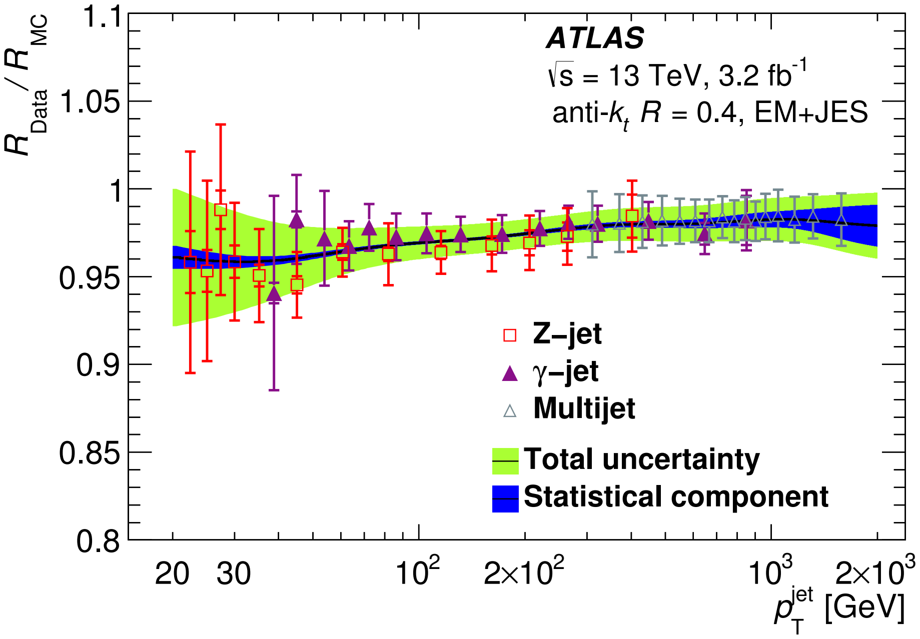

Figure 4.6.: Data to nominal MC event generator ratio as a function of jet p_T for γ/Z+jet and multijet processes. The black line presents the final calibration for the *In-Situ* combination with the corresponding statistical (dark blue) and total (light green) uncertainty bands.

Impact Parameter based Algorithm : IP2D and IP3D

Two track-based impact parameter taggers, IP2D and IP3D, are used for separating tracks associated to jets by a log-likelihood ratio (LLR) discriminant with the consideration of track-to-track correlations. The IP2D tagger is determined for the transverse impact parameter significance (d_0/σ_{d_0}), whereas the IP3D includes both transverse and longitudinal impact parameter significance ($Z_0 \sin\theta/\sigma_{Z_0 \sin\theta}$). Probability density functions are obtained from two impact parameter taggers. The transverse impact parameter (d_0) and longitudinal impact parameter ($Z_0 \sin\theta$) present the closest distance between the track and IP in r-ϕ plane. The LLR distributions of IP2D and IP3D, which are the input variables for MV2, are shown in Fig. 4.7 for b-, c- and light flavor-jets.

Secondary Vertex finding algorithm : SV

Secondary Vertex Finding Algorithm is used to reconstruct a secondary vertex, which carries a large fraction of jet energy due to the harder b-jet fragmentation, from high p_{T} IP tracks associated with the jet [130]. All combination of track pairs within a jet is tested with the two-track vertex hypotheses. The vertexes originating from the decay of photon conversions, a long-lived particle such as K_s and Λ or hadronic interactions with the detector material are discarded. Two track vertex candidates with the invariant mass > 6 GeV are removed. The distance between each track of two-track vertex candidates and the primary vertex is requested larger than 2, and IP2+IP3 of the track should also be higher than 2. Futhermore, $\chi^2 < 4.5$ [131] requirement is applied for the fitted tracks. Figure 4.8 shows several properties of the reconstructed SV for b-, c- and light-flavor jets, which are also one of the inputs for the final MV2 discriminator. An efficiency of the SV reconstruction is 80% for b-jets, while the efficiency on c-jets is only a few %.

Decay Chain Multi-Vertex Algorithm : JetFitter

JetFitter based on the Kalman Filter [133, 134] is a kinematic fitting algorithm, exploiting the topological structure of b- and c-hadron decays inside the jet and attempts to reconstruct the full b-hadron

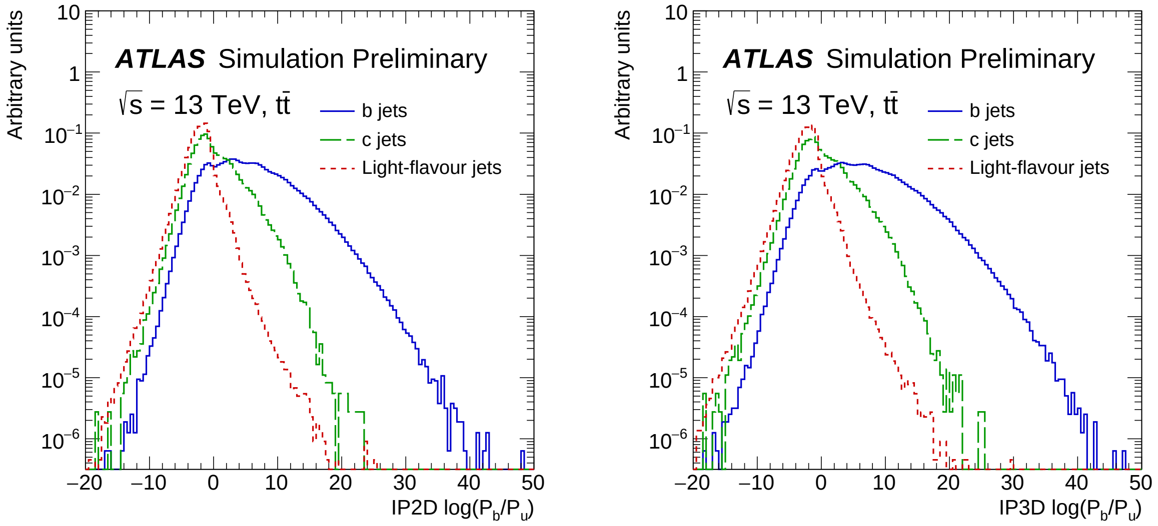

(a) **(b)**

Figure 4.7.: The LLR distributions for IP2D (a) and IP3D (b) sub-algorithm. The MC sample of $t\bar{t}$ events is used for b- (solid blue), c- (dashed green) and light-flavour (dotted red) jets [128].

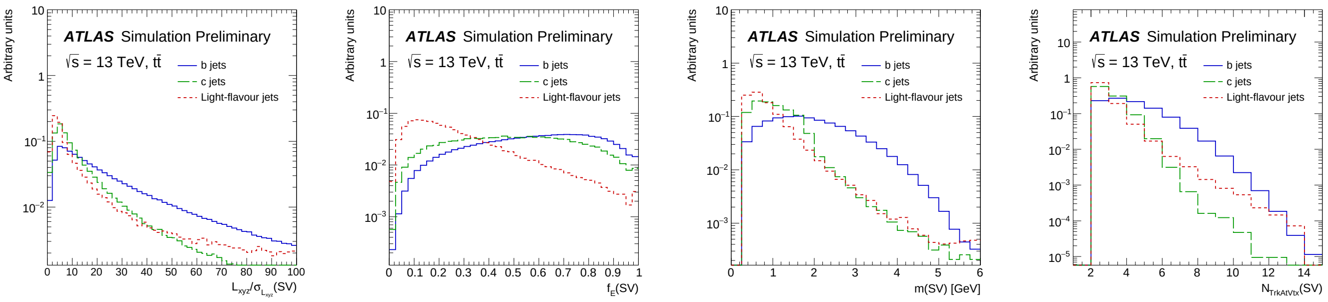

(a) **(b)** **(c)** **(d)**

Figure 4.8.: The properties of secondary vertexes reconstructed by the SV algorithm for b-, c- and light jets in $t\bar{t}$ events. (a) number of two-track vertexes, (b)the transverse decay length, (c) 3D decay length significance and (d) the energy fraction [132].

decay chain. JetFitter searches for three vertexes on the common axis based on the property of c-hadron decay vertex which is often close to b-hadron flight axis. Figure 4.9 shows the distributions for the JetFitter algorithm with a good agreement between data and simulation in $t\bar{t}$ events. The variables are exploited to maximize discriminating power for charm-tagging from b-hadron in the MV2 algorithm with the number, mass, and energy information of the particles associated with the secondary vertex.

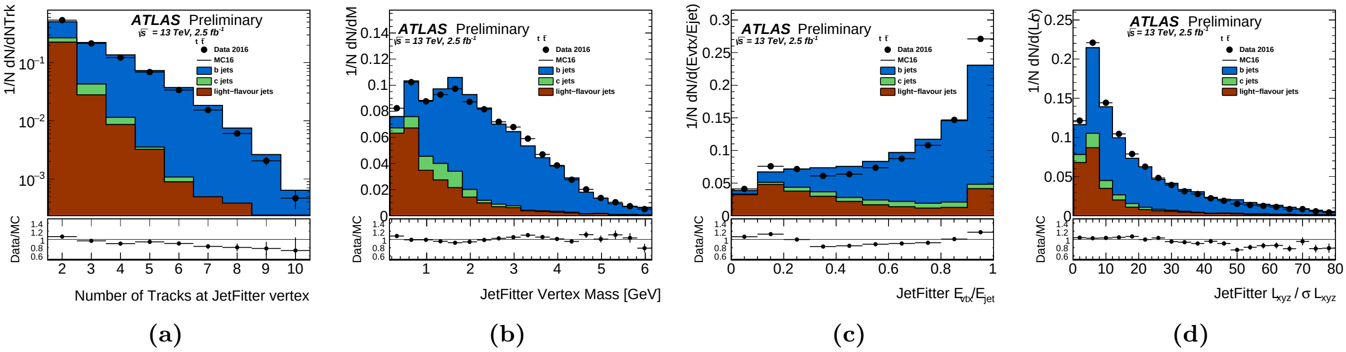

(a) (b) (c) (d)

Figure 4.9.: The distribution with MC-data comparison for the variables of JetFitter: the number of tracks associated with a JetFitter secondary vertex 4.9(a), the secondary vertex mass 4.9(b), the secondary vertex energy fraction 4.9(c) the 3D significance of the decay length 4.9(d) [132].

Multivariate Algorithm : MV2

A boosted decision tree (BDT) is used to achieve a single discriminant with the best performance with three sub-algorithm described above. The training procedure for Multivariate Algorithm (MV2) [135] is completed with the algorithmic strategies of IP2D, IP3D, SV and JetFitter to combine in a single very powerful discriminant.Three types of MV2 are provided as the *MV2c00*, *MV2c20*, and *MV2c10*. The MV2c10 is recommended for the a standard b-tagging discriminant in 2016 and also used in this analysis. The number in the tagger name expresses the component of background samples in the training. For instance, the mixture background with 10% c-jets and 90% light-flavor jets is used for the MV2c10 training. Fig 4.10 shows the MV2c10 BDT output for signal and background with the highly suppressing power for c- and light-flavor jet. In 77% b-jet efficiency working point chosen in this thesis, the rejection [3] for c-jets (light-flavor jets) is up to 6 (134) for the overall jet with pT above 20 GeV.

4.2.4 Pile-up Jet Tagging and Rejection

A further pile-up subtraction is applied, in addition to the jet area-based method as described in the previous section. In order to suppress the contamination, a pile-up jet rejection is applied using the Jet Vertex Tagger (JVT) discriminant exploiting the vertex information. An original track-based method, Jet Vertex Fraction (JVF), has been used for the pile-up suppression since 2012 [136]. It is developed by the DØ collaborations and applied to identify the jets originating in the hard-scatter interaction. The corresponding tracks are combined with their primary vertexes based on the JVF discriminant. This way reduces the effect from pile-up and the uncorrelated soft collisions. JVF updated with two new variables to improve the separated power between hard-scatter (HS) and pileup (PU) jets is referred to as "corrJVF". Furthermore, a new algorithm Jet Vertex Tagger (JVT) which consists of corrJVF and

---

[3] The rejection is typically defined as $1/\varepsilon$.

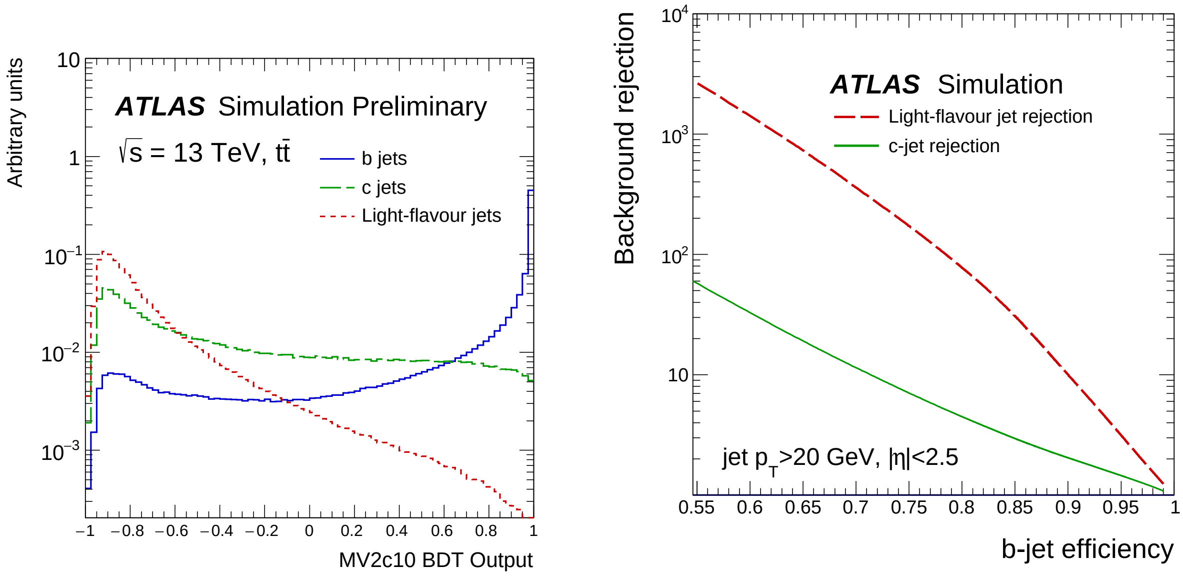

(a) (b)

Figure 4.10.: The MV2c10 output shows in (a) for b-jets (solid line), c-jets (dashed line) and light-flavour jets (dotted line) in $t\bar{t}$ events. (b) presents the curve for the background rejection of light-flavour jet (dashed line) and c-jet (solid line) versus signal b-jet tagging efficiency [132].

$R_{p_{\mathrm{T}}}$ is used during the Run2. The corrJVF and $R_{p_{\mathrm{T}}}$ defined as:

$$corrJVF = \frac{\Sigma_k p_{\mathrm{T}}^{\mathrm{trk_k}}(PV_0)}{\Sigma_l p_{\mathrm{T}}^{\mathrm{trk_l}}(PV_0) + \frac{\Sigma_{n\geq l}\Sigma_l p_{\mathrm{T}}^{\mathrm{trk_k}}(PV_n)}{(\kappa\cdot n_{\mathrm{trk}}^{\mathrm{PU}})}}, R_{p_{\mathrm{T}}} = \frac{\Sigma_k p_{\mathrm{T}}^{\mathrm{trk_k}}(PV_0)}{p_{\mathrm{T}}^{jet}} \tag{4.5}$$

where the hard-scatter vertex is written as PV_0 and PV_j with $j \geq l$ for the primary vertexes of pileup interactions in same bunch crossing. The $\Sigma_k p_{\mathrm{T}}^{\mathrm{trk_k}}(PV_0)$ and $\Sigma_{n\geq l}\Sigma_l p_{\mathrm{T}}^{\mathrm{trk_k}}(PV_n)$ show the p_T sum of all tracks of the jet in the hard-scatter vertex and any of pile-up interaction respectively. The scale factor $\kappa = 0.01$ is applied for the number of pileup tracks $n_{\mathrm{trk}}^{\mathrm{PU}}$ in corrJVF to correct for the linear increase in $\Sigma p_{\mathrm{T}}(PU)$. The p_{T}^{jet} of $R_{p_{\mathrm{T}}}$ is the transverse momentum of calibrated jet after the pile-up subtraction.

Finally, the new discriminant JVT is built with $R_{p_{\mathrm{T}}}$ and corrJVF with two dimensional likelihood ratio based on a k-nearest neighbor (kNN) algorithm [137]. It has been trained with HS signal and PU background in $20 < p_{\mathrm{T}} < 50$ GeV in $|\eta| < 2.4$ region by using a sample of $Z \rightarrow \mu\mu$ events. Figure 4.11 shows the distribution for corrJVF, $R_{p_{\mathrm{T}}}$, and the fake rate from pileup jets versus hard-scatter jet efficiency curves for JVT. The JVT (aqua dot line) shows the efficiency of 95% on the signal HS jet with the fake rate of less than 3%.

4.3 Electrons

Information from ID tracking and EM calorimeter detectors make precise measurements of trajectory, position and energy reconstruction possible. Since the full hadronic decaying τ is considered in this analysis, the electron object is important to remove backgrounds with leptons. Section 4.3.1 and Sec. 4.3.3 provide an introduction of reconstruction and identification for electrons. A brief overview of calibration for energy and resolution is described in Sec. 4.3.2. The more detail for the electron is shown in Reference [138].

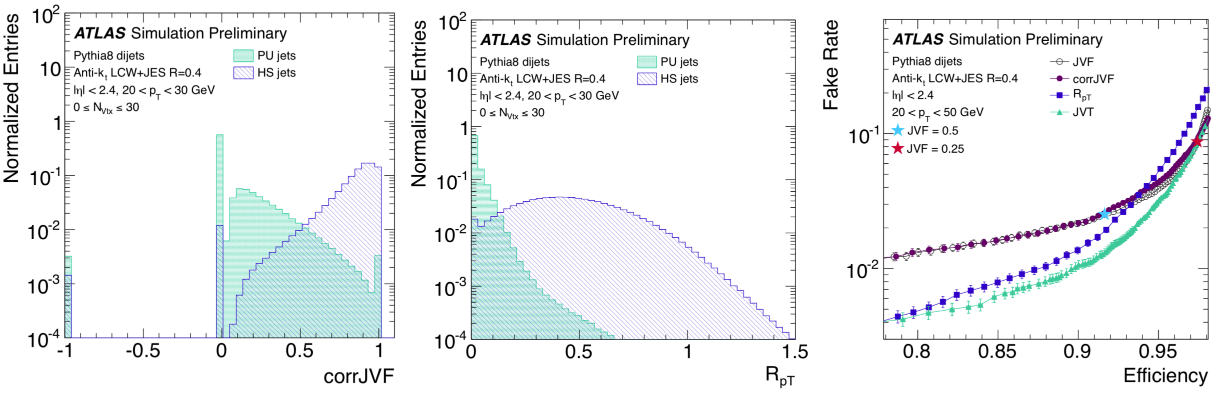

(a) **(b)** **(c)**

Figure 4.11.: The comparison plots for pileup (PU) and hard-scatter (HS) jets with $20 < p_{\mathrm{T}} < 30$ GeV. (a) shows the one for corrJVF and $R_{p_{\mathrm{T}}}$ is illustrated in (b). Fake rate from pileup jets versus hard-scatter jet efficiency curves shown in (c), JVT composed of corrJVF and $R_{p_{\mathrm{T}}}$ provides the good performance that signal jet efficiencies of 95% is achieved for the rejection of pileup fake rate 3% [137].

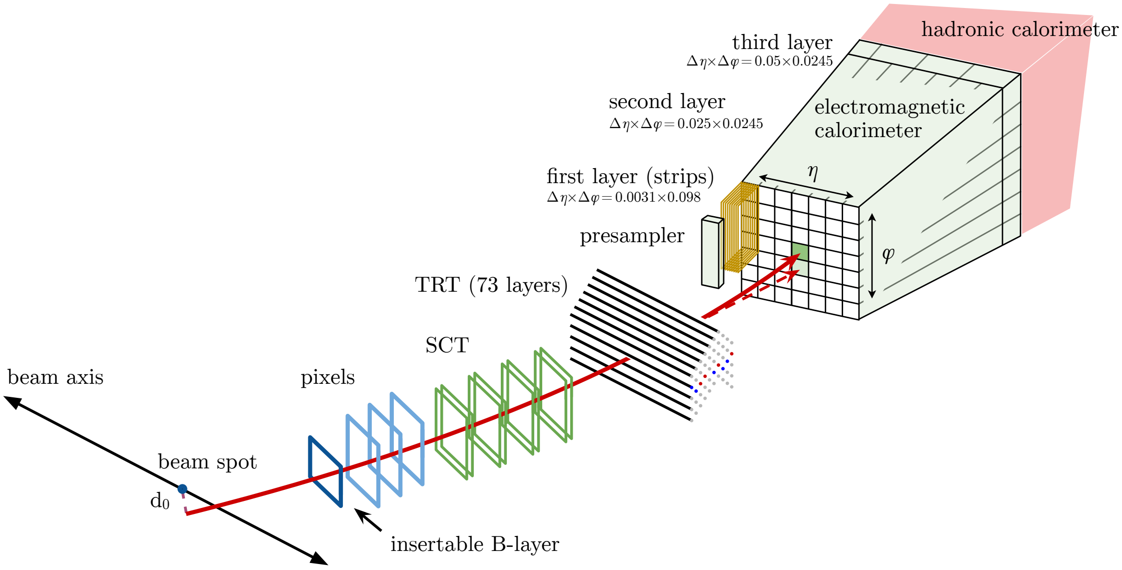

Figure 4.12.: The overview for electron trajectory in the ATLAS detector. The illustration presents an electron pass through ID detector and is absorbed by EM calorimeter. The full information of tracking system and calorimeter provide is useful for the electron reconstruction.(taken from Ref. [139].)

4.3.1 Electron Reconstruction

Several steps are applied for the reconstruction in the region of EM calorimeter ($|\eta| < 2.46$).

- Seed-cluster reconstruction : Electron cluster "seeds" are formed using a clustering algorithm based on information from 0.025×0.025 granularity of the EM calorimeter with the window size of 3×5 towers. The transverse energy threshold to the cluster is above 2.5 GeV, and the removal of the duplicates is applied also. The efficiency of cluster search ranges provide more than 95% at $E_T = 7$ GeV which is also the p_T threshold for the electron-veto selection in this analysis.

- Track reconstruction : The 30% energy loss in the detector due to the possible Bremsstrahlung [140] is expected based on the pion hypothesis for the pattern recognition study. In the pion hypothesis, the track with a transverse momentum larger than 1 GeV might not be successfully reconstructed within the EM cluster region of interest.The new pattern recognition using an electron hypothesis to allow energy loss is used for this issue. The final fit for track candidates by ATLAS Global χ^2 Track Fitter [141] with the pion or the electron hypothesis provides a minimal interference in track reconstruction. The hypothesis application depends on which one presents a success fit.

- Track matching : The angular distance, $\sqrt{(\Delta\eta)^2 + (\Delta\phi)^2}$, of the track is considered as a parameter of matching criteria between ID tracks to EM cluster. The matched track to EM cluster with precision hits (≥ 4) are refitted by Gaussian Sum Fitter (GSF) [142].

- Electron reconstruction : Using the seed-cluster and matched track as described above, electron reconstruction procedure can be completed. The further energy calibration of the clusters to the original electron energy based on simulation samples is done by multivariate algorithm [143].

The four-momentum of the electrons is calculated with the information of both the final calibrated energy cluster and matched track in the ID track. Since Run2, the primary interaction vertex of the HS has been also considered to the Track matching step of electron reconstruction, in order to reduce conversion particles. Study for the reconstruction efficiency and corresponding correction factors are based on the tag-and-probe method with $Z \to ee$ events. Figure 4.13 shows the comparison distribution used for the correction faction measurement as a function of E_T and η.

4.3.2 Electron Energy Scale and Resolution

This section provides the calibration for the reconstructed electron. The relative energy resolution for reconstructed EM objects (electron and γ) can be written as:

$$\frac{\sigma_E}{E} = \frac{a}{\sqrt{E}} \oplus \frac{b}{E} \oplus c, \tag{4.6}$$

where the stochastic term a, the noise term b and the constant term c are the parameters with a dependence on η. The stochastic term is assumed to be around $10\%/\sqrt{E[\mathrm{GeV}]}$. [4]. It shows the stochastic term depends on the energy of incoming particle measured in calorimeter [144, 145]. The noise term is composed of the source of electronic noise of the EM calorimeter and the pile-up. The pile-up noise is dominant at high η region. The constant term is dominant in the energy resolution in the higher energy. In the most of the central region, The energy resolution is better than 2% for $E_T > 25GeV$. However, in the region close to transition of the barrel and end-cap calorimeters, it exceeds 3% due to the large amount of passive material [146]. The resolution curve of electron is shown in Fig. 4.14. The invariant mass distributions are also shown.

---

[4] The stochastic term is computed as $3\%/\sqrt{E[\mathrm{GeV}]}$ for CMS electromagnetic calorimeter.

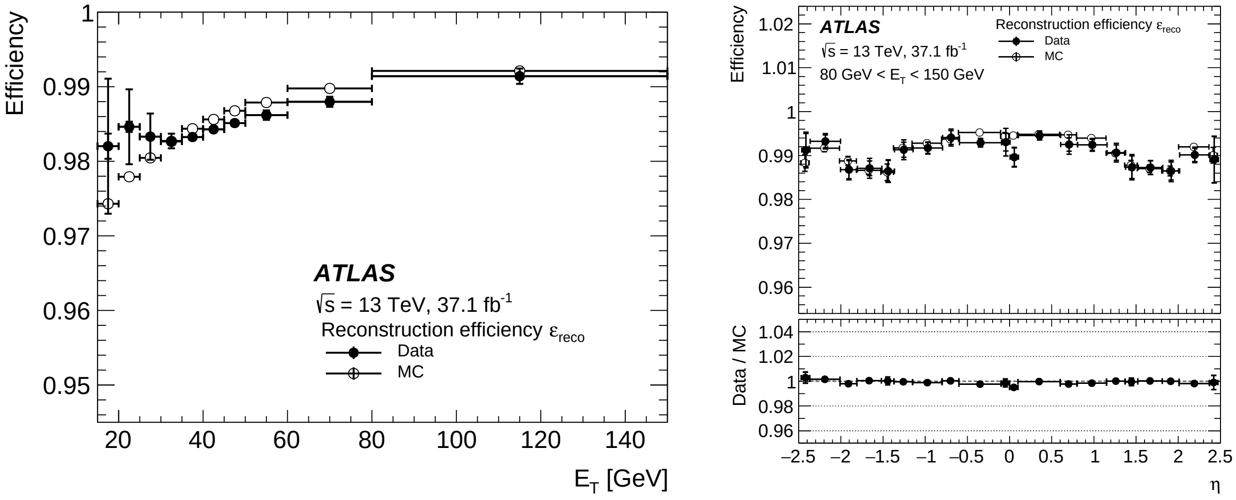

(a) **(b)**

Figure 4.13.: The reconstruction efficiency for the real data (closed points) and $Z \to ee$ simulation events (open points). (a) is the plot as a function of electron transverse energy, while the one for high E_T region $(80 - 150 GeV)$ for pseudo-rapidity is presented in (b) [143].

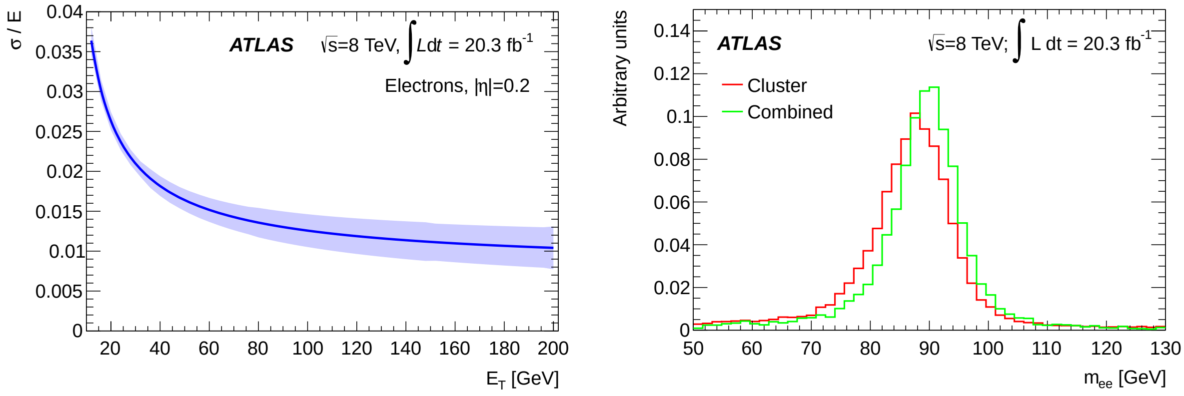

(a) **(b)**

Figure 4.14.: (a) is the resolution curve as a function for E_T of electrons with $|\eta| = 2$ requirement. (b) shows the electron pair invariant mass distribution for $Z \to ee$ events with one electron candidate in $1.37 < |\eta| < 1.52$. (taken from Ref. [143].)

The calibration steps illustrated in Fig. 4.15 are applied for the reconstructed electrons [143]. Though the energy of cell deposit in EM calorimeter and electron cluster are already calibrated in EM scale, it still suffers from the residuals due to the energy loss in the material upstream of the calorimeter, energy leakage out of the envelope of the cluster or the EM calorimeter. In order to equalize the response over cell's energy of the longitudinally segmented structure of EM calorimeter, the overall energy scales for each layer are computed with simulation. MC-based e/γ response calibration was employed for this issue by using a multivariate algorithm (MVA). The first-layer energy of the EM calorimeter are compared with the second-layer energy, the higher ratio value indicates the EM showers development is helpful to understand an energy excess in the simulation comparison. It performs the optimization in the separation power between electrons and γ.

The other correction for data is called "Inter-calibration of the calorimeter layers". Due to the shower development of the longitudinal layers in the calorimeter, the effects in the full p_{T} range need to be considered. The inter-calibration is used for first, second layers and PS in calorimeter for energy scale. [5] It effectively corrected possible mis-modeling of each layer from other material.

A set of corrections are applied to data to account for the non-uniformity of ϕ due to various instrumental effects that are not included in simulation, such as non-optimal high-voltage setting, geometrical effects or biases in the LAr calorimeter electronics calibration.

The other corrections to data and simulation are used for improving the electron energy resolution. The residual mis-calibration is defined as the difference between data and simulation as a function of ϕ. The residual mis-calibration is corrected by shifting the energy scale using a sample of $Z \to ee$ decays. Furthermore, since data provide a slightly worse performance with the pre-event selection in step 5 of Fig. 4.15 used in the simulation, the additional resolution smearing is used in the simulation. The energy dependent resolution smearing is performed by comparing the peak width of data and simulation in the Z invariant mass distribution.

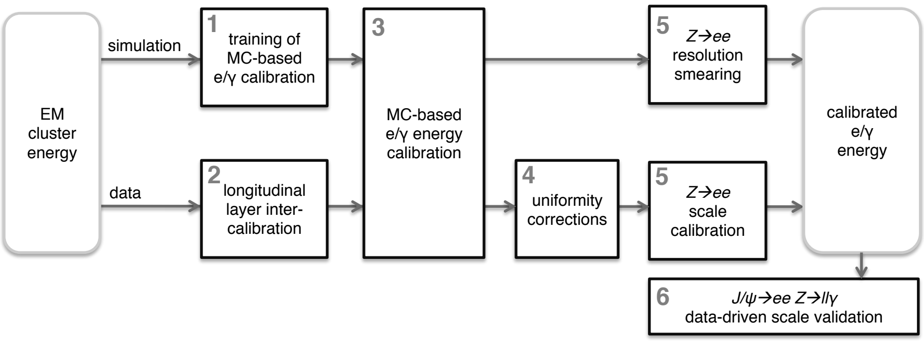

Figure 4.15.: The overview for the calibration of electron candidates in ATLAS [143].

4.3.3 Electron Identification and Isolation

Since the reconstructed electron still has huge background from heavy-flavour decay or photon conversion additional fake reductions are necessary. The background for the prompt electrons can be suppressed by a powerful identification (ID) based on the likelihood-based method. The ID for an electron is based on the tracking and calorimeter system information by the probability density functions defined as following formula:

$$\mathcal{L}_{S(B)}(\vec{x}) = \prod_{i=1}^{n} P_{S(B),i}(x_i), d_{\mathcal{L}} = \frac{\mathcal{L}_S}{\mathcal{L}_S + \mathcal{L}_B} \tag{4.7}$$

---

[5] No dedicated inter-calibration is applied for the third layer since the energy contribution is negligible.

where $\vec{x}$ is the variable value vector and $P_{S(B),i}(x_i)$ is signal (background) probability density function at variable x_i of the discriminant $\mathcal{L}_{S(B)}$. Significant discrimination power variables are selected as the inputs of ID training. EM calorimeter information detected in each layer and the information from TRT significantly improve the separated power for light-flavor jets (referred to as LF, all quarks beside the b- or c-quarks) and γ. $\Delta\eta$, $\Delta\phi$, and a ratio of the cluster energy to the track momentum from track-cluster matching also provide powerful discrimination for LF and γ. Heavy-flavor jets (b- or c-quarks, so call HF) background is rejected from prompt electrons with track condition such as shower width and the ratio of cell energy to the electron cluster position. The more detail of the input variables is shown in Reference [147]. Figure 4.16 shows the likelihood-based (LH) discriminant $d_{\mathcal{L}}$ used for ID of the reconstructed electron candidates.

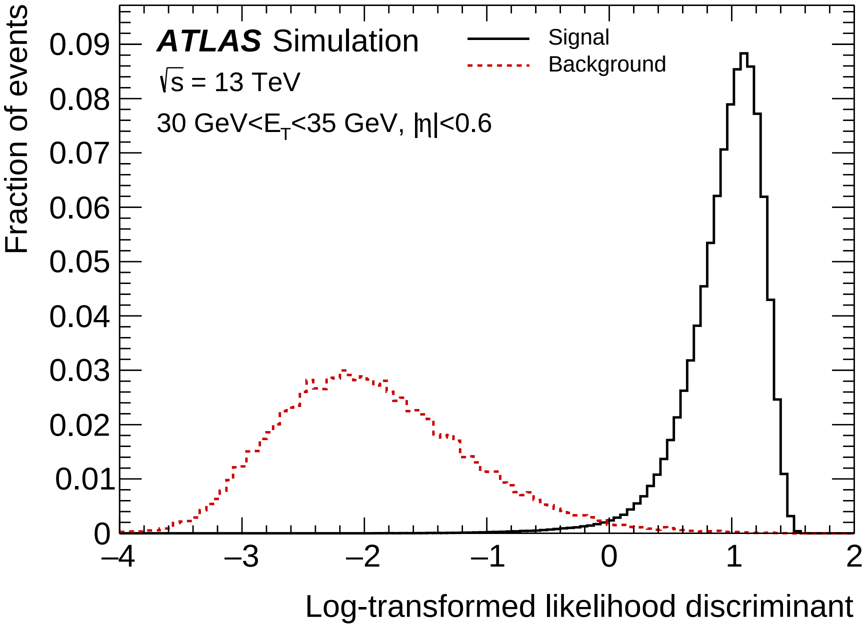

Figure 4.16.: The LH-based discriminant $d_{\mathcal{L}}$ for $Z \rightarrow ee$ signal simulation sample (black histogram) and the red histogram is for background from jets and γ conversion. The good quality tracks of the reconstructed electron candidates are requested with 30 GeV $< E_{\mathrm{T}} <$ 35 GeV and $|\eta|$ <0.6 [147].

Three different working points (WPs) are available, *Loose*, *Medium*, and *Tight*. The corresponding efficiencies are 93%, 88% and 80% for identifying a prompt electron with $E_T = 40GeV$. Figure 4.17 includes the electron-ID efficiencies with all measurement uncertainties in $Z \rightarrow ee$ simulation samples as a function of E_{T} and η. The range for scale factors, calculated with the data-to-simulation comparison, is from 0.5% to 10% with the largest uncertainties found at low E_{T}. In this analysis, Loose WP is applied for electron-veto selection to remove lepton background as much as possible.

4.4 Muons

Muons play a key role in many particles physics. However, comparing to other particles like electrons, it is very difficult to be detected due to its weak Bremsstrahlung behavior. Combined information from the ID and calorimeters supplements the information used for reconstruction. Muons escape from most of the detectors without leaving the signature and only the hadronic calorimeter provides a very small energy deposit beside the Muon spectrometers. The muon spectrometers are built with a strong magnetic field

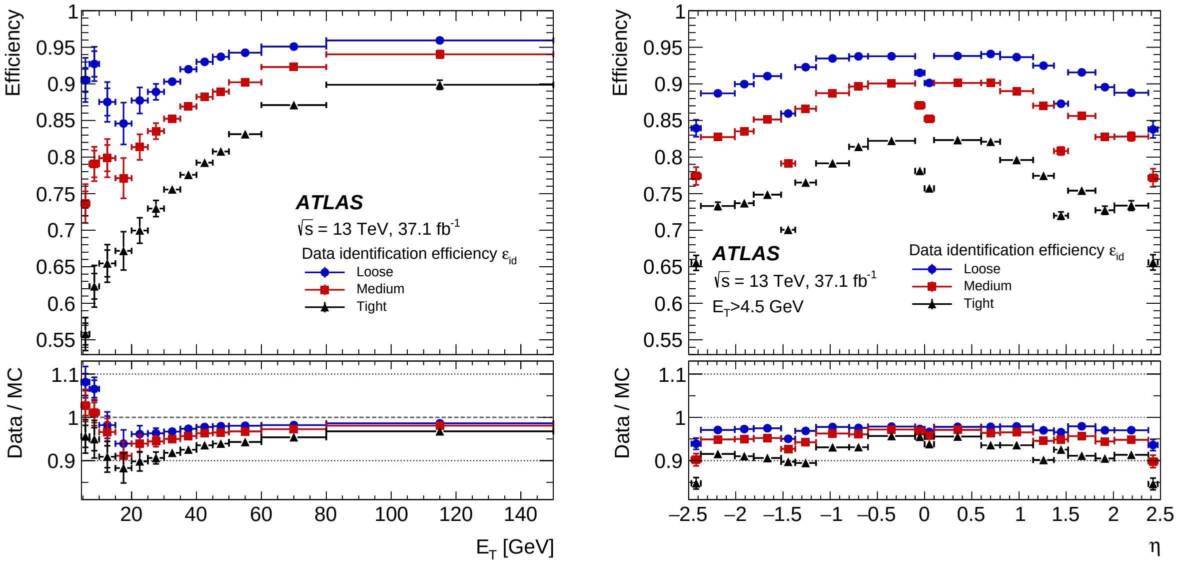

(a) (b)

Figure 4.17.: The electron-ID efficiencies in $Z \to ee$ simulation corresponding to Loose (blue), Medium (red), and Tight (black). The data-to-simulation ratio also presents the scale factor for three WPs used in the analysis. (a) is formed as function of E_{T} and (b) is the one in η function. The range for scale factor is from 0.5% to 10% with the largest uncertainties found at low E_{T}.

integral in ranging between 2 and 6 Tm for very high precision measurement of muon trajectory [6] [148]. Like the electron object, the muons are used in the veto requirement for the lepton background in this search. The muon reconstruction is described in Sec. 4.4.1 and the muon momentum calibration in Sec. 4.4.3. The identification algorithms and isolation efficiency study of muon candidates are described in Sec. 4.4.2. This Section widely refers to [149].

4.4.1 Muon Reconstruction

Each sub-detector in ATLAS, such as ID and MS, provides individual information for the properties of the muon track. ID track reconstruction was already explained in electron Section, so this section is focused on the Muon reconstruction in the MS.

The muon reconstruction is based on the hits patterns in the ID and MS. The four different muon objects for physics analysis are defined based on the muon trajectory recorded by the sub-detectors:

- Combined muons (CB): The primary muon object with a global χ^2 fit on ID track and MS track. A combination reconstruction for muon with an inside-out information was completed.
- Calorimeter tagged muons (CT): Only a track in the ID and a minimum-ionizing particle signature in the calorimeter are used for CT muon.
- Segment-tagged muons (ST): The ST muons are used to recover acceptance at low pT, where muons can reach only the first layers of the MS.
- Extrapolated muons (ME): MS track with no associated ID track, so-called Standalone muons, is used for reconstructing muons traveling outside the ID region.

---

[6] The position resolution for the chamber of MS is 35 μm.

Variable	Description
$q/psignificance$	Sum of the difference between the ratio of the charge and momentum in the ID and MS.
ρ'	The difference between transverse momentum measurements divide track p_T in ID and MS.
χ^2	χ^2 value of the combined track fit using for muon reconstruction.

Table 4.1.: The variables used in muon identification. They offer good discrimination for prompt muons and background muon candidates [150].

The additional overlap study between different muon types is completed by comparing the ID track and analyzing the track hit content. Not only CB muons and ME muon are used in this search, but also the ST muons and CT muons are also considered with the restriction.

4.4.2 Muon Identification and Isolation

Different requirements are imposed on the track information obtained from the ID and MS to identify good quality muons. The variables information used in the requirements are listed in the Tab. 4.1: Four different identification criteria (*Medium*, *Loose*, *Tight*, and High-p_T) are provided in the ATLAS. The *Loose* requirement is used in this high mass Higgs search. It is designed to maximize the reconstruction efficiency of the good-quality muon tracks and optimized for Higgs boson candidate reconstruction in four-lepton final state [151]. All muon types are used in Loose ID, while CT and ST muons are used within the restricted η region. The contribution of CB , CT and ST muons within $|\eta| < 2.5$ are 97.5%, 1.5% and 1%, respectively. The corresponding efficiency for signal muons in overall momentum is larger than 96% with the 0.5% fake rate of hadrons background. The efficiency study of muon ID is measured based on $J/\psi \to \mu\mu$ and $Z \to \mu\mu$ tag-and-probe analysis, and calculate the scale factor from the efficiency difference between the simulated and experimental data. Figure 4.18 shows the reconstruction efficiency for Loose working point and the corresponding SF.

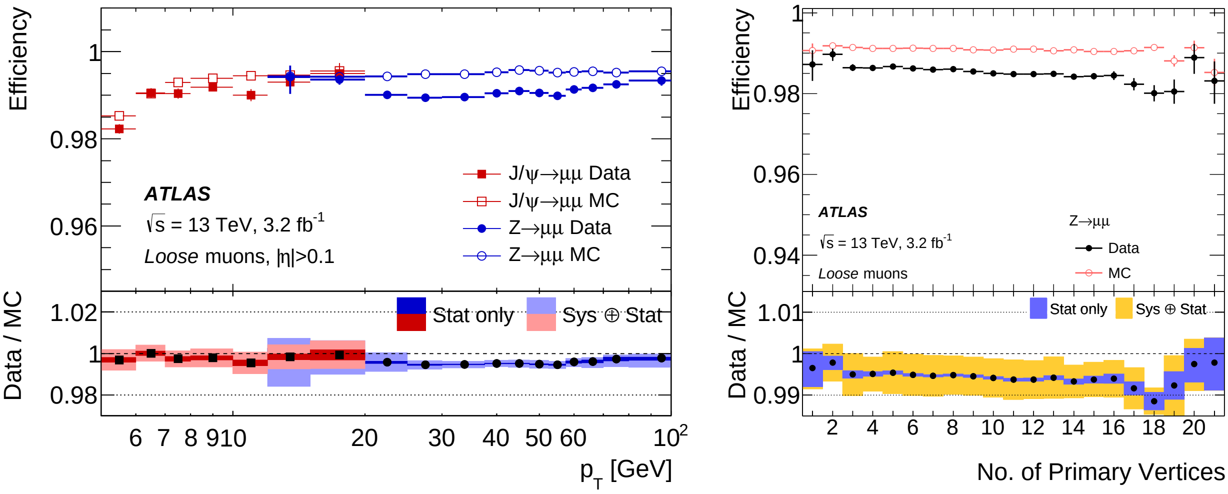

(a)

(b)

Figure 4.18.: The reconstruction efficiency for Loose working point and the corresponding SF as a function of (a) p_T and (b) the number of PVs. They are measured in $J/\psi \to \mu\mu$ and $Z \to \mu\mu$ tag-and-probe analysis with p_T >10 GeV for the muon candidates and several event selections. The panel at the bottom shows the ratio of the simulated and experimental data, which is used as the SF [151].

The other powerful method for rejecting background originating from semi-leptonic heavy flavor hadron decays is referred to as muon *isolation*, built based on the information from the detector property around a muon candidate. It consists of two based variables, track-based $p_T^{varcone30}$ and calorimeter-based $E_T^{varcone20}$. $p_T^{varcone30}$ presents the sum of the tracks (p_{T} larger than 1GeV) around the muon within a cone size $\Delta R = min(10GeV/p_T^{\mu}, 0.3)$, where p_T^{μ} is the transverse momentum of the muon. While $E_T^{varcone20}$, defined as the one based on transverse energy of topological clusters with cone size $\Delta R = 0.2$, improves the suppression power for the pile-up background. The *gradient* isolation working point provides $\geq 90(99)\%$ efficiency for the muons with $p_{\mathrm{T}} > 25(60)$ GeV, is used in this analysis. The systematic uncertainties are estimated smaller than 0.5% for overall region with $p_T > 20$ GeV. Figure 4.19 shows the efficiency included full systematic and statistical uncertainties in the overall p_{T} range of muons.

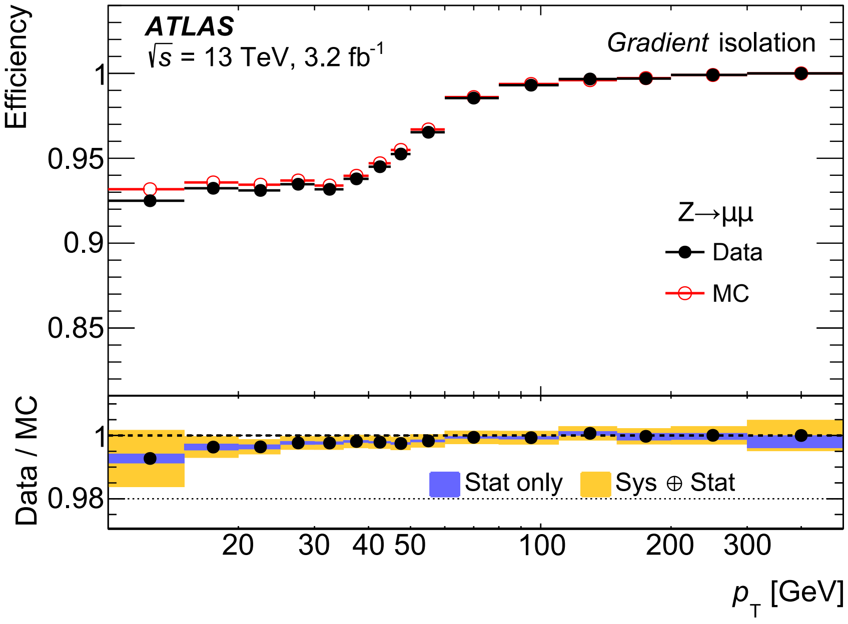

Figure 4.19.: The efficiency for isolation with *gradient* working point as a function of muon p_{T}. The error band of the bottom panel shows the statistical only, as well as the bottom panel presents the ratio between data and simulation with statistical uncertainties and combination with full systematic uncertainties. The measurement was studied in $Z \to \mu\mu$ events [151].

4.4.3 Muon Momentum Scale and Resolution

A set of corrections studied using $J/\psi \to \mu\mu$ and $Z \to \mu\mu$ samples is applied to the simulation. It is necessary to apply such corrections to account for the discrepancy between data and simulation. That muon transverse momenta constructed in the ID and MS must be calibrated with the identified corrections. $\Delta r_m^{Det}(\eta,\phi)$ and $s_n^{Det}(\eta,\phi)$ stand for the momentum resolution and the scale corrections for (η,ϕ) region. The significant improvement comparing to uncorrected simulation samples can be observed in the invariant mass distribution of both $J/\psi \to \mu\mu$ and $Z \to \mu\mu$ candidate events with CB muons.

4.5 Hadronic τ Decays

The tau lepton plays the most important role in this analysis for background rejection, background estimation, and final discriminant calculation. Due to a high mass of $m_\tau = 1776.86 \pm 0.12 MeV$ [152], the tau lepton known as the heaviest lepton is only lepton that can decay both hadronically and leptonically,

Decay Mode (Faction)			
Leptonic (35.2%)		Hadronic (64.0%)	
1-prong (35.2%)	3-prong (6.4×10^{-3}%)	1-prong (48.9%)	3-prong (15.1%)
$\mu^-\bar{\nu_\mu}\nu_\tau$ (17.4%)	$\mu^-e^-e^+\bar{\nu_\mu}\nu_\tau$ (3.6×10^{-3}%)	$\pi^-\nu_\tau$ (10.8%)	$\pi^-\pi^-\pi^+\nu_\tau$ (9.3%)
$e^-\bar{\nu_e}\nu_\tau$ (17.8%)	$e^-e^-e^+\bar{\nu_e}\nu_\tau$ (2.8×10^{-3}%)	$\pi^-\pi^0\nu_\tau$ (25.5%)	$\pi^-\pi^-\pi^+\pi^0\nu_\tau$ (4.8%)
		$\pi^-2\pi^0\nu_\tau$ (9.5%)	$\pi^-\pi^-\pi^+2\pi^0\nu_\tau$ (0.5%)

Table 4.2.: The table for the main decay mode of tau lepton. The leptonic or hadronic decay modes with one(three) charge particle are referred to as 1-prong(3-prong). The fraction of each main decay modes corresponding to total branching fractions was also described. The other modes with such as 5prong with a small fraction are not listed in this table. It widely reference from [152].

so called τ_{lep} and τ_{had}. [7] The summary table for the decay mode is described in Table. 4.4. Most of the hadronic decay modes are dominated with one or three charged particle, referred to as *1-prong* and *3-prong* decays, respectively, including charged pions, $\pi^{\pm}$, and kaons, $K^{\pm}$. The 3-prong leptonic decays with very small branching fractions are also considered in this analysis The main target of τ identification is to distinguish the τ_{had} decays from hadronic jets.

Section 4.5.1 shows the reconstruction for τ objects with the LCW topo-clusters with a smaller cone and the reconstructed tracks. A dedicated energy momentum calibration procedure is presented in Sec. 4.5.2 for τ_{had} candidates. To separate τ_{had} from hadronic jets from quark and gluon, the number of hits of ID detector is one of the most important variables and highly depends on the charged track's number from tau and their momenta. The two identification techniques are defined for 1-prong τ_{had} and 3-prong τ_{had} separately as shown in Sec. 4.5.3. The Tau Trigger (STT) is used in this analysis and shown in Sec. 4.5.4. The contribution of 2-prong τ_{had} is expected to be sizable in this analysis with high-p_{T} tau, hence the 2-prong tau reconstruction and identification are considered in this analysis for the first time in ATLAS. The further detail of 2-prong τ_{had} is shown in Sec. 4.6.

4.5.1 Tau Reconstruction

Discovery with $H \to \tau\tau$ decay relies not only on high-purity selection on τ_{had} candidates but the four-momenta reconstruction for the charged and neutral pion. The tau reconstruction is performed based on the method of ATLAS Run1, so-called "Baseline". Over 90% of hadronic taus decay into charged hadrons ($h^{\pm}$), neutral pions (π^0) and a tau neutrino as discussed above. π^0 decays exclusively to a pair of photons and photons convert into e^-e^+. $h^{\pm}$ stands for for $\pi^{\pm}$ and $K^{\pm}$ with small contribution. However, only the difference of charged hadrons between tau decay modes is taken into account. The fake track backgrounds like hadrons produced from pile-up interactions have affected the efficiency of τ_{had} reconstruction. A new method called "Tau Particle Flow" (TPF) is applied for reconstructing the individual charged and neutral hadrons in tau decay modes. The goals of TPF is to reduce those background by classifying the main five decay modes. [8] Charge and momentum of $h^{\pm}$ are determined using the ID track, however, the overestimation of $h^{\pm}$ is also expected due to the source coming from conversion electrons. The behavior of the five decay modes has been well-understood by the correlation of following three parameters of TPF: the branching fractions, tau selection efficiency of simulated tau without jet/electron, and fake rate of simulated tau passing electron or jet selection. The TPF algorithm is built by Toolkit for Multivariate Data Analysis (*TMVA*) in the reconstruction step and suppress those backgrounds effectively [9]. Boosted decision trees (BDT) of TMVA tool is employed with several input

---

[7] Since the neutrino in tau decays goes undetected by ATLAS detector, those particles are "invisible" and omitted in further reconstruction. Therefore, the reconstructed taus are also referred as $\tau_{\mathrm{lep-vis}}$ and $\tau_{\mathrm{had-vis}}$.

[8] $h^{\pm}$, $h^{\pm}\pi^0$, $h^{\pm} \geq 2\pi^0$, $3h^{\pm}$, $3h^{\pm} \geq 1\pi^0$

[9] TPF also often be referred to as TMVA tracking since it used TMVA to optimize the track resolution.

variables from π_0 candidates, such as energy fraction in the different layers of the EM calorimeters, η and depth of cluster used for reconstruction, and the number of cells. The final output of BDT score is shown in Fig .4.20 for the different tau-hadronic decay modes of $h^{\pm}$ and π^0. The BDT is trained using with $Z/\gamma^* \to \tau\tau$ signal sample and multijet and $W \to \tau\nu$+jets backgrounds. The number of τ_{had} candidates distribution and mode classification efficiency matrix compared to truth decay modes in simulation with separating of classified decay modes are presented in Fig. 4.21. The TPF reconstruction significantly improves the η and ϕ resolutions of the reconstructed τ_{had} candidates (Shown in Fig. 4.22).

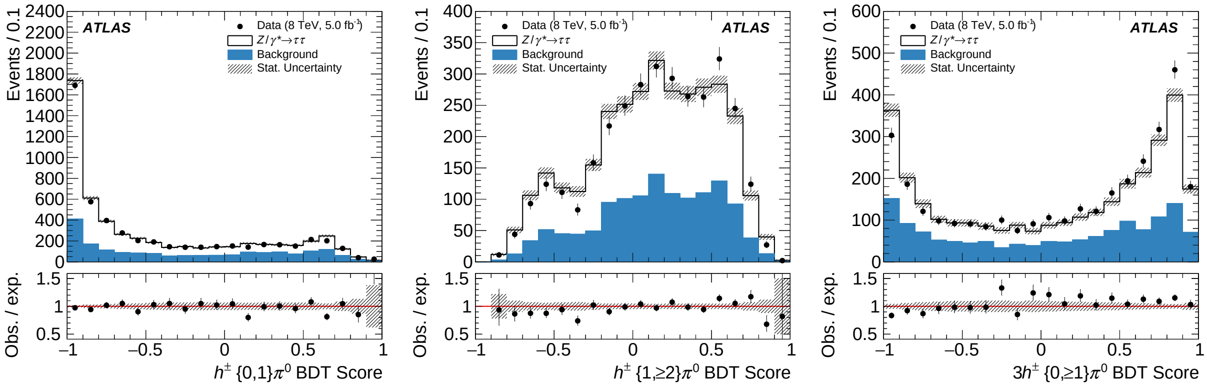

(a) **(b)** **(c)**

Figure 4.20.: Distribution of BDT score for separating the different decay modes of $h^{\pm}$ and π^0. The signal sample responds $Z/\gamma^* \to \tau\tau$. The background are dominated by multijet and $W \to \tau\mu$+jets production [153].

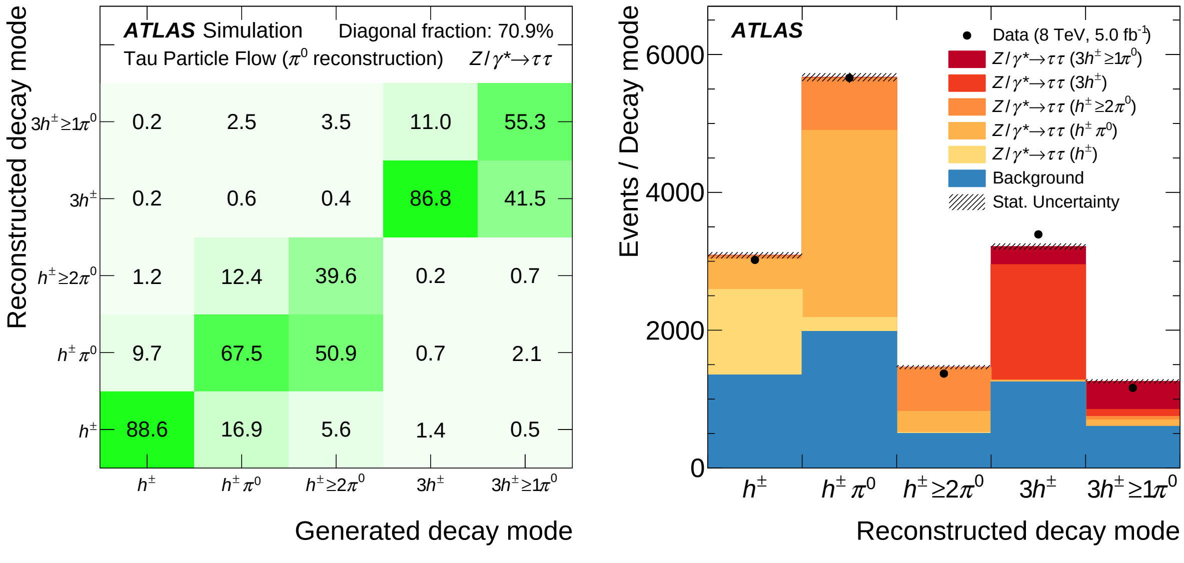

Reconstructed \ Generated	$h^{\pm}$	$h^{\pm}\pi^0$	$h^{\pm}\geq 2\pi^0$	$3h^{\pm}$	$3h^{\pm}\geq 1\pi^0$
$3h^{\pm}\geq 1\pi^0$	0.2	2.5	3.5	11.0	55.3
$3h^{\pm}$	0.2	0.6	0.4	86.8	41.5
$h^{\pm}\geq 2\pi^0$	1.2	12.4	39.6	0.2	0.7
$h^{\pm}\pi^0$	9.7	67.5	50.9	0.7	2.1
$h^{\pm}$	88.6	16.9	5.6	1.4	0.5

(a) **(b)**

Figure 4.21.: The number of τ_{had} candidates distribution (b) and decay mode classification efficiency matrix (a) [153].

The shower information of $h^{\pm}$ measured in calorimeters is used for the reconstruction of tau energy and direction. The energy of π^0 is deposited in the EM calorimeter. The energy reconstruction of τ_{had} starts with jet reconstruction from TC using anti-k_T algorithm with a distance parameter of 0.4 and is calibrated with a local hadronic calibration (LC) [154]. However, only the TCs within the new core

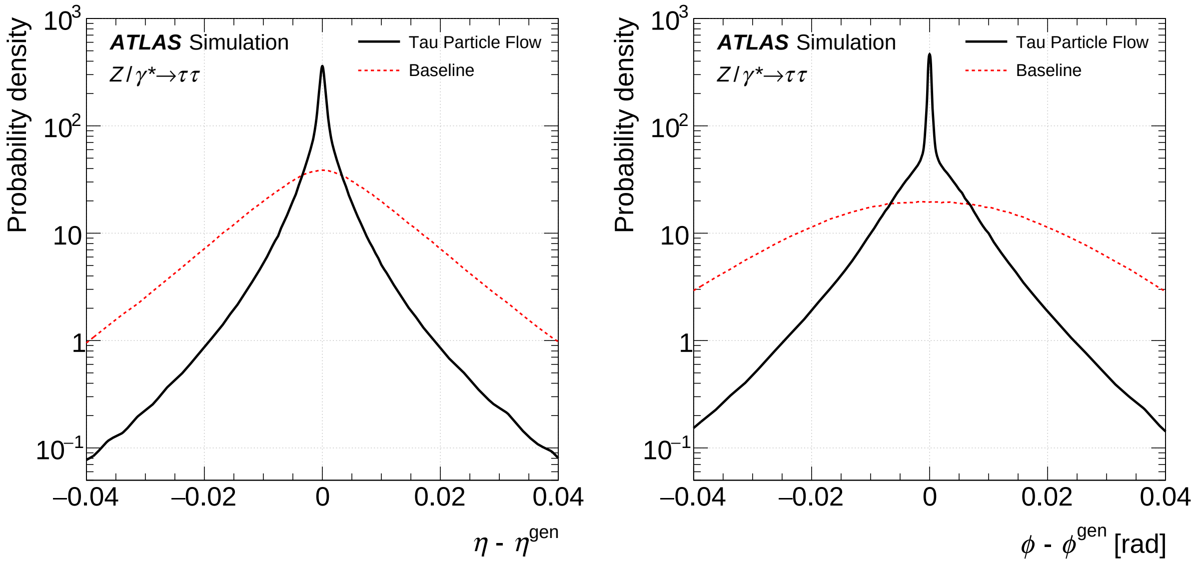

(a) **(b)**

Figure 4.22.: The comparison plots for the distribution of (a) τ_{had} η and (b) ϕ between Tau Particle Flow and Baseline reconstruction [153].

definition, around the tau candidate, referred to as *core region* ($\Delta R_{(\tau_{\text{had}},\text{jet}_{\text{initial}})} < 0.2$), is used to the calculation of the τ_{had} four-momentum. The outer core region ($0.2 < \Delta R_{(\tau_{\text{had}},\text{jet}_{\text{initial}})} < 0.4$) is used to suppress background as *isolation region*.

The primary vertex or pile-up vertex is not always the same with tau vertex. In order to reduce the effect from others vertices, the *tau vertex* (TV) association algorithm to separate decay vertex of τ_{had} is defined with all tau tracks information in the $\Delta R_{(\tau_{\text{had}},\text{jet}_{\text{initial}})} < 0.2$ described above [155] [156]. By finding the jet with the highest TV value, it contributes to the improvement for track selection efficiency as shown in Fig. 4.23. Compared with the track reconstruction efficiency with default primary vertex, TV algorithm shows a better performance, especially for high pile-up region.

By summing up the reconstructed $h^{\pm}$ and π^0 candidates, the four-momentum reconstruction and hadronic decay mode defination of $\tau_{\text{had}}, \text{jet}_{\text{initial}}$ are finished. Figure 4.24 shows the reconstruction efficiency as a function of p_{T} in overall transverse momentum region and the decay mode classification of $\tau_{\text{had}}, \text{jet}_{\text{initial}}$ candidates. The overall efficiency for $\tau_{\text{had}}, \text{jet}_{\text{initial}}$ is around 70% for 1-prong and 3-prong $\tau_{\text{had}}, \text{jet}_{\text{initial}}$. The figure displays the efficiency slightly drop in high p_{T} region for 3-prong $\tau_{\text{had}}, \text{jet}_{\text{initial}}$ due to the merged phenomenon for the ID tracks. For a instance, two high p_{T} tracks with the same charge from a 3-prong τ_{had} might be reconstructed to the similar trajectory in the ID due to the boosting property.

4.5.2 Tau Energy Calibration

The energy of τ_{had} is reconstructed with TC clusters and calibrated with LC scale [157]. In order to further correct the energy measurement in the detector to true visible energy obtained at the generated level, the tau energy scale (TES) is applied in simulation. The calibrated energy of τ_{had} is calculated as:

$$E_{\text{calib}} = \frac{E_{\text{LC}} - E_{\text{pileup}}}{R(E_{\text{LC}} - E_{\text{pileup}}, |\eta|, n_{\text{prong}})}, \tag{4.8}$$

where E_{LC} and E_{pileup} is a random pileup contribution at the LC-calibrated energy within the cone of $\Delta R < 0.2$ of tau candidate and the one from the pileup. Since E_{pileup} linearly increases with number

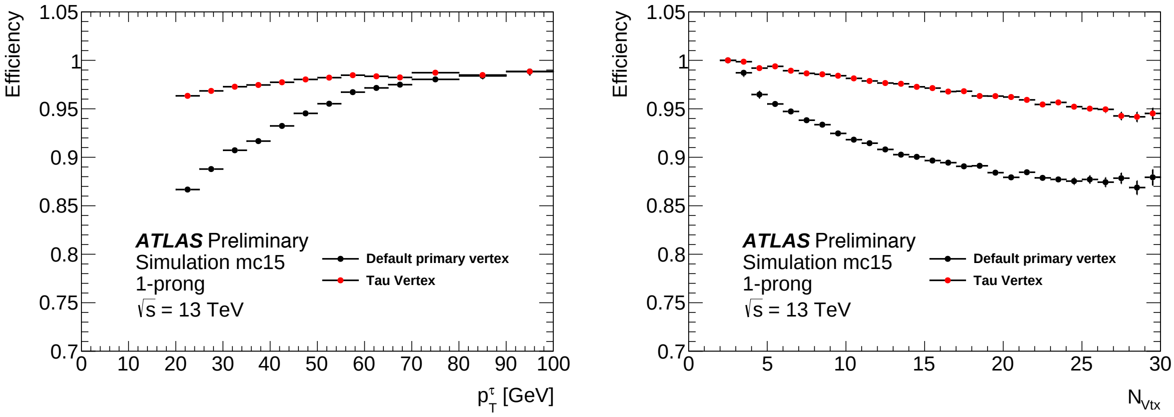

(a) (b)

Figure 4.23.: Due to the difference of decay mode for 1-prong and 3-prong, the TV algorithm is employed for the 1-prong and 3-prong separately. (a) presents the efficiency of track selection for 1-prong $\tau_{\mathrm{had}}, \mathrm{jet}_{\mathrm{initial}}$ with default PV (black) and TV(red) as a function of $\tau_{\mathrm{had}}, \mathrm{jet}_{\mathrm{initial}}$ p_{T}. (b) shows the one for the average number of pile up interactions. Obviously, TV improves the association efficiency of 1-prong for high pile-up region [155, 156].

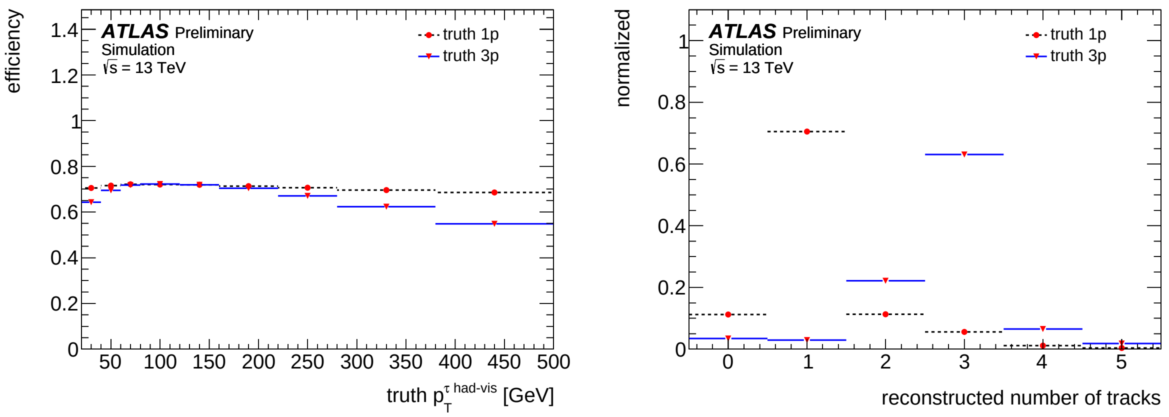

(a) (b)

Figure 4.24.: The combined efficiency of reconstruction and classification as a function of p_{T} in overall transverse momentum region and the decay mode classification of $\tau_{\mathrm{had}}, \mathrm{jet}_{\mathrm{initial}}$ candidates. As shown in (b), there are the mis-reconstruction tau to 2-prong from truth 1-prong. In the case that the not clear pile-up jets or photon conversion tracks in the inner detector passed the track selection, the overestimation of the number of prongs is happened. The one from truth 3-prong is because the similar trajectory reconstructed by the ID track of multiple tracks with the same charge and high p_{T} are merged and cannot be well-reconstructed.

of PV, the E_{pileup} is derived as $E_{\text{pileup}} = A \times (N_{\text{PV}} - \langle N_{\text{PV}} \rangle)$ with average number of primary vertex $\langle N_{\text{PV}} \rangle \sim 14$. The linear coefficient A is from the fitting result of E_{LC} of the simulation samples and R extracted as the Gaussian mean of the $(E_{\text{LC}} - E_{\text{pileup}})/E^{vis}_{true}$. The contribution of pileup correction factor A and the calibration function of the detector response R are shown in Fig. 4.25 and applied as the TES to the tau candidate. The corresponding systematic uncertainty is discussed in Sec 7.1.

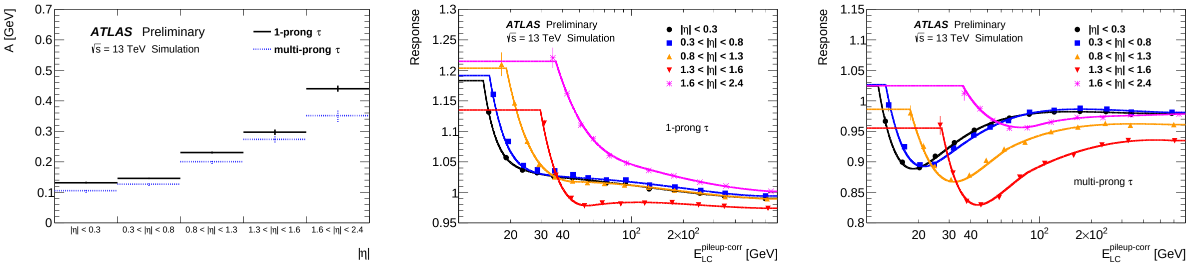

(a) (b) (c)

Figure 4.25.: The pileup correction factor A in bins of $|\eta|$ for 1-prong τ_{had}, $\text{jet}_{\text{initial}}$ and multi-prong τ_{had}, $\text{jet}_{\text{initial}}$ shown in (a). The detector response R for 1-prong and multi-prong tau decays as the function of $E_{\text{LC}}^{\text{pileup-corr}}$, which indicates the average pileup-corrected energy, are present in (b) and (c) respectively [153].

The resolution of τ_{had} is computed based on Gaussian width of the $E_{\text{calib}}/E^{\text{vis}}_{\text{true}}$ with fit. The final resolution curve is illustrated in Fig. 4.26 in separate bins of $|\eta|$ and n_{prong} bins.

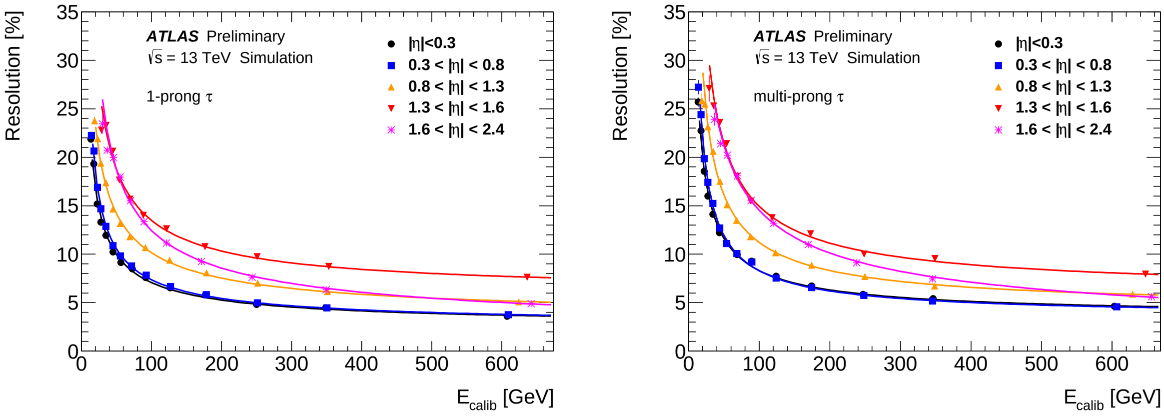

(a) (b)

Figure 4.26.: The curve for the resolution of reconstructed 1-prong (a) and multi-prong (b) tau decays in the calibrated energy bins [153].

4.5.3 Tau Identification

The leptonic decay tau (electron or muon decaying modes) cannot be identified due to the limit of ATLAS detector and the tau decay length. Identification for tau on charged and neutral pions modes is only considered in this analysis. Since quark- and gluon-initiated jets are the dominated background for τ_{had} after the reconstruction, the combined information of shower shape in the calorimeter and tracks in ID [137] provides a powerful discrimination ability from jets. A multivariate tau identification algorithm applied separately for 1-prong and 3-prong τ_{had}, so-called Tau ID, is trained by boosted decision trees (BDTs) of MVA tools. Furthermore, only the τ_{had} candidates that have $p_{\text{T}} > 15$ GeV and $|\eta| < 2.5$

and have one or three associated tracks are used for the Tau ID training. [10] The useful discriminating variables are described as the following items, and the difference between 1-prong and 3-prong inputs is summarized in Table. 4.3. Each variable is corrected by applying an additional correction, which linearly depends on the average number of pileup interactions per bunch crossing ($\langle\mu\rangle$). This correction reduces the pileup dependence on the efficiency of Tau ID.

- **Central energy fraction (f_{cent}):** Transverse energy deposit of the topo-clusters of the calorimeter within a small cone region ($\Delta R < 0.1$ around τ_{had} candidate) divided by the one within larger cone region ($\Delta R < 0.2$ around τ_{had} candidate). The energy deposit is also calibrated in the EM-scale.
- **Leading track momentum fraction ($f^{-1}_{\text{leadtrack}}$):** Transverse energy of the EM scale topo-cluster in the τ_{had} core region divided by the charged track with leading transverse momentum p_{T} in the same core region.
- **Track radius ($R^{0.2}_{\text{track}}$):** ΔR weighted by the track transverse momentum of the τ_{had} and the associated tracks in core region.
- **Leading track IP significance ($|S_{\text{leadtrack}}|$):** The impact parameter of the highest p_{T} tracks in core region by calculating with the TV and its estimated uncertainty.
- **Fraction of tracks p_{T} in the isolation region ($f^{\text{track}}_{\text{iso}}$):** Ratio of the transverse momentum p_{T} scalar sum of the associated tracks of τ_{had} candidate in isolation core region ($0.2 < \Delta R < 0.4$) with respect to the one of all associated tracks.
- **Maximum ΔR (ΔR_{Max}):** The maximum distance in between the associated track and the τ_{had} candidate based on ΔR. Only the associated tracks in core region are considered.
- **Transverse flight path significance (S^{flight}_{T}):** Define the flight path based on the decay length from the secondary vertex of the associated tracks in core region. It is calculated with respect to the TV divided by its uncertainty
- **Track mass (m_{track}):** Invariant mass of all tracks in both core and isolation regions with the assumption of each track being pion.
- **Fraction of EM energy from charged pions ($f^{\text{track-HAD}}_{\text{EM}}$):** Ratio of two values related with the energy deposit associated with the τ_{had} candidate in the EM calorimeter and TC energy deposit in the hadronic calorimeter. The numerator is the difference between the momentum sum of all tracks in core region and TC energy deposited in the hadronic calorimeter including Back layer of EM calorimeter information. The denominator is sum of TC energy in EM calorimeter with only pre-sampler, Front-layer and Middle-layer information.
- **Ratio of EM energy to track momentum ($f^{\text{EM}}_{\text{track}}$):** Ratio of the sum of EM cluster energy and sum of the momentum of tracks in core region. The TC and tracks are associated with the τ_{had} candidate and calibrated with the LC energy scale.
- **Track-plus-EM-system mass ($m_{\text{EM+track}}$):** Invariant mass of the system composed of all tracks and two highest energetic EM cluster in the core region. Only the cluster from leading three layers of the EM calorimeter is considered. [11] In addition, the hypothesis of zero mass with TC seed direction is applied to the four-momentum calculation of an EM cluster.

---

[10] ATLAS suggests using only 1-prong and 3-prong only for any physics analysis. However, this thesis provides the first try with the τ_{had} candidate with two associated tracks.

[11] presampler, Front-layer and Middle-layer only. Back layer designed specially to measure the tail of EM showers is not considered in this variable.

Variable Name	1-prong	3-prong
f_{cent}	○	○
$f^{-1}_{leadtrack}$	○	○
$R^{0.2}_{track}$	○	○
$\|S_{leadtrack}\|$	○	
f^{track}_{iso}	○	
ΔR_{Max}		○
S^{flight}_{T}		○
m_{track}		○
$f^{track-HAD}_{EM}$	○	○
f^{EM}_{track}	○	○
$m_{EM+track}$	○	○
$p^{EM+track}_{\mathrm{T}}/p_{\mathrm{T}}$	○	○

Table 4.3.: The discriminating input varaibles to Tau ID BDT training for 1-prong and 3-prong τ_{had} respectively [153].

- **Ratio of track-plus-EM-system to $p_{\mathbf{T}}$ ($p^{\mathrm{EM+track}}_{\mathbf{T}}/p_{\mathbf{T}}$):** The variable related with the measurement τ_{had} p_{T}. Ratio is the vector sum of track momenta combined EM cluster and ID track information divide to the one for two highest energetic EM cluster of the calorimeter only in core region.

The background rejection versus signal efficiency, which is also referred to as "ROC curve", with each optimized working points are displayed in Fig. 4.27. The multi-jet dominated simulation background events and signal $Z/\gamma^* \to \tau\tau$ events are used in BDT discriminant training. The three working points for physics analysis, *loose, medium and tight*, are optimized based on the signal efficiencies (0.6, 0.55, 0.45) for truth 1-prong τ_{had} and (0.5, 0.4, 0.3) for truth 3-prong τ_{had}. For this high mass Higgs analysis, the corresponding efficiency after each tau ID working points requirements of truth 1-prong (3-prong) τ_{had} are presented in Fig 4.28. The black point in the histogram also presents the rate of the generated level τ_{had} object being reconstructed as a corresponding τ_{had} candidates. To deal with the discrepancy of data and MC simulation after tau ID application, the corresponding scale factor are applied as the corrections for MC simulation. A special uncertainty is predicted for high-pT τ_{had} region to cope with the low statistical problem in data. The larger combined uncertainties up to around 55%(40%) are applied for 1-(multi-)prong modes to cover both uncertainties associated with reconstruction and identification efficiency. Due to the high-p_{T} τ in this analysis, the tau ID uncertainty is the main systematic uncertainties.

4.5.4 Tau Trigger

The Region of Interest (RoI) has been defined in level 1 trigger built with the electromagnetic (EM) and hadronic (HAD) calorimeter trigger tower of typical granularity in $\Delta\phi \times \Delta\eta = 0.1 \times 0.1$. The precision tracking consists of calorimeter clustering and tracking information from the Level-1 Tau RoI. Events for $\tau_{\mathrm{had}}\tau_{\mathrm{had}}$ channel are recorded using the single tau trigger (STT). The STT is with the requirements on tau p_{T}, Tau ID threshold and the number of tau tracks for having high efficiency as well as good resolution. The two levels of the number of tracking requirement, so-called as *tracktwo*, is applied on the pre-selection step of the τ_{had} objects for identifying candidates and against hadronic backgrounds. Tau trigger identification working point *medium1* is built with a slightly higher signal efficiency compared to Tau ID *medium* working point for reconstructed τ_{had}. The L1 Tau seed objects are also requested with 60 GeV and 100 GeV p_{T} cuts, therefore the pT thresholds at HLT are adjusted accordingly. The lowest p_{T} threshold of STT in this analysis is 80 GeV. In the further high luminosity environment, the p_{T} threshold has been harder and raised to 125 GeV and 160 GeV. The tau trigger efficiencies at the L1 and HLT are

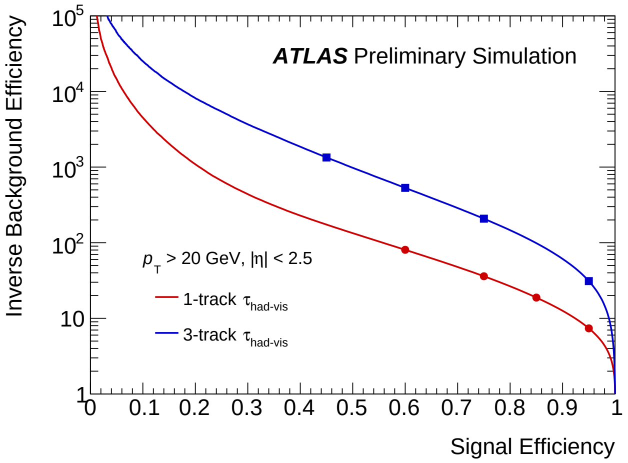

Figure 4.27.: The inverse background efficiency versus signal efficiency of Tau ID for 1-prong τ_{had} (red line) and 3-prong τ_{had} (blue line). *(tight, medium, loose)* working points are also represents as the dots on the curve from left to right, while the fourth (rightmost) point corresponds to the signal efficiency of 95 % is called *very loose* working point, which never used in this analysis [158] [159].

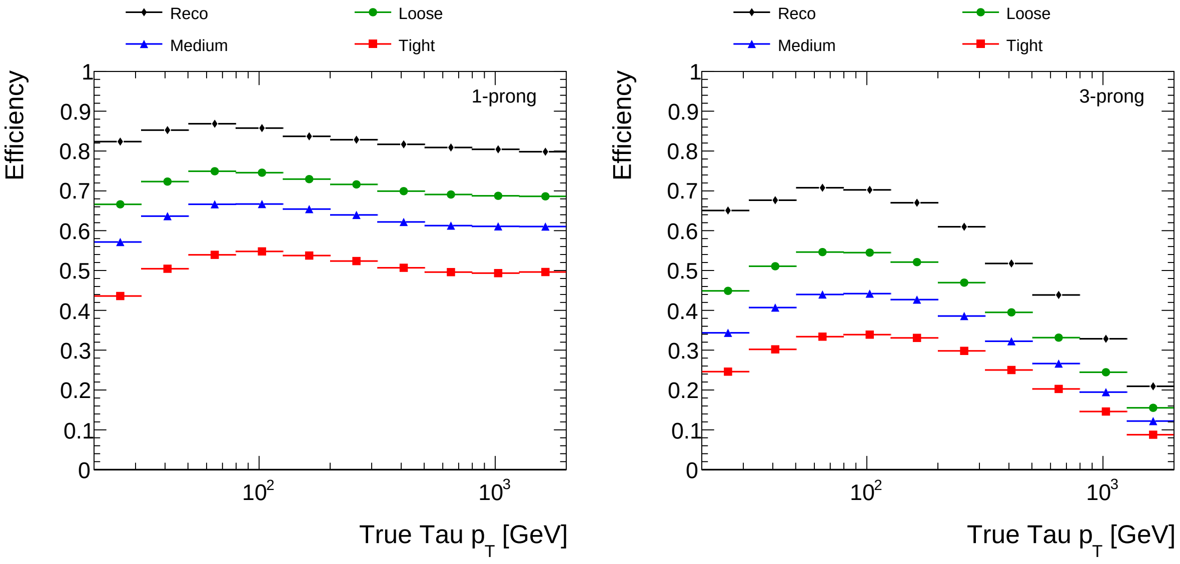

(a) (b)

Figure 4.28.: (a) and (b) show the p_{T} distribution of τ_{had} objects matched with the generated level objects for 1-prong and 3-prong. The black point shows the reconstructed rate of the generated level τ_{had}. While the efficiency of each working point includes the reconstruction rate are shown in green (for *loose*), blue (for *medium*) and red (for *tight*) points.

Trigger name	For Years	Luminosity (fb^{-1})
$HLT\_tau80\_medium1\_tracktwo\_L1TAU60$	2015-2016	5.3
$HLT\_tau125\_medium1\_tracktwo$	2015-2016	9.3
$HLT\_tau160\_medium1\_tracktwo$	2016-2018	103.4
$HLT\_tau160\_medium1\_tracktwo\_L1TAU100$	2017-2018	22.3

Table 4.4.: Table of STT used in this analysis. Each STT used for different data taking year corresponding to its luminosity.

shown in Fig. 4.29 as a function of p_{T} of τ_{had} or the number of pp interaction vertices. The STT used in this search are listed in Table 4.4:

The efficiency of STT is studied in the $Z \to \tau\tau$ events. It is calculated using the probe τ_{had} candidates that passing the STT. The difference between the data subtracted backgrounds and the simulated $Z \to \tau\tau$ events is computed as a scale factor for simulation in the analysis. Figure 4.30 shows the result of single tau trigger with isolated requirement for the objects at L1, and the offline p_{T} cut are also applied for τ_{had} candidates. Tau trigger shows very good performance especially for high-p_{T} region. For 1-prong τ_{had}, the efficiency is almost full above $p_{\mathrm{T}} > 40\ GeV$.

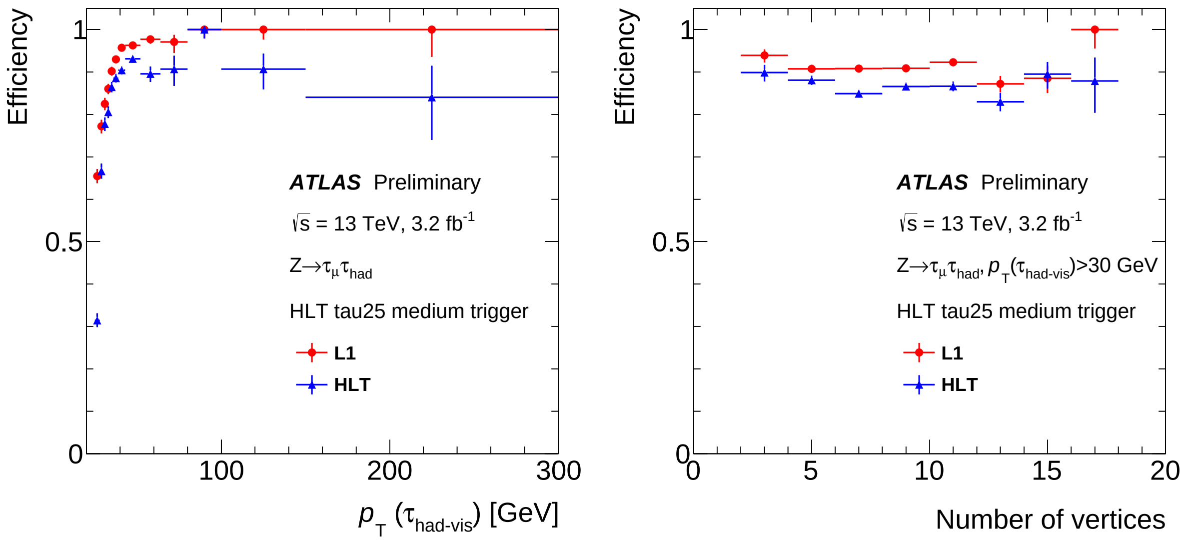

(a) (b)

Figure 4.29.: The tau trigger efficiency estimated by data subtracted backgrounds as the functions of τ_{had} p_{T} (a) and number of vertices (b). Red and blue dots show the efficiency for Level 1 and High Level Trigger respectively [160].

4.6 Hadronic τ Decays with Two Charged Particles

The track reconstruction and identification are important for reliable reconstruction of τ_{had} object. It highly depends on the geometrical information from ATLAS detector and the technology of fake background suppression. In the search for heavy Higgs to di-τ_{had} channel, the final state with high p_{T} τ_{had} is expected. As discussed in Sec 4.5, τ_{had} is generally dominated in the final state with one or three charged tracks. However, the τ_{had} with mis-reconstructed charged tracks, such as 2-prong τ_{had}, appears due to

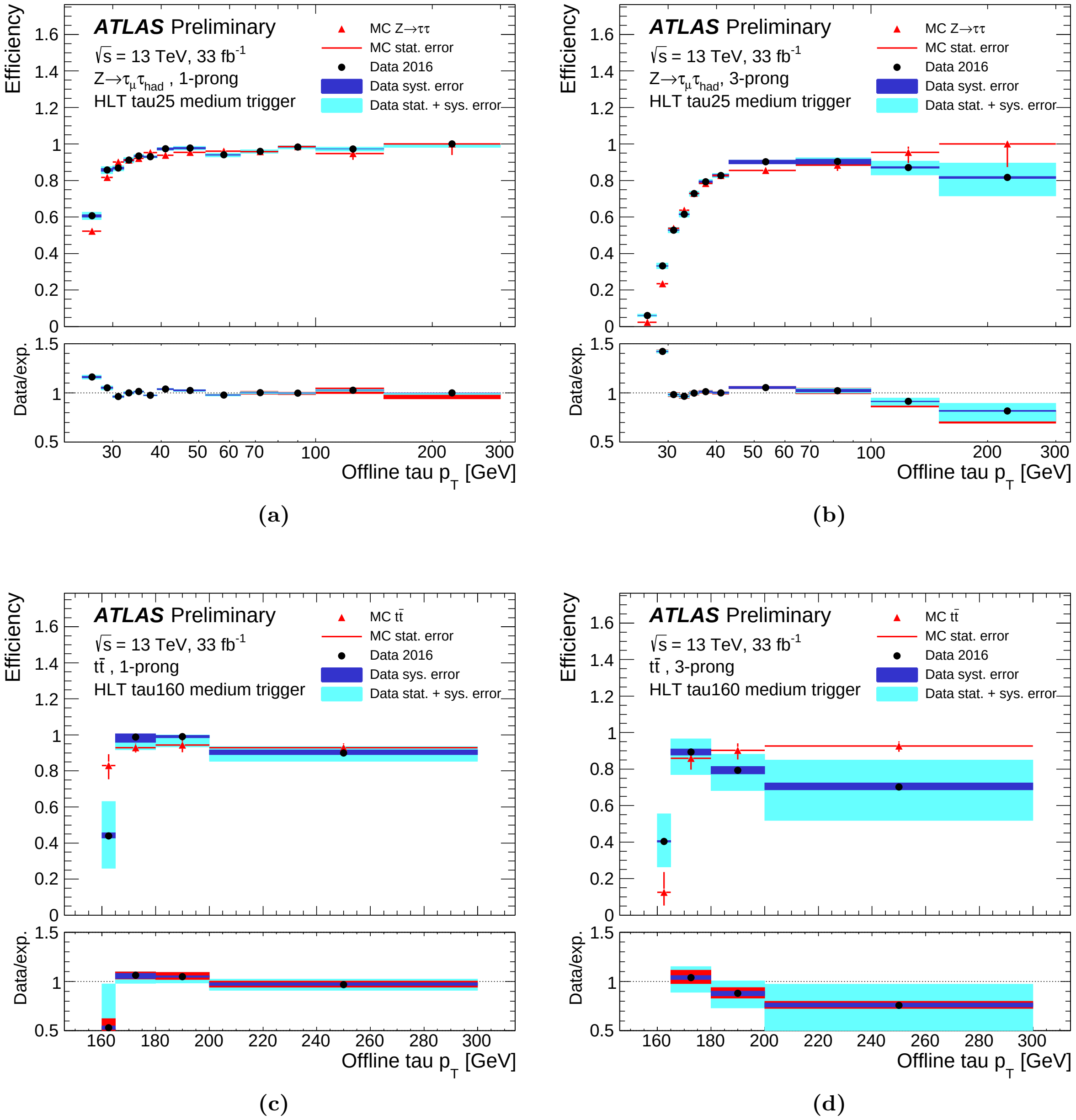

Figure 4.30.: The trigger efficiency with the corresponding scale factors for (a) 1-prong and (b) 3-prong. The efficiency is measured by tag-and-probe method in $Z \to \tau\tau$ control region with data and simulation. The bottom two plots show the efficiency measured by tag-and-probe method in $t\bar{t}$ events for high-p_{T} (c) 1-prong and (d) 3-prong τ_{had} [161].

the possible reasons illustrated in Fig 4.31.

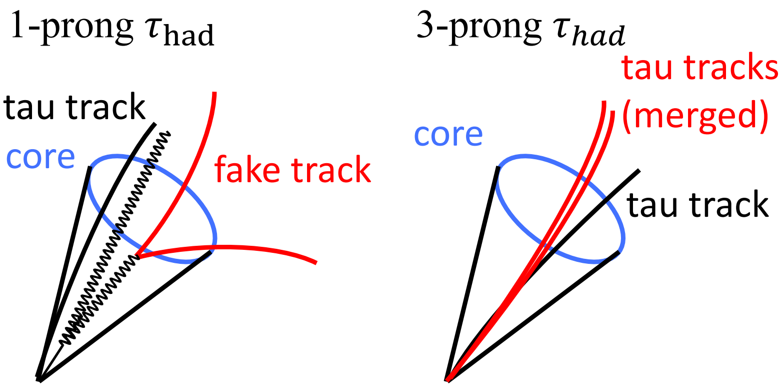

(a) 1-prong → 2-prong case **(b)** 3-prong → 2-prong case

Figure 4.31.: The reasons for hadronic τ reconstructed with two charged tracks. In 1-prong τ_{had} → to 2-prong τ_{had} case, an additional fake track passed the tau track core selections is expected from π^0 decay and taken into the hadronic τ reconstruction. For the 3-prong → 2-prong case, the high p_{T} τ_{had} produces two geometrically close tracks are merged due to the boosting phenomenon.

When the τ_{had} is produced with high p_{T}, the tau decay products are highly collocated and the two same charged tracks from 3-prong tau are merged into a single track. In this case, many 3-prong τ are mis-reconstructed as 2-prong τ. On the other hand, around 30% contribution of 2-prong τ of this analysis comes from 1-prong τ due to an additional fake track from e^+e^- pair-creation associated with $\pi^0 \rightarrow \gamma\gamma$. Since an additional fake track is taken into τ_{had} reconstruction, it causes the 1-prong → 2-prong case. In most of ATLAS analysis, 2-prong tau is not exploited due to the negligible contribution in low p_{T} region. There is no the support staff from the ATLAS for 2-prong τ application.

In this analysis with high p_{T} τ_{had}, there are many 2-prong τ_{had} in the high mass signal. Ah shown in Fig. 4.32, the p_{T} distribution of τ_{had} shows that the τ_{had} object from heavy Higgs is with high p_{T}. Moreover, the 2-prong τ_{had} contribution of 1500 GeV signal is larger than the one of 300 GeV signal. The signal efficiency is significantly improved by adding the 2-prong τ_{had}. In the gluon-gluon fusion signal with Higgs mass of 1500 GeV, the contribution of 2-prong τ_{had} with $p_{\text{T}} > 50$ GeV is around 15%. After event selection and trigger application in this analysis, 2-prong τ_{had} application saves the ggH signal efficiency of about 20%. Approximately 65% of reconstructed 2-prong τ_{had}s originate from the 3-prong taus in this analysis. The corresponding identification, calibration and systematic uncertainties are discussed in the section.

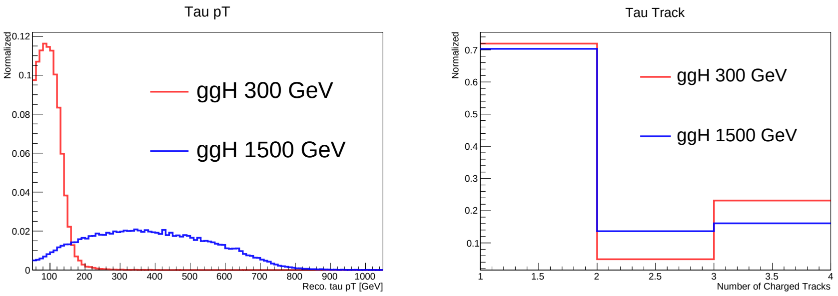

(a) τ_{had} p_{T} **(b)** number of charged track of τ_{had}

Figure 4.32.: The p_{T} distribution of gen-matching τ_{had} in (a) shows the importance of high-p_{T} τ_{had} in the heavy Higgs search. (b) shows the number of charged tracks associated to τ_{had} in signal with different mass region.

4.6.1 Identification Investigation

An identification of 2-prong tau requires a algorithm. It is developed based on boosted decision trees, similarly to the 1- and 3-prong tau identification. The Toolkit for Multivariate Data Analysis (TMVA) [137] is applied for the 1-prong and 3-prong τ_{had} identification algorithms. The same schemes are also used for the investigation of identification algorithms of 2-prong τ_{had}. The training program for 1-prong τ_{had} is not considered since most of the 2-prong τ_{had} comes from 3-prong τ_{had}. Each input variables of TMVA training for 3-prong τ_{had} algorithms are surveyed for 2-prong τ_{had} candidates. The comparison of input variables and training output scores are summarized in Appendix F. Due to the similar distributions between 3-prong τ_{had} and 2-prong τ_{had}, it supports to use 3-prong identification algorithm for 2-prong τ_{had}. Figure 4.33 presents the fake rate of hadron jets in three working points of identification (*loose*, *medium* and *tight*) together with signal efficiency and background rejection, so called as "ROC" curve [12]. Based on the background rejection curve shown in Fig 4.33(b), the strong rejection power of identification is expected to suppress fake 2-prong τ_{had} background. Fig 4.33(c) shows the signal efficiency. The slightly low signal efficiency for truth 2-prong τ_{had} due to the 1-prong→2-prong τ_{had} case (yellow line).

The current 3-prong identification algorithms is used for 2-prong τ_{had} in this analysis. It is acceptable due to the strong rejection power. The performance improvement for the detectors is necessary to improve the signal efficiency.

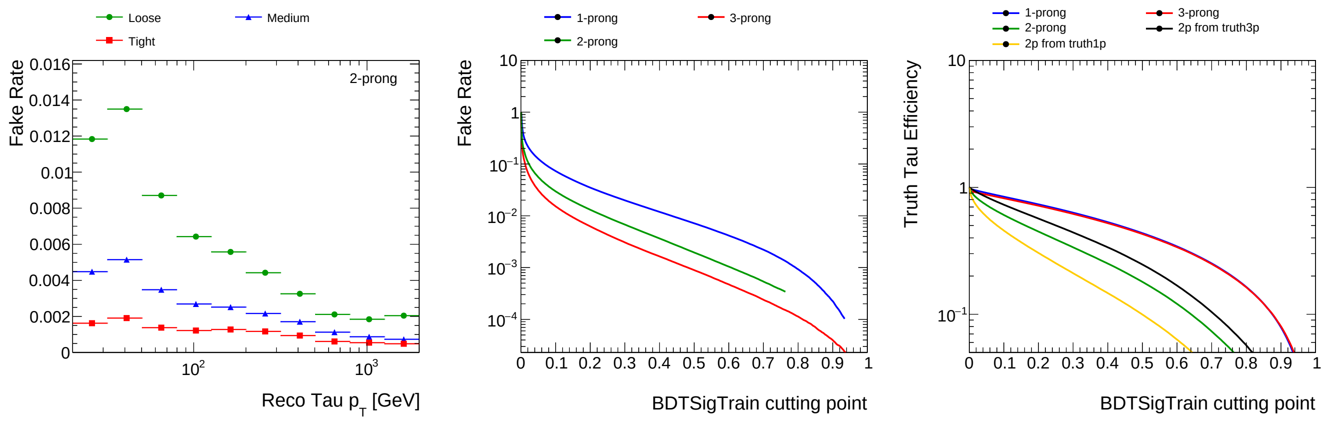

(a) (b) (c)

Figure 4.33.: Performance of 2-prong τ_{had} to a training 3-prong identification. (a) shows fake rate of multi-jet background with the *loose*, *medium* and *tight* working point applications. The fake rate comparison with 1-prong and 3-prong τ_{had} in the function of training output score is presented in (b). The corresponding signal efficiency is illustrated in (c).

4.6.2 Calibration

Introduction

The correction for 2-prong τ_{had} identification is computed based on the tag-and-probe analysis. Considering 2-prong τ_{had} is dominated in high-p_{T} region, a $t\bar{t}$ control region is chosen for scale factor measurement for the wide p_{T} region. The higher mass of top quark compared to the Z boson provides a higher p_{T} spectrum for decaying tau lepton as shown in Fig 4.34 [162]. It provides enough statistics for the scale factor measurement of 2-prong τ_{had}.

---

[12] Receiver Operating Characteristic of TMVA is called as ROC for short.

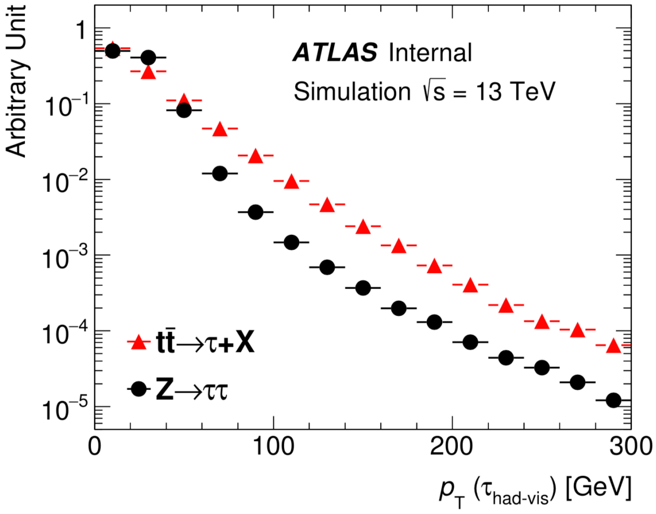

Figure 4.34.: The p_{T} normalized distribution of gen-matched tau candidates from $t\bar{t}$ and $Z \to \tau\tau$ events [162].

Compared with the electron object, the muon is much harder to deposit enough energy in the calorimeters. In order to choose a suited tag object, the muon object with high resolution is used in the $t\bar{t}$ tag-and-probe analysis with probe τ_{had}. The $t\bar{t} \to b\mu\nu_{\mu} + b\tau\nu_{\tau}$ process is exploited to measure the fraction of efficiency between analyzed data and MC simulation.

Event Selection

A single-muon trigger with the threshold of 50 GeV is selected to choose $t\bar{t}$ control region. Muon candidates are requested to satisfy the $p_{\mathrm{T}} > 55GeV$ threshold within the $|\eta| < 2.5$ region and the medium quality as well as the isolation [163]. The events are required to include exactly one selected muon candidate. The events with the one electron passing loose identification, $p_{\mathrm{T}} > 15$ GeV and cone region selection are rejected. In order to maximize the purity of $t\bar{t}$ events in the control region, the transverse mass requirement of the muon candidate and E_{T}^{miss} ($m_{\mathrm{T}} = \sqrt{2p_{\mathrm{T}}^{\mu} \cdot E_{\mathrm{T}}^{miss}(1 - \cos\Delta\phi(\mu, E_{\mathrm{T}}^{miss}))}$) is applied. The b-tagged algorithm is used with *MV2c10* algorithm in 70% efficiency working point. The events with at least two btagged jets with $p_{\mathrm{T}} > 20$ GeV is required. The probe object is defined as the leading p_{T} τ_{had} candidate selected with p_{T} larger than 40 GeV and with two charged tracks. In order to obtain high purity τ_{had} and reduce the effect from fake jets, a lower identification with BDT score > 0.04 is applied for the probe object.

Signal and background processes

The $t\bar{t}$ events with at least one truth τ_{had} accounts as the signal process (so called truth $t\bar{t}$). The $t\bar{t}$ events without truth τ_{had} are the fake background process (so called fake $t\bar{t}$). The signal and background are shown in Fig 4.35. The opposite sign charge requirement (OS) of tag and probe objects is applied to reduce fake $t\bar{t}$ events. The number of non-b jets is different between the signal and background processes considered here (see Fig. 4.35). The distributions of number of non-b-tagged jet is used to extract the tau ID efficiency. Figure 4.36 shows the signal region number of non-btagged jets distribution before tau ID application and the corresponding shape comparison between signal and background. The correction factor is obtained as the ratio of the tau ID efficiency derived from data to that from simulation The numerator is the tau ID efficiency of estimated data by fitting. The denominator is the tau ID efficiency of truth $t\bar{t}$ MC simulation.

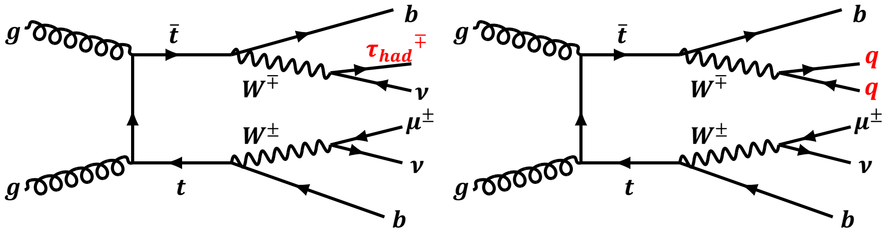

(a) (b)

Figure 4.35.: Feynman diagrams for $t\bar{t}$ event. (a) shows the signal process with one τ_{had}, and (b) present the background process includes W boson decay to quark production.

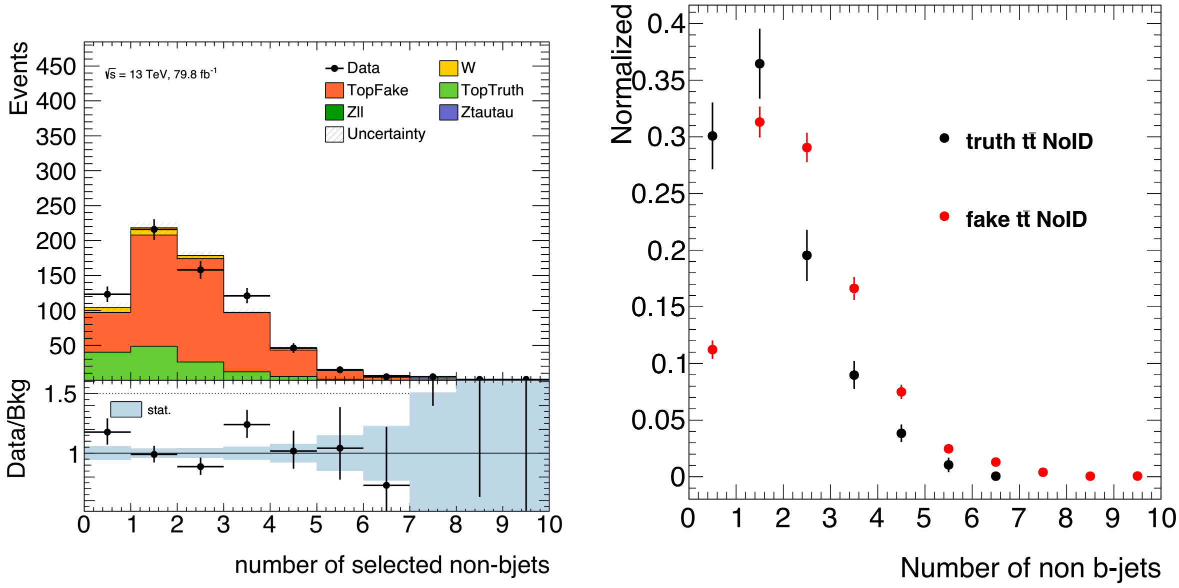

(a) data vs. MC **(b)** MC templates

Figure 4.36.: Number of non-btagged jets distribution before tau ID application. (b) The histograms of signal and background used in fitting are normalized to unit.

Result

The scale factor for 2-prong τ_{had} is measured with respect to the efficiency of tau ID and single tau trigger. Since the *medium* ID selection with single tau trigger and only *loose* ID selection are applied to the leading and sub-leading τ_{had} in heavy Higgs search, the corresponding scale factors are considered. Comparison of the simulation events and data are shown in the upper part of Fig 4.37. The bottom three plots show the fitting result (*post-fit* plots) from data. The scale factor for 2-prong τ_{had} is computed in one bin due to the statistical issue. Table 4.5 shows the number of simulation signal and estimated event in data.

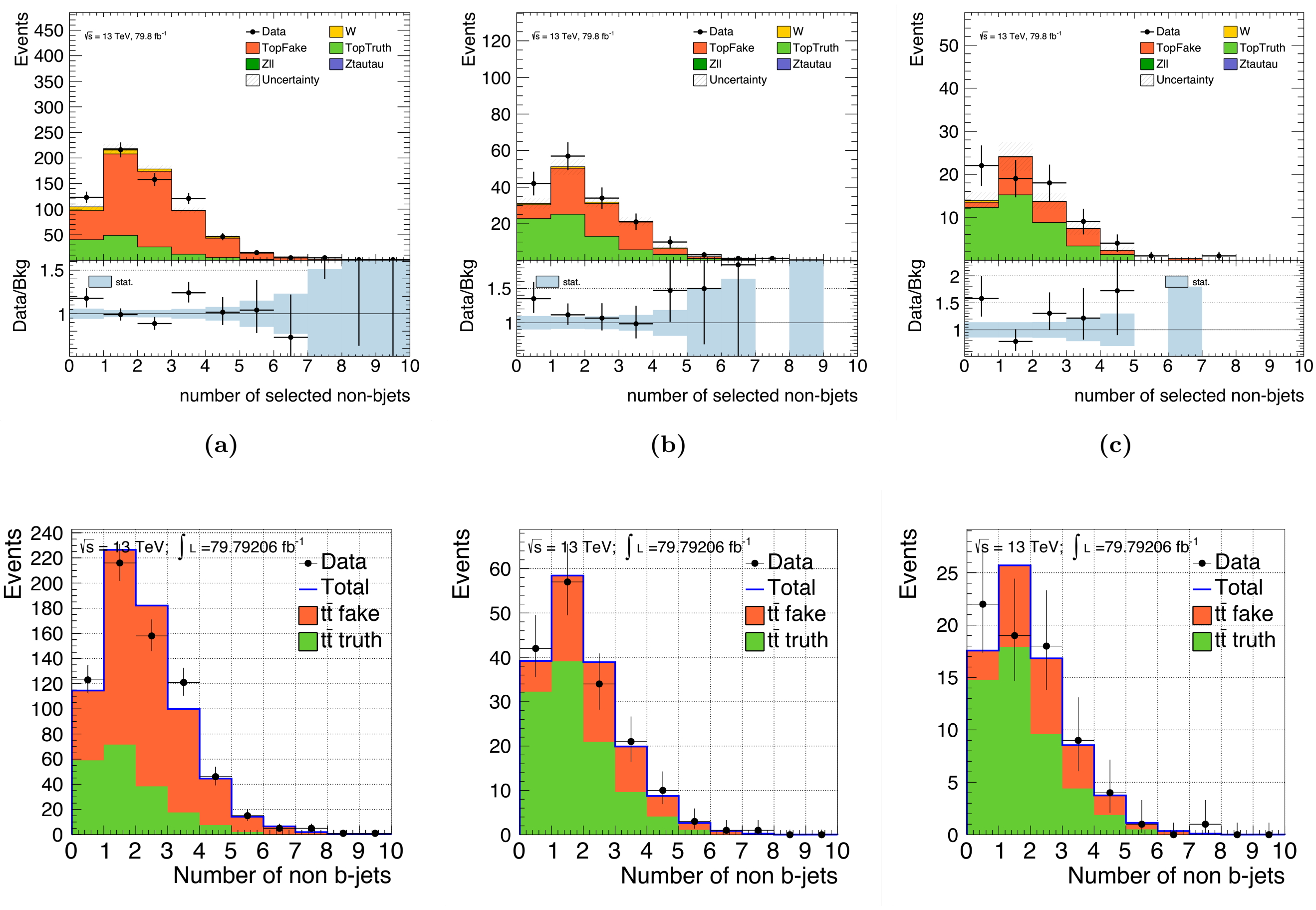

(a) (b) (c)

(d) (e) (f)

Figure 4.37.: Number of non-btagged jets distribution used for 2-prong τ_{had} scale factor measurement. Upper three pre-fit plots show the comparison with the simulation samples and analyzed data. The bottom post-fit plots present the estimated event from data by fitting with signal and background templates. From left to right plots, it shows the distribution given for the probe τ_{had} without any ID requirement (shown in (a) and (d)), with *loose* ID (shown in (b) and (e)) and with *medium* ID plus single tau trigger (shown in (c) and (f)).

The dominated systematic uncertainty of scale factor measurement comes from data statistics. The uncertainty and scale factor are written as:

$$SF = \frac{\epsilon_{data}}{\epsilon_{mc}}. \tag{4.9}$$

$$\sigma_{SF} = SF \times \sqrt{(\frac{\sigma_{\epsilon_{mc}}}{\epsilon_{mc}})^2 + (\frac{\sigma_{\epsilon_{data}}}{\epsilon_{data}})^2}, \tag{4.10}$$

Sample Name	No-ID	Loose	Med. + trigger
		Pre-fit result	
$t\bar{t}$ fake	508.8 ± 12.4	71.0 ± 4.8	20.2 ± 2.6
$t\bar{t}$ truth	133.3 ± 6.8	71.0 ± 4.6	40.9 ± 3.8
Total MC	642.1 ± 14.1	142.0 ± 6.6	61.1 ± 4.6
Data	691.00 ± 26.3	169.00 ± 13.0	74 ± 8.6
		Post-fit result	
$t\bar{t}$ fake	494.6 ± 46.5	61.9 ± 21.5	24.9 ± 13.2
$t\bar{t}$ fake	196.4 ± 43.2	107.2 ± 22.5	49.1 ± 14.0
Total MC	691.0 ± 63.5	169.1 ± 31.1	74.0 ± 19.2
Data	691.00 ± 26.3	169.00 ± 13.0	74 ± 8.6

Table 4.5.: The yield of each simulation events and data before and after ID and trigger selections. The error part of pre-fit result are only presented the standard statistical uncertainties, while the error part of post-fit result includes the fitting uncertainties. The uncertainty of total MC is computed based on the propagation principle for error calculation.

	Loose	Medium + trigger
ϵ_{data}	0.546 ± 0.140	0.250 ± 0.084
ϵ_{mc}	0.533 ± 0.044	0.307 ± 0.033
Scale Factor	1.024 ± 0.276	0.814 ± 0.287

Table 4.6.: The numerator of the data efficiency and the denominator is the tau ID efficiency of truth $t\bar{t}$ MC simulation are taken into account for the scale factor measurement. The systematic uncertainties of SF are computed following the propagation error principles.

where the statistical uncertainty of data efficiency $\sigma_{\epsilon_{data}}$ is investigated by the propagation method. Propagation of uncertainty is written as a common formula with neglecting correlations:

$$\sigma_f = \sqrt{\Sigma_i (\frac{\partial f}{\partial X_i}^2) \sigma_{X_i}^2}, \tag{4.11}$$

where f is a function with the neglecting correlation variables X_i. The function shows that the uncertainties is relative with the event number of the passing and failing regions. The systematic uncertainties are computed with scale factor and summarized in Table 4.6.

4.7 Missing Transverse Energy

ATLAS detector provides the precision measurement for most of the particles, however, neutrinos are not detected. For any process with neutrino like tau lepton decay or weakly-interacting, the reconstruction of the neutrino is indispensable and crucial. In ATLAS physics analysis, the intrinsic momentum in the transverse plane is negligible that helps to measure the transverse momentum of the undetectable neutrino with all other detectable particles. Based on the fact that the momentum in the transverse plane to the beam axis should be summed as zero, any disproportion is called as *Missing Transverse Energy* (MET) or referred to as $E_{\mathrm{T}}^{\mathrm{miss}}$ as shown in Fig. 4.38 [13]. To understand the missing energy from the particles originated from neutrino, $E_{\mathrm{T}}^{\mathrm{miss}}$ is calculated from all calibrated physics objects. Selected physics objects

---

[13] Illustration to explain the structure of $E_{\mathrm{T}}^{\mathrm{miss}}$ calculation. It is also used to measure the relative systematic uncertainty as shown in Reference [164].

like electrons, photons, $\tau_{\text{had-vis}}$, muons and jets coming from the primary vertex are known as *hard term*. On the other hand, the reconstructed tracks from the objects, which are associated with the hard-scatter vertex and not associated to the hard term, are taken into account as a *soft term*, which is expected to be perfectly balanced against hard term if there is no missing energy. Pile-up event is hard to predict as described in the previous section, while it affects the calculation both of the hard term and the soft term. Therefore, the fully calibrated and corrected methods are considered for *hard term* and *soft term*. In addition, $E_{\mathrm{T}}^{\mathrm{miss}}$ is highly dependent on the calibration and accuracy of the measurement for all hard terms if there is no real $E_{\mathrm{T}}^{\mathrm{miss}}$ in events. Due to extremely complex condition for $E_{\mathrm{T}}^{\mathrm{miss}}$ reconstruction, the resolution is always the key point for analysis. Sec. 4.7.1 present the detailed reconstruction procedure of $E_{\mathrm{T}}^{\mathrm{miss}}$, and the corresponding performance is shown in Sec. 4.7.2. This section is widely referenced in [165].

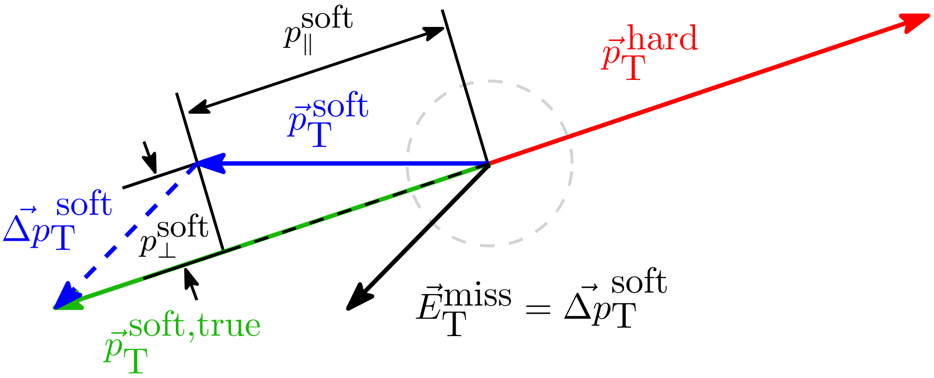

Figure 4.38.: Sketch shows that the an imbalance in the event would be computed as Missing Transverse Energy (E_T^{miss}) [165].

4.7.1 $E_{\mathrm{T}}^{\mathrm{miss}}$ Reconstruction

Calorimeter signal of the hard term and the not associated soft term are taken into account for the E_T^{miss} reconstruction. The soft term can be reconstructed in two ways: the track-based soft term from ID track and calorimeter-based soft term from calorimeter signals. In order to avoid the track which is unassociated with primary vertex, the calorimeter-based soft term is not considered for the reconstruction. The $E_{\mathrm{T}}^{\mathrm{miss}}$ is computed with $E_{\mathrm{x(y)}}^{\mathrm{miss}}$ components defined as:

$$E_{\mathrm{x(y)}}^{\mathrm{miss}} = E_{x(y)}^{\mathrm{miss},e} + E_{x(y)}^{\mathrm{miss},\gamma} + E_{x(y)}^{\mathrm{miss},\tau_{\mathrm{had-vis}}} + E_{x(y)}^{\mathrm{miss,jets}} + E_{x(y)}^{\mathrm{miss},\mu} + E_{x(y)}^{\mathrm{miss,soft}} \tag{4.12}$$

$$E_{\mathrm{T}}^{\mathrm{miss}} = \sqrt{(E_x^{\mathrm{miss}})^2 + (E_y^{\mathrm{miss}})^2}, \phi^{\mathrm{miss}} = \arctan(E_y^{\mathrm{miss}}/E_x^{\mathrm{miss}}) \tag{4.13}$$

$$\Sigma E_{\mathrm{T}} = \Sigma p_{\mathrm{T}}^{e} + \Sigma p_{\mathrm{T}}^{\gamma} + \Sigma p_{\mathrm{T}}^{\tau_{\mathrm{had-vis}}} + \Sigma p_{\mathrm{T}}^{\mathrm{jets}} + \Sigma p_{\mathrm{T}}^{\mu} + \Sigma p_{\mathrm{T}}^{\mathrm{soft}} \tag{4.14}$$

, where the $E_{x(y)}^{\mathrm{miss,(objects)}}$ is the sum of x(y)-components of the momenta of individual objects. $E_{\mathrm{T}}^{\mathrm{miss}}$ and ϕ^{miss} are the magnitude and azimuthal angle of $E_{\mathrm{T}}^{\mathrm{miss}}$, respectively. ΣE_{T} is another related observable defined as the scalar sum of transverse momenta of all hard and soft terms.

Unlike hard term, a dedicated algorithm is necessary to develop $E_{\mathrm{T}}^{\mathrm{miss}}$ soft term. The main purpose is to maximize the reduction power for pile-up interactions. Track Soft Term (TST) is build with ID tracks information and the association of the primary vertex. Only tracks not matched to any hard term with $p_{\mathrm{T}} > 0.4$ GeV within $|\eta| < 2.5$ and several minor reconstruction quality requirements are used in TST. Cuts on transverse and longitudinal impact parameter of $d_0 < 1.5$ cm and $z_0 < 1.5$ cm are also applied to the vertices reconstructed by track with the hit requirements in the ID. In additional requirement in

TST, the overlap removal between track and calorimeter clusters is defined as the following items. Based on the rigorous requirement, the TST provides a highly precise measurement for the soft term used in $E_{\mathrm{T}}^{\mathrm{miss}}$ reconstruction.

- Removing tracks around other tracks , electron or photon cluster (Default value : $\Delta R < 0.05$)
- Removing tracks around other tracks , τ lepton (Default value : $\Delta R < 0.2$)
- Removing tracks associated with jets based on the ghost-association technique
- Removing tracks in ID associated with muons based on combined ID+MS fit.
- Removing tracks with large momentum uncertainties ($> 40\%$)

4.7.2 $E_{\mathrm{T}}^{\mathrm{miss}}$ Performance

Since the $E_{\mathrm{T}}^{\mathrm{miss}}$ performance depends strongly on the selection of jets, two different working points are defined based on selection criteria of jets [164]. Loose working point includes all jets with criteria of $p_{\mathrm{T}} >$ 20 GeV within $|\eta| < 2.4$ or $p_{\mathrm{T}} > 60$ GeV for E_T^{miss} reconstruction. While the forward jets with $|\eta| > 2.4$ and $20 < p_{\mathrm{T}} < 30$ GeV are excluded in Tight working point. On this thesis, the *Loose* working point is used for avoiding degradation of reconstruction since the hard-scatter might be removed with *Tight* working point. The performance study of E_T^{miss} is based on $Z \to ll$ events thanks to good modeling in the current ATLAS simulation and the final state for E_T^{miss} rebuilding. The resolution of E_T^{miss} performed for $Z \to ee$ event topologies are shown in Fig 4.39 as function of the number of primary vertices and $\langle\mu\rangle$ in the event. The resolution increases linearly to approximately 24 GeV as a function of a number of primary vertices.

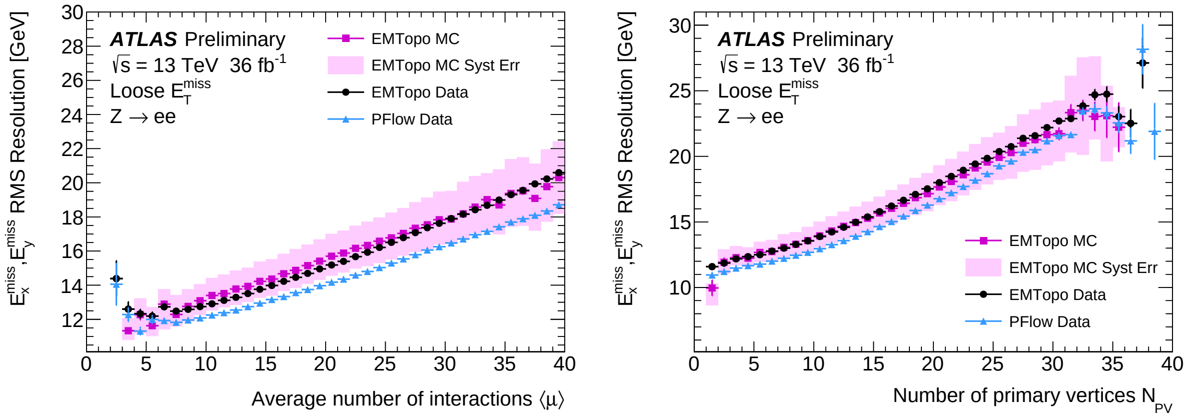

(a) (b)

Figure 4.39.: The RMS resolution distributions of E_x^{miss} and E_y^{miss} for data and simulation using *Loose* working point in a $Z \to ee$ events. (a) shows the distribution as a function of average number of interactions, and (b) shows the one as a function of number of primary vertices [164, 165].

The corresponding uncertainty is computed by all systematics associated with hard term and soft term employed in the reconstruction step. Figure 4.40 shows the agreement between data and simulation with the dominated systematic uncertainties coming from soft term evaluated by the specific method and pile-up modeling. It is clear the resolution in simulation is slightly smaller than the observed data while the discrepancy can be covered with the uncertainties.

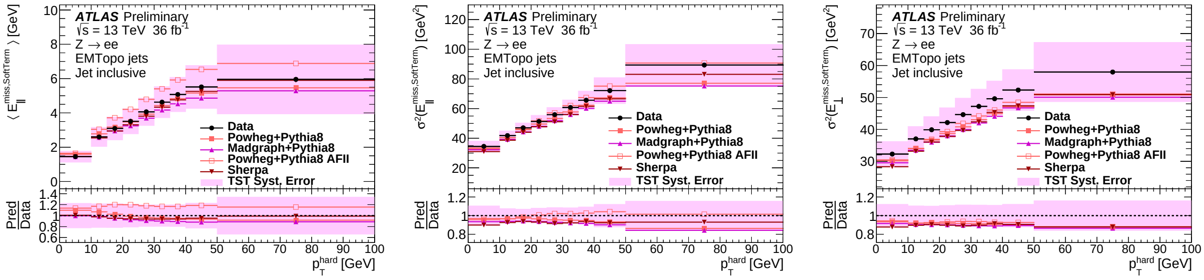

(a) **(b)** **(c)**

Figure 4.40.: The parallel scale (a), parallel resolution squared (b) and transverse resolution squared (c) distribution as a function of p_{T}^{hard} comparing with the different Monte Carlo simulation generations and observed data in $Z \to ee$ events. The pink band shows the final systematic uncertainties applied to the simulation in the analysis [164, 165].

5 Search for Neutral Heavy Higgs Bosons to $\tau_{\mathrm{had}}\tau_{\mathrm{had}}$ Decay

This chapter describes an overview of the analysis. Details of the collision data and the background simulation samples are described in Sec. 5.1. The event selection, including the triggering strategy and the offline event selection, is discussed in Sec. 5.2. The categorization is applied to maximize the search sensitivities, the details of which are presented in Sec. 5.3.

5.1 Collision Data and Simulation Data Samples

5.1.1 Collision Data

This analysis uses the 139 fb^{-1} of proton-proton collision data at a center-of-mass energy of $\sqrt{s} = 13$ TeV recorded by the ATLAS detector in 2015, 2016, 2017, and 2018, which is referred to as the “Run2” data-taking period. As discussed in Sec. 5.2.1, the single-tau trigger algorithm is used to collect data. To be selected in the analysis, events are required to satisfy a set of basic data-quality selection criteria with respect to the system operation status, which guarantees all the relevant sub-detectors of the ATLAS systems are functional in a good condition.

5.1.2 Simulated Samples

The simulation is used to model the signal and background processes. The simulated samples are used to estimate yields of signals and some of the backgrounds remaining after the event selection.

Signal Process

The major production process of neutral heavy Higgs bosons are the bottom-annihilation and gluon-gluon fusion processes as shown in Fig. 5.1. The details of the simulation setup, used in the signal sample simulations in total 8 mass points between 200 and 2500 GeV, for such as the Matrix element calculation, Parton Distribution Function (PDF), Parton-Shower simulation, are summarized in Tab. 5.1 The simulated events are interfaced to Geant 4 [166, 167], the full ATLAS detector simulator for the gluon-gluon fusion process, and AtlasfastII [168] fast simulation framework for the bottom-annihilation process. The production cross sections and decay branching fractions of the heavy Higgs bosons are estimated in the MSSM frameworks [29], and the details are summarized in Tab. 5.2 for various M_A and $\tan\beta$ scenarios.

Backgrounds Processes

Some of backgrounds processes are estimated with assistance of the Monte Carlo simulation as discussed in Chapter 6, for those associated with top-quark production (denoted as $t\bar{t}$, single top), W boson

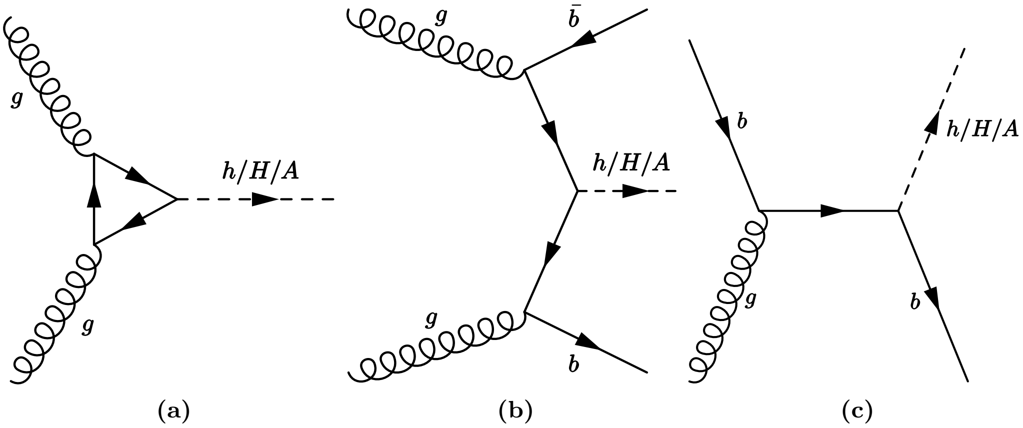

Figure 5.1.: Lowest-order Feynman diagrams of three main production proceese of the neutral MSSM Higgs boson; (a) gluon-fusion processes, (b) four-flavour schemes bottom-annihilation process, and (c) five-flavour schemes bottom-annihilation process.

Process	Generator (PDF)	Shower	Tune	Hadronisation
gluon-gluon fusion	Powheg-v2 (CT10)	Pythia8	AZNLO	CTEQ6L1
bottom-annihilation	MadGraph5 aMC@NLO 2.1.2 (CT10nlo nf4)	Pythia8	A14	NNPDF2.3LO

Table 5.1.: The generator and shower model used for the simulation of the signal processse in this analysis [169–174].

production (denoted as W+jets), the Drell-Yan process (denoted Z/γ^*+jets). The diagrams are shown in Fig. 5.2 and Fig. 5.3. These background processes are simulated with the setup as shown in Tab. 5.2. The simulated events are interfaced to the full detector simulation with Geant 4 [166].

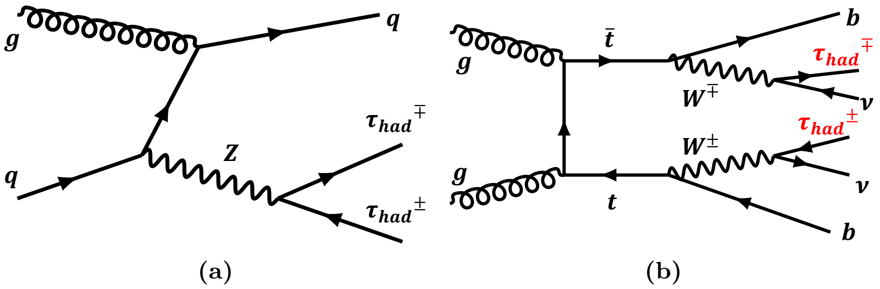

Figure 5.2.: Feynman diagrams of irreducible background in this analysis with the final state charactorized with a pair of τ_{had}; (a) Z/γ^*+jets (b) $t\bar{t}$ in the final state with at least truth two τ_{had}.

5.2 Event selection

To extract the $H/A \to \tau_{\text{had}}\tau_{\text{had}}$ signals from backgrounds, an optimal set of event selection criteria are used in this analysis.

Process	Generator (PDF)	Shower	Tune	σ (pb)	Order
$Z/\gamma^* + \text{jets}$	Powheg-v2 (CT10)	Pythia8	AZNLO	1901	NLO
$t\bar{t} + \text{jets}$	Powheg-v2 (CT10)	Pythia8	A14	730	NNLO
single-top, s-channel	Powheg-v2 (CT10)	Pythia8	A14	10	NLO
single-top, t-channel	Powheg-v2 (CT10)	Pythia8	A14	216	NLO
single-top, Wt-channel	Powheg-v2 (CT10)	Pythia8	A14	75	NNLO
$W \to \ell\nu$	Sherpa 2.2 (NNPDF30NNLO)	Sherpa 2.2	-	20080	NLO
Diboson	Sherpa 2.2 (NNPDF30NNLO)	Sherpa 2.2	-	45	NLO

Table 5.2.: The generator and shower model used for the simulation of the background processse in this analysis. [175–177]

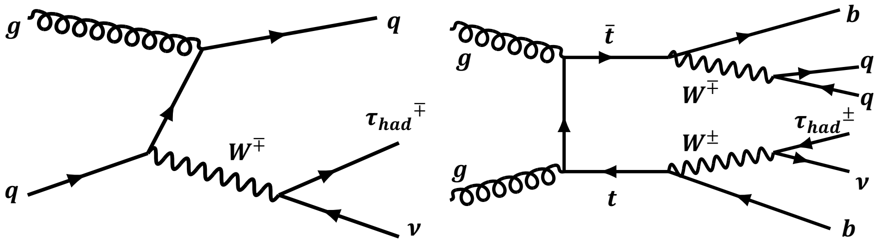

(a) **(b)**

Figure 5.3.: Feynman diagrams of reducible background in this analysis with fake τ_{had}; (a) W+jet process, (b) $t\bar{t}$ process with at least W decays to non-τ_{had} channel.

5.2.1 Triggering

The single-tau trigger (STT) is used to collect the data for this analysis. The details of the tau trigger algorithm and performance can be seen in Sec. 4.5.4. The STT with p_{T} thresholds of 80 GeV, 125 GeV, and 160 GeV are used in the data taking. The p_{T} thresholds depend on the instantaneous luminosity as shown in Table. 4.4. The trigger efficiency is measured with the collision data, and the efficiency of the simulation samples is corrected accordingly.

5.2.2 Event Reconstruction and Basic Selection

This analysis uses reconstructed muon, electron, hadron jets, and hadronically decaying tau objects, which are introduced in Chapter 4. The selection criteria for each object in this analysis are summarized in Table. 5.3. The leading tau leptons are required to satisfy the requirement of triggering with STT algorithm in terms of p_{T} threshold and the ID requirement. The corresponding offline p_{T} cuts are 5 GeV above the p_{T} thresholds of triggering selection, namely 85 GeV, 130 GeV, and 165 GeV for different trigger thresholds. The Tau identification cuts for sub-leading τ_{had} is used in the categorization which is discussed in Sec. 5.3. Electrons and muons are used for a veto selection to reduce the weak-interaction backgrounds, which often are associated with additional electrons or muons. As summarized in the Table. 5.3, a loose threshold is used, which is found to be optimal for the veto selection. Jet reconstruction and b-tagging are used to distinguish the gluon-gluon fusion and the bottom-annihilation processes.

The geometrical overlap between selected objects is solved in preference of precision measurement of muons, electrons, taus, and jets. The overlap removal procedure consists of four steps as shown in Table. 5.4 with respect to the distance defined as ΔR between objects.

Further, the background jets from beam-induced backgrounds, cosmic particles, and detector noise signals can affect the features of the event and $E_{\text{T}}^{\text{miss}}$ calculation. It is known that such background jets

1^{st} τ_{had}	2^{nd} τ_{had}	muon	electron	jet
Medium-id	Loose-id	Loose quality	Loose-id	JVT
$p_{\text{T}} > 85, 130, 165$ GeV	$p_{\text{T}} > 65$ GeV	$p_{\text{T}} > 7$ GeV	$p_{\text{T}} > 15$ GeV	$p_{\text{T}} > 20$ GeV
$\lvert\eta\rvert < 2.5$	$\lvert\eta\rvert < 2.5$	$\lvert\eta\rvert < 2.5$	$\lvert\eta\rvert < 2.47$	$\lvert\eta\rvert < 2.5$
no crack region	no crack region		no crack region	70% efficiency with b-tagging
1,2 or 3 tracks	1,2 or 3 tracks			
|charge| == 0,1 or 2	|charge| == 0,1 or 2			

Table 5.3.: The table to list the selections used for the physics objects. Electron and tau are excluded the "crack region" corresponding to the transition region between the barrel and end-cap calorimeters at $1.37 < |\eta| < 1.52$.

Gradation	Benchmark	Discarded object	Matching condition
step1	muon	electron	ΔR <0.2
step2	electron or muon	τ_{had}	ΔR <0.2
step3	electron or muon	jet	ΔR <0.4
step4	τ_{had}	jet	ΔR <0.2

Table 5.4.: Four steps for overlap removal based on ΔR between objects in preference of precision measurement of muons, electrons, taus and jets. The selections shown in Table. 5.3 beside the one for τ_{had} are applied for each objects.

have typically low $p_{\text{T}} < 60$ GeV. A basic selection, which is referred to as "event cleaning" selection, is designed and used in the analysis to reject events that are possibly affected by such components. If a selected jet object with $p_{\text{T}} < 60$ GeV) does not pass the quality cut in an event, the event will be discarded to avoid the effects on the $E_{\text{T}}^{\text{miss}}$ reconstruction. This event cleaning helps to reduce the negative effects on $E_{\text{T}}^{\text{miss}}$ from the non-collision components.

5.2.3 Event Selection

Following the basic selection discussed in the previous section, a series of event selection criteria is applied in this analysis to suppress background contributions while keeping signal acceptance as high as possible. To be selected, the candidate events are required to have at least two identified τ_{had} to select the $H/A \to \tau_{\text{had}}\tau_{\text{had}}$ signals, following the object selection criteria which are summarized in Table. 5.3. Backgrounds with additional electrons and muons in the final state can be suppressed by zero electron and zero muon selection, so-called the lepton veto selection. An opposite charge requirement of two p_{T} leading τ_{had} is used as long as both of the τ_{had}s are associated with an odd number of charged tracks. It is known to suppress fake τ_{had} contributions effectively. If "2-prong" τ_{had} candidate is included in the selected events, the sum of the charge of two tracks of the τ_{had} candidate should be 0 or opposite to the other τ_{had}. This cut is referred to as an opposite sign or OS requirement. A geometrical selection of $\Delta\phi$, which is an opening angle of two p_{T} leading τ_{had} in the transverse plane, is requested to be $\Delta\phi > 2.7$ to more purity signals, considering the signal event topology of heavy Higgs decaying two τ_{had} is expected with high p_{T} and the approximately opposite direction in the transverse plane. Figure 5.4 presents the distributions $\Delta\phi$ for signals and backgrounds after the OS requirement is applied. In order to avoid bias due to the statistical fluctuation of the data sample in the optimization, the data can not be directly surveyed in the signal region before confirming background estimation. In this analysis, the validation regions, referred to as "VR"s, are defined to verify the multijet background from the data-driven method, which is discussed in Sec. 6.2.1. the events are required to pass the all selection criteria as the signal selection but required to fail the opposite charge requirement. It allows selecting the validation samples with multijet backgrounds enhanced and suppress the potential signal contribution in the validation sample.

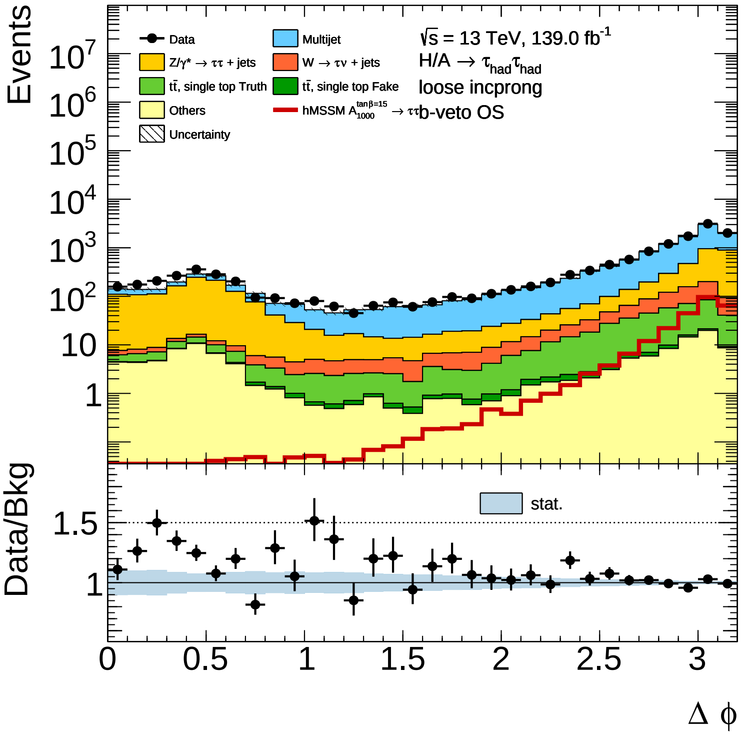

Figure 5.4.: $\Delta\phi$ distribution in OS before the $\Delta\phi > 2.7$ cut. The mis-modeling in low $\Delta\phi$ region is expected since only the $\Delta\phi$ region larger than 2.7 are considered in fake factor estimation for multi-jet background. The cut value on $\Delta\phi$ is computed to extract best signal significant.

5.2.4 Di-tau mass reconstruction

The final discriminant is defined to provide the best separation power between signals and background after all the event selection criteria are applied. A "total transverse mass" ($m_{\mathrm{T}}^{\mathrm{tot}}$) is chosen as the final discriminant in this analysis, which is defined as a sum of the visible decay product of the two τ_{had} (denoted as $\tau_{\mathrm{had},1}$ and $\tau_{\mathrm{had},2}$) and $E_{\mathrm{T}}^{\mathrm{miss}}$.

$$m_{\mathrm{T}}^{\mathrm{tot}} = \sqrt{m_{\mathrm{T}}(\tau_{\mathrm{had},1}, \tau_{\mathrm{had},2})^2 + m_{\mathrm{T}}(\tau_{\mathrm{had},1}, E_{\mathrm{T}}^{\mathrm{miss}})^2 + m_{\mathrm{T}}(\tau_{\mathrm{had},2}, E_{\mathrm{T}}^{\mathrm{miss}})^2}. \tag{5.1}$$

$$m_{\mathrm{T}}(i,j) = \sqrt{2p_{\mathrm{T}}^{i} p_{\mathrm{T}}^{j}(1 - \cos\Delta\phi_{i,j})}. \tag{5.2}$$

For the high mass resonance of $\tau_{\mathrm{had}}\tau_{\mathrm{had}}$ events, the $m_{\mathrm{T}}^{\mathrm{tot}}$ will be the very different distribution for each SM background and therefore can be a good final discriminant. As shown in Figure 5.5, the QCD multijet background is expected to be dominant in lower $m_{\mathrm{T}}^{\mathrm{tot}}$ region with the low $E_{\mathrm{T}}^{\mathrm{miss}}$ and with low p_{T} of jets which are typical for the multijet process. The high $m_{\mathrm{T}}^{\mathrm{tot}}$ region is dominated by $t\bar{t}$ and $Z \to \tau\tau$ SM background which contain at least two true τ_{had} in the final state. The $t\bar{t}$ and $Z \to \tau\tau$ events contain neutrinos in the final state and the $E_{\mathrm{T}}^{\mathrm{miss}}$ will be larger than the multijet backgrounds. It results in the fact that $t\bar{t}$ and $Z \to \tau\tau$ background are dominant processes in the large $m_{\mathrm{T}}^{\mathrm{tot}}$ region.

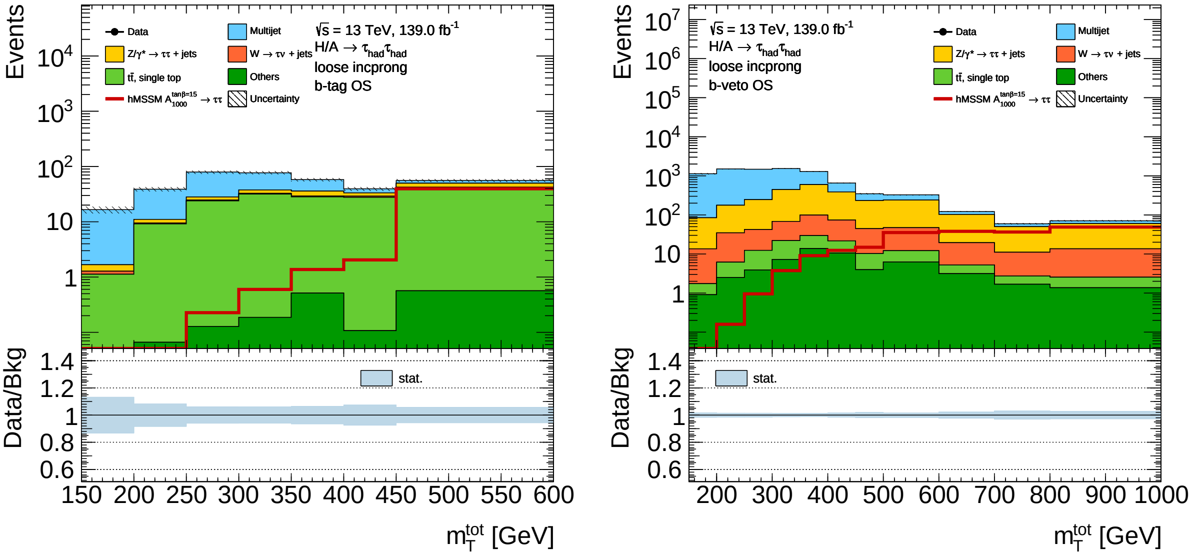

(a) BTAG

(b) BVETO

Figure 5.5.: $m_{\mathrm{T}}^{\mathrm{tot}}$ distribution in the BTAG (at least one b-tagged jet) and BVETO (without b-tagged jet) signal regions after event selection.

5.3 Categorization Definition

In order to maximize the search sensitivity, a categorization technique is used. The categorization is built with respect to the tightness of tau identification of the sub-leading τ_{had}, the number of tracks associated with the sub-leading τ_{had} and number of b-tagged jets of the events as illustrated in Fig 5.6. The 2-prong τ_{had} discussed in the previous section is also used in the categorization. To cover both of gluon-gluon fusion and bottom annihilation processes with the best signal sensitivities, the candidate events are categorized with respect to the number of b-tagged jets in the events. Events with at least one selected b-tagged jet is accommodated into the “BTAG” category, and the inverse events (0 b-jets events) are brought into “BVETO” category. The main background process in BVETO categories is multijet. The $t\bar{t}$ is dominant in the BTAG region. Given the multijet process is the major background in the low $m_{\mathrm{T}}^{\mathrm{tot}}$ region, a tighter tau identification can help the analysis improve the signal sensitivity for low mass scenarios. The currently available working point of tau ID, *loose*, *medium* and *tight*, which are discussed in Sec.4.5.3, are exploited in the BVETO categorization. The following categorization is introduced based on the identification information; *loose*-not-*medium* (*lnm* for short), *medium*-not-*tight* (*mnt* for short), and *tight*. The BVETO region takes advantage of the categorization based on the number of tracks associated with the sub-leading τ_{had}. The BTAG region does not use the categorization based on the number of tracks associated with the sub-leading τ_{had} due to the limited statsitcs mainly in the validation region of 3-prongs if b-tagging requirement is applied. A particular category, which is denoted to be “2P category”, is built to accommodate events with at least one high p_{T} 2-prong τ_{had}. The additional separation based on tau ID is not applied for 2P category due to the statistical problem occurred in the validation region.

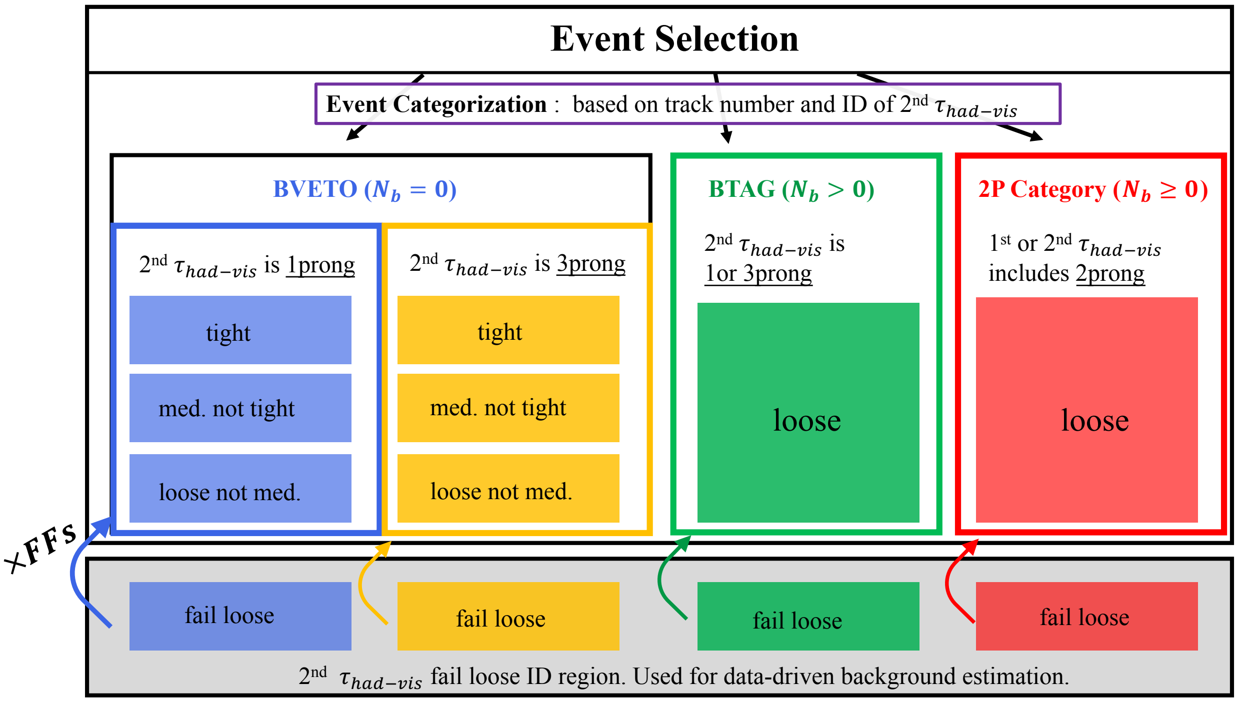

Figure 5.6.: Illustration of the event categorization used in this analysis. The number of b-tagged jets, the number of tracks of sub-leading p_{T} τ_{had} and the tightness of tau identification are exploited for the BVETO categorization. BVETO and BTAG regions correspond to event without b-jets and with at least one b-tagged jet, respectively. The additional categorization is only used for BVETO region based on tau ID tightness of sub-leading and the number of the track associated to the sub-leading τ_{had}. The additional 2P categorization presents the performance for the events with at least one 2-prong τ_{had} (leading τ_{had} or sub-leading τ_{had}). 2P categorization and BTAG region don’t have the further categorization.

6 Background Events Estimation

This section describes the estimation of the background components of the analysis. Background processes are separately discussed for the "irreducible" backgrounds, which are characterized by two hadronically decaying tau leptons in the final state, and for "reducible" backgrounds, which contain at least one reconstructed τ_{had} originated from a hadron jet but not a tau lepton. Such misidentified τ_{had} is referred to as "fake" τ_{had}. The major contributions in the class of the irreducible backgrounds are $Z/\gamma^* \rightarrow \tau\tau$ in "BVETO" categories while $t\bar{t}$ in the "BTAG" categories. Multijet background is the most major component of the reducible backgrounds, which can pass the signal selection due to two fake τ_{had} originated from hadron jets. Although the tau identification can reject fake backgrounds effectively as discussed in Sec. 4, the very large cross-section of the multijet production process still results in a non-negligible contribution in the analysis. A full data-driven technique, which is called *fake factor* (FF) method in this analysis, is employed for the multijet estimation to obtain an accurate estimation of the backgrounds, avoiding uncertainties for the possible wrong model of the fake τ_{had} leptons in the multijet backgrounds. Top production and $W(\rightarrow \tau\nu) + \text{jets}$ processes can be a part of the reducible backgrounds with one genuine τ_{had} and one fake τ_{had}. The backgrounds are estimated based on simulations with the assistance of measurements of the τ_{had} *fake rate* (FR). Top production and $W(\rightarrow \tau\nu) + \text{jets}$ events with one fake τ_{had}, events in the simulation which contain hadron jets that can be potentially wrongly selected in the analysis are weighted by fake rate measured in $W + \text{jets}$ and top-quark control regions. Other reducible production processes due to leptons mimicking the τ_{had}, such as di-boson, $(Z \rightarrow ee)$ or $\mu\mu$ and $(W \rightarrow e\nu$ or $\mu\nu)$+jets, are turned to have a negligible impact in the analysis owing to the lepton veto selection.

The irreducible background estimation is discussed in Sec. 6.1. For the reducible background, the fake factor method is presented in the Sec. 6.2.1, and Sec. 6.2.2 describes the background estimation with the fake rate. The expected results with the background events estimation are shown in Sec 6.3.

6.1 Estimation of the Irreducible Backgrounds

MC simulation is used to estimate the irreducible backgrounds. As discussed in Sec. 4, corrections are applied to the simulation with respect to the performance measurements of the trigger, reconstruction, isolation, and isolation selection efficiencies to account the mis-modeling of the detector performance in the simulation samples. The main systematic uncertainties are also introduced in the Chapter. 7.

6.2 Estimation of the reducible backgrounds

6.2.1 Fake Factor Method (FF)

The multijet background is the most major component of the reducible backgrounds due to its large production cross section. A data-driven FF method has been applied to obtain an accurate estimation of this background. A "di-jet control region" is used to estimate the fake-factor, which is defined as the ratio of the number of τ_{had} candidates that pass to those that fail the tau identification criteria. The selection of the di-jet control region is designed to be as similar to the signal selection as possible while enhancing the fake τ_{had} candidate and suppress the contribution of the genuine τ_{had} candidates. The di-jet control region samples are collected by the single-jet triggers with the jet p_{T} thresholds of 420, 400, 380, 360, 260, 175, 110, 85, 60, 45, 35, 25 and 15 GeV. The event is required to have at least two τ_{had} candidates. The leading τ_{had} is required to fail the "medium" tau identification condition to enhance the multijet backgrounds and guarantee the statistical independence from the data samples selected by the analysis selection for the signal extraction. The leading τ_{had} candidate has to have the $p_{\mathrm{T}} > 85$ GeV and also exceed the trigger threshold by 10%. The sub-leading τ_{had} is required to fulfill the $p_{\mathrm{T}} > 65$ GeV condition. The two τ_{had} candidates have to satisfy the opposite sign charge requirement and have a back-to-back topology in the transverse plane with respect to $\Delta\phi > 2.7$. The p_{T} of the sub-leading τ_{had} candidate must be at least 30% of the p_{T} of the leading τ_{had} candidate. As shown in Fig. 6.1, the p_{T}-balance selection discard a tiny fraction of multi-jets in order to reduce the impact of tail events.

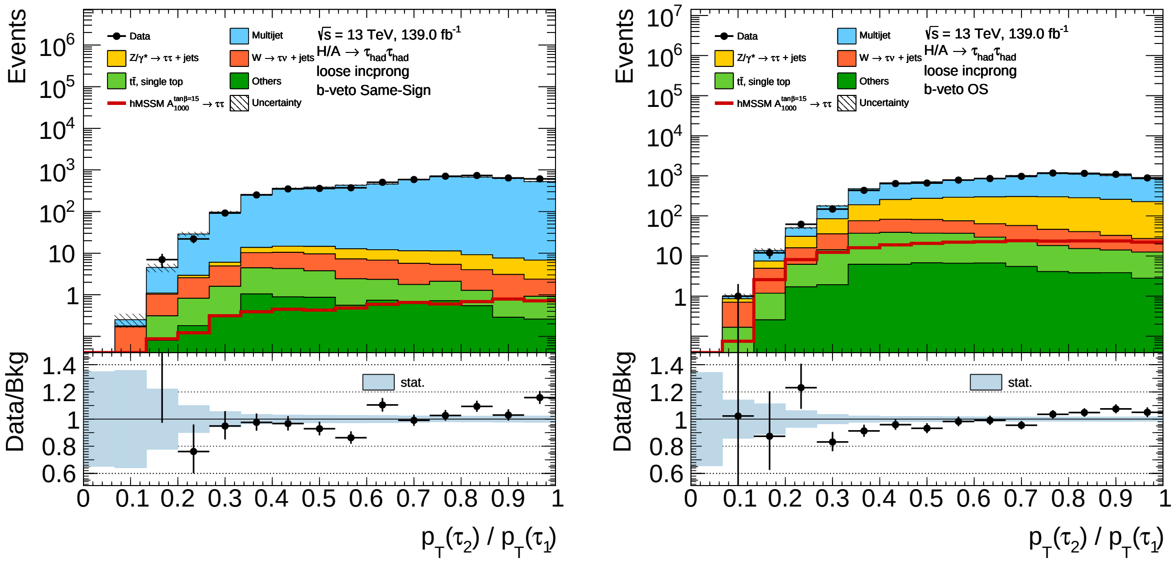

(a) SS BINC. **(b)** OS BINC.

Figure 6.1.: Fake factor is expected to be depending on the ratio of leading and sub-leading tau in the di-jet control region. A selection of p_{T}-balance larger than 30% is considered to reduce the impact of any residual dependency: (a) same-side plot and (b) opposite-side plot as a function of p_{T}-balance also show the low value region with low distribution of multi-jet process is unimportant in the signal region.

The sub-leading τ_{had} is used to measure the fake factors to avoid trigger bias. A loose selection on the tau identification score (BDT score > 0.03) is applied to control the quark and gluon composition in the FF calculation. As defined above, the FF is computed as follows:

$$FF = \frac{N_{\mathrm{passID}}(p_{\mathrm{T}}, N_{\mathrm{track}})}{N_{\mathrm{failID}}(p_{\mathrm{T}}, N_{\mathrm{track}})}\,|_{\mathrm{di-jet}}\ . \tag{6.1}$$

The fake factors are measured for the different tau ID tightness used in the category definition (see Fig. 5.6), and fake factors are estimated with the various types of numerator for the different tau ID tightness, corresponding to the target signal region categories. The FF is measured as a function of the number of tracks (i.e. 1-, 2-, or 3-prong) and p_{T} of the sub-leading τ_{had} candidate. The multi-jets background in the signal region is estimated with the fake factors as shown in Eq. 6.2.

$$N^{\mathrm{SR}}_{\mathrm{pass}} = FF \times N^{\mathrm{SR}}_{\mathrm{fail}}, \tag{6.2}$$

where $N^{\mathrm{SR}}_{\mathrm{fail}}$ is the number of events that pass the same selection as the signal region except for the tau identification conditions for sub-leading τ_{had}. In counting $N^{\mathrm{SR}}_{\mathrm{fail}}$, the sub-leading τ_{had} candidates are required to fail the tau identification selection. The concept of the Eq. 6.2 is illustrated in Fig. 6.2. This way the evaluated fake factor keep the consistency with their application to the $N^{\mathrm{SR}}_{\mathrm{fail}}$.

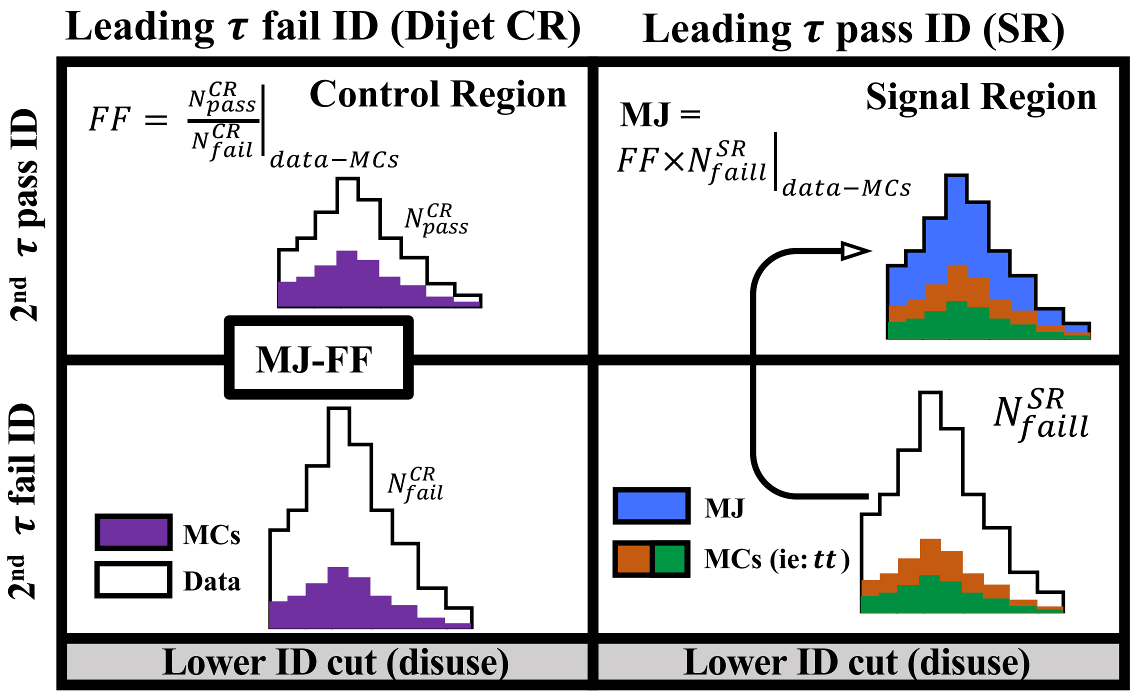

Figure 6.2.: Sketch for the FF measurement and application in the signal region. The left pattern shows the di-jet control region with single jet trigger, and the right pattern presents the signal region with single tau trigger. The di-jet control region is requested leading τ_{had} candidate fail medium ID to orthogonality with signal region. The lower Tau ID cut (BDT score > 0.03) is applied in di-jet control region to avoid the different property to signal region. The FFs are computed with respect to sub-leading τ_{had} and trained to as a function of p_{T}. The MCs (purple part) are used for the subtraction on data to obtain high purity of multi-jet process. The FFs are applied to signal region to estimate the multi-jet process (blue part) passing ID.

Accounting the categorization applied in the signal region, the fake factors are computed with respect to 1-prong, 2-prong and 3-prong of sub-leading tau separately in di-jet control region. The difference between BTAG and BVETO categories are not accounted but a fake factor is estimated in an inclusive manner for the b-tagging conditions (referred to as “B-inc.”). It is mainly due to the limited statistics in control regions. Although there is no significant difference found in the fake factor between BTAG and BVETO categories, minor differences of the fake factors between BTAG and BVETO regions are accounted as the systematic uncertainties (see Sec 7.3).

The fake factors for BVETO category are also measured in dijet samples as summarized in Fig. 6.3. The fake factors for BVETO and 2P categories are summarized in Fig. 6.4. The same-sign (SS) fake factors are used to validate the data-driven method in SS region as described below. The opposite-sign (OS) fake factors are applied to $N^{\mathrm{SR}}_{\mathrm{fail}}$ to measure multi-jets process background in signal region. The statistical uncertainty from data and MC used for the subtraction are shown on the plots.

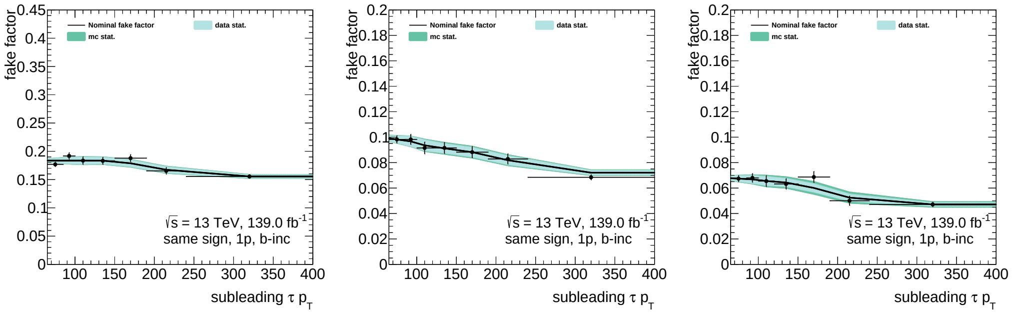

(a) SS 1p loose-not-med. **(b)** SS 1p med.-not-tight **(c)** SS 1p tight

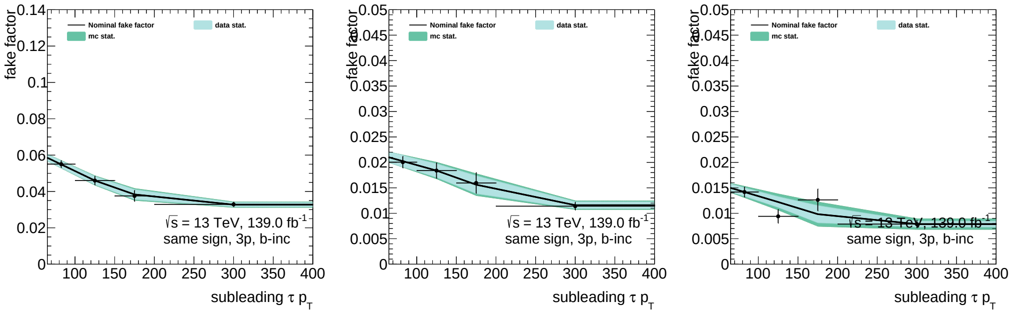

(d) SS 3p loose-not-med. **(e)** SS 3p med.-not-tight **(f)** SS 3p tight

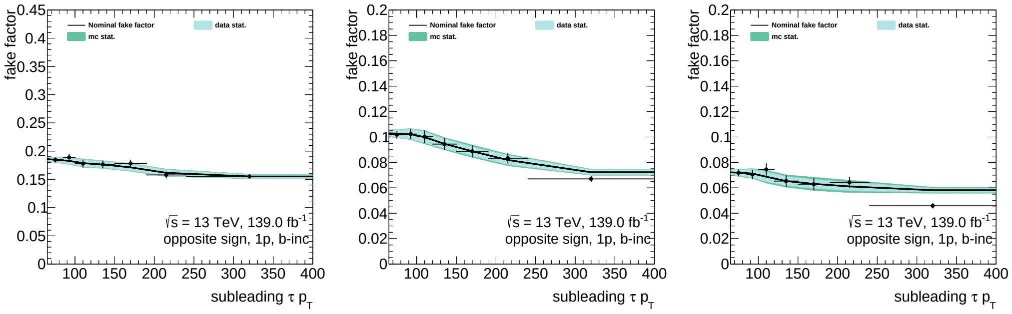

(g) OS 1p loose-not-med. **(h)** OS 1p med.-not-tight **(i)** OS 1p tight

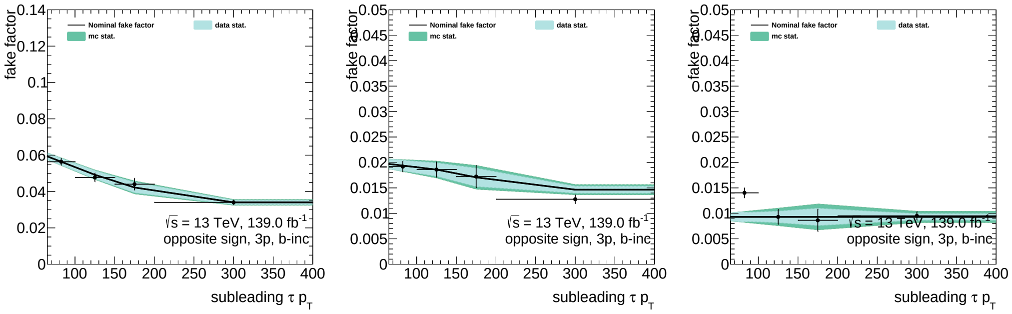

(j) OS 3p loose-not-med. **(k)** OS 3p med.-not-tight **(l)** OS 3p tight

Figure 6.3.: Tau fake factors for the BVETO category in same-sign validation region and opposite-sign signal region. The same-sign FFs for 1-prong tau candidates are shown in the plots on the first row, for 3-prong tau candidates are shown in the plots on second row. The bottom two rows are shown for opposite-sign FFs for 1-prong and 3-prong tau candidates. From left to right plots, the FF is corresponding to *loose-not-med*, *med-not-tight* and *tight* tau ID.

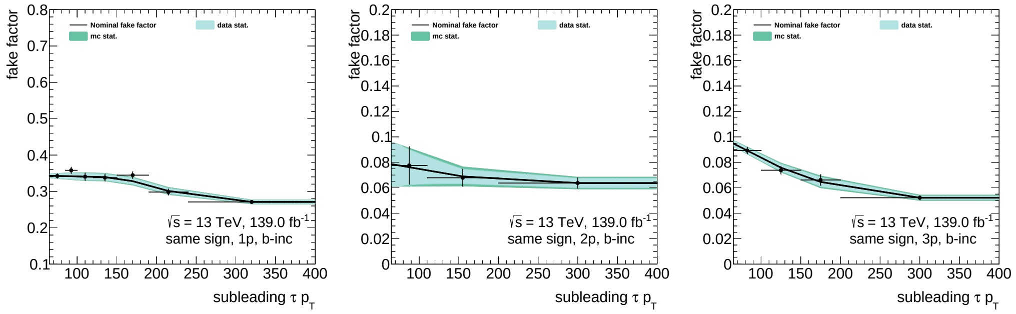

(a) SS 1p loose **(b)** SS 2p loose **(c)** SS 3p loose

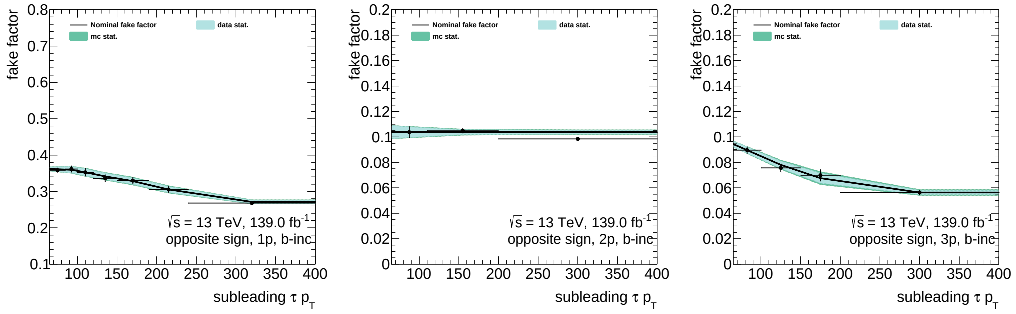

(d) OS 1p loose **(e)** OS 2p loose **(f)** OS 3p loose

Figure 6.4.: Tau fake factors for the BTAG and 2P categories in same-sign validation region and opposite-sign signal region. Only *loose* is available to BTAG and 2P categories. The same-sign FFs are shown in the top plots, and opposite-sign FFs are shown in the bottom plots. From left to right plots, the FF is corresponding to 1-prong tau, 2-prong tau, and 3-prong tau candidates.

Validation Region for QCD Multi-jets Background

A fake factor measurement is validated with the use of samples selected by a requirement of the same sign of charge of di-τ pairs. The same selection criteria with the signal region are applied except for the charge condition. A validation region with the same sign (SS) of charge of di-τ is designed to enhance the fake τ_{had} candidate from the multijet process while suppressing the other background process. FF method for multi-jet background in the SS validation region is found to provide a good model of the m_T^{tot} distribution of fake background, as shown in Fig. 6.5 and Fig. 6.6. The validation region corresponding to the total eight signal regions based on the categorization method are presented. The FF method is investigated carefully in the validation region with $m_{\mathrm{T}}^{\mathrm{tot}}$ as well as other variables. All the plots for the valuation study are shown in Appendix D.

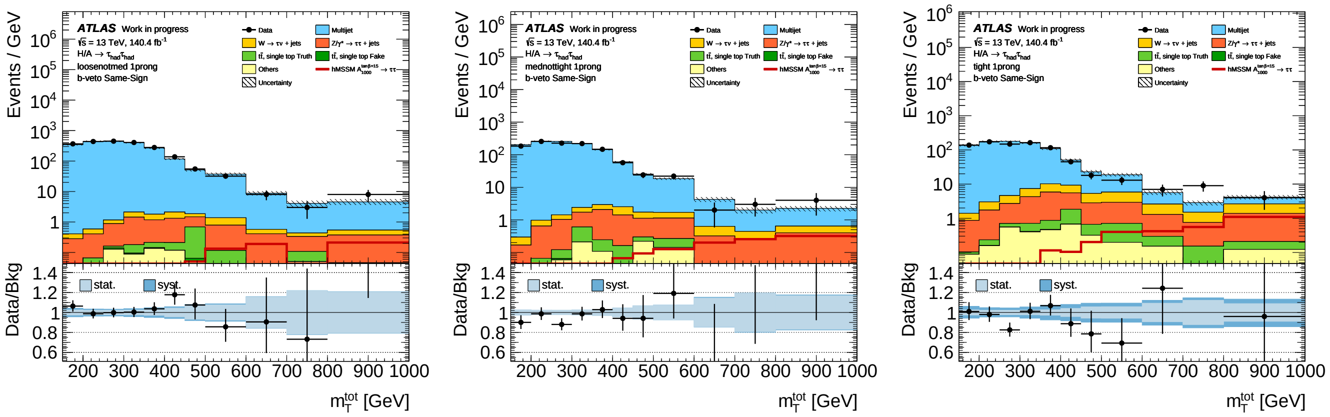

(a) SS BVETO 1p loose-not-med **(b)** SS BVETO 1p med-not-tight **(c)** SS BVETO 1p tight

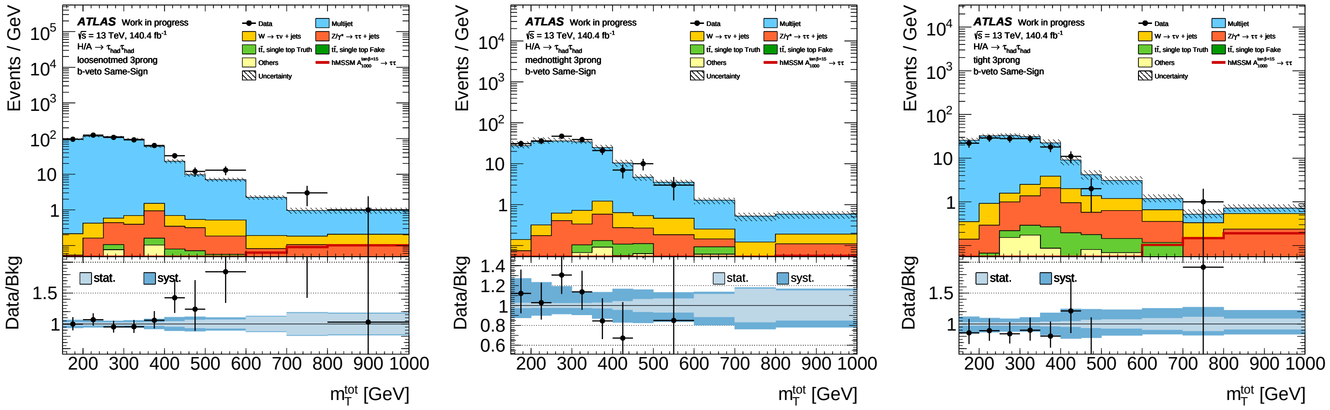

(d) SS BVETO 3p loose-not-med **(e)** SS BVETO 3p med-not-tight **(f)** SS BVETO 3p tight

Figure 6.5.: The six validation regions as a function of m_T^{tot} are investigated for BVETO category. The plots for 1-prong (3-prong) sub-leading τ are shown in upper (bottom) plots. From left to right, the plots present the region with sub-leading τ passing *loose-not-med*, *med-not-tight* and *tight* tau ID selection. The FF method presents good modeling for multi-jet background in validation region.

6.2.2 Fake Rate Method (FR)

Reducible backgrounds other than multijet production are estimated with Monte Carlo simulation and measured "fake-rates". Instead of applying the actual tau identification selection to the hadron jets in the simulation, they are weighted according to the probability for the hadron jets to pass the signal tau

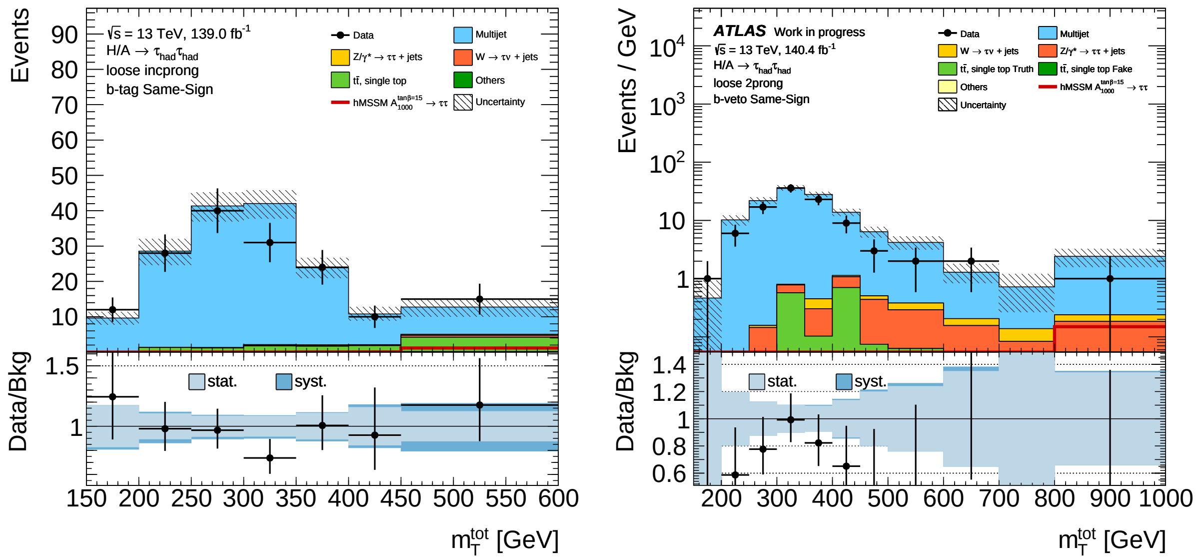

(a) SS BTAG 1p+3p loose **(b)** SS BINC 2p loose

Figure 6.6.: The two validation regions as a function of m_T^{tot} are investigated for BTAG (a) and 2P (b) categories. The plot (a) presents the region with sub-leading τ, which can be 1-prong or 3-prong, passing *loose* tau ID selection for BTAG category. The plot (b) shows the validation region for 2P category which is built for the events with at least one 2-prong τ_{had}. They show good modeling for multi-jet background for BTAG and 2P categories in validation region.

trigger as well as the tau identification criteria, which is referred to as a “fake-rate” in this analysis. The fake-rate is measured in the control regions as discussed below. The fake rate are used to hadron jets of the simulations instead of trigger or identification application for leading or sub-leading τ_{had} candidates. This method allows not only an accurate estimation based on the measured fake-rates but also an efficient use of the simulated samples without discarding a large fraction of events with the tau identification selection.

The fake-rate method is used for the following dominant processes; single top, $t\bar{t}$ and $W(\to \tau\nu) + \text{jets}$. It is known that the fake-rate for quark-initiated jets is higher than gluon-initiated jets. Given that the composition of the hadron jet flavor is different between top-quark production (single top and $t\bar{t}$) and $W(\to \tau\nu) + \text{jets}$, two control regions are built for the top-quark production and the W production backgrounds, separately. Control regions characterized by the final state of $\mu\nu + \text{jets}$ are exploited. The $\mu\nu$ final state is used to enhance the purity of the target processes, and the associated jets are used for the measurement of fake-rates in the processes. The number of b-tagged jets is used to separate the data samples into the following two control regions; a control region to measure fake-rates for $W(\to \tau\nu) + \text{jets}$ processes and the other region to measure fake-rates for top-quark production processes.

The single muon trigger with the 50 GeV threshold is used to collect data for the $\mu\nu$+jets control regions. The medium quality requirement with $p_{\text{T}} > 70$ GeV threshold is used for muon candidate. The candidate events are required to have at least one τ_{had} candidates with $p_{\text{T}} > 50$ GeV, which are supposed to be originated from hadron jets in the $W + \text{jets}$ and top-quark processes. If an event has an additional muon which passes loose quality cut with $p_{\text{T}} > 7$ GeV, the event will be discarded. Similarly, if an event has an additional electron which passes loose identification with $p_{\text{T}} > 15$ GeV, the event will be discarded. For the leading τ_{had} candidates and the selected muons, a requirement for the opposite charge configuration and a requirement on the opening angle $(\Delta\phi(\mu, \text{jet}) > 2.4)$ are applied to guarantee the similar quark/gluon composition as the signal region. $m_{\text{T}}(\mu, E_{\text{T}}^{\text{miss}}) > 40$ GeV is required to reduce the multijet contributions. Finally, samples with at least one b-tagged jet is categorized into “top control

Process	$W(\to \mu\nu)$+jets	Top	Other
Top control region	4.7%	88.5%	6.7%
W control region	83.2%	15.5%	1.3%
High p_{T} W control region	14.0%	79.8%	6.1%

Table 6.1.: The purity of SM processes in W, top and high p_{T} W control regions. The purity of $W(\to \mu\nu)$+jets is expected around 90% in the W control region and the purity of top-quark process in the top control region is around 80%.

region", and the other samples (i.e. a sample with no b-tagged jet) are categorized into "W control region". As a part of the W control region, a dedicated control region is defined for W production simulation to measure fake-rates for events with highly boosted W. The "high p_{T} W control region" is defined with an increased muon p_{T} requirement ($p_{\mathrm{T}} > 110$ GeV). The data and simulation comparison in each control regions is shown in Fig. 6.7. The purity of each control region is summarized in Table. 6.1.

The leading τ_{had} candidates in control regions are used for the fake-rate measurements, which are supposed to be originated from hadron jets in the $W+$jets and top-quark processes. The fake rate to a given single tau trigger as well as tau identification criteria are computed based on following formula:

$$\mathrm{FR}(p_{\mathrm{T}}) = N_{\text{pass ID}}/N_{\text{all}}. \tag{6.3}$$

Minor contributions of true τ_{had} candidates are subtracted based on the simulation as backgrounds in the fake-rate measurements. The fake rate is computed for 1-prong, 2-prong, and 3-prong of sub-leading tau, separately. The fake-rates are measured also as a function of p_{T} of the τ_{had} candidates. The measured fake-rates are shown in Fig. 6.8, Fig. 6.9 and Fig. 6.10 for 1-prong τ_{had}, 3-prong τ_{had} and 2-prong τ_{had}. For bins in which the data statistics are limited in the control regions for fake-rate measurements, the τ_{had} identification criteria are exceptionally applied for these backgrounds instead of weighting with the measured fake-rates. All the results of the fake rate measurements are summarized in Appendix C.

Given that the $\mu\nu+$jets control regions have an event topology compatible with the signal of $H/A \to \tau\tau$ if one of the tau leptons decays into $\mu\nu\nu$ and the other decays hadronically, it is shown that the possible impact of the signal contributions in the control region is small enough for signals with 1000 GeV and 300 GeV of the neutral heavy Higgs boson mass. The expected impact on the fake-rate measurements due to possible signals is shown in Fig. 6.11 as a function of the p_{T} of τ_{had} and the cross-section times branching-fraction of $H/A \to \tau\tau$ signals. Since the potential effect on the fake rate is smaller than 1%, the signal contribution in the control region is found to be significantly smaller than the uncertainty on the measurement.

6.3 Expected Event Yields in the Signal Regions

After background modeling for ,the expected yield and $m_{\mathrm{T}}^{\mathrm{tot}}$ distribution are investigated before the statistical analysis with likelihood method. The "pre-fit" (before the likelihood fit discussed in Sec. 8.1) of signal and background are summarized in the Table 6.2 and Table 6.3. Figure 6.12 and Fig. 6.13 show the $m_{\mathrm{T}}^{\mathrm{tot}}$ distribution in BVETO, BTAG and 2P categories. Appendix D presents the pre-fit distribution of other variables. The background expectation estimated by simulation and data-driven method presents a good agreement with observed data in the pre-fit distribution. The systematic uncertainties illustrated in the figures will be discussed in the chapter 7.

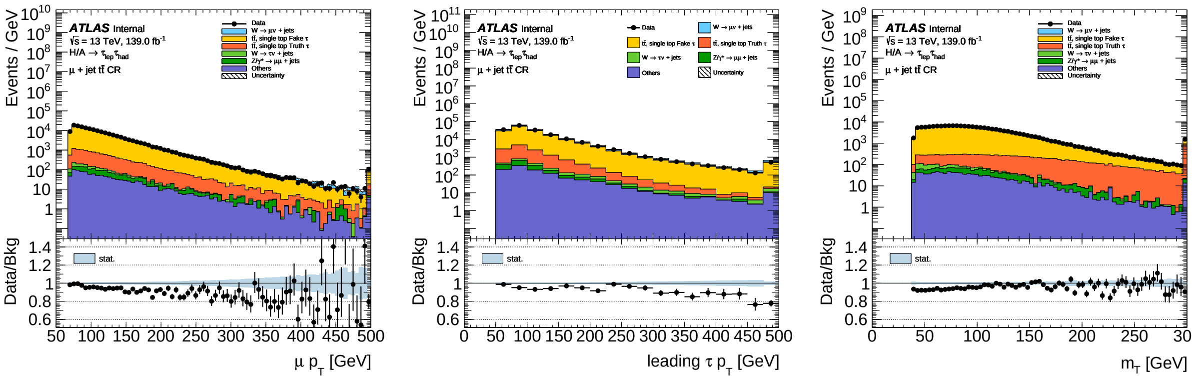

(a) top CR muon p_{T} **(b)** top CR tau p_{T} **(c)** top CR m_{T}

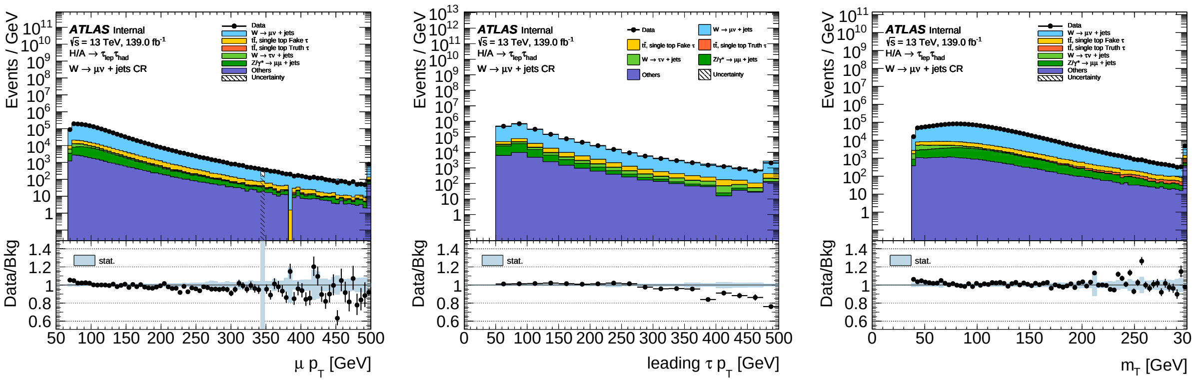

(d) W CR muon p_{T} **(e)** W CR tau p_{T} **(f)** W CR m_{T}

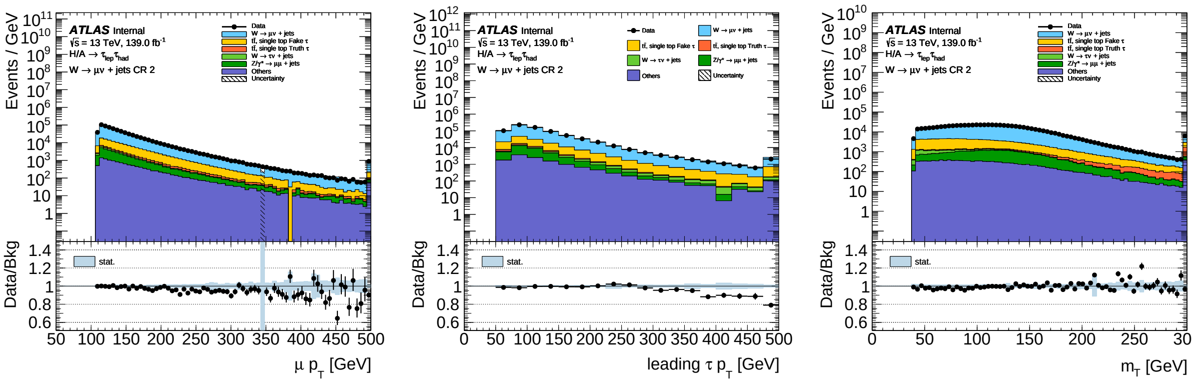

(g) High p_{T} W CR muon p_{T} **(h)** High p_{T} W CR tau p_{T} **(i)** High p_{T} W CR m_{T}

Figure 6.7.: The event distribution in $t\bar{t}$ (upper plots) and W($\rightarrow \mu\nu$) (middle plots) control regions. For left to right: μ p_{T}, τ p_{T} and $m_T(\mu, E_T^{\mathrm{miss}}$. The W($\rightarrow \mu\nu$) control region with higher p_{T} selection for μ object is shown in the bottom.

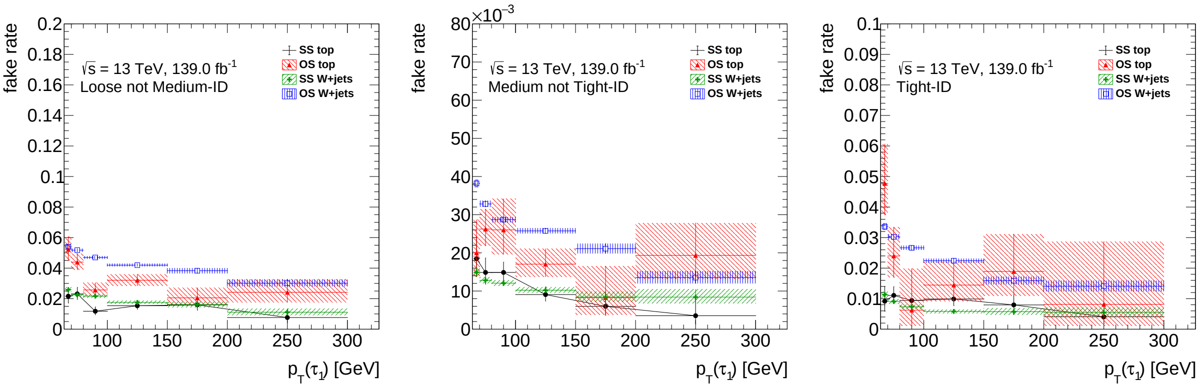

(a) loose-not-med 1-prong **(b)** med-not-tight 1-prong **(c)** tight 1-prong

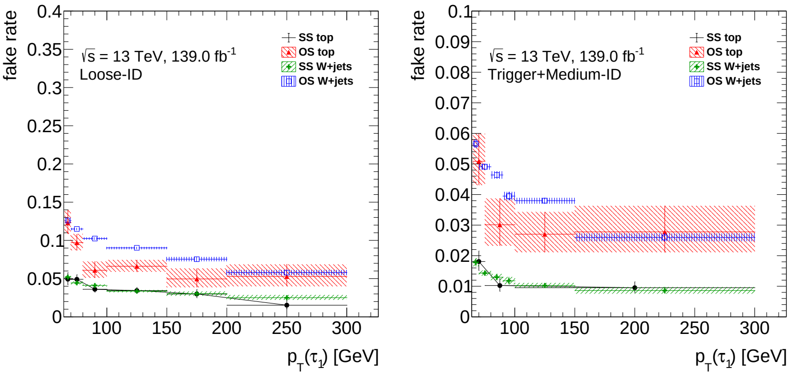

(d) loose 1-prong **(e)** med+trig. 1-prong

Figure 6.8.: The overall fake rate measured from data in $t\bar{t}$ and W($\rightarrow \mu\nu$). FRs corresponding to the different working points for 1-prong are shown in the plots.

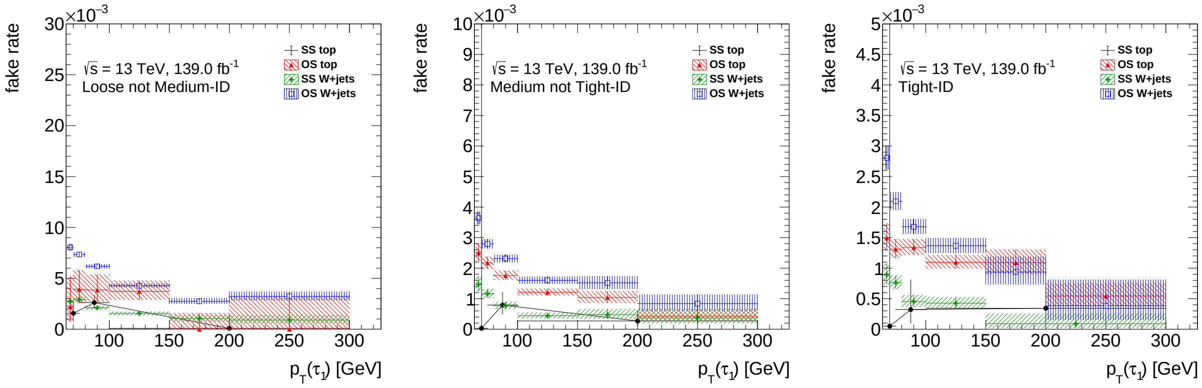

(a) loose-not-med 3-prong **(b)** med-not-tight 3-prong **(c)** tight 3-prong

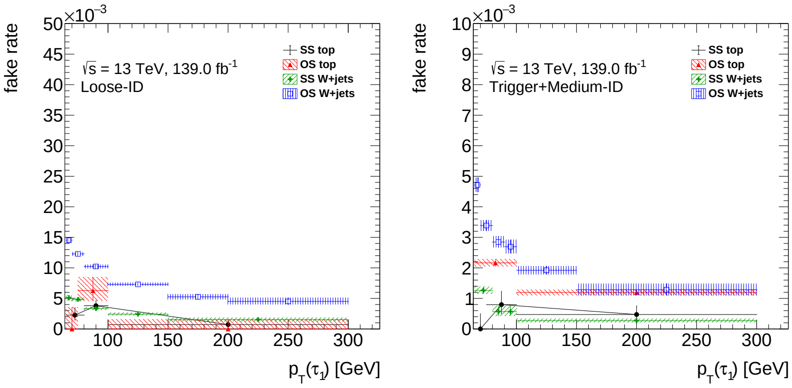

(d) loose 3-prong **(e)** med+trig. 3-prong

Figure 6.9.: The overall fake rate measured from data in $t\bar{t}$ and W($\rightarrow \mu\nu$). FRs corresponding to the different working points for 3-prong are shown in the plots.

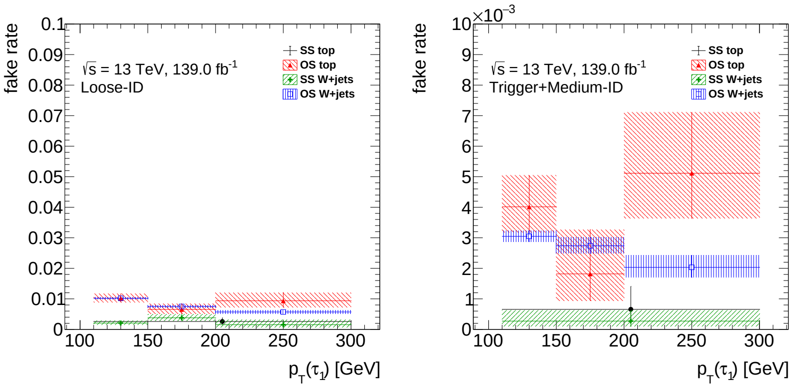

(a) loose 2-prong **(b)** med+trig. 2-prong

Figure 6.10.: The overall fake rate measured from data in $t\bar{t}$ and W($\rightarrow \mu\nu$). 2-prong FRs given to the *loose* and *med.+trigger* working points are used for sub-leading and leading τ_{had}.

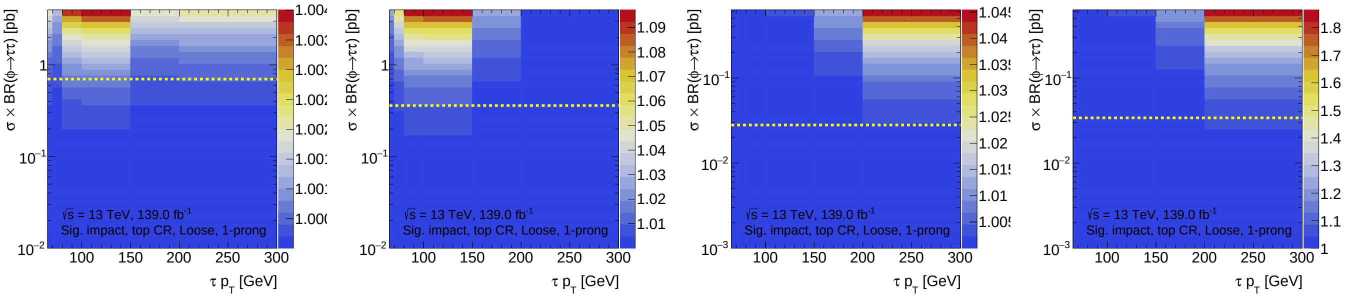

(a) ggH300 **(b)** bbH300 **(c)** ggH1000 **(d)** bbH1000

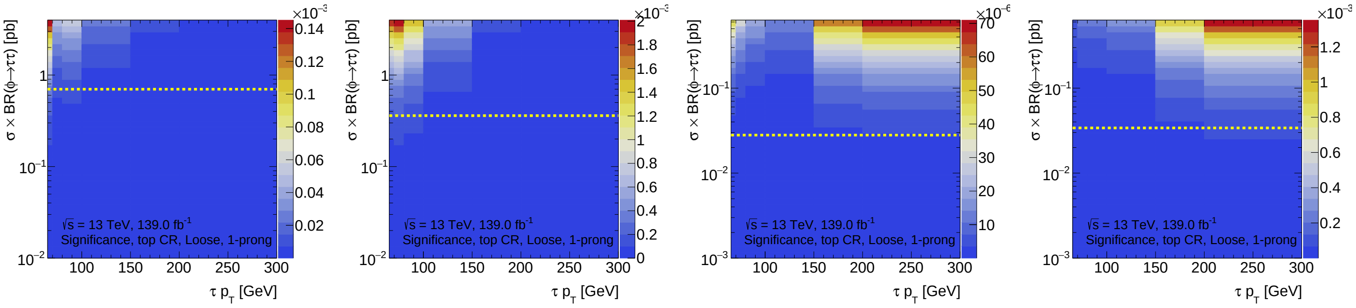

(e) Significance ggH300 **(f)** Significance bbH300 **(g)** Significance ggH1000 **(h)** Significance bbH1000

Figure 6.11.: Impact of a potential $H/A \to \tau_{\mathrm{had}}\tau_{\mathrm{lep}}$ signal with 1000 GeV mass on the measured 1-prong fake rates of loose ID in $t\bar{t}$ control region as a function of the p_{T} of τ_{had} and the cross-section times branching-fraction of $H/A \to \tau\tau$ signals. The exclusion limit results of publish result with 36 fb^{-1} are illustrated in white line [65]. The "probe" tau leptons of signal passes the loose ID criterion and are taken into account. Upper plots show the change in the fake rates with the different signal events in $t\bar{t}$ control regions. Bottom plots show the corresponding significances of the shifts in the fake rate.

Processes	**1P BVETO loose-not-med**	**1P BVETO med-not-tight**	**1P BVETO tight**
Multijet	2501 ± 92	1370 ± 80	959 ± 38
Wtaunu	32 ± 1	43 ± 3	178 ± 7
Ztautau	183 ± 7	278 ± 16	1289 ± 52
Top	7 ± 0	10 ± 1	37 ± 1
Others	4 ± 0	7 ± 0	31 ± 1
Bkg	2728 ± 0.81%	1708 ± 0.77%	2494 ± 0.46%
data	2780	1769	2356
data/Bkg	1.02	1.04	0.94
ggH1500	1030 ± 38	1594 ± 93	8501 ± 341
bbH1500	466 ± 17	816 ± 48	5425 ± 218
ggH300	42 ± 2	60 ± 4	243 ± 10
bbH300	28 ± 1	48 ± 3	232 ± 9
Processes	**3P BVETO loose-not-med**	**3P BVETO med-not-tight**	**3P BVETO tight**
Multijet	644 ± 87	232 ± 69	115 ± 24
Wtaunu	17 ± 2	18 ± 5	59 ± 12
Ztautau	73 ± 10	84 ± 25	292 ± 60
Top	4 ± 0	3 ± 1	11 ± 2
Others	2 ± 0	2 ± 1	8 ± 2
Bkg	740 ± 0.86%	338 ± 0.94%	485 ± 0.88%
data	779	347	464
data/Bkg	1.05	1.03	0.96
ggH1500	264 ± 36	291 ± 85	1182 ± 244
bbH1500	144 ± 19	190 ± 56	733 ± 151
ggH300	21 ± 3	24 ± 7	67 ± 14
bbH300	20 ± 3	15 ± 4	69 ± 14

Table 6.2.: The events yields before the fit. Only statistical uncertainties are considered and listed in the table. The expected contributions from signal events with masses of 300 and 1500 GeV and cross sections of 1 pb are shown.

Processes	**BTAG loose**	**2P loose**
Multijet	168 ± 45	3551 ± 92
Wtaunu	8 ± 2	87 ± 2
Ztautau	29 ± 8	189 ± 5
Top	159 ± 44	32 ± 1
Others	2 ± 0	6 ± 0
Bkg	365 ± 2.62%	3864 ± 0.74%
data	389	4012
data/Bkg	1.07	1.04
ggH1500	376 ± 103	1965 ± 51
bbH1500	5302 ± 1452	2031 ± 53
ggH300	8 ± 2	19 ± 0
bbH300	184 ± 50	23 ± 1

Table 6.3.: The events yields before the fit. Only statistical uncertainties are considered and listed in the table. The expected contributions from signal events with masses of 300 and 1500 GeV and cross sections of 1 pb are shown.

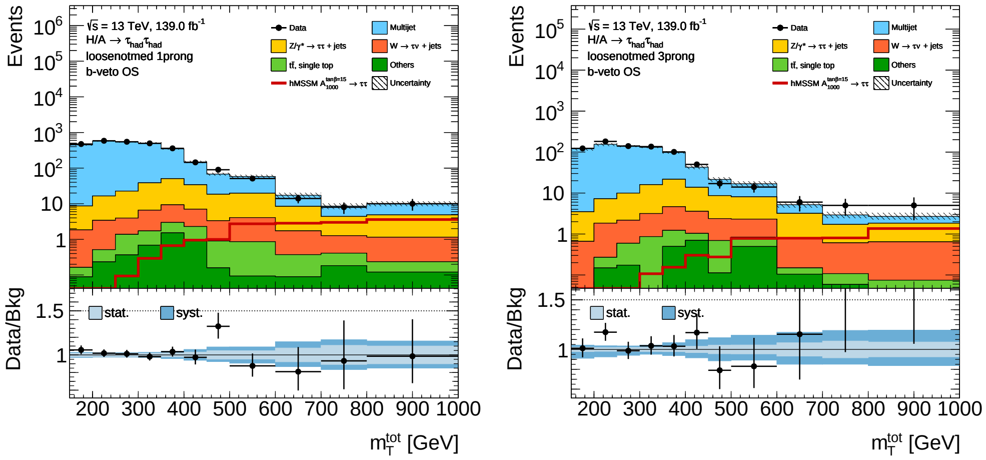

(a) 1p BVETO loose-not-med **(b)** 3p BVETO loose-not-med

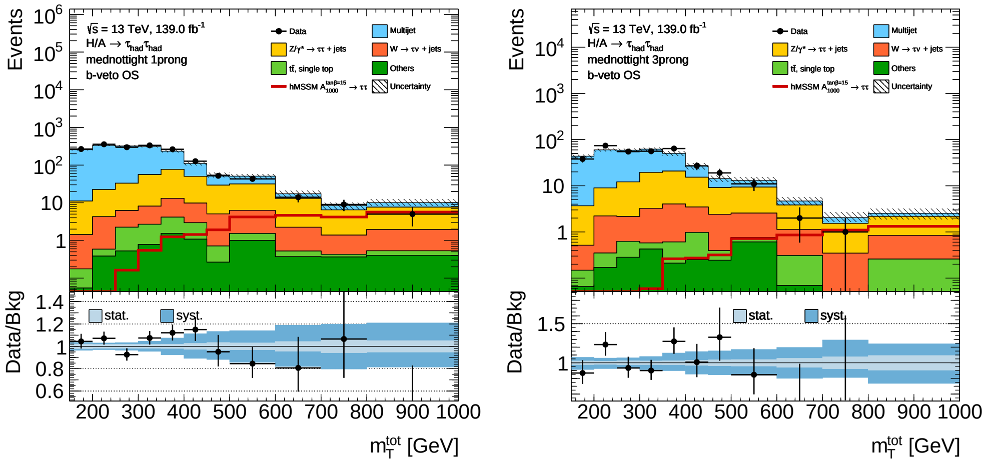

(c) 1p BVETO med-not-tight **(d)** 3p BVETO med-not-tight

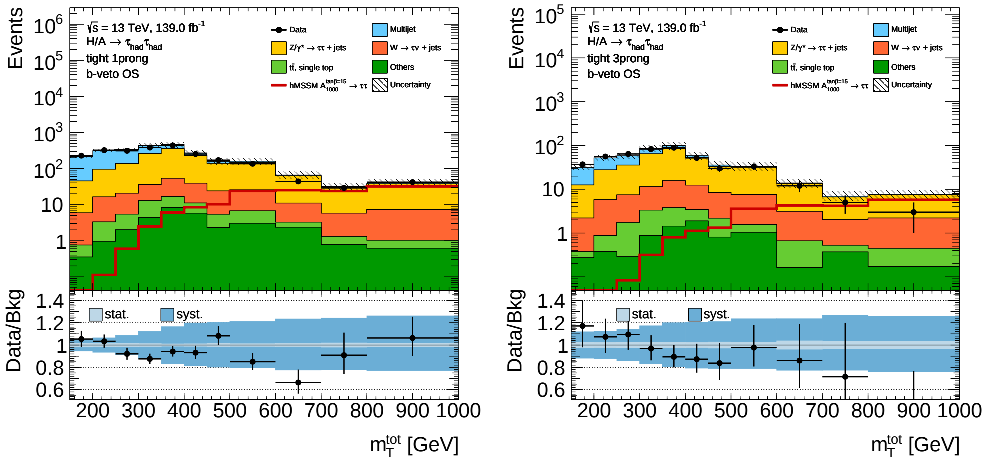

(e) 1p BVETO tight **(f)** 3p BVETO tight

Figure 6.12.: Distributions of total transverse mass for BVETO category. The plots show the expected distribution before the likelihood fit. Events containing 1-prong sub-leading τ_{had} are illustrated in left plots and the events containing 3-prong sub-leading τ_{had} are shown in right plots. From top to bottom, the plots is made with respect to tau identification for sub-leading τ_{had} (loost-not-med., med-not-tight and tight). The underflow events and overflow evnets are included in the first and last bins, respectively. In the label, "Others" background refers to contributions from diboson, $Z/\gamma^*(\to \ell\ell)$+jets and $W(\to \ell\nu)$+jets production. The "Top" containing the $t\bar{t}$ and single top production. The data is shown as the black point in the histogram. The red line shows signal contribution of gluon-fusion and bottom-annihilation productions which are normalized to $\tan\beta = 15$ based on the ATLAS publish result [65]. In the lower panels, the fraction of data and overall background is illustrated.

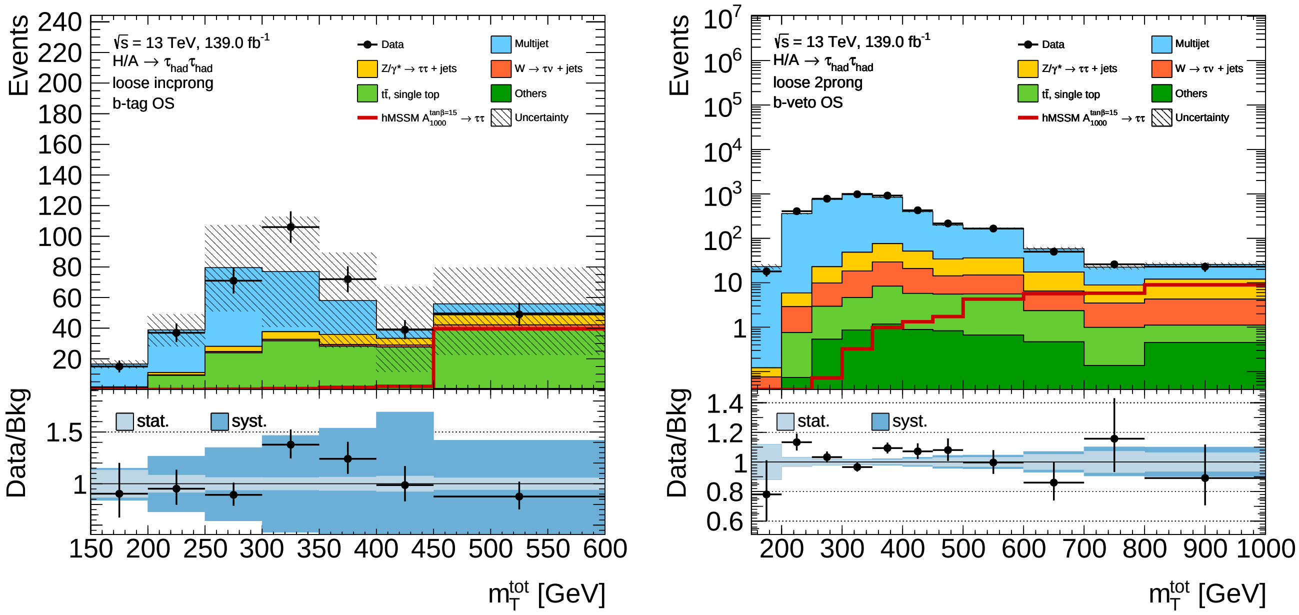

(a) 1p+3p BTAG loose

(b) 2p B-inc. loose

Figure 6.13.: Distributions of total transverse mass for BTAG (left) and 2P (right) categories. The plots show the expected distribution before the likelihood fit. The underflow events and overflow evnets are included in the first and last bins, respectively. In the label, "Others" background refers to contributions from diboson, $Z/\gamma^*(\to \ell\ell)$+jets and $W(\to \ell\nu)$+jets production. The "Top" containing the $t\bar{t}$ and single top production. The data is shown as the black point in the histogram. The red line shows signal contribution of gluon-fusion and bottom-annihilation productions which are normalized to $\tan\beta = 15$ based on the ATLAS publish result [65]. In the lower panels, the fraction of data and overall background is illustrated.

7 Systematic Uncertainties

The systematic uncertainties are taken into account in the statistical analysis. They significantly affect to the yield result of signal and background. In this section, the systematic uncertainties are classified into several sources. Instrumental uncertainties are relate to the physics object reconstruction with the calibration shown in Sec. 7.1. This section also provides the exposition for other uncertainties from luminosity, pile-up, muon and electron object. The uncertainties for Monte Carlo modeling are presented in Sec. 7.2. They explain the theoretical modeling for SM backgrounds. The evaluation of uncertainties on background which derived from the mis-identified tau using data-driven method is described in Sec. 7.3. Uncertainties described above are treated for the result of analysis in the two types to investigate the effect on signal and background yield and kinematic shape of the final discriminant variable $m_{\mathrm{T}}^{\mathrm{tot}}$.

7.1 Experimental uncertainties

Due to imperfect detector simulation, uncertainties on reconstructed physics objects are estimated in the calibration step. This section focuses reconstruction, calibration and identification uncertainties for the main physics objects, which are τ_{had}, jets and E_{T}miss, in this analysis. The experimental systematics for this analysis are summarized in Table 7.1.

Hadronic tau

The τ_{had} object plays a primary role in this analysis. It is widely used in the trigger step, signal extraction and final discriminant calculation. The detectors related uncertainties, such as τ_{had} trigger, identification, reconstruction, as well as energy calibration, are essential and should be carefully investigated. The reconstruction efficiency of τ_{had} have been described in Sec 4.5.1, and the corresponding systematic uncertainties are illustrated in Fig. 7.1. Pileup and the inner detector material are the main sources of reconstruction uncertainties since they strongly affect the correctness performance of tau vertex (TV) which provides the identification for vertex reconstruction efficiency in the events [178]. Total uncertainty of the τ_{had} reconstruction is around 2% to 4.5%.

Uncertainty of τ_{had} identification is different in the central region $|\eta| < 1.37$ and forward region $1.52 < |\eta| < 2.47$. It has been estimated for each region with different working point separately. $Z/\gamma^* \to \tau\tau$ events are used to tune the τ_{had} identification efficiency and estimate corresponding uncertainties. This uncertainty highly depends on the input variables of tau ID BDT training, for example, the calorimeter-based and tracking-based input variables show huge variation in shapes. In $p_{\mathrm{T}} > 100$ GeV region, it provides around 10% uncertainty for 3-prong in barrel region. The pileup effect and material uncertainties also play the major roles in 1-prong decays. They provide large impact on the leading track IP significance ($|S_{\mathrm{leadtrack}}|$) which is a variable only used in 1-prong BDT training. The systematic uncertainty with Medium ID working point for 1-prong and 3-prong in the central and forward region are shown in Fig 7.2. They are approximately 10% uncertainties in wide p_{T} range of the forward region for both 1-prong

Uncertainty	Description	Scheme (number of NPs)
$Lumi$	Integrated luminosity measurement	1
TAU	τ_{had} reconstruction and identification	6
TES	τ_{had} energy scale	3
$MUON$	muon systematics, including trigger, reconstruction, isolation, identification and energy scale	13
EG	electron systematics, including trigger, reconstruction, isolation, identification and energy scale	6
$METSoft$	$E_{\text{T}}^{\text{miss}}$ soft terms	2
JER, JES, Jvt	jet energy scale and resolution	7
$btag$	flavor-tagging	14
PRW	pile-up	1

Table 7.1.: Summary table for the experimental systematics with number of nuisance parameterss, which is referred to as NPs, for likelihood fit and brief description.

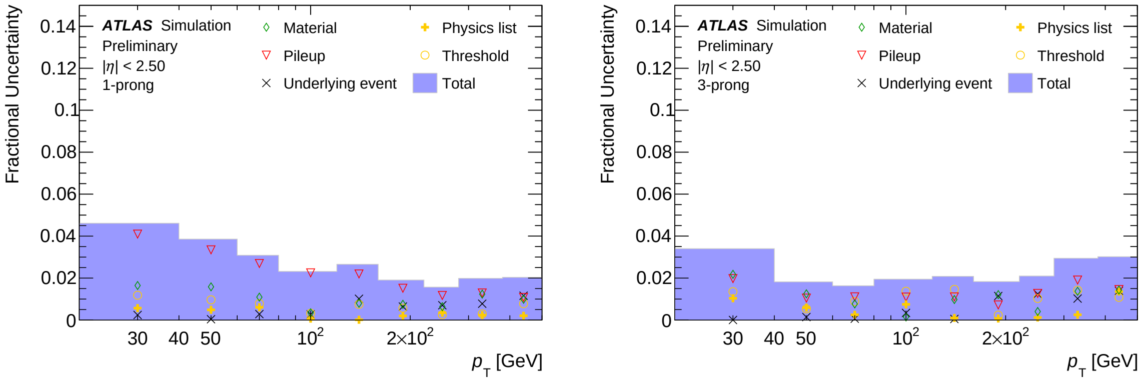

(a) (b)

Figure 7.1.: Uncertainties for reconstruction efficiency for 1-prong in (a) and 3-prong in (b). Each source of systematic uncertainties is also shown in the figure as a function of τ_{had} p_{T}. The sources of uncertainties, such as calorimeter noise thresholds, are discussed in Ref. [178].

and 3-prong. Therefore, the maximum values for 1-prong and 3-prong in central reach 15% and 20%, respectively.

The uncertainty of τ_{had} energy scale calibration (TES) is the one of dominant uncertainties in this analysis. It is computed using Monte Carlo simulation with a reconstructed τ_{had} passing Loose ID based on the Gaussian mean of the $E_{\text{T,calib}}/E_{\text{T,true}}^{vis}$ which is also used in resolution calculation. A small effect of uncertainty from pileup is computed to be lower than 1%. Alternative *Geant 4* hadronic shower model, which is significant to the uncertainty in central regions, provides an important source of uncertainties. It also affects the energy deposited in TC. Moreover, the material modeling and the variation of the calorimeter noise in MC simulation are also considered as the uncertainty sources. They affect the material correction weights and the modeling of the calorimeter calibration. The total uncertainty is computed and orthogonality with each systematic uncertainty as a function of the calibrated transverse energy as displayed in Fig 7.3 and Fig 7.4 for 1-prong and 3-prong, respectively. Overall uncertainties vary within the range of 2% to 6% depending on p_{T} and $|\eta|$.

The trigger efficiency with the relative uncertainty is computed with $Z \to \tau_{\mu}\tau_{\text{had}}$ events using the tag-and-probe method. The tau trigger uncertainties consist of three components, which are statistical uncertainties associated with data and simulation, and the systematic uncertainty. Jet fake background, muon performance, pileup and soft component of MET are the main sources of systematic uncertainties

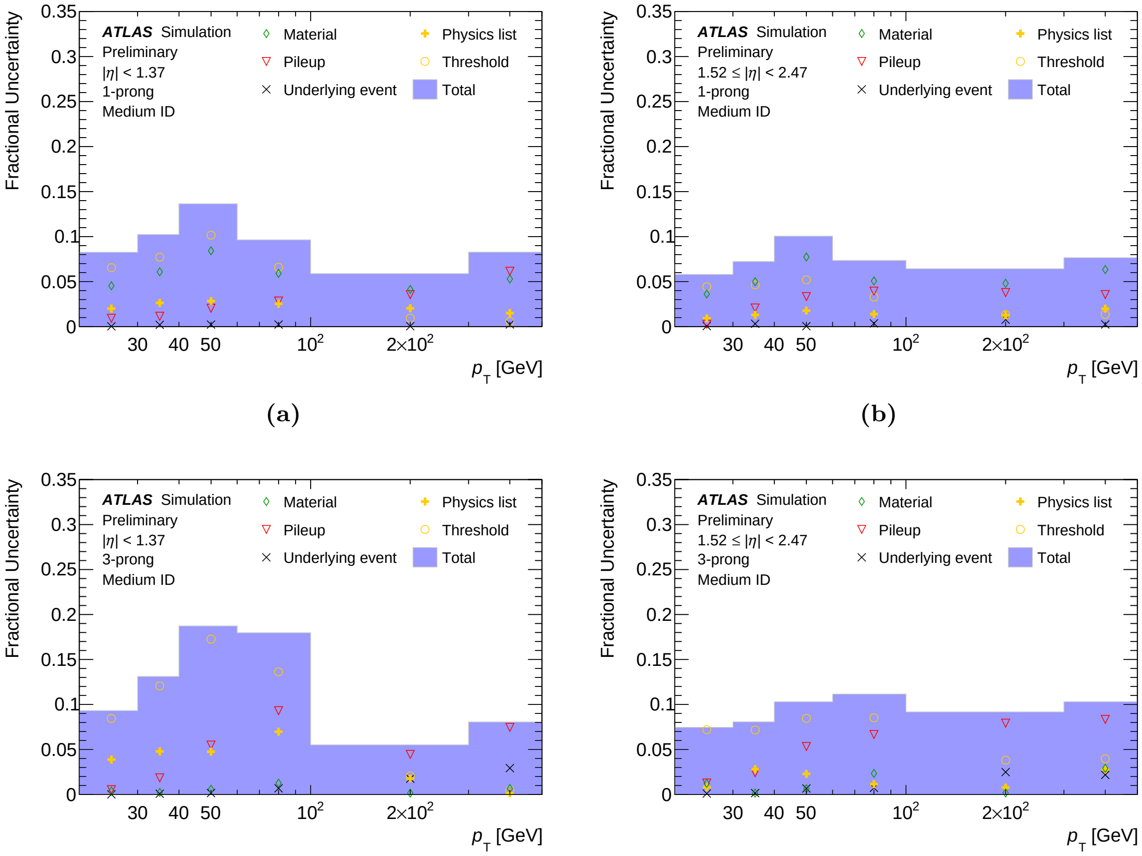

(a) (b)

(c) (d)

Figure 7.2.: Systematic uncertainty for τ_{had} efficiency with Medium ID working point as a function of τ_{had} p_{T} for 1-prong is shown in the upper two plots (a) (b), and for 3-prong is shown in the bottom two plots (c) (d). The systematic uncertainties are measured in the central $|\eta| < 1.37$ and $1.52 < |\eta| < 2.47$ forward region separately [178].

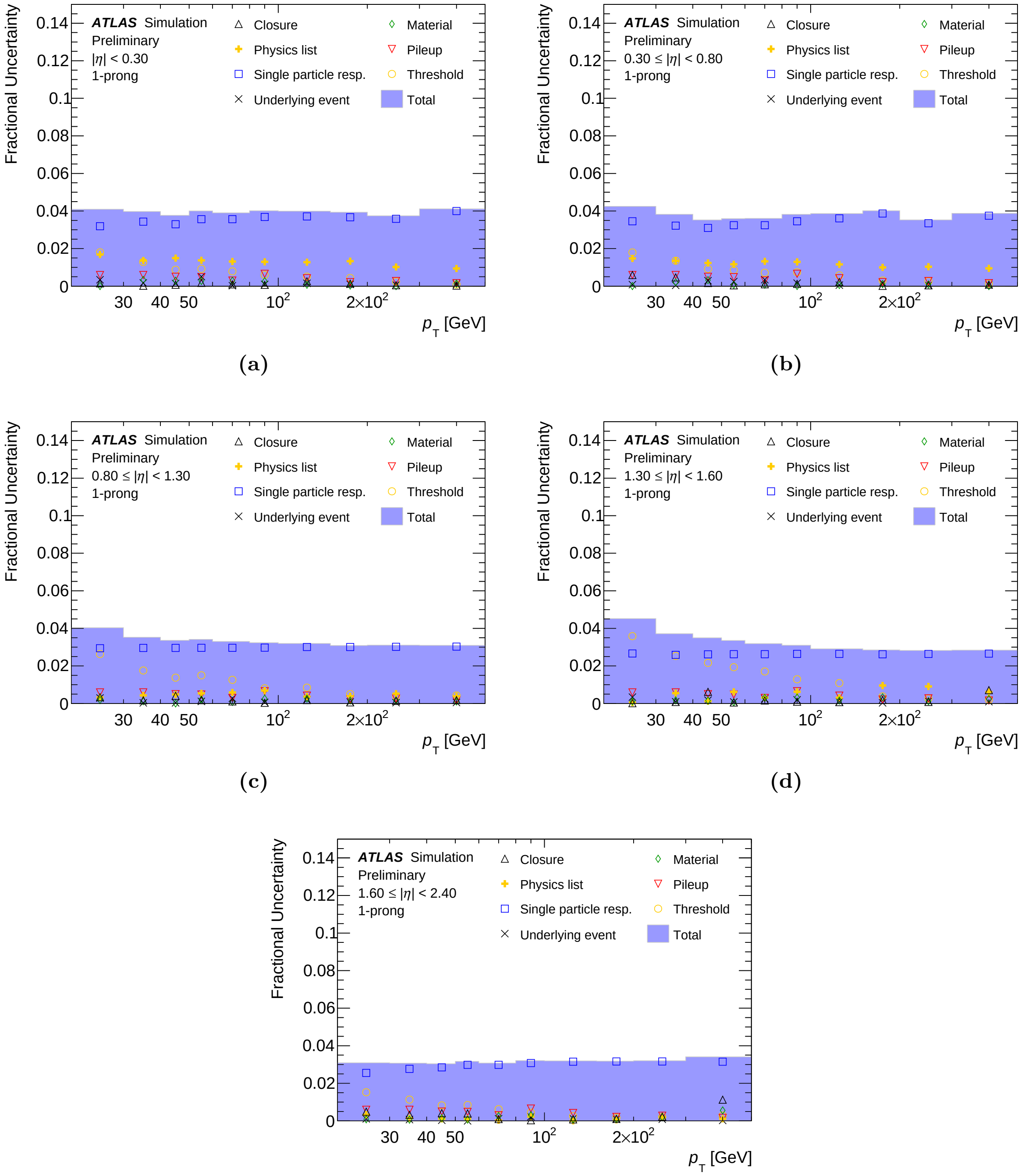

(a) (b) (c) (d) (e)

Figure 7.3.: Uncertainties of TES calibration for 1-prong τ_{had} as a function of p_{T}. They are separated to five regions depend on $|\eta|$. Each corresponding source of systematic uncertainties is also displayed in the histograms [178].

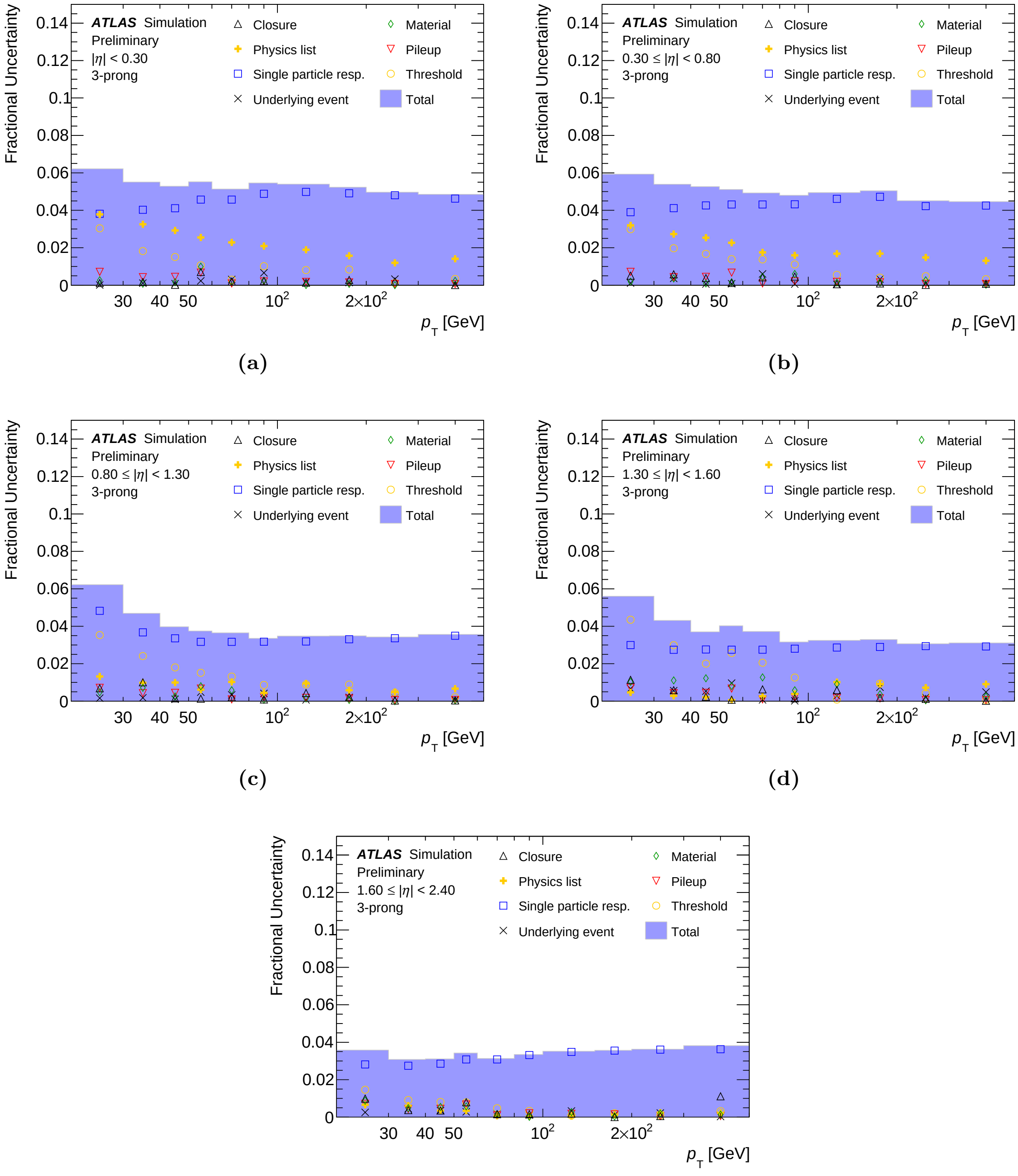

(a)

(b)

(c)

(d)

(e)

Figure 7.4.: Uncertainties of TES calibration for 3-prong τ_{had} as a function of p_{T}. They are separated to five regions depend on $|\eta|$. Each corresponding source of systematic uncertainties are also displayed in the histograms [178].

of the background subtraction for the efficiency measurement. As shown in the Fig. 4.30, the tau trigger systematic uncertainties provide a larger uncertainty in low-p_{T} region than the one in high-p_{T} region due to higher background contribution [161, 162].

Jets

Main systematic uncertainties of jet object come from energy and tagging. Jet energy scale (JES) provides 80 propagated sources from electron, photon, and muon energy scale calibrations [179]. Four pile-up sources for uncertainties are considered due to MC mis-modeling of the dependence for the different variables. Moreover, six other independent uncertainties are considered for the jet object. They are inter-calibration, statistic, method non-closure and the response of the difference from a jet composition of light-quark, b-quark, and gluon-initiated jets.

The JES uncertainties are shown in Fig. 7.5 as the function of η and p_{T}. The uncertainties are expected at a level 5% for the low-p_{T} region and 2% at the most for the high-p_{T} region.

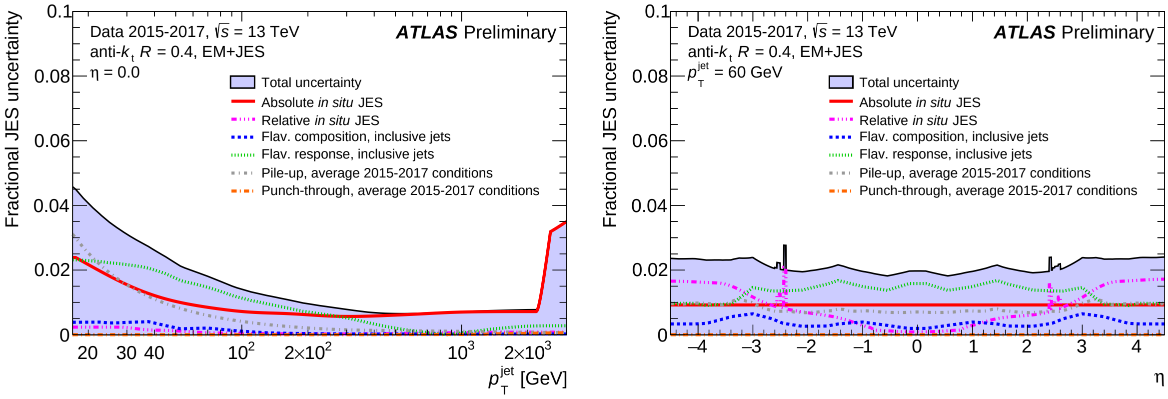

(a) (b)

Figure 7.5.: The combined uncertainty in the JES with over 90 components include instrumental, pile-up and jet composition effect. (b) shows the one as a function of $p_{\mathrm{T}}^{\mathrm{jet}}$ at $\eta = 0$. (a) is as a function of η with $p_{\mathrm{T}} = 60$ selection [127].

Jet vertex tagging (JVT) calibration measured in $Z \to \mu\mu$ events provides a small contribution to the systematic uncertainty based on the jet efficiency of MC and data. The systematic uncertainty of JVT consists of two components; the discrepancy between MC and data in $\Delta\phi$(Z,jet) distribution and the non-negligible difference in hard-scatter efficiency of *Sherpa* and *Powheg* MC generators. The overall uncertainties are found in the 2% to 1% range in 20 GeV $< p_{\mathrm{T}} <$ 60 GeV

The systematic uncertainties for flavor tagging are measured based on the b-tagging efficiency and the corresponding scale factor which is defined as $\epsilon_{\mathrm{b}}^{\mathrm{data}}/\epsilon_{\mathrm{b}}^{\mathrm{sim.}}$. Since the flavor tagging and scale factor are measured in $t\bar{t}$ control region, the $t\bar{t}$ modeling is considered as a main source of uncertainties. The difference between *Powheg+Pythia 8* and *MC@NLO+Pythia 8* is taken into account for $t\bar{t}$ modeling. Illustration of scale factor shows in Fig. 7.6 with the related statistical and systematic uncertainties. The combined uncertainty of the statistical and systematic uncertainties with the 77% operating working point for this analysis is below 7% in low p_{T} range (60 GeV $< p_{\mathrm{T}} <$ 300 GeV), and the uncertainty increases up to approximately 10% due to the dominated statistical uncertainty [180].

Missing Transverse Energy, E_T^{miss}

Uncertainty of missing transverse energy is highly related with each physics objects.Due to the precision measurement of hard term, the main uncertainty of MET comes from soft term. Figure 4.38 shows a sketch for two projection component of the soft term which are used to define three input parameters of

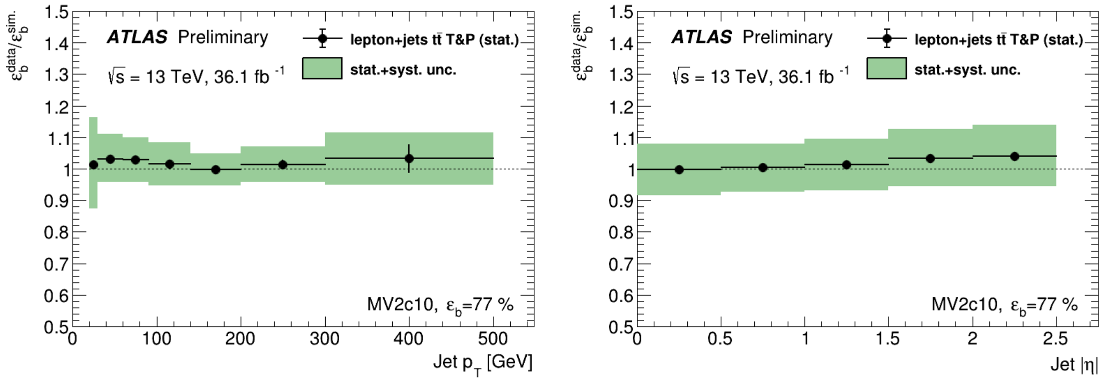

(a) **(b)**

Figure 7.6.: The scale factor for b-tagging efficiencies for the *MV2c10* algorithm at the 77% working point as a function of jet transverse momentum (a) and the absolute pseudo-rapidity (b). The mean value of scale factors and corresponding total uncertainties are shown black dots and green band respectively. (taken from Reference [180])

the systematic uncertainty calculation. The parallel scale $E_{\parallel}^{\text{miss,soft-term}}$ and parallel resolution squared $\sigma^2(E_{\parallel}^{\text{miss,soft-term}})$ show the mean value and root-mean-square (RMS) of the parallel projection of $p_{\text{T}}^{\text{soft}}$ to $p_{\text{T}}^{\text{hard}}$, respectively. The final parameter, transverse resolution squared $\sigma^2(E_{\perp}^{\text{miss,soft-term}})$, presents the RMS information for perpendicular projection of $p_{\text{T}}^{\text{soft}}$. Figure 4.40 shows the agreement of three parameters between data and the simulation with the different generators in the $Z \to ee$ final states events. The systematic uncertainty, which is illustrated as the pink band in the figure, is computed as the function of three parameters based on the maximal differences between data and simulations. The systematic uncertainties (at most 20% depending on $p_{\text{T}}^{\text{hard}}$ value) are employed to the simulations in this analysis. It provides a small impact ($< 0.5\%$) on the distribution of the final discriminant variable.

Other Uncertainties

Other insignificant sources of systematic uncertainties come from luminosity, pile-up, electron and muon objects. ATLAS luminosity is determined by the *LUCID* detector as described in Sec 3.2.4 with the corresponding uncertainties for each data-taking year independently. There dominated uncertainties are considered as the bunch charge production, beam condition, and instrumental effects. The uncertainties of the integrated luminosity measurement for the 2015 to 2018 data-taking year are estimated separately as 2.1%, 2.2%, 2.4%, and 2.0%, and total uncertainty for the combined run-2 dataset is around 1.7%. Considering the integrated luminosity as 139 fb^{-1} is used in this analysis, the absolute uncertainty is quoted as around ± 2.4 fb^{-1}.

The *Pileup* re-weighting uncertainty is measured. MC is compared with data as a function of the instantaneous luminosity. Since the re-weighting is applied into the simulation to correct the μ, the uncertainties are defined as the propagation value for MC by recalculating the re-weighting with $\pm 1\sigma$ [181]. These uncertainties are considered in the analysis with respect to data period.

The muon identification and reconstruction uncertainty are computed with efficiency measurement based on both $J/\psi \to \mu\mu$ and $Z \to \mu\mu$ tag-and-probe method [149, 182]. Additional uncertainties are measured from the correlation of ID-MS efficiencies and different kinematic distributions between the selected muon and probe muon up to 1-2% in the small $|\eta|$ region. The total uncertainties for muon reconstruction and identification of around 3% are taken into account in this analysis. For the muon objects, there are around 1% and 5% uncertainties in wide p_{T} range.

The uncertainties of electron object are considered. Since only ID, p_{T} and η selection are applied for electron objects in this analysis, the electron isolation uncertainty is not taken into account. The

Source	Generator	PDF	Tune
hadronization model	Herwig	CTEQ6L1	UE-EE-5-CTEQ6L1
hard scatter	MG5_aMC@NLO	CT10	A14

Table 7.2.: The generator and shower model used for $t\bar{t}$ systematic samples.

combined uncertainties of reconstruction and identification efficiencies are measured using $J/\psi \to ee$ and $Z \to ee$ tag-and-probe methods. These uncertainties of 2% and 5% are given in the barrel and end-cap region, respectively. Considering the effect from calorimeter with $Z \to ee$ analysis, the energy resolution uncertainty for electron are obtained by the simulation. The minimal relative uncertainty for electrons at $E_{\mathrm{T}} = 40GeV$ is around 5%, while it increases at a higher transverse energy region due to the detector material.

The uncertainties from muon and electron objects are expected to provide small impact ($< 0.1\%$) in this analysis.

7.2 Theoretical Uncertainties on Monte Carlo Simulation

Uncertainties for the theory of Monte Carlo simulation must be taken into account.

cross section

The overall theoretical cross section of backgrounds provides general 5 to 6% uncertainties for three main backgrounds in the signal region, Z/γ^*+ jets, W+jets, and Top sample [183]. The uncertainties of the minor background, di-boson, is 6% for the theoretical cross section of MC modeling [184].

Z/γ^*+jets

The theoretical systematic uncertainties of Z/γ^*+ jets modeling due to the chosen PDF, beam energy, parton shower model and α_s are produced as the weights by a factor calculation tool [185]. The total uncertainties of Z/γ^*+ jets modeling in the acceptance are in the amount of 5%.

W+jets

Based on the W+jets control region discussed in Sec 6.2.2, no big discrepancy from data indicates that the W$\to \mu\nu$ background modeling is good and no further uncertainty is needed. Since the W boson decay production is independent of the W+jets process modeling, it is fair to determine the same situation for W$\to e\nu$ and W$\to \tau\nu$. The sources of W+jets process modeling come from the CKKW parameter, renormalization scale, factorization scale and the PDF in the *SHERPA* Monte Carlo generator [186]. The parameters are modified in sample generation and computed in the expected limit checking. Since the result shows the small impact on the limit (around <0.5%), additional systematic uncertainty of W$\to \tau\nu$ modeling is not considered [65].

Top

The nominal pair and single production of top quark processes are applied for background modeling in this analysis. Therefore, the different setting for the generating parameters [1] are considered for the $t\bar{t}$ and single top modeling. The generators with different matrix-element and parton-shower are used [177]. The samples for systematic uncertainties are listed in Table. 7.2.

---

[1] For instance, there are PDF, scale and top-quark mass variations

Uncertainty	Description	Scheme (number of NPs)
LPX	(Mainly on Z+jets) systematics on PDF choose, QCD scale, stronge interaction coefficient	10
xsec for Diboson or top	Cross section prediction uncertainty	2
TTBAR	Top modeling sys (mainly shape sys)	4
Fakes Rate	Fake rate uncertainties for the backgrounds such as top and W+jets with fake τ_{had}	2
Fake Factor	Fake QCD sys, which is related withp_{T} binning and number of tracks of sub-leading τ_{had}	30

Table 7.3.: Summary table for the background modeling systematics with number of NPs for likelihood fit and brief description.

Moreover, the impact from the variations are studied by modifying the factorization and renormalization scale by factor two up and down for the transverse mass setting $\sqrt{m_t^2 + (p_{T,t}^2 + p_{T,\bar{t}}^2)/2}$. The systematic variations of multi-parton interaction and ISR/FSR parameters are included in *Var1*-*Var3c* parameter variations of *A14* tune [187].

Total uncertainties of top quark modeling present the large systematic uncertainties ($\sim$ 80% in the normalization) for the BTAG category in the high mass region (larger than 400 GeV). The impact in the b-veto category is very limited since the $t\bar{t}$ is not a main background in this signal region.

Signal Acceptance

Like systematic uncertainty study of SM background modeling, the several sources affect the simulation signal sample and must to be taken into account as the signal acceptance. To compare the different sample generation with varying generator parameters, the systematic variations for all configurations of simulation can be obtained. The normalization uncertainties are based on the truth particle information. The different PDF setting, such as *NNPDF30_nlo_as_0118_nf_4*, *CT14nlo_NF4* and *MSTW2008nlo68cl_nf4* are exploited to estimate the uncertainty. To measure the uncertainties of the generator tune in ISR, FSR, and MPI, the different scale factor are applied in the parameter of these shower model. For instance, systematic uncertainties of modeling ISR, FSR and MPI are discussed in *AZNLO* tune [188]. Based on the fitting result for systematic variations of the tuning, it only covers the ISR uncertainty. The uncertainty is computed utilizing a factor of 2 up and down to scale FSR shower parameter and variations of the MPI cut-off between 1.91 to 2.05 to cover the full range of PS and MPI uncertainties. For the QCD scale used in cross sections measurement, the factorization and renormalization scale up and down by a factor of two.

The systematic uncertainty of signal acceptance provides small impact on the cross section limit (smaller than 0.1%).

7.3 Uncertainties on the Data-Driven Background Estimation

As discussed in Sec. 7.2, all the background modeling systematics containing data-driven techniques and theoretical Uncertainties are summarized in Table 7.3.

fake factor

For the fake factor method for the multi-jet background in this analysis, three main sources of uncertainties are considered. The biggest uncertainty comes from the statistical uncertainty of the measured events of data, as well as the MC simulation background. [2] The statistical uncertainties are treated uncorrelated with respect to number of tracks as well as the p_T bins of sub-leading τ_{had}.

The fake factors are measured in an inclusive manner for the b-tagging conditions. The difference between BTAG and BVETO fake factors must be taken into account for the corresponding category. Figure 7.7 presents the shape difference between BTAG and BVETO categories for 1-prong and 3-prong fake factor in OS di-jet control region.

Figure 7.8 shows the total systematic uncertainties (data stat., mc stat. and systematic uncertainty from the b-tagging conditions) in the p_T dependence of the fake factors for 1-prong and 3-prong tau candidates in BVETO category of this analysis.

Overall fake factor uncertainties for BVETO, BTAG and 2P categories are summarized in Appendix B.

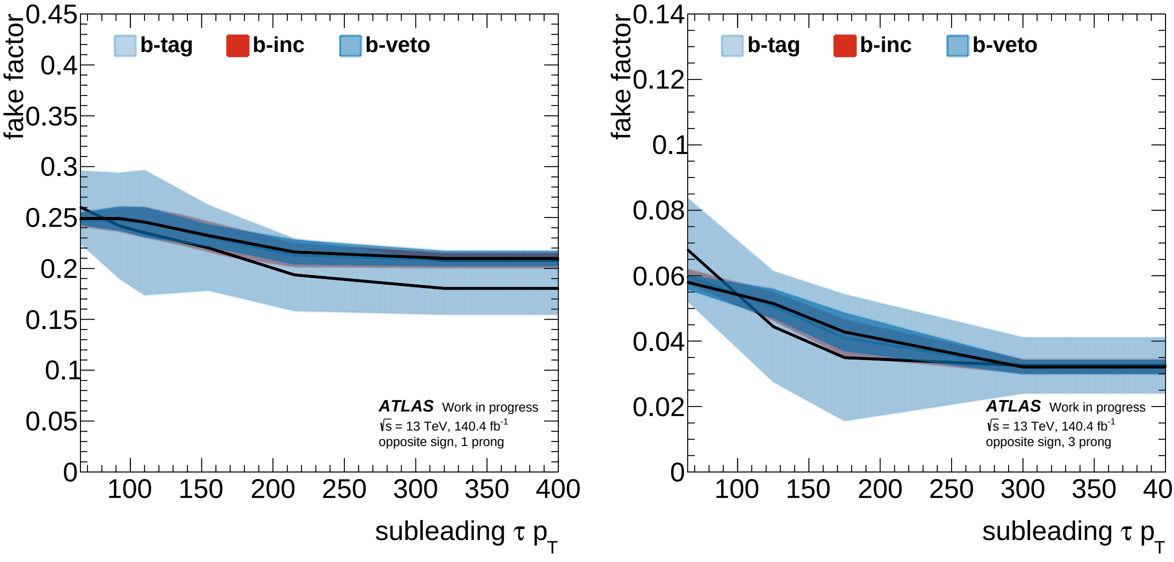

(a) 1-prong

(b) 3-prong

Figure 7.7.: Shape difference comparing with BTAG and BVETO in OS di-jet control region with *loose-not-med.* tau identification applied on sub-leading τ_{had}. The difference is taken into account as an additional source of fake factor uncertainties.

fake rate

In the uncertainties of the fake rate measurement for the other backgrounds with fake τ_{had}, the main uncertainties come from the data statistical uncertainty. The effect of true τ_{had} MC simulation used for subtraction of fake rate method is negligible due to the low contribution of MC in each control regions. The uncertainties are treated to affect the shape of fake τ_{had} in p_T dependence and the expected background yields. Overall fake rates with the uncertainties in this analysis are summarized in Appendix C.

---

[2] As described in Sec. 6.2.1, those background with truth τ_{had} is used for subtraction in the di-jet control region.

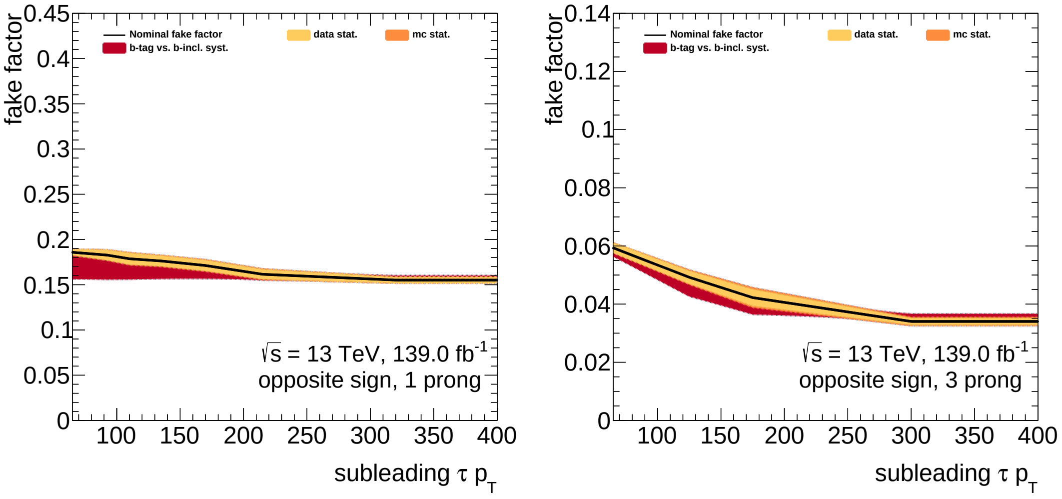

(a) 1-prong BVETO

(b) 3-prong BVETO

Figure 7.8.: Fake factors for 1-prong (left) and 3-prong (right) tau candidates in the BVETO category with *loose-not-med.* tau ID application. The sum of all sources of uncertainties is shown as the orange uncertainty bands which include the statistical uncertainties and difference with the fake factor of BTAG or BVETO.

8 Result

The number of observed events in $H/A \to \tau_{\rm had}\tau_{\rm had}$ search is investigated based on the statistical analysis. A general binned likelihood function is exploited to construct the product of probability terms with background-only or signal-plus-background hypothesis. The combined likelihood function is discussed in Sec 8.1. Section 8.2 presents the statistical result for each signal region in this analysis. The limit for the cross section times branching fraction are computed for both gluon-gluon fusion and bottom-annihilation production at the 95% confidence level (CL) as shown in Sec. 8.3. The interpretation with respect to MSSM m_A-tan β space is discussed in the chapter 9 based on the context of hMSSM benchmark scenario.

8.1 Statistical Analysis

To inspect the signature of neutral heavy Higgs $H/A \to \tau\tau$ signal, the construction of the likelihood ratio and the hypothesis test are introduced in this section. The continuous parameter of interest (PoI) in the statistical analysis is defined as the "signal strength" μ. It is obtained by the maximum-likelihood fit from the observed data to estimate the discovery significance or the exclusion limits. In the investigation for the observed events, the "likelihood ratio" is known as the most efficient test for the statistical hypotheses based on the Neyman-Pearson lemma [189].

The hypothesis test provides the likelihood-based method to quantify the exclusion or observed significance of new physics search. The hypothesis with $\mu = 0$, which is corresponds to background-only one, is referred to a *null* hypothesis, so-called H_0. The hypothesis with $\mu = 1$ corresponding to signal plus background is defined as alternative hypothesis, so-called H_1. A quantified parameter, "p-value (p_μ)", corresponding to μ is obtained via maximum-likelihood fit for the H_0 or H_1 investigation (reject H_0 or accept H_0).

The CL_s technique is appropriate to derive the upper limit for the constraint and discovery significance of search results [190, 191]. The upper limit on cross section times branching fraction with respect to hypothesis test are investigated based on the confidence level of 95% which is also corresponding to p_μ of 0.05. This value is defined as a common enactment for new physics search in LHC.

The full reconstruction and fitting tools for the statistical analysis are contained in the software packages *HistFactory* [192] , *RooStats* [193] and *RooFit* [194] in the *RooStats* framework. The detail of the profile likelihood function, the hypothesis test and Asymptotic formula with Asimov dataset are discussed in the following sections.

8.1.1 The Profile Likelihood Function

The binned likelihood function is implemented based on the Poisson probability term for the final discriminant x, which is a total transverse mass in this analysis, of signal and SM backgrounds. The expected number of total signal and background events are symbolized as S and B in this analysis. The s_i and b_i correspond to the expected events of signal and background in each bin i of the discriminant

x. The expected number in the bin i is given by the model $\mu s_i + b_i$. The binned likelihood function is typically built as:

$$\mathcal{L}(\mu; x_i) = \prod_{i}^{n_{\text{bins}}} Pois(n_i|\mu s_i + b_i), \tag{8.1}$$

where the Poisson probability term is defined as $Pois(n|\lambda) = \lambda^n e^{-\lambda}/n!$. It provides probability to observe n_i events while expecting the number of signal plus background of λ. The systematic uncertainties are treated as nuisance parameters $\boldsymbol{\theta}$ in the fit, which are constrained by Gaussian probability density function $G(\boldsymbol{\theta})$. A default sigma of $\pm 1\sigma$ deviation is used for each NP. The Gaussian PDF for the systematic uncertainties is written as:

$$G(\boldsymbol{\theta}) = \frac{1}{\sqrt{2\pi}\sigma} \exp(-\frac{\boldsymbol{\theta}^2}{2\sigma^2}). \tag{8.2}$$

The full representation of the likelihood is given as :

$$\mathcal{L}(\mu, \boldsymbol{\theta}; x_i) = \prod_{i=1}^{N} \frac{(\mu s_i + b_i)^{n_i}}{n_i!} e^{-(\mu s_i + b_i)} \prod_{k \in \text{sys.}} G(\boldsymbol{\theta}), \tag{8.3}$$

The *MINUIT* framework [195] is used in this analysis to handle the statistical study with the given likelihood. It provides a simple method for the complex statistical problem such as the optimized value of a multi-parameter likelihood functions (so called FCN) [196]. A solution of the combined likelihood function is obtained by minimizing the negative logarithm of the likelihood function (NLL). The best-fit parameter values of NLL contains the uncertainties and correlations between each parameters. The $\hat{\mu}$ ($\hat{\boldsymbol{\theta}}$) is defined as the best-fit value μ ($\boldsymbol{\theta}$) of the likelihood fit in this analysis. The maximum-likelihood estimators (MLEs) ($\hat{\mu}$,$\hat{\boldsymbol{\theta}}$) are obtained following the formula: $-ln\mathcal{L}(\hat{\mu}, \hat{\boldsymbol{\theta}})) = \min(-ln\mathcal{L}(\mu, \boldsymbol{\theta}))$. The conditional MLE is formed as $\hat{\hat{\boldsymbol{\theta}}}(\mu)$ ($\hat{\hat{\boldsymbol{\theta}}}(0)$) with the given μ ($\mu = 0$).

8.1.2 Hypothesis Test

The hypothesis test is a likelihood-based method to quantify the upper limit on on signal strength of new physics search. In a hypothesis test, a *profile likelihood ratio* (PLR), which is a choice of the LHC, is built for the search. The PLR is determined as the optimal discriminator as described in the following formula:

$$\lambda(\mu) = \frac{\mathcal{L}(\mu, \hat{\hat{\boldsymbol{\theta}}}(\mu))}{\mathcal{L}(\hat{\mu}, \hat{\boldsymbol{\theta}})}. \tag{8.4}$$

For the agreement of H_1 in a physical theory, the $\mu \geq 0$ is used for the positive signal process. In the case of $\hat{\mu}$ with a value smaller than 0, it leads to use the boundary value $\mu = 0$ to instead of $\mu < 0$. Since non-negative values is expected for signal, $\mu = 0$ is used to inspect the agreement between the data and background (H_0 hypothesis) [197]. The alternative PLR $\widetilde{\lambda}(\mu)$ is then modified as:

$$\widetilde{\lambda}(\mu) = \begin{cases} \frac{\mathcal{L}(\mu, \hat{\hat{\boldsymbol{\theta}}}(\mu))}{\mathcal{L}(\hat{\mu}, \hat{\boldsymbol{\theta}})} & \text{for} \quad \hat{\mu} \geq 0 \\ \frac{\mathcal{L}(\mu, \hat{\hat{\boldsymbol{\theta}}}(\mu))}{\mathcal{L}(0, \hat{\hat{\boldsymbol{\theta}}}(0))} & \text{for} \quad \hat{\mu} < 0 \end{cases} \tag{8.5}$$

The test statistic q_μ is defined based on the PLR as the following formula. It is a quantified value for upper limits at signal strength μ.

$$q_\mu = \begin{cases} -2ln\widetilde{\lambda}(\mu) & \text{for} \quad \hat{\mu} \le \mu \\ 0 & \text{for} \quad \hat{\mu} > \mu \end{cases} = \begin{cases} -2ln\frac{\mathcal{L}(\mu,\hat{\hat{\boldsymbol{\theta}}}(\mu))}{\mathcal{L}(0,\hat{\hat{\boldsymbol{\theta}}}(0))} & \text{for} \quad \hat{\mu} < 0 \\ -2ln\frac{\mathcal{L}(\mu,\hat{\hat{\boldsymbol{\theta}}}(\mu))}{\mathcal{L}(\hat{\mu},\hat{\boldsymbol{\theta}})} & \text{for} \quad 0 \le \hat{\mu} \le \mu \\ 0 & \text{for} \quad \hat{\mu} > \mu \end{cases} \tag{8.6}$$

A higher value of test statistic q_μ indicates the disagreement with the assumption. The p-value provides a judgment for the discovery significance as well as the exclusion limits. The p-value and the corresponding significance are given as following using on the test statistic $q_\mu = -2ln\widetilde{\lambda}(\mu)$:

$$p_\mu = \int_{q_\mu,obs.}^{\infty} f(q_\mu|\mu, \hat{\hat{\theta}}(\mu, obs))dq_\mu. \tag{8.7}$$

$$Z_\mu = \Phi^{-1}(1 - p_\mu), \tag{8.8}$$

where the $f(q_\mu|\mu, \hat{\hat{\theta}}(\mu, obs))$ shows the distribution of test statistic. The Φ^{-1} is the inverse of the cumulative distribution for a Gaussian with unit parameters.

Moreover, the CL_s technique provides a estimation method for the exclusion or discovery limit based on the p-value. The formula is constructed based on the ratio of p_μ and $1 - p_b$ as: $CL_s = p_\mu/(1 - p_b)$. The $1 - p_b$, which is the p-value of H_0 hypothesis, is given as:

$$1 - p_b = \int_{q_\mu,obs.}^{\infty} f(q_\mu|0, \hat{\hat{\theta}}(0, obs))dq_\mu \tag{8.9}$$

At 95% confident level, the upper limit for μ is computed based on the p_μ value of 0.05.

In general, the discovery limit is discussed based on q_0 for $\mu = 0$ background-only hypothesis. It effectively leads to discovery of signal with rejecting H_0 hypothesis. The equations of q_0 and p_0 are written as:

$$q_0 = \begin{cases} -2ln\widetilde{\lambda}(0) & \text{for} \quad \hat{\mu} \ge 0 \\ 0 & \text{for} \quad \hat{\mu} < 0 \end{cases} \tag{8.10}$$

$$p_0 = \int_{q_0,obs.}^{\infty} f(q_0|0, \widehat{\hat{\theta}}(0, obs))dq_0. \tag{8.11}$$

The q_0 clearly against background-only hypothesis ($\mu = 0$) to show the discovery of a new signal. The p_0 is defined to quantify this disagreement between data and hypothesis of $\mu = 0$. Based on the equivalent significance of p-value, 5-σ Gaussian standard deviation is sorted as the standard discovery significance as the LHC. It corresponds to p-value (p_0) of 2.87×10^{-7}.

For the p_0 and p_μ of hypothesis test, they are usually investigated via Monte Carlo calculations, so-called "toy Monte Carlos" method. The Monte Carlo is used to simulate the distribution of the quantified number, $f(q_\mu|\mu)$. However, this method is computationally expensive. [1] Based on the Wilks [198] and Wald [199] theorem, a approximate method is introduced as *Asymptotic* formulae [197] for the large sample case. The *Asymptotic* formulae is assumed to follow Gaussian distribution with mean of $\hat{\mu}$ and the standard deviation σ of $\hat{\mu}$. A data set, which is related to σ measurement, is discussed as "Asimov" dataset [200]. [2] The test statistic of *Asymptotic* formulae is given as:

$$-2\lambda(\mu) = \frac{(\mu - \hat{\mu})^2}{\sigma^2} + \mathcal{O}(\frac{1}{\sqrt{N}}), \tag{8.12}$$

---

[1] One LHC collision might take around 10 mins to generate.

[2] Name of Asimov data set is enlightened from a short story *Franchise* written by American writer, Isaac Asimov.

where N responds the data sample size.

The profile likelihood ratio λ_A are evaluated as following with "Asimov likelihood" $\mathcal{L}_A$:

$$\lambda_A = \frac{\mathcal{L}_A(\mu, \hat{\hat{\theta}})}{\mathcal{L}_A(\hat{\mu}, \hat{\theta})} = \frac{\mathcal{L}_A(\mu, \hat{\hat{\theta}})}{\mathcal{L}_A(\mu', \theta)}, \tag{8.13}$$

where a strength parameter μ' (zero or nonzero) is defined as the mean of Gaussian distribution with a standard deviation σ_A. The Gaussian distribution is used to suppose the distribution of data. Equation 8.12 and test statistic $q_{\mu,A}$ are obtained with Asimov dataset as following:

$$-2ln\lambda_A(\mu) \approx \frac{(\mu - \mu')^2}{\sigma_A^2} = \Lambda. \tag{8.14}$$

$$q_{\mu,A} = -2ln\lambda_A(\mu). \tag{8.15}$$

$$\sigma_A^2 = \frac{(\mu - \mu')^2}{q_{\mu,A}}. \tag{8.16}$$

Considering the exclusion limit (assuming $\mu' = 0$ for no signal found) based on the signal-plus-background hypothesis (μ), the σ_A^2 is equivalent to $\mu^2/q_{\mu,A}$. For the case of discovery with background-only hypothesis ($\mu = 0$), the σ_A^2 is written as $\mu'^2/q_{0,A}$. Eventually, Wald approximation shows that the test statistics is only related to $\hat{\mu}$.

The cumulative distribution of Λ and corresponding the p-value of the μ hypothesis as following function:

$$F(q_\mu|\mu') = \Phi(\sqrt{q_\mu} - \frac{\mu - \mu'}{\sigma}). \tag{8.17}$$

$$p_\mu = 1 - F(q_\mu|\mu'). \tag{8.18}$$

The upper limit is then computed based on $p_\mu \leq 0.05$ at 95% CL as discussed above. The upper limit μ_{up} is defined as $\hat{\mu} + \sigma\Phi^{-1}(1 - 0.05)$. On the other hand, the discovery significance is obtained by a simple formula : $Z_0 = \Phi^{-1}(1 - p_0) = \sqrt{q_0}$. The ± 1 or $\pm 2\sigma$ variation of Gaussian distributed $\hat{\mu}$ corresponding to the 68% and 95% bands are used to calculate error bands of the median significance. The μ_{up} PDF distribution is used to derive the error bands (frequently uses green and yellow to illustrate) around the median μ_{up}.

8.2 Observed Data in the Signal Regions

The events yield of analyzed data is investigated for each signal region based on the null hypothesis, H_0. The result of the background-only hypothesis is obtained based on the conditional MLEs with the given $\mu = 0$ ("post-fit"). [3] The post-fit yields of likelihood fit are summarized in the Table 8.1 and Table 8.2. Figure 8.1 and Fig. 8.2 show the corresponding $m_{\mathrm{T}}^{\mathrm{tot}}$ distribution for each signal region. The observed local p-values in this analysis for the gluon-fusion and bottom-annihilation production with respect to mass hypothesis are shown in Fig 8.3. The local p-value based on H_0 or H_1 investigation from the MLEs exhibits no significant excess of data events.

---

[3] The "pre-fit" results are discussed in Sec. 6.3. They show the results before the likelihood fit.

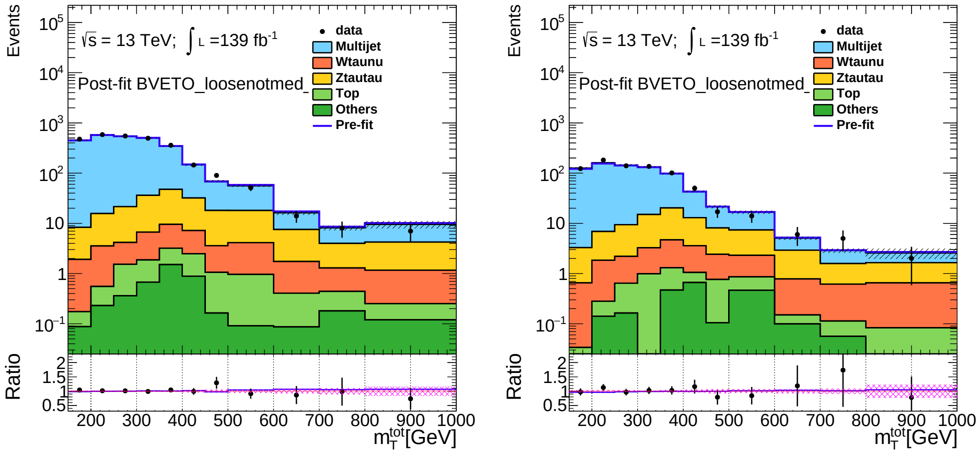

(a) 1p BVETO loose-not-med

(b) 3p BVETO loose-not-med

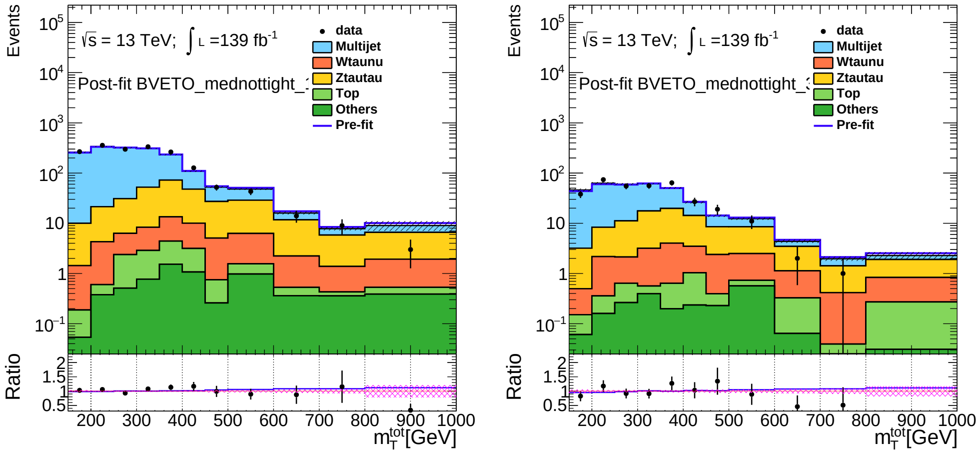

(c) 1p BVETO med-not-tight

(d) 3p BVETO med-not-tight

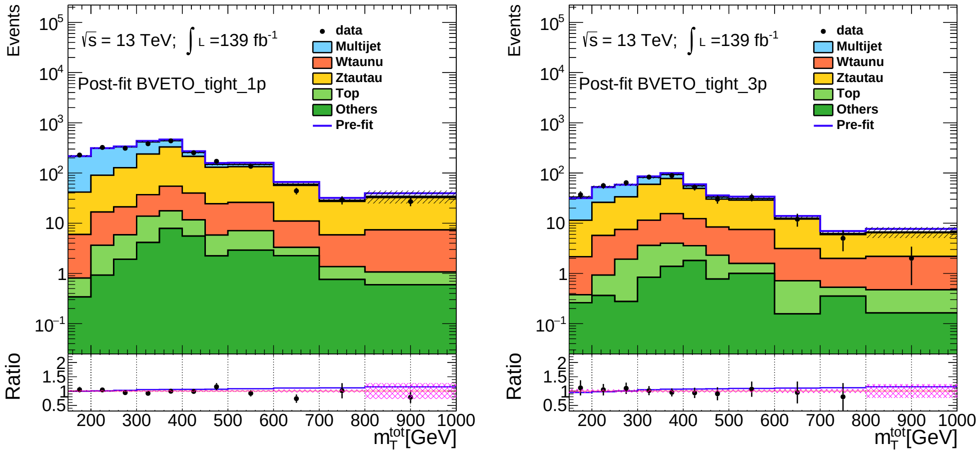

(e) 1p BVETO tight

(f) 3p BVETO tight

Figure 8.1.: Distributions of total transverse mass for BVETO category. The plots correspond to post-fit result with $\mu = 0$ hypothesis. Events containing 1-prong sub-leading τ_{had} are illustrated in left plots and the events containing 3-prong sub-leading τ_{had} are shown in right plots. From top to bottom, the plots is made with respect to tau identification (loost-not-med., med-not-tight and tight). The underflow events and overflow evnets are included in the first and last bins, respectively. In the label, “Others” background refers to contributions from diboson, $Z/\gamma^{*}(\rightarrow \ell\ell)$+jets and $W(\rightarrow \ell\nu)$+jets production. The “Top” containing the $t\bar{t}$ and single top production. The data is shown as the black point in the histogram. The blue lines show the total expected background from pre-fit. In the lower panels, the fraction of data and overall background is illustrated.

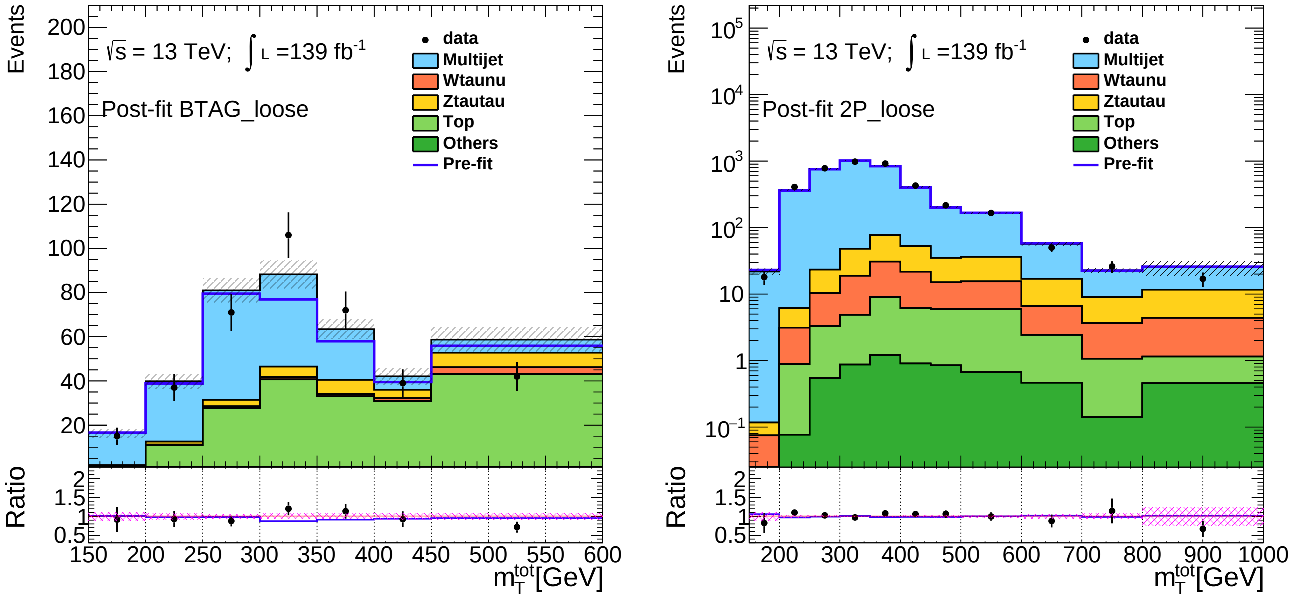

(a) 1p+3p BTAG loose

(b) 2p BINC. loose

Figure 8.2.: Distributions of total transverse mass for BTAG (left) and 2P (right) categories. The plots correspond to post-fit result with $\mu = 0$ hypothesis. The underflow events and overflow evnets are included in the first and last bins, respectively. In the label, "Others" background refers to contributions from diboson, $Z/\gamma^*(\rightarrow \ell\ell)$+jets and $W() \rightarrow \ell\nu$+jets production. The "Top" containing the $t\bar{t}$ and single top production. The data is shown as the black point in the histogram. The blue lines show the total expected background from pre-fit. In the lower panels, the fraction of data and overall background is illustrated.

Processes	**1P BVETO loose-not-med**	**1P BVETO med-not-tight**	**1P BVETO tight**
Multijet	2510 ± 19	1386 ± 16	968 ± 12
Wtaunu	33 ± 2	45 ± 3	184 ± 13
Ztautau	168 ± 6	254 ± 9	1171 ± 41
Top	7 ± 1	8 ± 3	38 ± 5
Others	4 ± 0	7 ± 1	30 ± 3
Bkg	2723 ± 21	1700 ± 18	2390 ± 39
data	2780	1769	2356
Processes	**3P BVETO loose-not-med**	**3P BVETO med-not-tight**	**3P BVETO tight**
Multijet	665 ± 16	243 ± 8	125 ± 8
Wtaunu	17 ± 1	18 ± 2	60 ± 5
Ztautau	67 ± 3	76 ± 3	265 ± 10
Top	4 ± 1	3 ± 1	8 ± 2
Others	2 ± 0	2 ± 0	8 ± 1
Bkg	755 ± 16	343 ± 8	466 ± 13
data	779	347	464

Table 8.1.: The events yields after the global fit with $\mu = 0$. Overall systematic and statistical uncertainties are considered and listed in the table.

Processes	**BTAG loose**	**2P loose**
Multijet	168 ± 5	3575 ± 24
Wtaunu	8 ± 1	94 ± 11
Ztautau	26 ± 2	185 ± 9
Top	186 ± 20	35 ± 9
Others	2 ± 0	6 ± 0
Bkg	390 ± 19	3894 ± 31
data	389	4012

Table 8.2.: The events yields after the global fit with $\mu = 0$. Overall systematic and statistical uncertainties are considered and listed in the table.

8.3 Constraints on the Cross Section

No indication of an excess over the SM background is found in this analysis. The upper limits of the cross section for the gluon-fusion and the bottom-annihilation processes are obtained via MLE with the asymptotic method. The model-independent upper limits with the impact for each NP are introduced in Sec. 8.3.1.

8.3.1 Independent Cross-Section limits

The independent upper limits of $H/A \to \tau\tau$ with 95% and 68% confidence interval for the gluon-fusion and the bottom-annihilation models in the different mass hypotheses are shown in Fig. 8.4. The figures also show the upper limits of $\sigma \times \mathbf{BF}(H/A \to \tau\tau)$ for two signal production modes in each category containing BVETO, BTAG and 2P categories. The BTAG category presents a better sensitivity for the bottom-annihilation signal as shown in the left plot. In the right plot, the result shows that the best sensitivity of gluon-fusion production signal is from BVETO category. The orange broken line, so called as “paper method” in this analysis, shows a investigation with the previous method used in the ATLAS 36 fb^{-1} paper [65]. In this method, the 2-prong τ_{had} and new categorization are not applied.

The new categorization strategy presents the significant improvement in the low mass region. Compared with orange broken line, the gluon-gluon fusion production limit improves around 54% at $M_A = 300$ GeV.

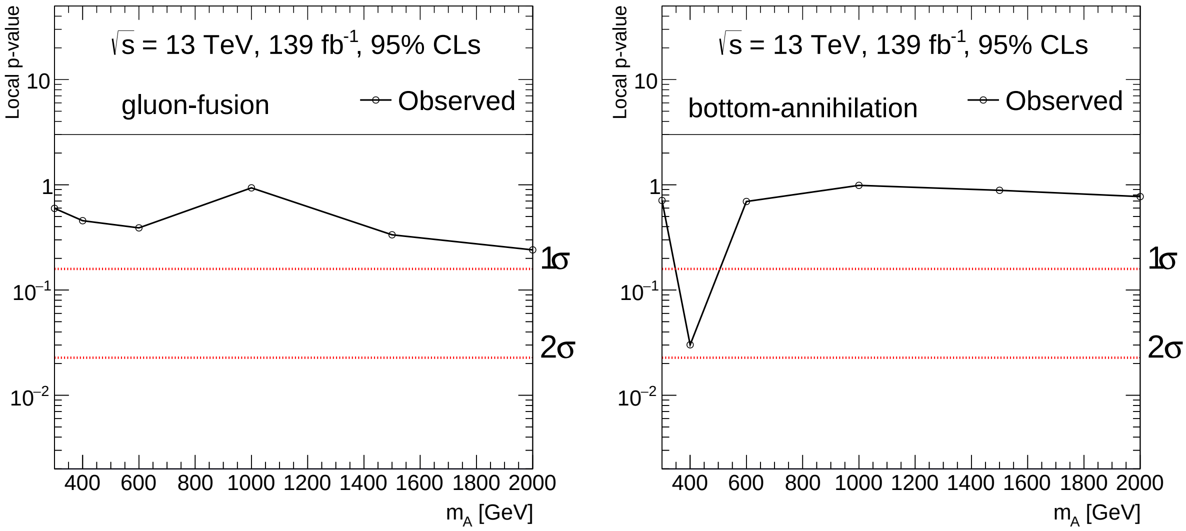

(a) gluon-fusion **(b)** bottom-annihilation

Figure 8.3.: (a) and (b) show the observed local p-values in this analysis for the gluon-fusion and bottom-annihilation. The figures show that there is no significant excess in this analysis.

The bottom-annihilation production limit improves around 24% at M_A = 300 GeV. Moreover, around 20% events of signal is saved by an additional 2P category in the analysis as discussed in Sec 4.6. It results in the 2% to 10% improvement in the upper limit of the high mass hypotheses (larger than 1.5 TeV) as shown in the upper limit plots.

The exclusion limits from the observed data are drawn as the solid line. In the single production hypothesis of the gluon-gluon fusion the exclusion limit is 236(2) fb at $m_A = 300(1500)$ GeV. The exclusion limit is 145(1) fb at $m_A = 300(1500)$ GeV in the bottom-annihilation only hypothesis.

The impact of each systematic uncertainty on μ is investigated. Figure 8.5 presents the 15 most important nuisance parameters for μ of the combined likelihood fit with m_A = 300 GeV (low mass) and m_A = 1500 GeV (high mass) signal mass hypotheses. The corresponding $\tan\beta$ hypotheses for m_A = 300 GeV and m_A = 1500 GeV Higgs are assumed as 2 and 23 based on the result discussed in Chapter 9. The impacts on pre-fit and post-fit result are investigated via shifting the nuisance parameter to the 1σ boundaries. Each nuisance parameter is fixed to its $\pm 1\sigma$ and found the best-fit $\hat{\mu}$ via the combined likelihood fit. Obviously, the major systematic uncertainty comes from tau energy scale as well as tau-ID, and other sources are considered as minor uncertainties. Overall, the systematic uncertainties are much smaller than statistical uncertainties in both low mass and high mass hypotheses as shown in top part of Fig. 8.5.

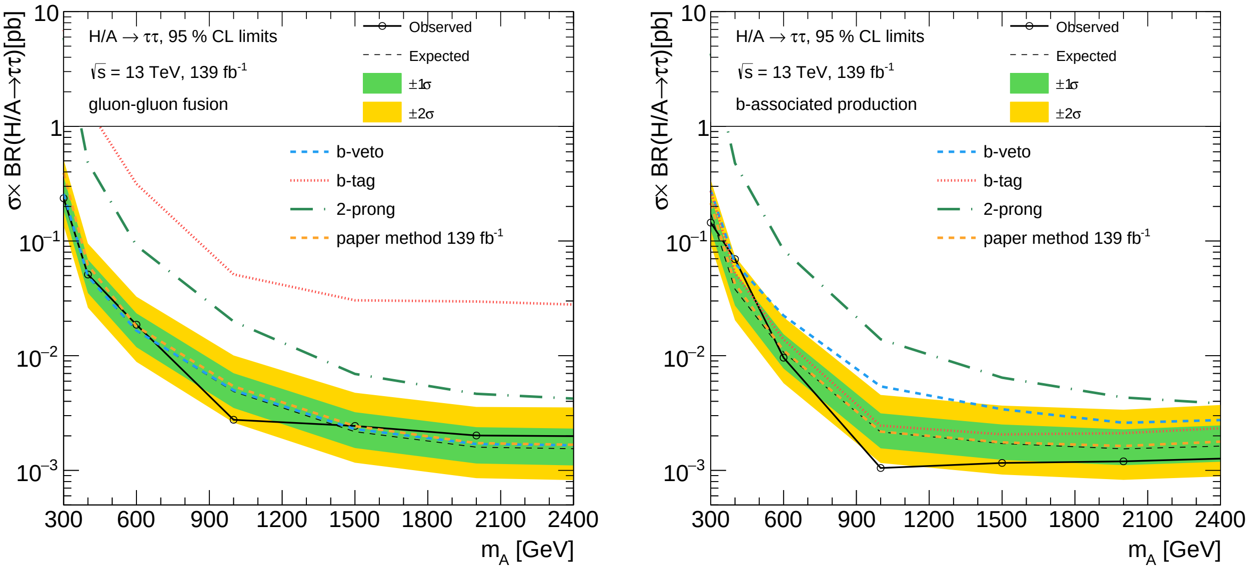

(a) gluon-fusion **(b)** bottom-annihilation

Figure 8.4.: The upper limits on the cross section times branching fraction to $\tau\tau$ for bottom-annihilation production (a) and gluon-fusion (b) at the different mass hypotheses. The limits of $\sigma \times \mathbf{BF}(H/A \to \tau\tau)$ are set as a function of the boson mass. The dashed lines and solid lines are shown for the expected limit and observed limit at 95% confidence level, along with $\pm 1\sigma$ (green) and $\pm 2\sigma$ (yellow) uncertainty bands for the expected limit. The independent upper limits for BVETO, BTAG, and 2P categories are illustrated as blue, red, and green dot lines, respectively.

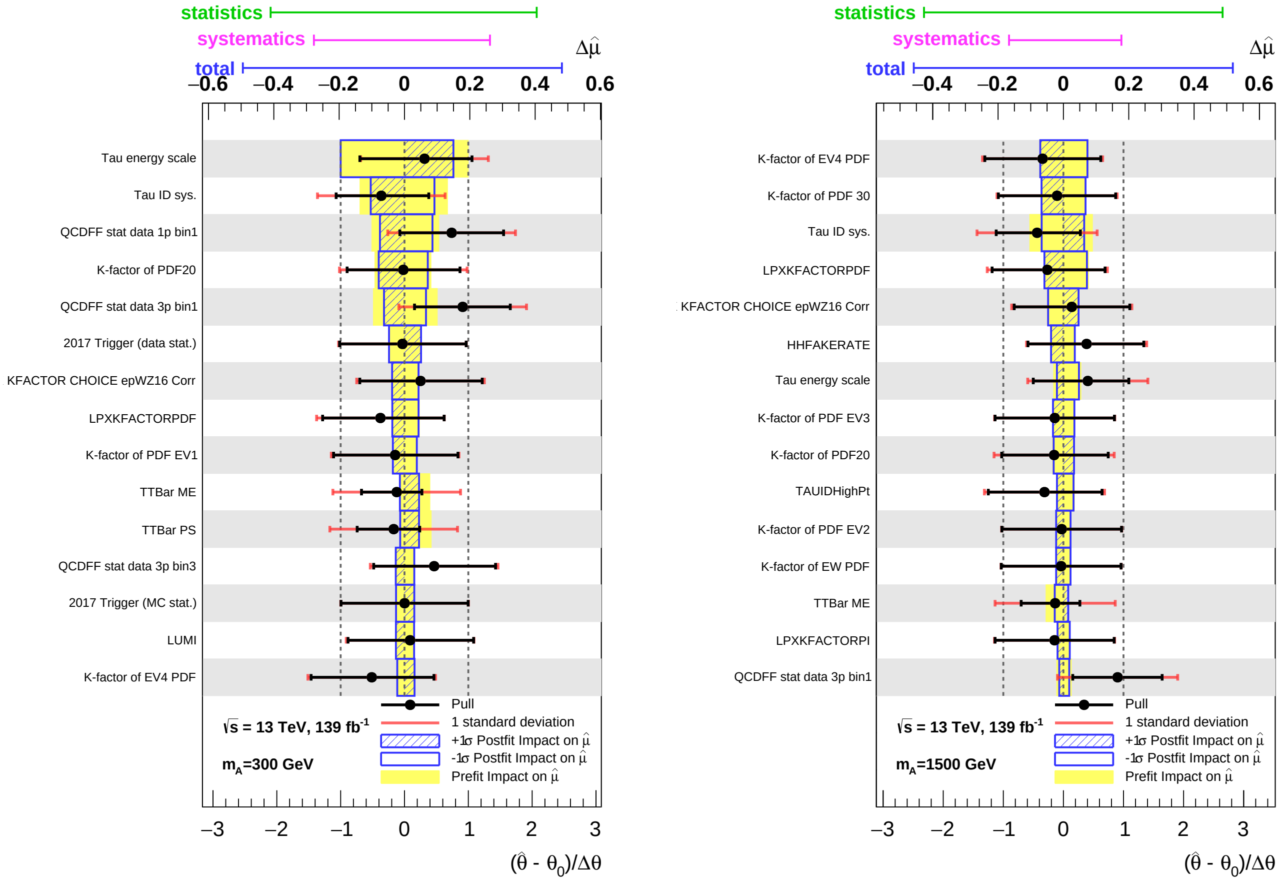

(a) $m_A = 300\ GeV$ **(b)** $m_A = 1500\ GeV$

Figure 8.5.: Impact from each nuisance parameter on the fitted signal strength for $m_A = 300$ GeV and $m_A = 1500$ GeV. The corresponding $\tan\beta$ hypotheses for $m_A = 300$ GeV and $m_A = 1500$ GeV Higgs are assumed as 2 and 23. The red lines in the ranking plots are shown as “1 standard deviation”. The black points with the black lines in the plots are the fitted value and corresponding $\pm 1 - \sigma$ values after the shifting, so called as “pull value”. The pull value is quantified to as $\text{pull}(\boldsymbol{\theta}) = (\hat{\boldsymbol{\theta}} - \boldsymbol{\theta}_0)/\sigma_{\boldsymbol{\theta}}$ [201]. It shows the difference between the expected value and the fitting result of MLE. The nuisance parameters are ordered by their impact on the signal strength $\hat{\mu}$. The blue opened box presents the impact on post-fit result and the impact on the pre-fit result is shown as the yellow box. The impact on $\hat{\mu}$ from overall systematic uncertainties is illustrated as pink line in the top of ranking plots. The statistical uncertainty is also presented as green line. The combined uncertainty of statistic and systematic is shown as blue line.

9 Discussion

9.1 MSSM interpretations

The observed $m_{\mathrm{T}}^{\mathrm{tot}}$ distributions show good agreement with the background predictions. With respect to the results, upper limits on the signal production rate of $\sigma \times BF(H/A \to \tau^{+}\tau^{-})$ are set for gluon-gluon fusion production and bottom-annihilation production scenarios, as discussed in Chapter 8. The limits are combined and interpreted in the context of the MSSM scenarios, in particular, in the hMSSM scenario as the benchmark of this analysis. [1] A set of hypotheses with a various $\tan\beta$ values is tested by a comparison between the observed upper limit and the prediction of the signal production rates per $M_{H/A}$ point. The exclusion on $\tan\beta$ has been evaluated in the mass range up to 1800 GeV. Figure 9.1 shows the exclusion limit on $m_A - \tan\beta$ plane in terms of the hMSSM benchmark scenario. The observed upper limit of signal production rate excludes $\tan\beta > 2$ hypothesis for $m_A = 300$ GeV and $\tan\beta > 23$ region for $m_A = 1500$ GeV. As the discussion of the current experimental constraints of heavy neutral Higgs bosons searches in Sec 2.5, this is the most stringent observed constraints for the hMSSM scenarios with addition high mass heavy neutral Higgs bosons and high $\tan\beta$.

9.2 Major achievements in the thesis work

The search for additional heavy neutral Higgs bosons have been performed with an improved search sensitivities, compared to the previous result with 36 fb^{-1}.

The reducible backgrounds are estimated by data-driven techniques. Taking advantage of the improved statistics of the control region data, the precision for multi-jet backgrounds has been significantly improved. Reducible backgrounds associated with W and top-quark productions are carefully studied with measurements of fake-rates and assistance of Monte Carlo Simulation. A difference of the fake-rates between quark-initiated jets and gluon-initiated jets have been studied to achieve accurate estimate for these backgrounds, accounting possible topology dependence.

In addition to the improvement of the data statistics, this thesis work has improved the search sensitivities by introducing the following new techniques with data-driven techniques.

- **Categorization of signal regions:** A new categorization with respect to the tightness of tau identification criteria has been introduced. It allows effective use of a tight tau identification cut to suppress fake τ_{had} backgrounds while a good signal selection efficiency will be maintained by keeping a looser condition. This technique introduces a major improvement in a low $M_{H/A}$ region ($M_{H/A} < 1$ TeV). In the $M_{H/A} = 300$ GeV scenario, the categorization techniques improve the sensitivity of gluon-fusion production over 54% and bottom-annihilation production limit about 24%.

---

[1] The constraint presented here is applicable more generally to type II 2HDM, which has been discussed for the phenomenology of SUSY [30].

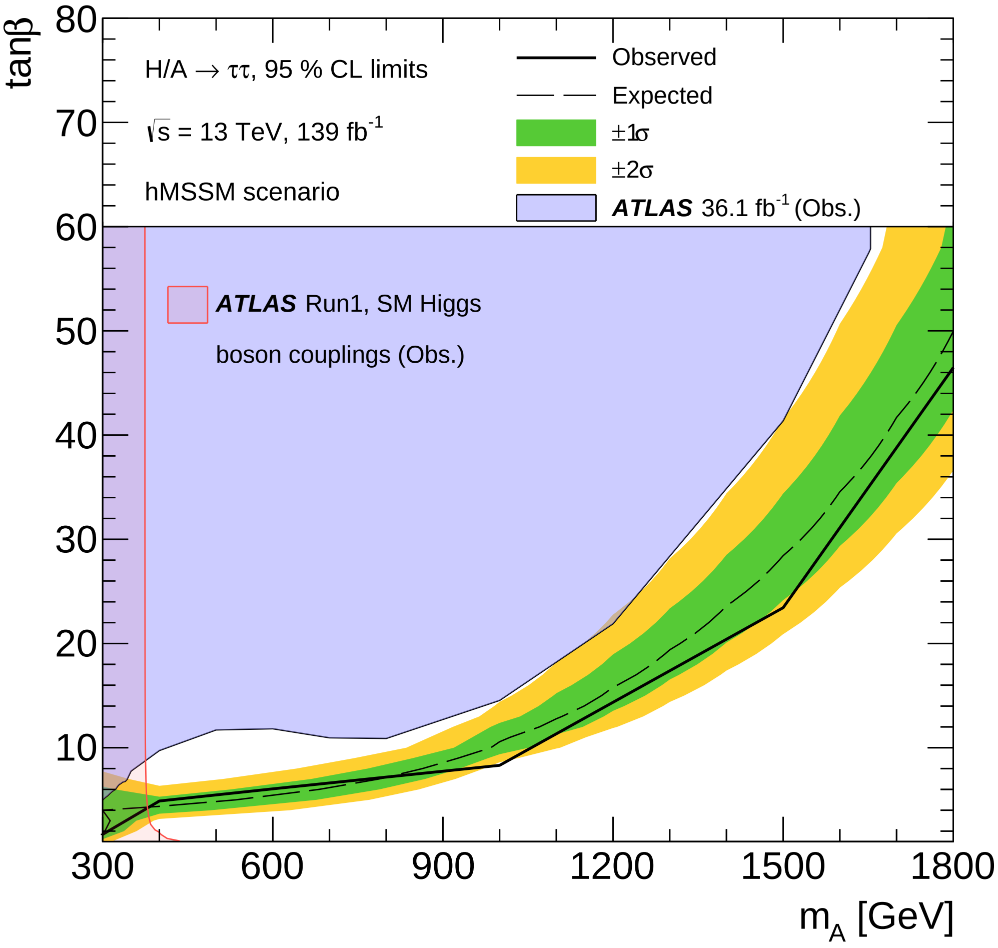

Figure 9.1.: The exclusion limits (black solid line) in the two dimension m_A - $\tan\beta$ parameter space at 95% confidence level, along with $\pm1\sigma$ (green) and $\pm2\sigma$ (yellow) uncertainty bands for the expected limit (black dot line). The previous result with 36 fb^{-1} (light purple block) [65] and the MSSM interpretation for the SM 125 GeV Higgs (red line) [202, 203] are shown.

- **2-prong τ_{had} reconstruction:** To maximize the signal efficiency, reconstructed τ_{had} candidates which are associated with two reconstructed charged tracks are considered in this analysis in addition to the 1-prong and 3-prong τ_{had} signatures. The additional 2-prong signature introduces a major improvement of the sensitivities for high mass heavy neutral Higgs scenarios ($M_{H/A} > 1.5$ TeV). In the $M_{H/A} = 1.5(2.4)$ TeV scenario, it provides around 12% (8%) and 2% (10%) improvement for gluon-fusion production and bottom-annihilation production, respectively.

9.3 Future Prospect

The LHC is going to collect more proton-proton collision data with an integrated luminosity of 150 fb^{-1} at a center-of-mass energy of 14 TeV in Run3, which will start 2021 and run util 2025. In the High-Luminosity LHC (HL-LHC) physics runs, the integrated luminosity will reach up to 3000 to 4000 fb^{-1} [204, 205]. It is ten times more than the combined luminosity of the LHC Run1 to Run3. Furthermore, a Future Circular Collider facility (FCC) is designed as a 100 TeV proton–proton Collider [206]. Although no evidence is shown with the current data, the new data allow heavy Higgs in few TeV scale for large M_A, $\tan\beta$ in the contest of hMSSM. The limit of the 2σ sensitivity for the heavy neutral Higgs search is illustrated in Fig. 9.2.

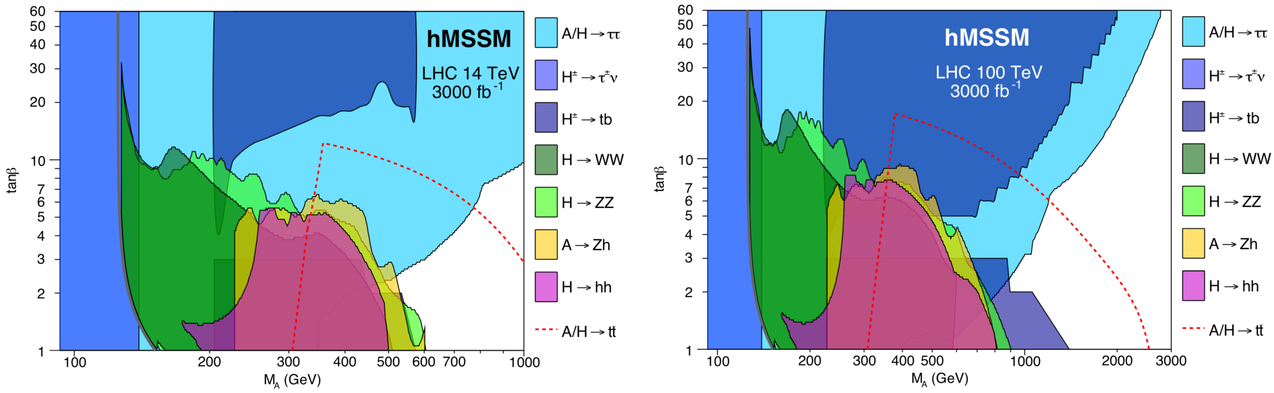

(a) $\sqrt{s} = 14\,\text{TeV}$, 3000 fb^{-1} **(b)** $\sqrt{s} = 100\,\text{TeV}$, 3000 fb^{-1}

Figure 9.2.: Projections for the limit of the 2σ sensitivity in the hMSSM ($\tan\beta, m_A$) plane corresponding to 3000 fb^{-1} data. (a) shows the one for the HL-LHC at a center-of-mass energy of $\sqrt{s} = 14\,\text{TeV}$ and the expected limit for FCC at a center-of-mass energy of $\sqrt{s} = 100\,\text{TeV}$ is presented in (b) [34, 204].

10 Conclusions

The supersymmetry is one of the most motivated extensions of the SM as it may address the remained problems after the discovery of the scalar Higgs boson with the mass of 125 GeV at the Large Hadron Collider. It requires the Higgs sector of the SM to be extended at least five physical Higgs bosons; the SM 125 GeV Higgs (h), two heavy neutral Higgs bosons (H/A) and a charged Higgs bosons ($H^{\pm}$). Two heavy neutral Higgs bosons H/A provide important insight into the nature of the SUSY. The coupling of H/A constants to down-type fermions are enhanced for a large $\tan\beta$ hMSSM scenario. This analysis is focused on the neutral heavy Higgs boson hadronic decaying into a pair of tau leptons ($H/A \rightarrow \tau^{+}\tau^{-}$), which provides best sensitivity at the LHC. This thesis uses an integrated luminosity of 139 fb^{-1} of proton-proton collision data recorded by the energy frontier ATLAS experiment at a center-of-mass energy of $\sqrt{s} = 13$ TeV during Run2 data.

Possible backgrounds remaining after the selection are estimated with the data-driven methods, which provide significant improvement for the precision of reducible backgrounds associated with W, top-quark productions and multi-jet backgrounds taking advantage of large data statistics in the control region. In order to improves search sensitivity, 2-prong τ_{had} reconstruction and the categorization have been developed in this analysis. The 2-prong τ_{had} reconstruction improves sensitivity in high mass region while the categorization improves sensitivity in low mass region. The sensitivities of gluon-gluon fusion production (bottom-annihilation production) improve 12% (2%) and 54% (24%) at a high mass hypothesis $m_A = 1500$ GeV and a low mass hypothesis $m_A = 300$ GeV with the two new techniques.

Since no indication of an excess over the expected SM background is found, this thesis sets the upper limits on the cross section times branching fraction to $\tau\tau$ [1] for the production of heavy neutral Higgs bosons H/A at 95% confidence level for bottom-annihilation and gluon-gluon fusion processes.

In the single production hypothesis of the gluon-gluon fusion and bottom-annihilation, the exclusion limits are around 236(2) fb and 145(1) fb at $m_A = 300(1500)$ GeV, respectively. In the context of the hMSSM scenario, the observed upper limit of signal production rate excludes $\tan\beta > 2$ hypothesis for $m_A = 300$ GeV and $\tan\beta > 23$ region for $m_A = 1500$ GeV.

---

[1] The cross section times branching fraction to $\tau\tau$ is labeled as $\sigma \times \mathbf{BF}(H/A \rightarrow \tau\tau)$

Appendix

A Cutflow for Event Selection

The number of expected events for SM background and signal after each event selection are shown in the table. The one for the observed data is also shown. The tables are separated to BTAG and BVETO categories. The opposite sign is the signal region and same sign is for validation region. Only statistical uncertainties are shown in the table and multijet background is estimated by data-driven method.

BVETO							
Names:	Data	Others	W $\rightarrow \tau\nu$	$Z/\gamma* \rightarrow \tau\tau$	hMSSM $A_{1000}^{tan\beta=15}$	$t\bar{t}$, single top	Multijet
ALL	515967425.0	49154955.0	30394663.0	10077689.0	2184492.0	82871406.0	—
MC WEIGHT	515967425.0	49154955.0	30394663.0	10077689.0	2184492.0	82871406.0	—
MIN TWO TAUS	110184781.0	26055781.0	18113578.0	8280969.0	1915168.0	46369457.0	—
MUON VETO	103185115.0	16718428.0	16336027.0	7483878.0	1588419.0	28980295.0	—
ELE VETO	101805104.0	9207611.0	15671624.0	5701622.0	1313021.0	25281098.0	—
OLR + Event Cleaning + 1PV	3006433.0	2884518.0	5215876.0	2809880.0	474141.0	2498261.0	—
Loose 2nd tau + Trigger	37505.0	2809120.0	4678123.0	2337690.0	396520.0	2411705.0	—
Opposite Sign							
OS	27836.0	1950917.0	3325877.0	2080581.0	368845.0	1645263.0	—
K-factor for EW	27836.0	1950917.0	3325877.0	2080581.0	368845.0	1645263.0	—
delta Phi	17167.0	960984.0	1845786.0	1945037.0	329577.0	727730.0	79426.0
leading tau pT	14343.0	873733.0	1631293.0	1912883.0	323494.0	642011.0	66228.0
Same Sign							
SS	9669.0	858203.0	1352246.0	257109.0	27675.0	766442.0	—
K-factor for EW	9669.0	858203.0	1352246.0	257109.0	27675.0	766442.0	—
deltaPhi	6546.0	410425.0	706381.0	211224.0	12367.0	335125.0	30301.0
leading tau pT	5266.0	364077.0	617779.0	206759.0	11783.0	288219.0	24615.0

Table A.1.: Cutflow for SM background and $m_{\mathrm{H/A}}$ signal in BVETO region

BTAG							
Names:	Data	Others	W → $\tau\nu$	$Z/\gamma* \rightarrow \tau\tau$	hMSSM $A_{1000}^{tan\beta=15}$	$t\bar{t}$, single top	Multijet
ALL	515967425.0	49154955.0	30394663.0	10077689.0	2184492.0	82871406.0	—
MC WEIGHT	515967425.0	49154955.0	30394663.0	10077689.0	2184492.0	82871406.0	—
MIN TWO TAUS	110184781.0	26055781.0	18113578.0	8280969.0	1915168.0	46369457.0	—
MUON VETO	103185115.0	16718428.0	16336027.0	7483878.0	1588419.0	28980295.0	—
ELE VETO	101805104.0	9207611.0	15671624.0	5701622.0	1313021.0	25281098.0	—
OLR + Event Cleaning + 1PV	148642.0	207702.0	359162.0	62457.0	275955.0	3652972.0	—
Loose 2nd tau + Trigger	2190.0	201962.0	326748.0	51837.0	229275.0	3529218.0	—
Opposite Sign							
OS	1697.0	139401.0	229392.0	44004.0	213718.0	2451562.0	—
K-factor for EW	1697.0	139401.0	229392.0	44004.0	213718.0	2451562.0	—
deltaPhi	783.0	57018.0	100419.0	36041.0	177645.0	931538.0	3159.0
leading tau pT	619.0	51135.0	89009.0	35447.0	174734.0	801205.0	2473.0
Same Sign							
SS	493.0	62561.0	97356.0	7833.0	15557.0	1077656.0	—
K-factor for EW	493.0	62561.0	97356.0	7833.0	15557.0	1077656.0	—
deltaPhi	222.0	25425.0	41020.0	4980.0	6537.0	395414.0	1159.0
leading tau pT	165.0	22270.0	35682.0	4820.0	6232.0	331703.0	905.0

Table A.2.: Cutflow for SM background and $m_{\mathrm{H/A}}$ signal in BTAG region

B Fake Factor

Since multijet background is estimated by data-driven method, so called fake factor (FF) method. The overall fake factors for all tau ID working points (loose, loose-not-medium, medium, medium-not-tight, tight) are investigated as following plots. The fake factors are computed for 1-prong, 2-prong and 3-prong, respectively. The fake factors are also separated to OS and SS for signal and validation regions, respectively.

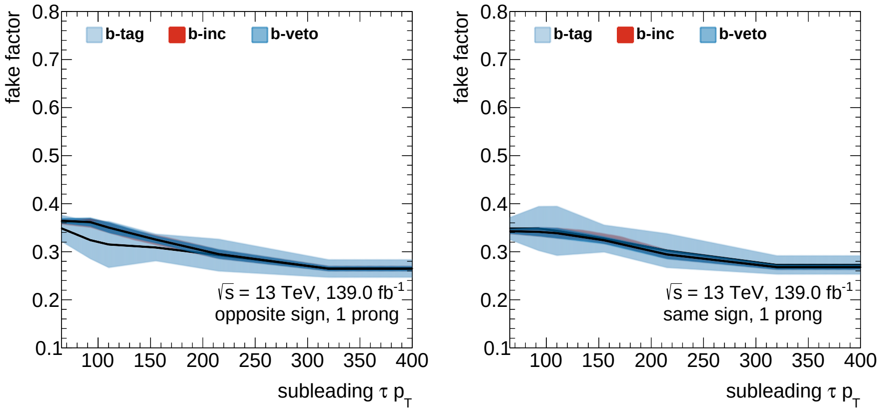

(a) Loose 1-prong OS **(b)** Loose 1-prong SS

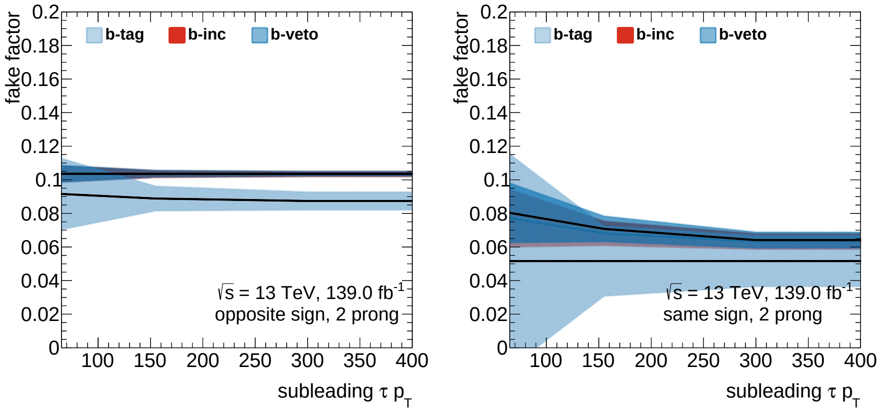

(c) Loose 2-prong OS **(d)** Loose 2-prong SS

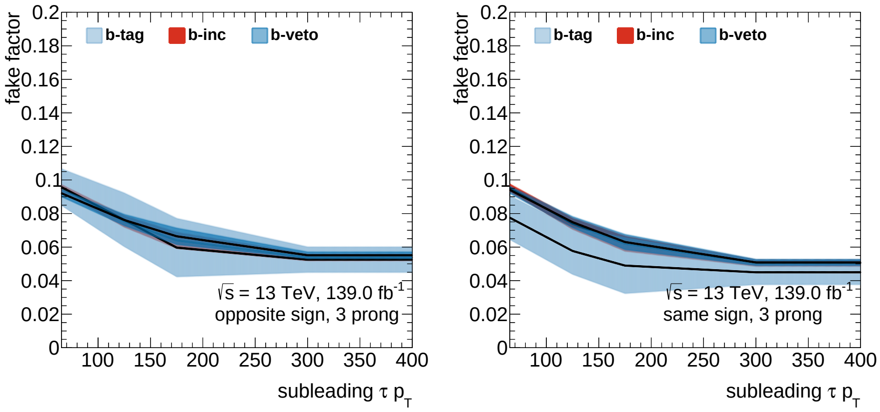

(e) Loose 3-prong OS **(f)** Loose 3-prong SS

Figure B.1.: Comparison of BINC FF to BTAG and BVETO FFs. The loose-not-med. FFs of 1-prong (top), 2-prong (middle) and 3-prong (bottom) for signal region (left) and validation region (right) are shown. The loose FFs of 1-prong and 3-prong are not used in this analysis.

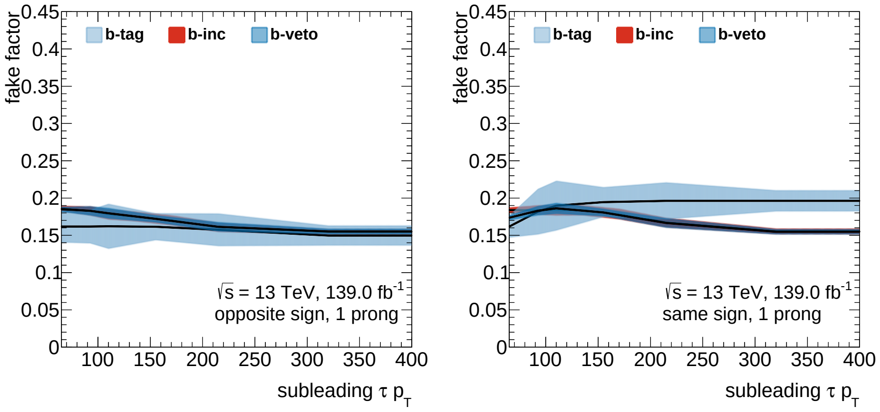

(a) Loose-not-med 1-prong OS **(b)** Loose-not-med 1-prong SS

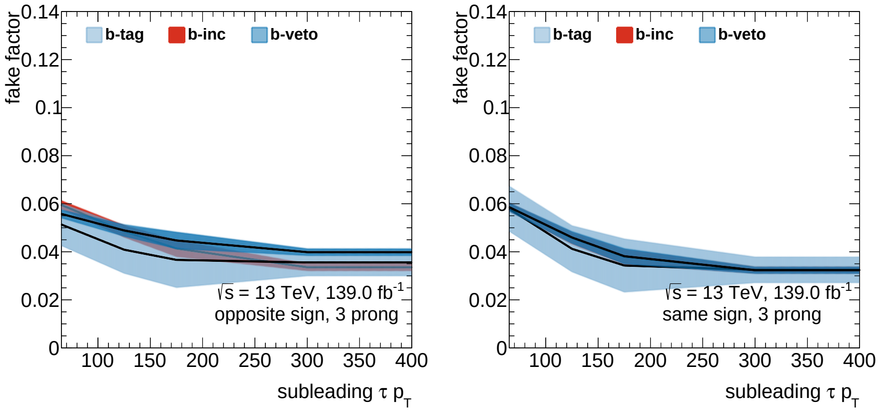

(c) Loose-not-med 3-prong OS **(d)** Loose-not-med 3-prong SS

Figure B.2.: Comparison of BINC FF to BTAG and BVETO FFs. The loose-not-med. FFs of 1-prong (top) and 3-prong (bottom) for signal region (left) and validation region (right) are shown. The loose-not-med. FFs of 2-prong are not used in this analysis.

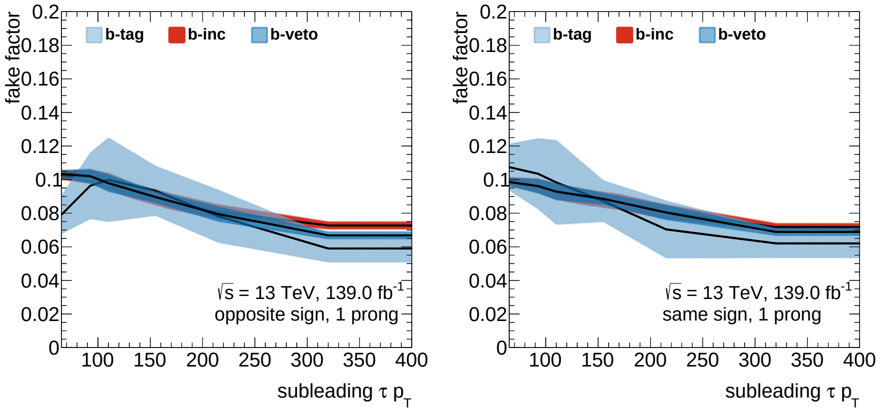

(a) Med-not-tight 1-prong OS **(b)** Med-not-tight 1-prong SS

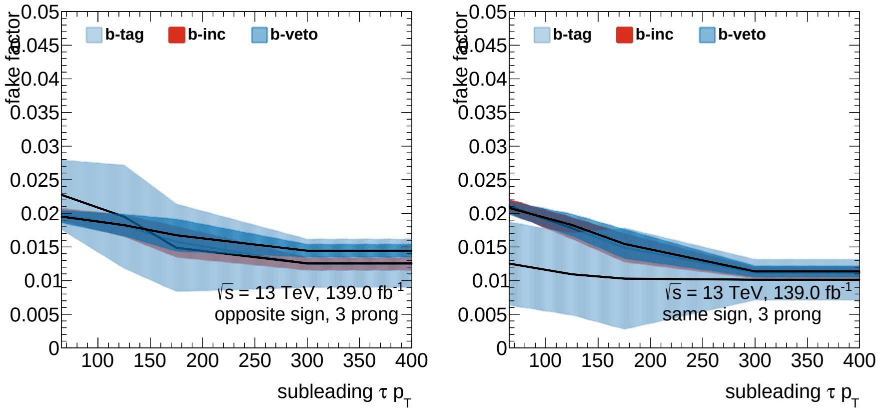

(c) Med-not-tight 3-prong OS **(d)** Med-not-tight 3-prong SS

Figure B.3.: Comparison of BINC FF to BTAG and BVETO FFs. The med-not-tight FFs of 1-prong (top) and 3-prong (bottom) for signal region (left) and validation region (right) are shown. The med.-not-tight FFs of 2-prong are not used in this analysis.

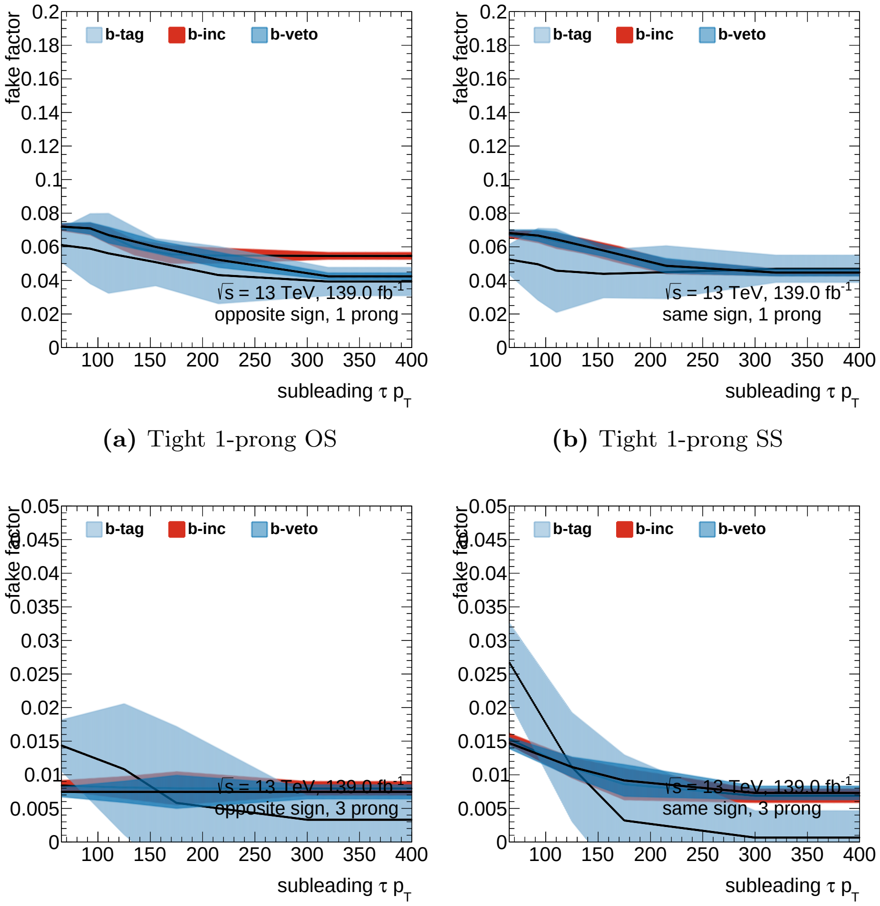

(a) Tight 1-prong OS **(b)** Tight 1-prong SS

(c) Tight 3-prong OS **(d)** Tight 3-prong SS

Figure B.4.: Comparison of BINC FF to BTAG and BVETO FFs. The tight FFs of 1-prong (top) and 3-prong (bottom) for signal region (left) and validation region (right) are shown. The tight FFs of 2-prong are not used in this analysis.

C Fake Rate

The other data-driven method applied in this analysis is called as fake rate method. They are used to measure the misidentified rate of jet based on tau ID. Considering the different fake rates for quark- and gluon-initiated jets, the fake rates are measured in top and W control regions, respectively. Like the fake factor measurement, the fake rate is separated to 1-prong, 2-prong and 3-prong, as well as OS and SS region. An additional tau ID working points (medium + trigger) is also investigated for fake rate of the leading tau candidate which is used to match to STT in this analysis Due to the statistical limitations of data for the tighter ID criteria, some bins for fake rate calculation emerge zero event which is considered to present the incorrect fake rate. In that case, the Monte Carlo fake rates validated in $\mu\nu$+jets control region is exploited.

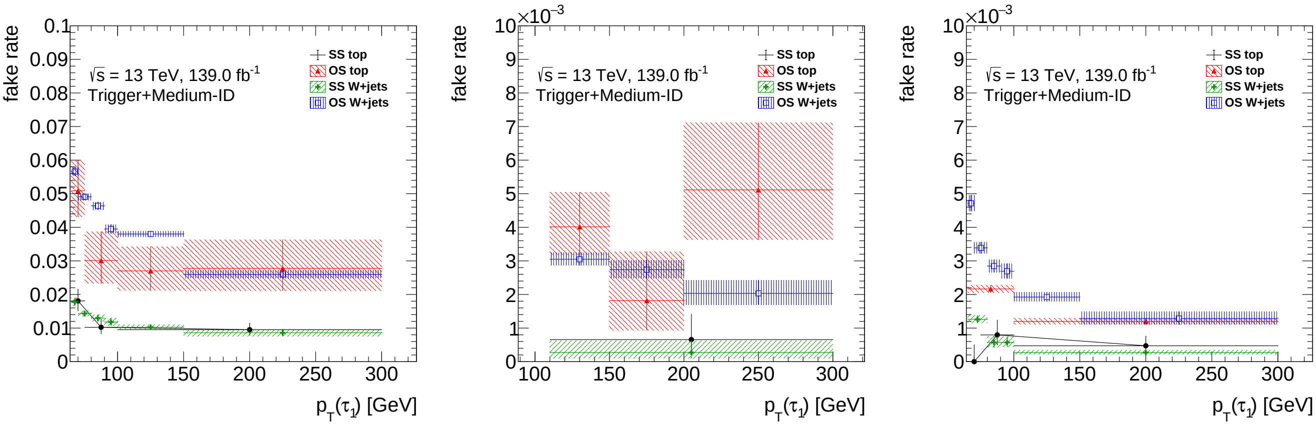

(a) Med+trigger 1-prong

(b) Med+trigger 2-prong

(c) Med+trigger 3-prong

Figure C.1.: The fake rates for leading τ_{had} passing trigger + medium tau ID working point in this analysis.

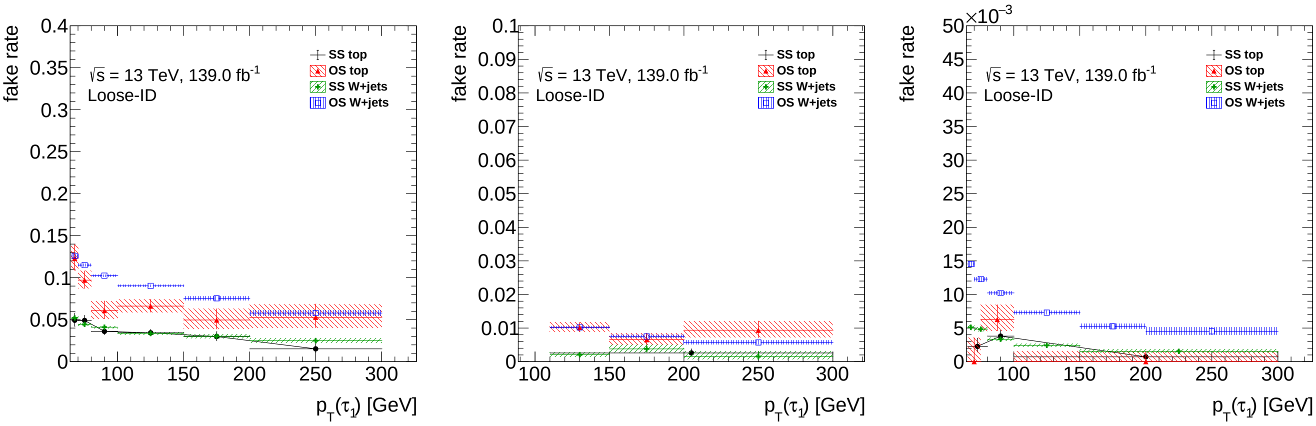

(a) Loose 1-prong **(b)** Loose 2-prong **(c)** Loose 3-prong

Figure C.2.: The fake rates for sub-leading $\tau_{\rm had}$ passing loose tau ID working point in BTAG and P2 categories.

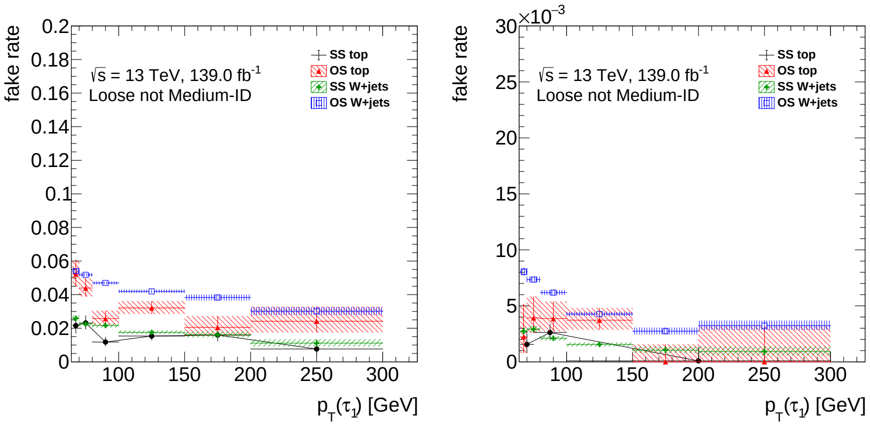

(a) Med+trigger 1-prong

(b) Med+trigger 3-prong

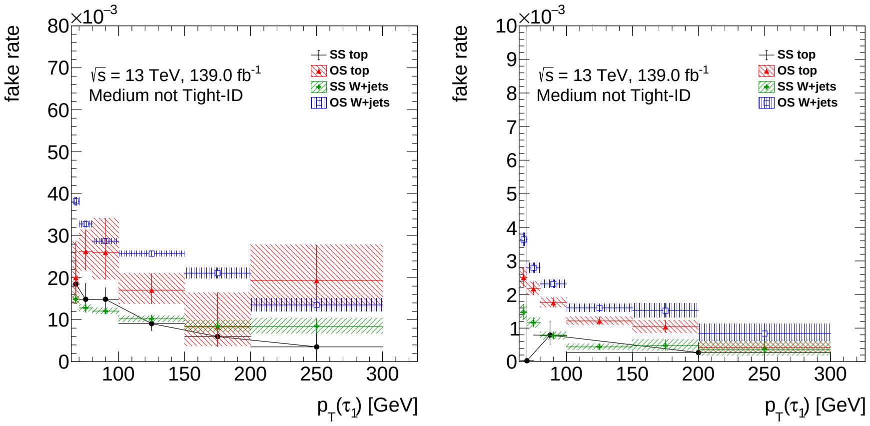

(c) Med+trigger 1-prong

(d) Med+trigger 3-prong

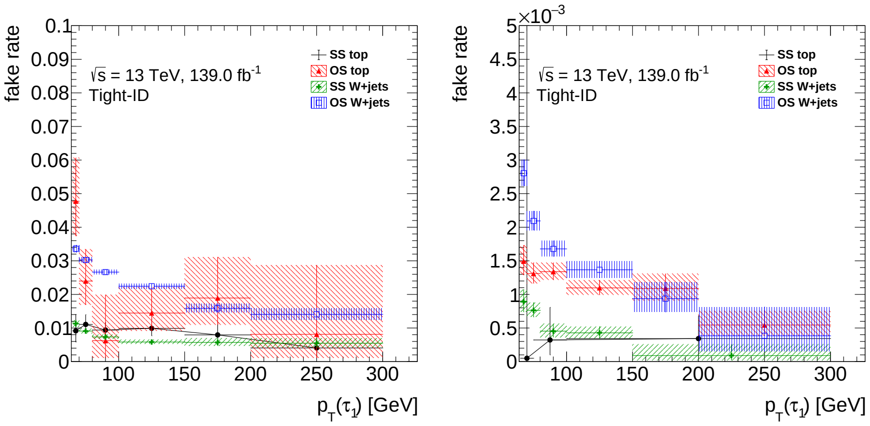

(e) Med+trigger 1-prong

(f) Med+trigger 3-prong

Figure C.3.: The fake rates for sub-leading τ_{had} passing loose-not-med.(top), med-not-tight(middle) and tight(bottom) tau ID working point in BVETO category.

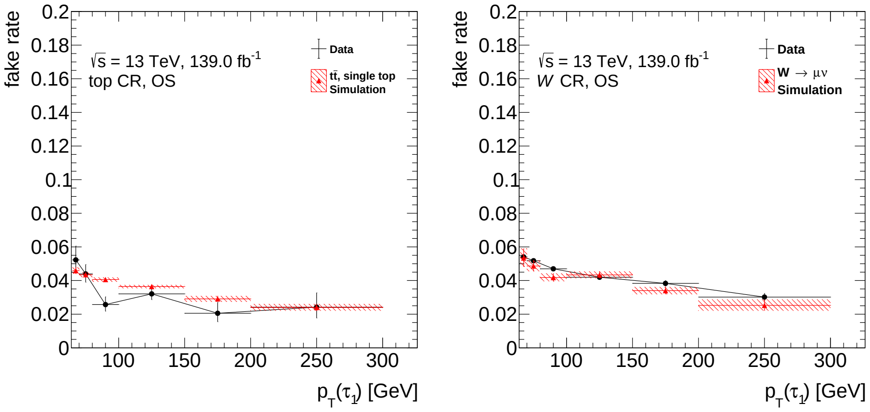

(a) Loose-not-med TCR OS 1-prong **(b)** Loose-not-med WCR OS 1-prong

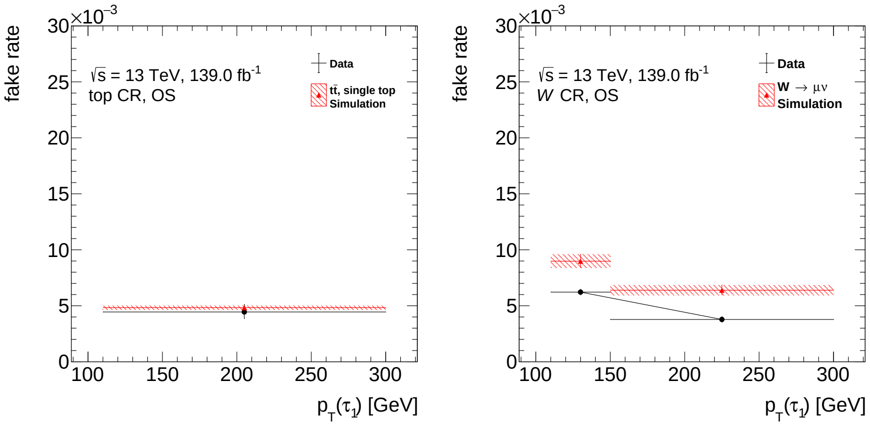

(c) Loose-not-med TCR OS 2-prong **(d)** Loose-not-med WCR OS 2-prong

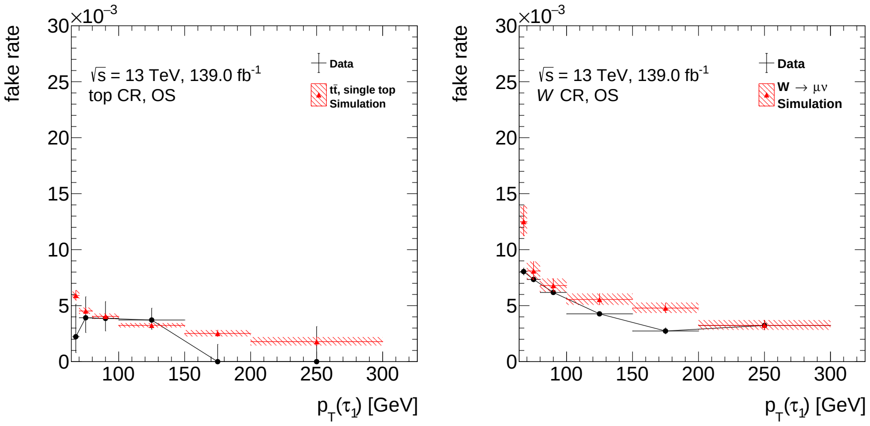

(e) Loose-not-med TCR OS 3-prong **(f)** Loose-not-med WCR OS 3-prong

Figure C.4.: Comparison of data FR to MC FRs. The loose-not-med. FRs of 1-prong (top), 2-prong (middle) and 3-prong (bottom) in top control region (left) and W control region (right) are shown. The loose-not-med. FRs of 2-prong are not used in this analysis.

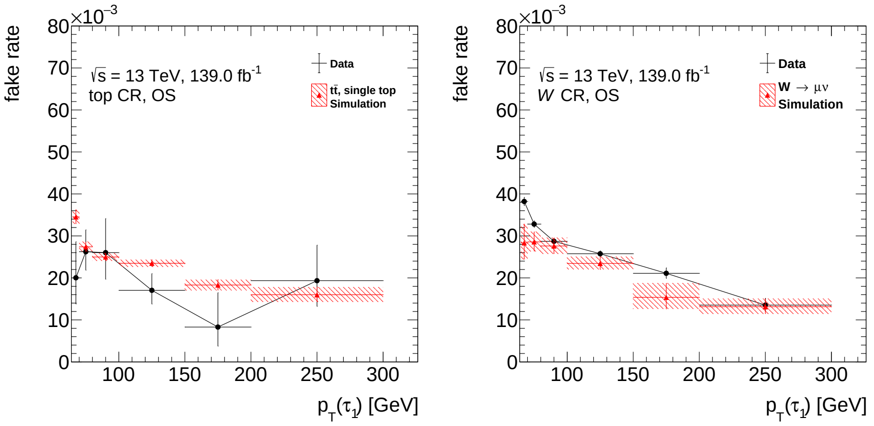

(a) Med-not-tight TCR OS 1-prong **(b)** Med-not-tight WCR OS 1-prong

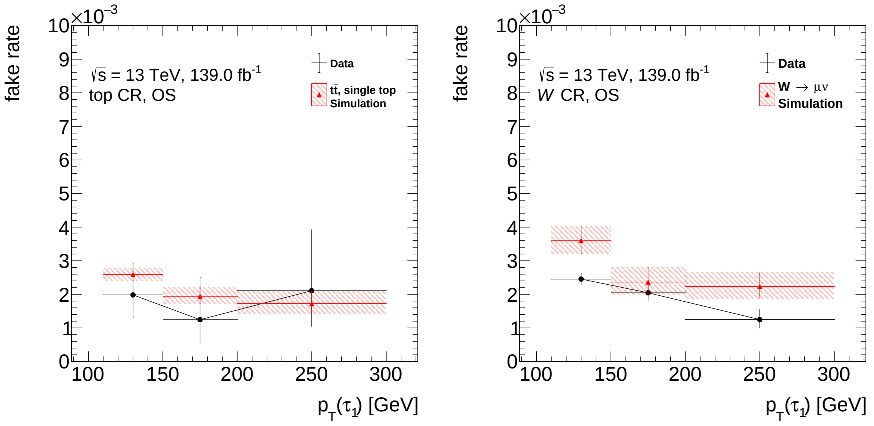

(c) Med-not-tight TCR OS 2-prong **(d)** Med-not-tight WCR OS 2-prong

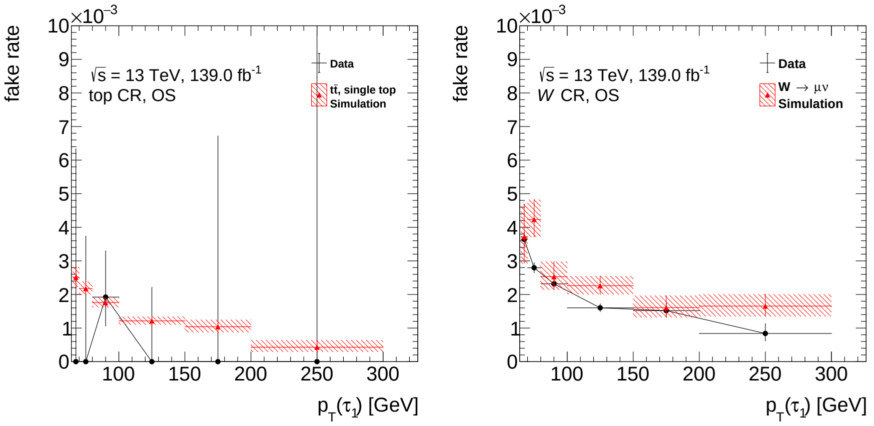

(e) Med-not-tight TCR OS 3-prong **(f)** Med-not-tight WCR OS 3-prong

Figure C.5.: Comparison of data FR to MC FRs. The med-not-tight FRs of 1-prong (top), 2-prong (middle) and 3-prong (bottom) in top control region (left) and W control region (right) are shown. The med-not-tight FRs of 2-prong are not used in this analysis.

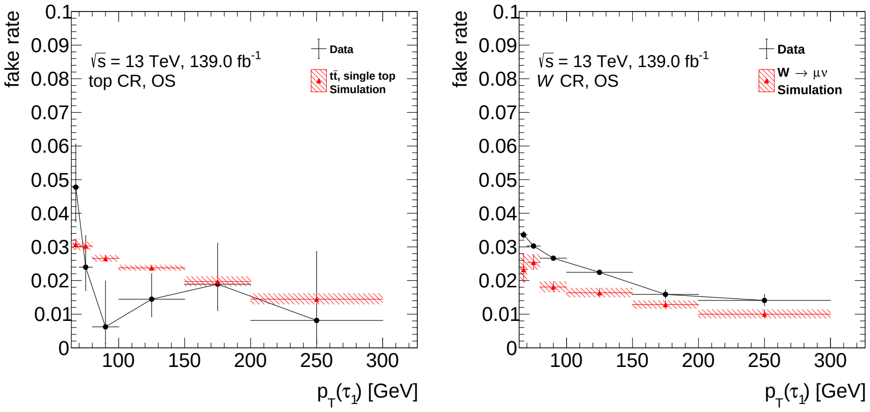

(a) Tight TCR OS 1-prong **(b)** Tight WCR OS 1-prong

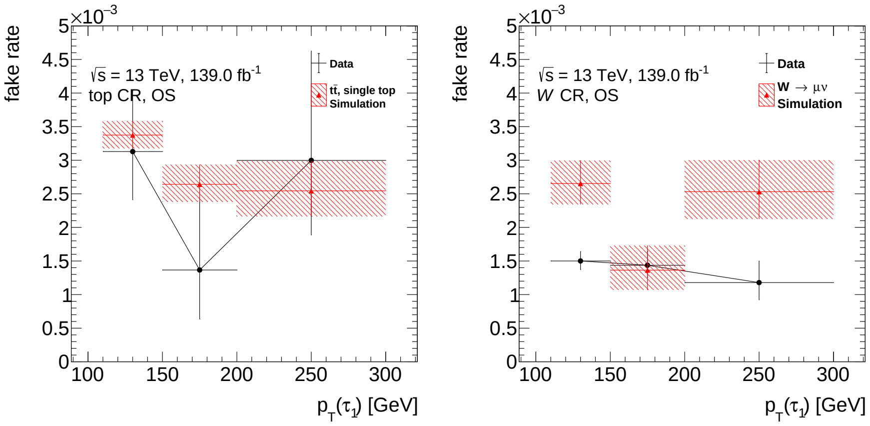

(c) Tight TCR OS 2-prong **(d)** Tight WCR OS 2-prong

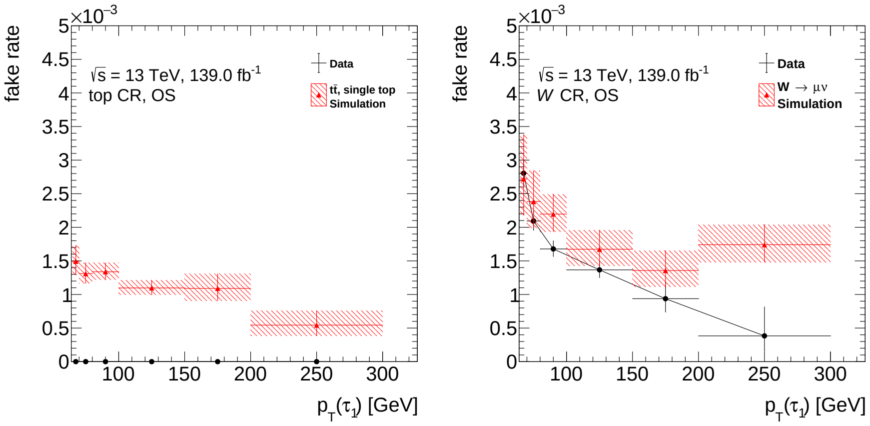

(e) Tight TCR OS 3-prong **(f)** Tight WCR OS 3-prong

Figure C.6.: Comparison of data FR to MC FRs. The tight FRs of 1-prong (top), 2-prong (middle) and 3-prong (bottom) in top control region (left) and W control region (right) are shown. The tight FRs of 2-prong are not used in this analysis.

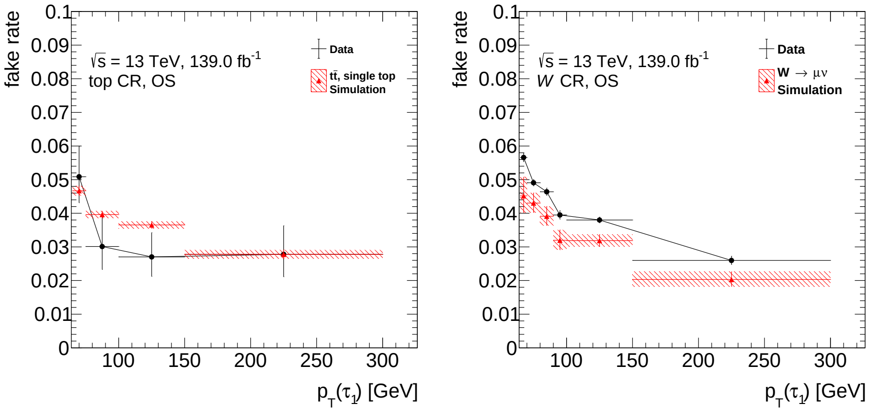

(a) Med+trigger TCR OS 1-prong **(b)** Med+trigger WCR OS 1-prong

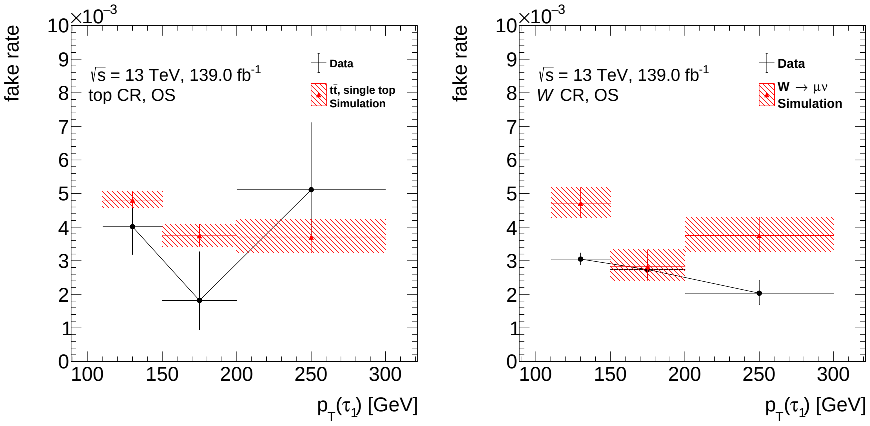

(c) Med+trigger TCR OS 2-prong **(d)** Med+trigger WCR OS 2-prong

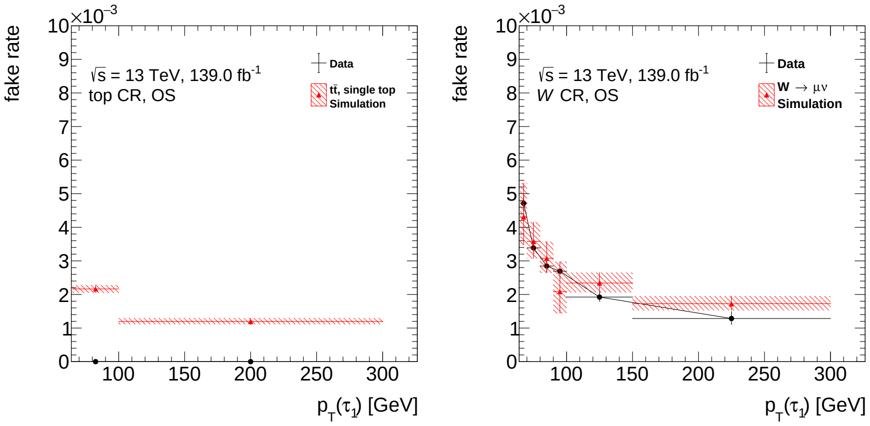

(e) Med+trigger TCR OS 3-prong **(f)** Med+trigger WCR OS 3-prong

Figure C.7.: Comparison of data FR to MC FRs. The medium + tau trigger FRs of 1-prong (top), 2-prong (middle) and 3-prong (bottom) in top control region (left) and W control region (right) are shown. The medium + tau trigger FRs of 2-prong are not used in this analysis.

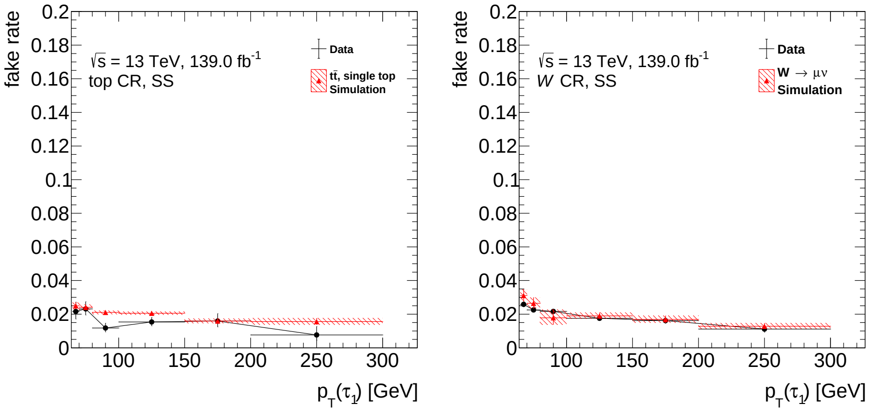

(a) Loose-not-med TCR SS 1-prong **(b)** Loose-not-med WCR SS 1-prong

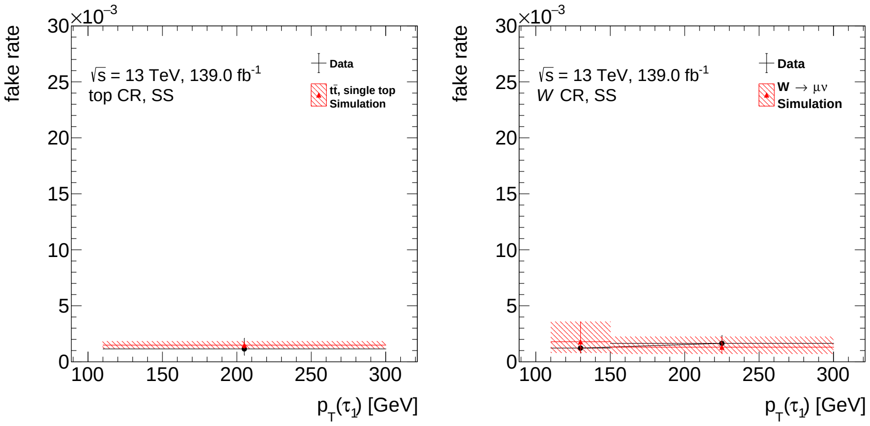

(c) Loose-not-med TCR SS 2-prong **(d)** Loose-not-med WCR SS 2-prong

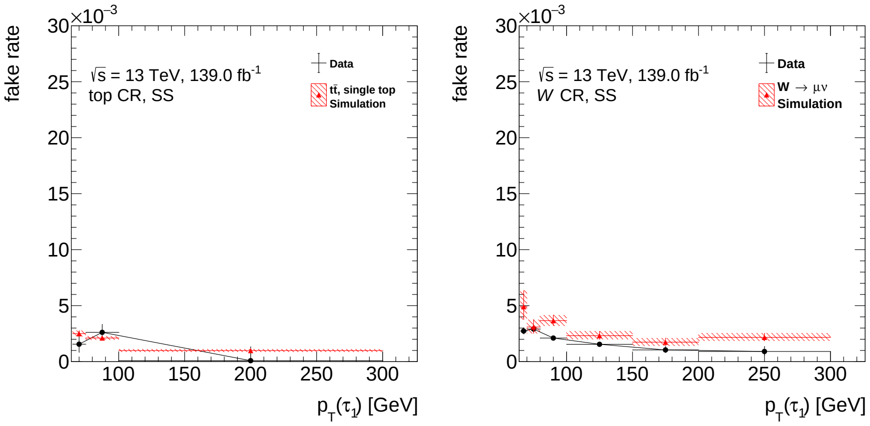

(e) Loose-not-med TCR SS 3-prong **(f)** Loose-not-med WCR SS 3-prong

Figure C.8.: Comparison of data FR to MC FRs. The loose-not-med. FRs of 1-prong (top), 2-prong (middle) and 3-prong (bottom) in top control region (left) and W control region (right) are shown. The loose-not-med. FRs of 2-prong are not used in this analysis.

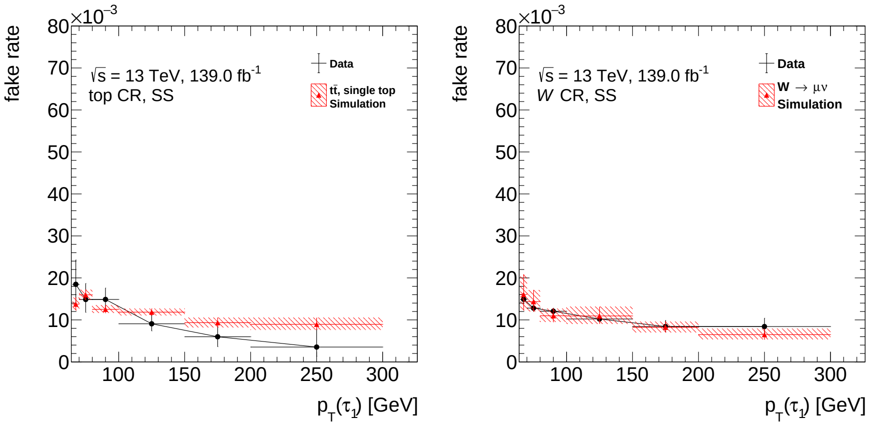

(a) Med-not-tight TCR SS 1-prong **(b)** Med-not-tight WCR SS 1-prong

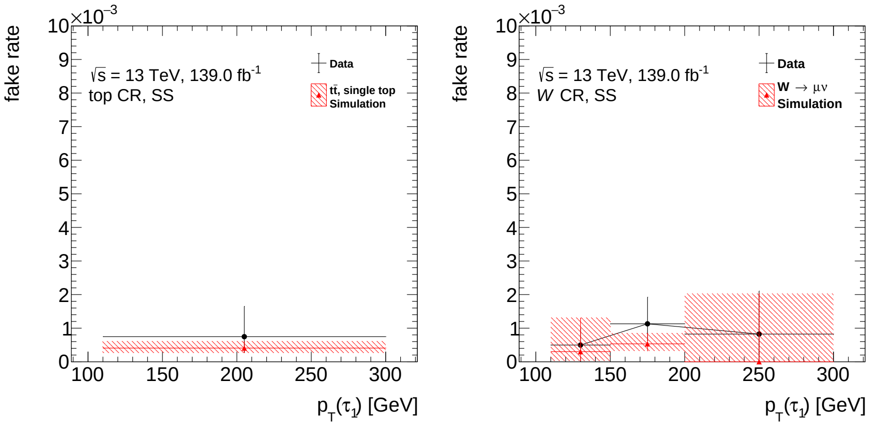

(c) Med-not-tight TCR SS 2-prong **(d)** Med-not-tight WCR SS 2-prong

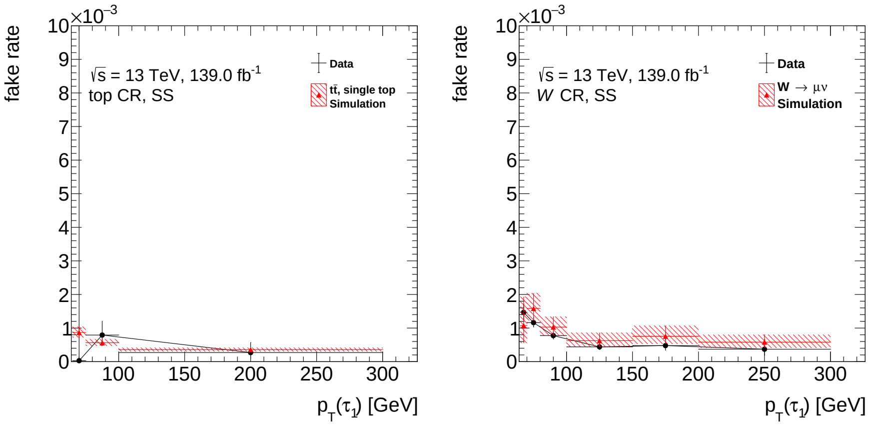

(e) Med-not-tight TCR SS 3-prong **(f)** Med-not-tight WCR SS 3-prong

Figure C.9.: Comparison of data FR to MC FRs. The med-not-tight FRs of 1-prong (top), 2-prong (middle) and 3-prong (bottom) in top control region (left) and W control region (right) are shown. The med-not-tight FRs of 2-prong are not used in this analysis.

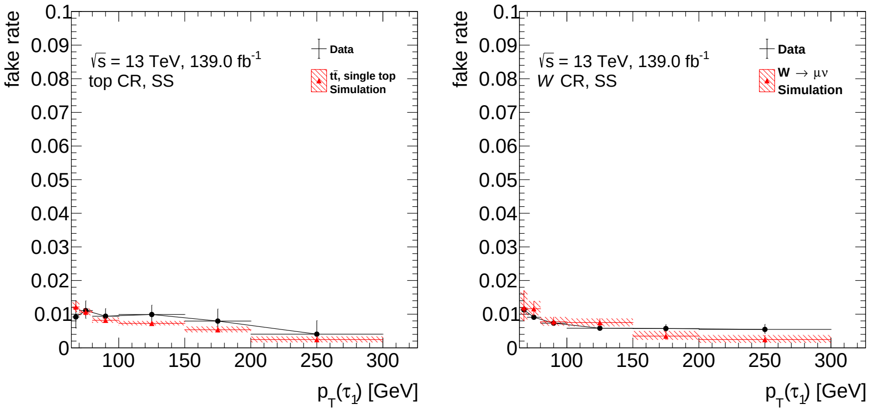

(a) Tight TCR SS 1-prong **(b)** Tight WCR SS 1-prong

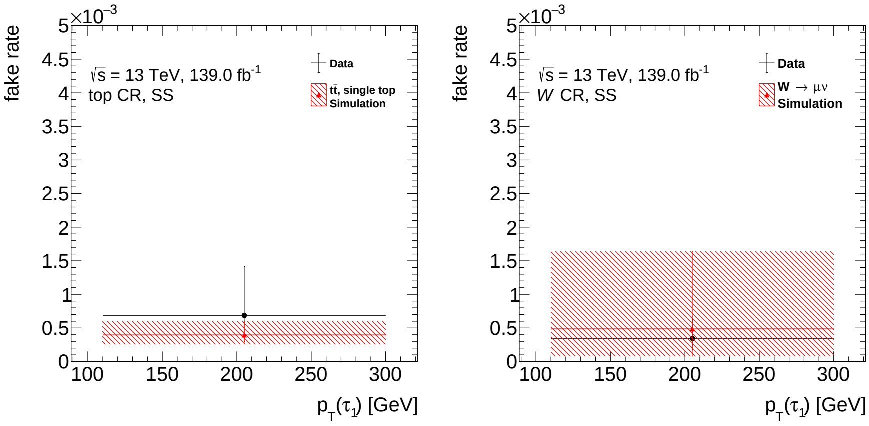

(c) Tight TCR SS 2-prong **(d)** Tight WCR SS 2-prong

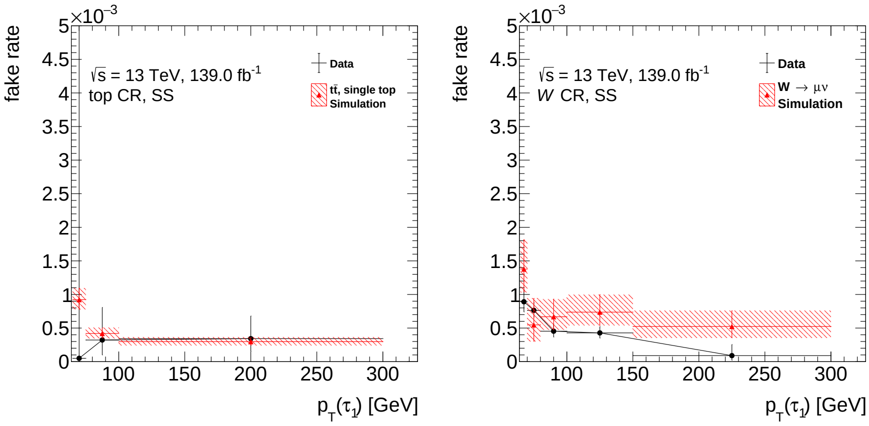

(e) Tight TCR SS 3-prong **(f)** Tight WCR SS 3-prong

Figure C.10.: Comparison of data FR to MC FRs. The tight FRs of 1-prong (top), 2-prong (middle) and 3-prong (bottom) in top control region (left) and W control region (right) are shown. The tight FRs of 2-prong are not used in this analysis.

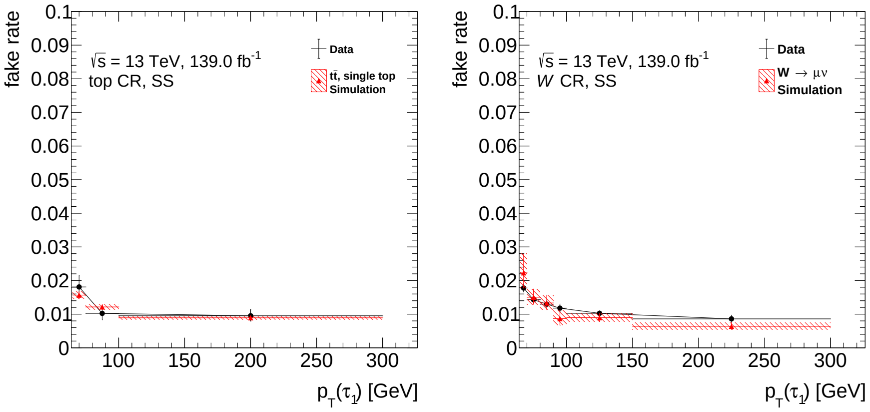

(a) Med+trigger TCR SS 1-prong **(b)** Med+trigger WCR SS 1-prong

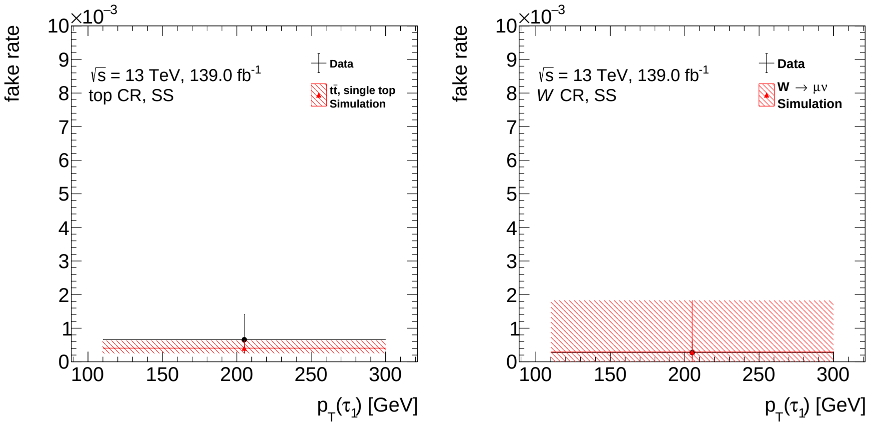

(c) Med+trigger TCR SS 2-prong **(d)** Med+trigger WCR SS 2-prong

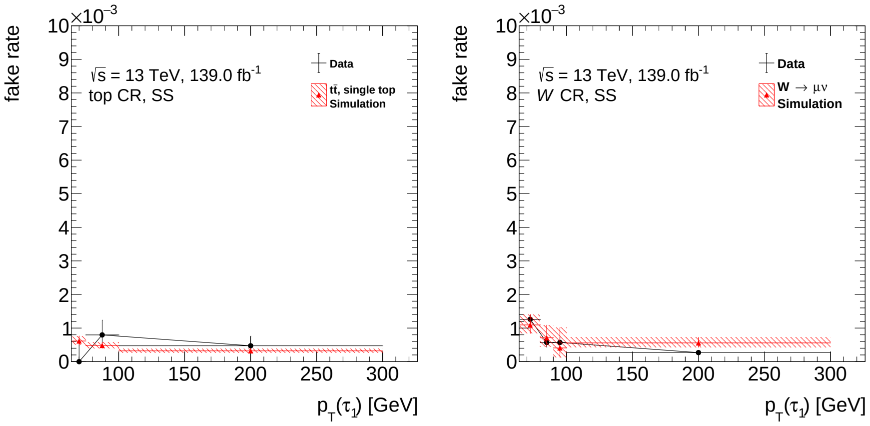

(e) Med+trigger TCR SS 3-prong **(f)** Med+trigger WCR SS 3-prong

Figure C.11.: Comparison of data FR to MC FRs. The medium + tau trigger FRs of 1-prong (top), 2-prong (middle) and 3-prong (bottom) in top control region (left) and W control region (right) are shown. The medium + tau trigger FRs of 2-prong are not used in this analysis.

D Distribution in SS Validation Region and OS Signal Region

The distributions of the different varaibles are shown in following plots in the signal region (OS) and validation region (SS). The agreement between MC and data is investigated with these variable comparison in each validation region of the categorization.

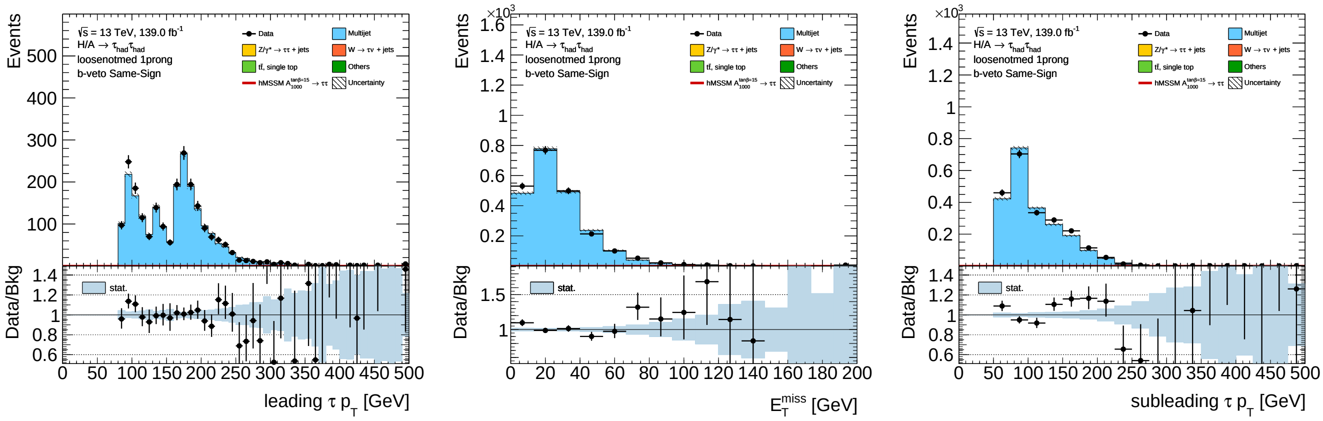

(a) loosenotmed 1-prong 1st tau p_T **(b)** loosenotmed 1-prong met **(c)** loosenotmed 1-prong 2nd tau p_T

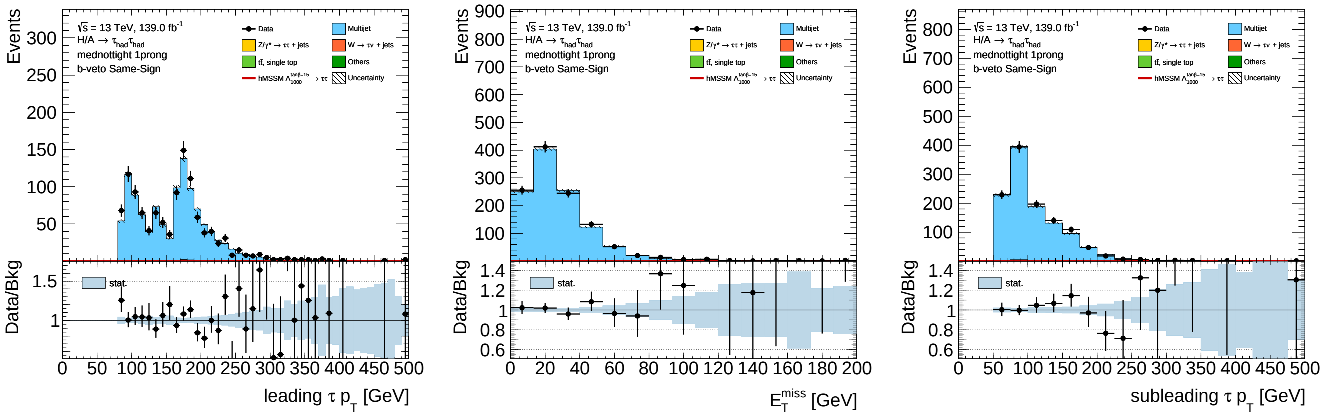

(d) mednottight 1-prong 1st tau p_T **(e)** mednottight 1-prong met **(f)** mednottight 1prong 2nd tau p_T

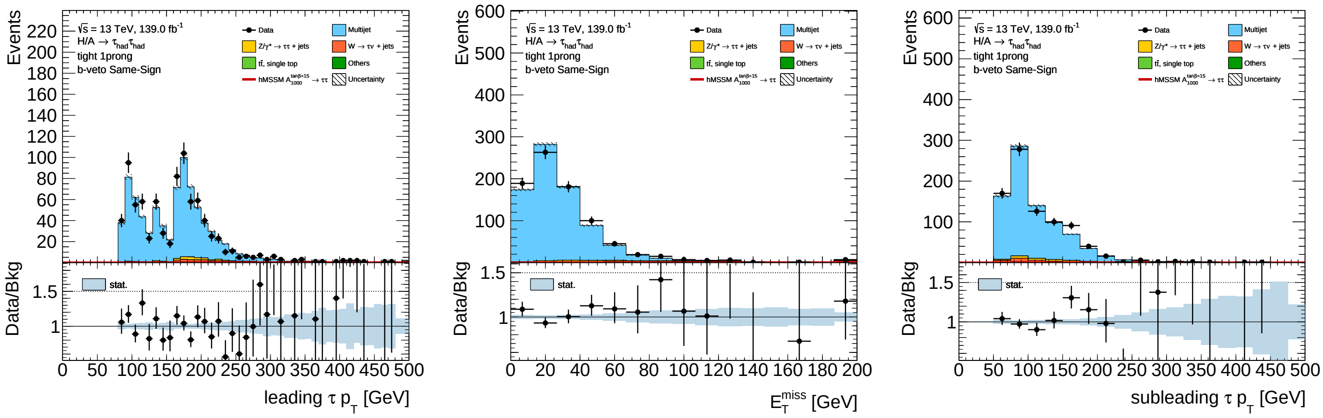

(g) tight 1-prong 1st tau p_T **(h)** tight 1-prong met **(i)** tight 1-prong 2nd tau p_T

Figure D.1.: The distribution of 1st tau p_T, met and 2nd tau p_T for BVETO SS validation region.

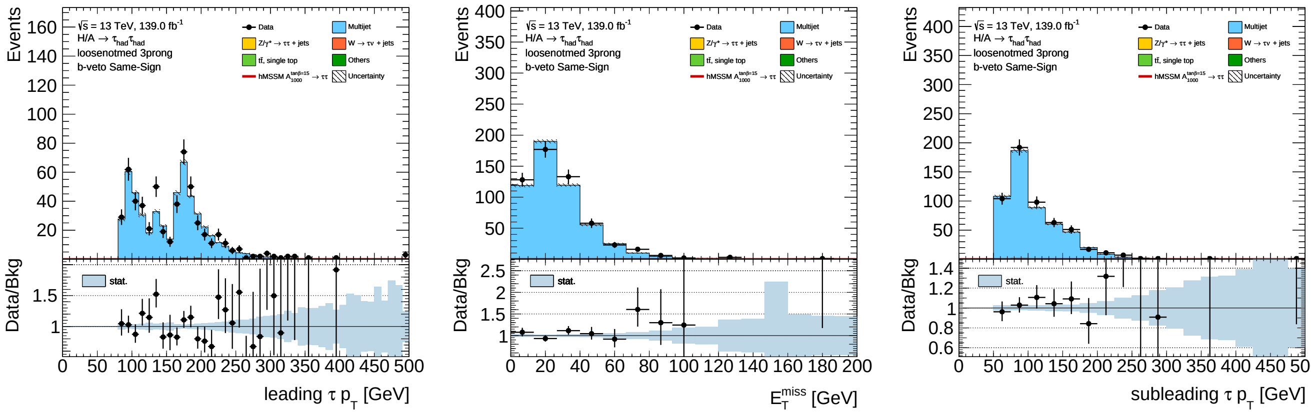

(a) loosenotmed 3-prong 1st tau p_{T} **(b)** loosenotmed 3-prong met **(c)** loosenotmed 3-prong 2nd tau p_{T}

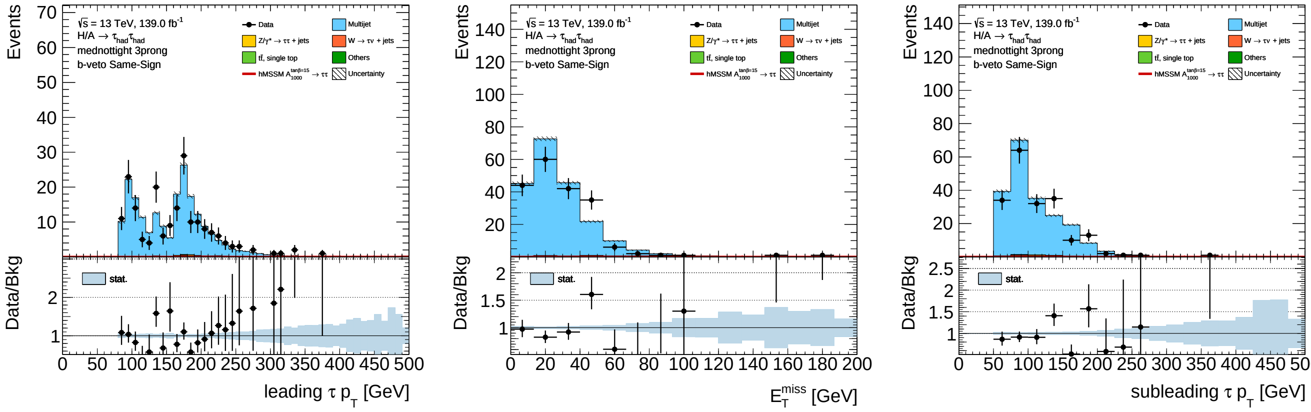

(d) mednottight 3-prong 1st tau p_{T} **(e)** mednottight 3-prong met **(f)** mednottight 3-prong 2nd tau p_{T}

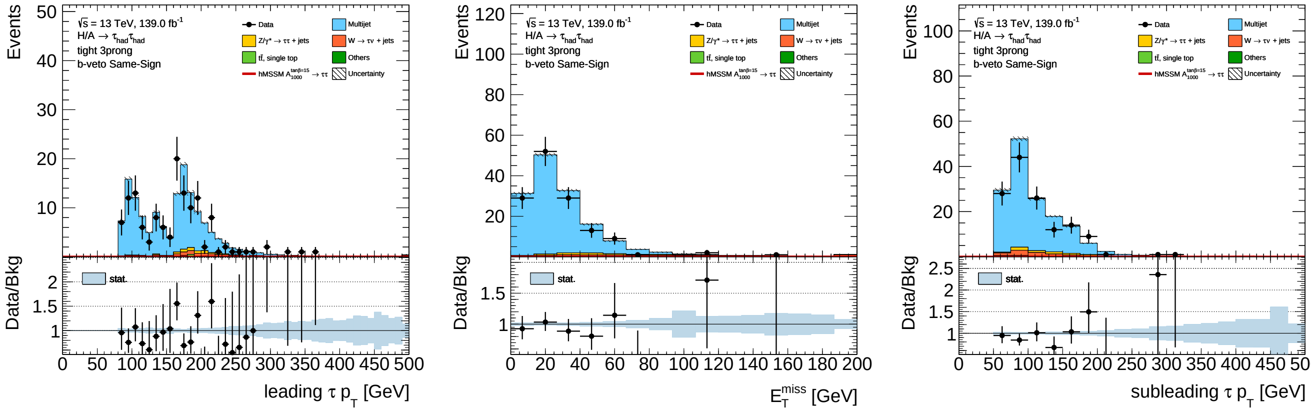

(g) tight 3-prong 1st tau p_{T} **(h)** tight 3-prong met **(i)** tight 3-prong 2nd tau p_{T}

Figure D.2.: The distribution of 1st tau p_{T}, met and 2nd tau p_{T} for BVETO SS validation region.

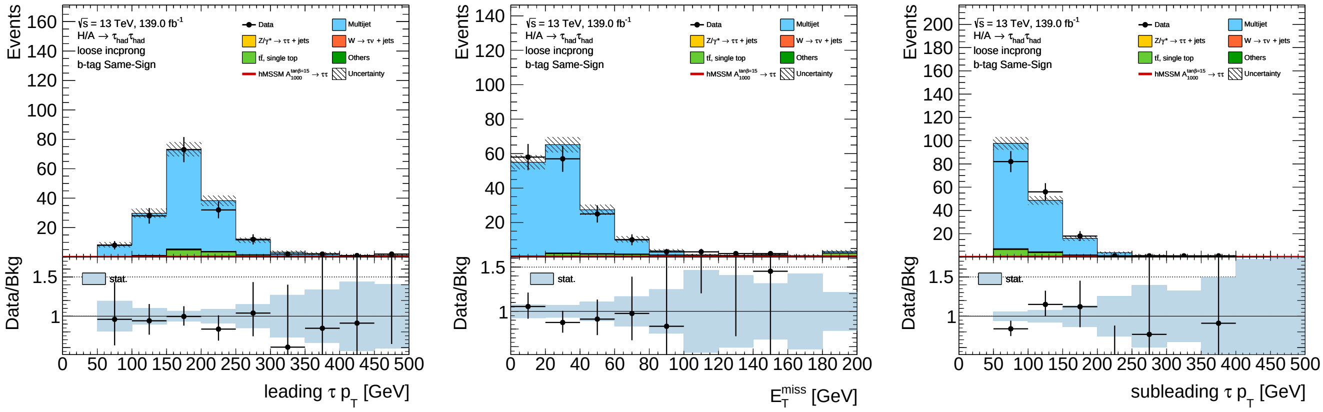

(a) loose 1st tau p_{T} **(b)** loose met **(c)** loose 2nd tau p_{T}

Figure D.3.: The distribution of 1st tau p_{T}, met and 2nd tau p_{T} for BTAG SS validation region.

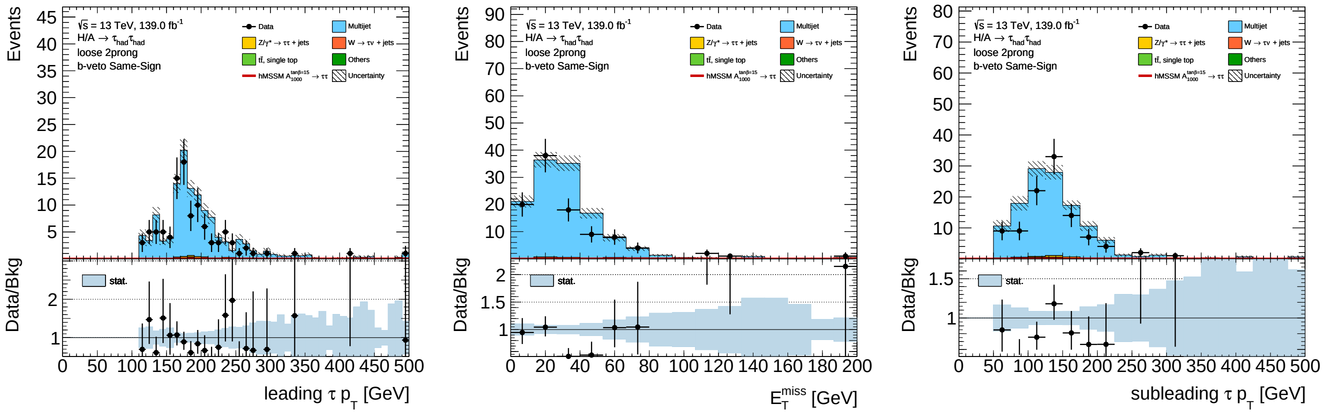

(a) loose 1st tau p_{T} **(b)** loose met **(c)** loose 2nd tau p_{T}

Figure D.4.: The distribution of 1st tau p_{T}, met and 2nd tau p_{T} for 2P validation region.

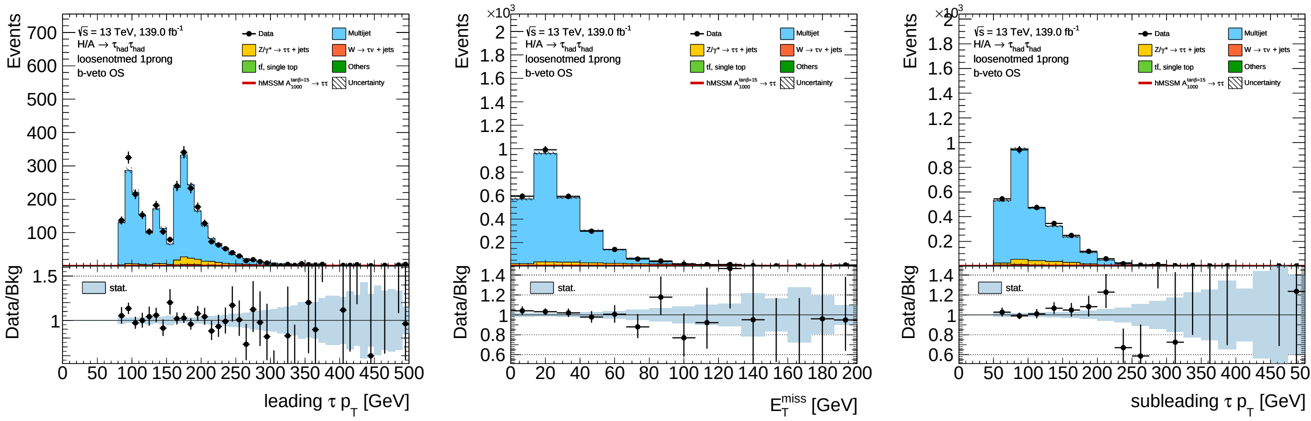

(a) loosenotmed 1-prong 1st tau p_T **(b)** loosenotmed 1-prong met **(c)** loosenotmed 1-prong 2nd tau p_T

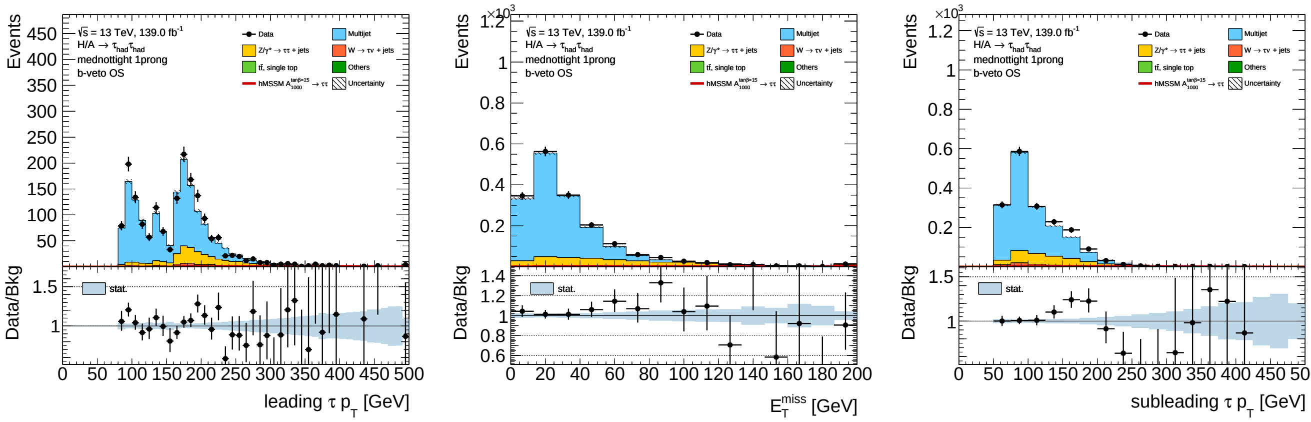

(d) mednottight 1-prong 1st tau p_T **(e)** mednottight 1-prong met **(f)** mednottight 1prong 2nd tau p_T

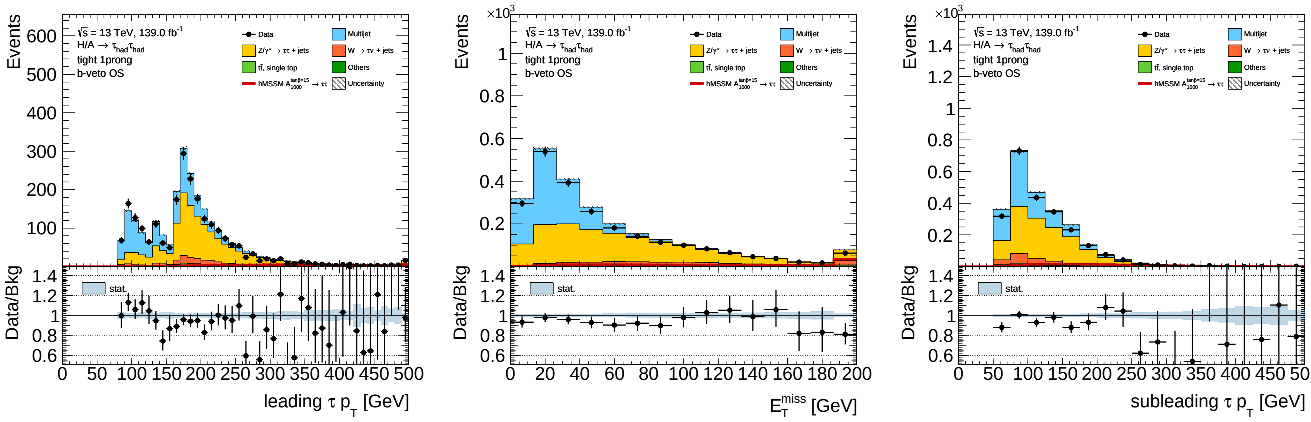

(g) tight 1-prong 1st tau p_T **(h)** tight 1-prong met **(i)** tight 1-prong 2nd tau p_T

Figure D.5.: The distribution of 1st tau p_T, met and 2nd tau p_T for BVETO OS signal region.

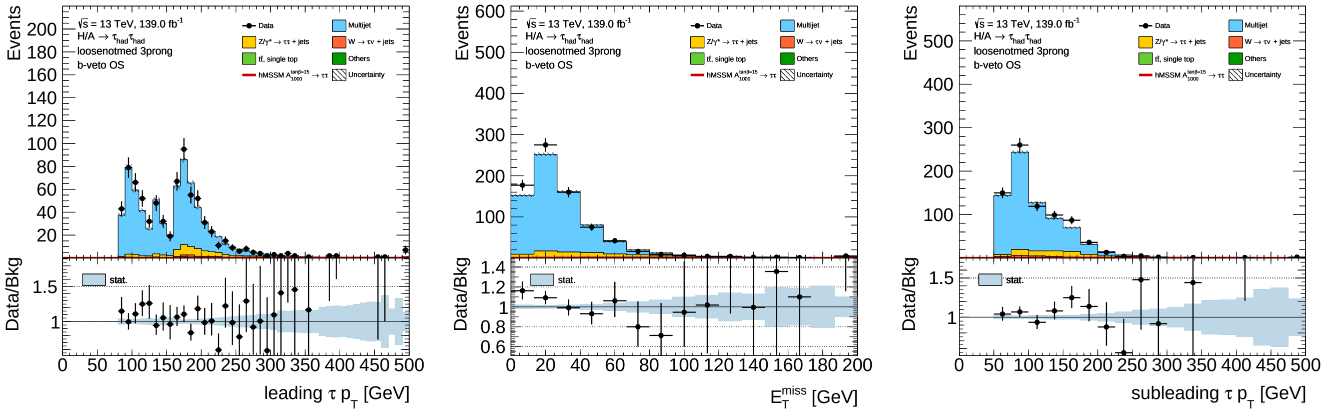

(a) loosenotmed 3-prong 1st tau p_{T} **(b)** loosenotmed 3-prong met **(c)** loosenotmed 3-prong 2nd tau p_{T}

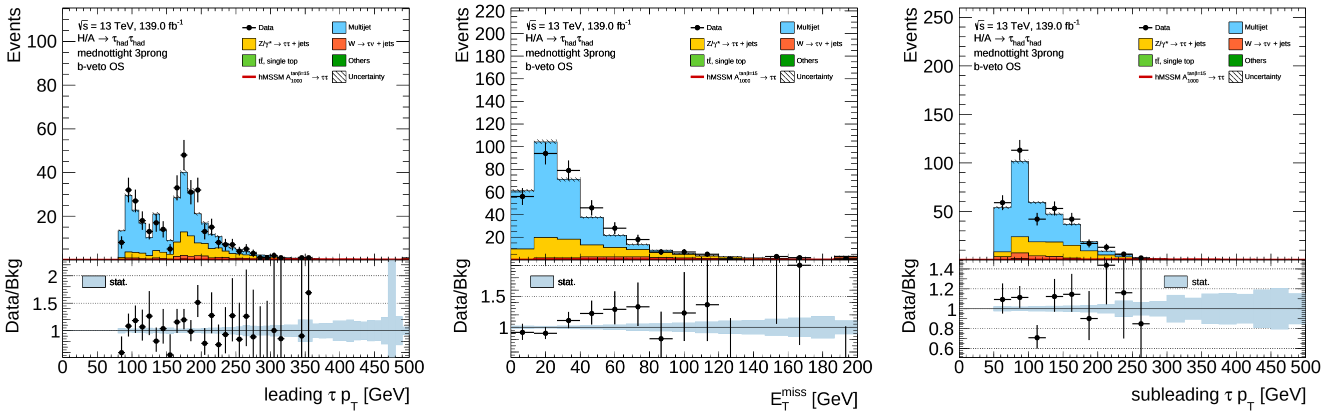

(d) mednottight 3-prong 1st tau p_{T} **(e)** mednottight 3-prong met **(f)** mednottight 3-prong 2nd tau p_{T}

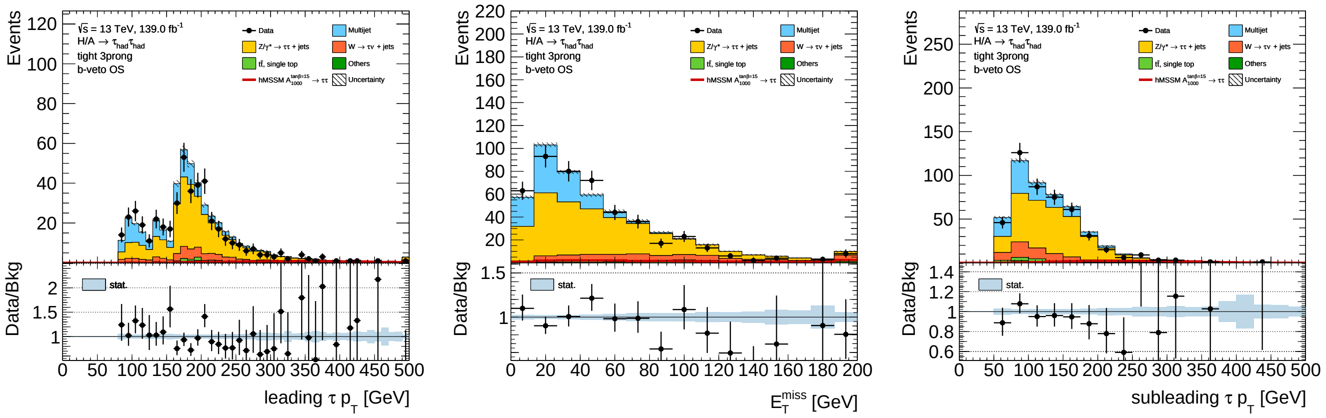

(g) tight 3-prong 1st tau p_{T} **(h)** tight 3-prong met **(i)** tight 3-prong 2nd tau p_{T}

Figure D.6.: The distribution of 1st tau p_{T}, met and 2nd tau p_{T} for BVETO OS signal region.

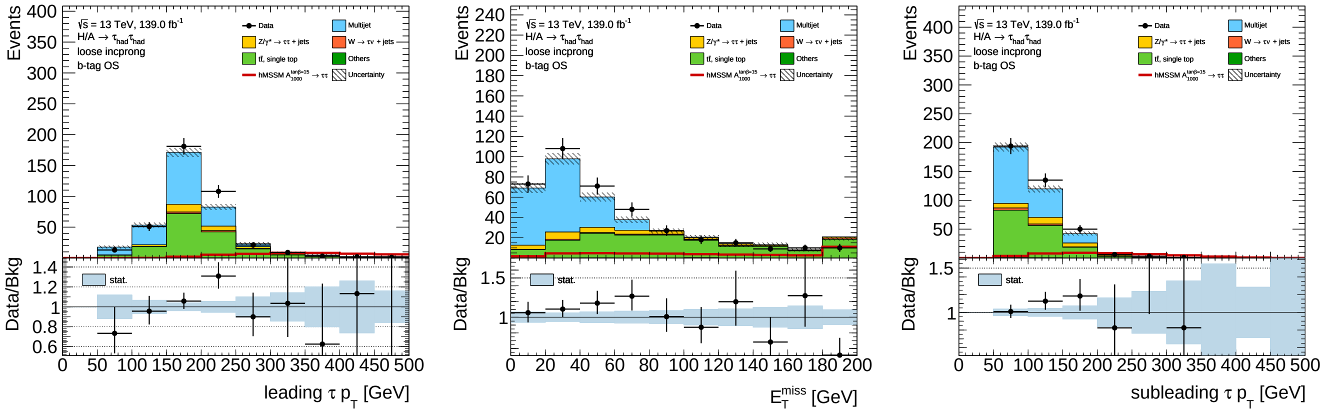

(a) loose 1st tau p_{T} **(b)** loose met **(c)** loose 2nd tau p_{T}

Figure D.7.: The distribution of 1st tau p_{T}, met and 2nd tau p_{T} for BTAG OS signal region.

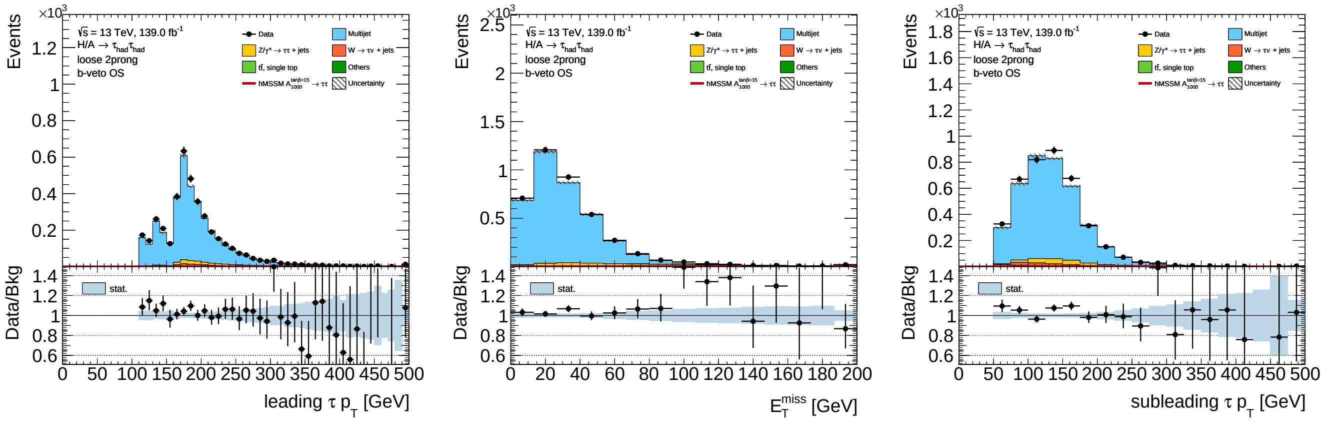

(a) loose 1st tau p_{T} **(b)** loose met **(c)** loose 2nd tau p_{T}

Figure D.8.: The distribution of 1st tau p_{T}, met and 2nd tau p_{T} for 2P signal region.

E QCD Background Estimation in the Di-jet Control Region

The di-jet control region is very pure in QCD with negligible amount of background as shown in the following plots. The p_{T} distributions of sub-leading 1-prong tau in each category are presented. The W+jets and top-backgrounds are main background. Although MC background is less important in di-jet control regions, these backgrounds are subtracted for the fake factor measurement.

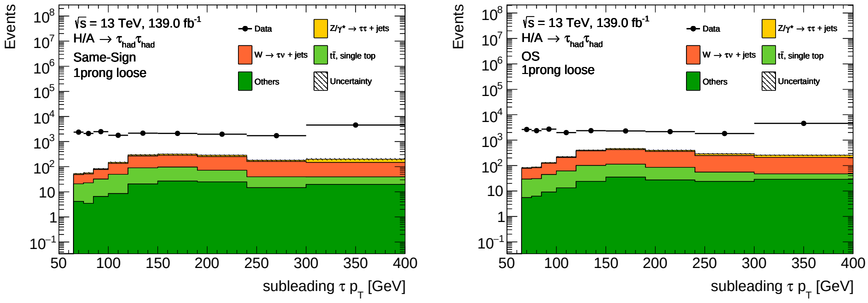

(a) loose SS **(b)** loose OS

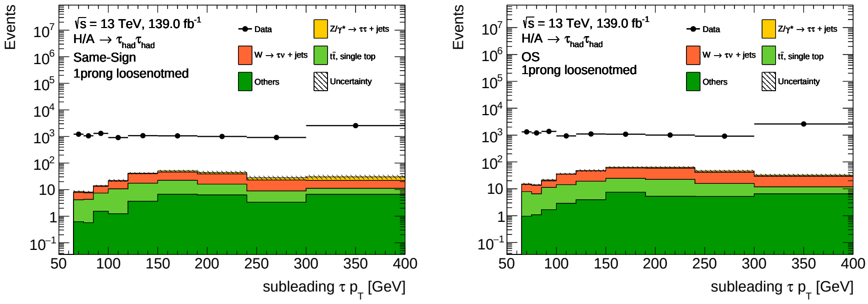

(c) loose-not-med SS **(d)** loose-not-med OS

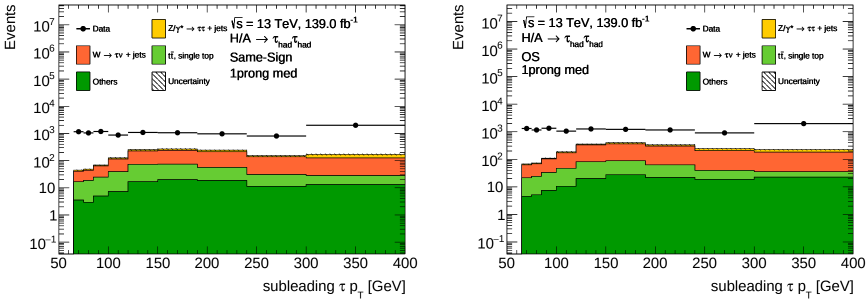

(e) medium SS **(f)** medium OS

Figure E.1.: The p_T distributions of 1-prong sub-leading tau passing “loose” (top), “loose-not-med.” (middle) and “medium” (bottom) tau identification working points for opposite sign (right) and same sign regions (left).

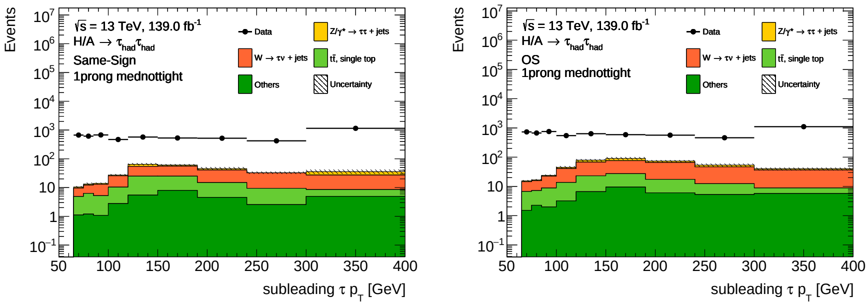

(a) med-not-tight SS

(b) med-not-tight OS

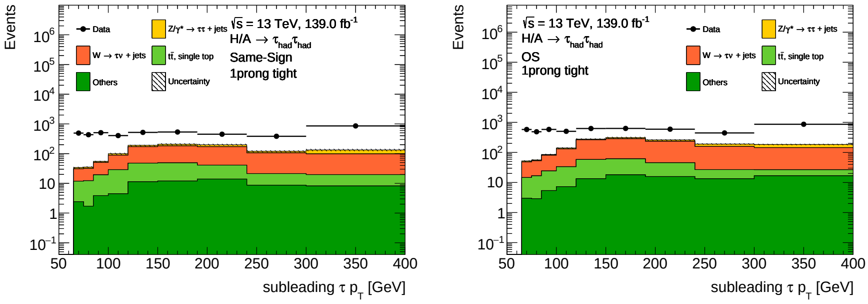

(c) tight SS

(d) tight OS

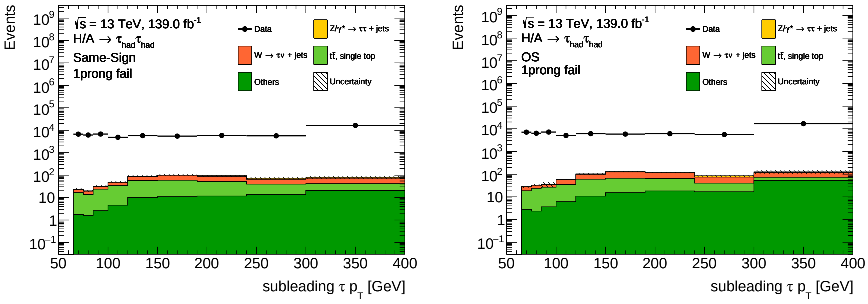

(e) fail loose SS

(f) fail loose OS

Figure E.2.: The p_{T} distributions of 1-prong sub-leading tau passing “med-not-tight” (top) and “tight” (middle) tau identification working points for opposite sign (right) and same sign regions (left). The bottom plots show the 1-prong sub-leading tau failing “loose” tau identification.

F Investigation of BDT input variables for 2-prong tau

The distribution comparison between $Z/\gamma^* \to \tau\tau$ signal and multi-jets background candidates in 3-prong τ_{had} (upper plots) and 2-prong τ_{had} (bottom plots) cases are shown in Fig. F.1, Fig. F.2 and Fig. F.3. (Detail of each variables are also described in Sec 4.5.3)

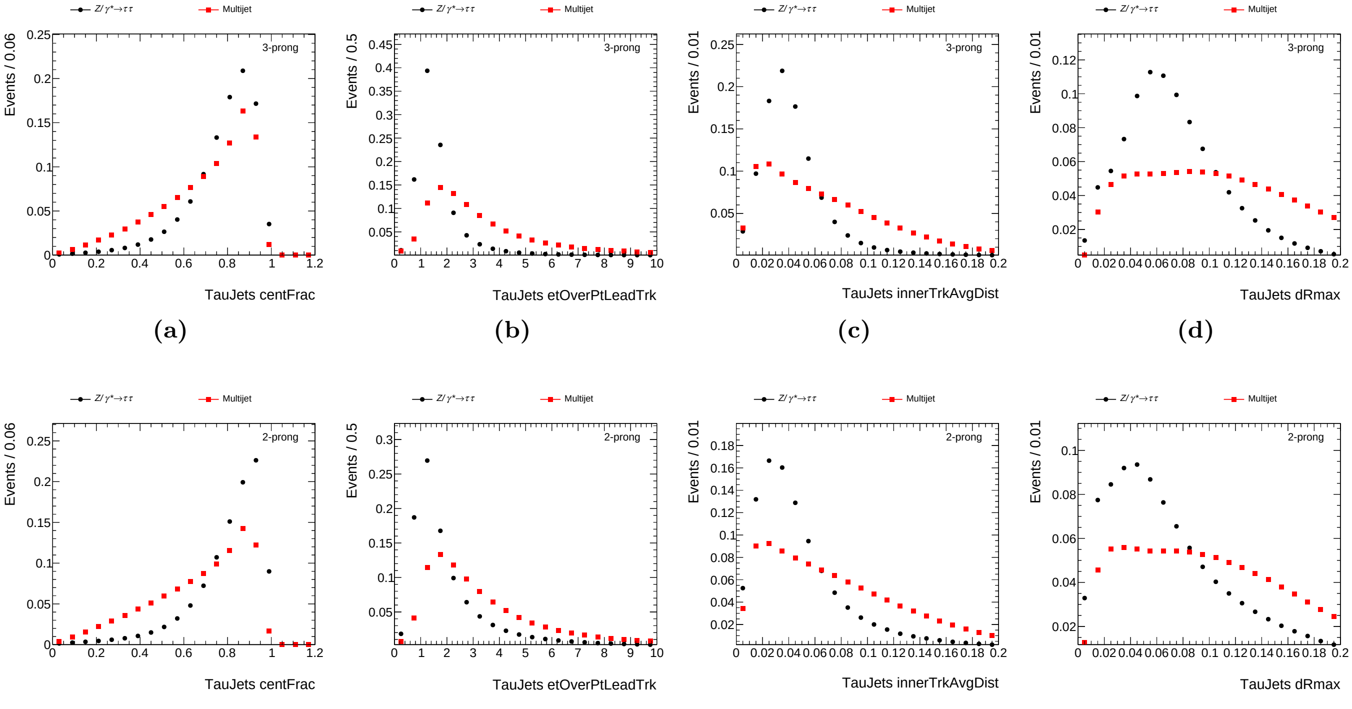

(a) (b) (c) (d)

(e) (f) (g) (h)

Figure F.1.: The $Z/\gamma^* \to \tau\tau$ signal versus multi-jets background candidates distribution of the BDT training input variables for 3-prong τ_{had} (2-prong τ_{had}) are shown in upper (bottom) plots. From left to right, it responds "central energy fraction", "leading track momentum fraction", "track radius" and "maximum ΔR".

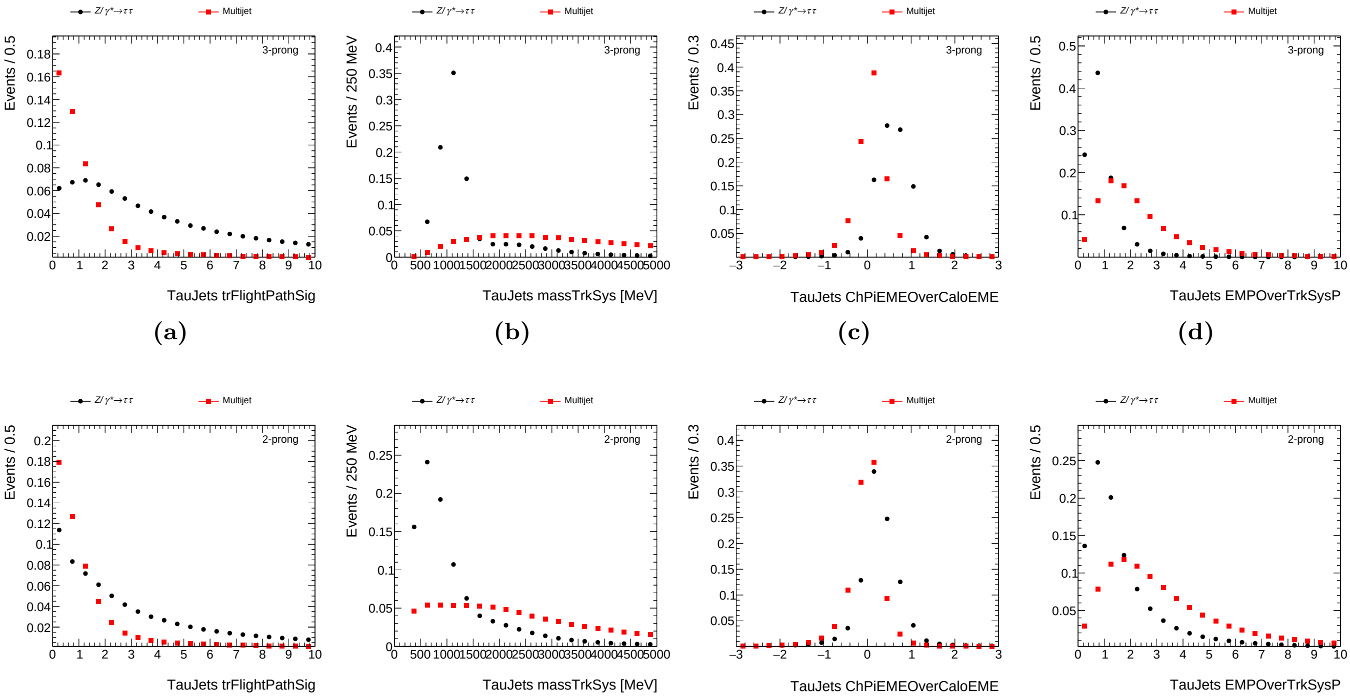

(a) (b) (c) (d)

(e) (f) (g) (h)

Figure F.2.: From left plot to right plot, it presents the distribution for ”transverse flight path significance”, ”track mass”, ”fraction of EM energy from charged pions” and ”ratio of EM energy to track momentum”. The distribution for 3-prong τ_{had} and 2-prong τ_{had} are shown in upper and bottom part, respectively.

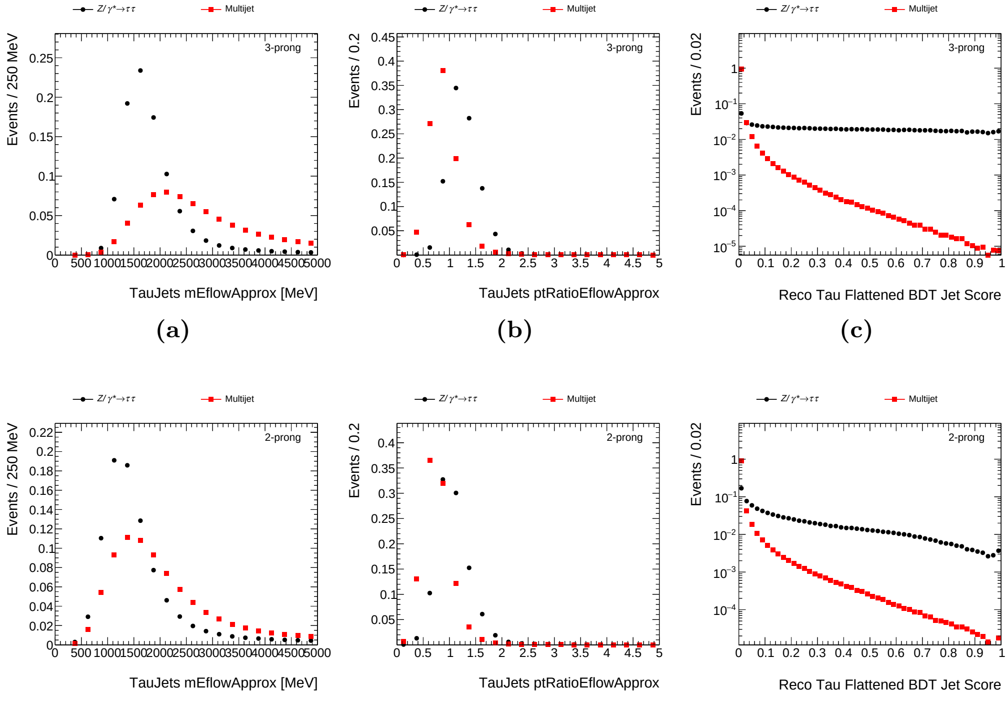

(a) **(b)** **(c)**

(d) **(e)** **(f)**

Figure F.3.: The $Z/\gamma^* \to \tau\tau$ signal versus multi-jets background candidates distribution of the BDT training input variables for 3-prong τ_{had} (2-prong τ_{had}) are shown in upper (bottom) plots. Left plot and middle plot responds "track-plus-EM-system mass" and "ratio of track-plus-EM-system to p_{T}" respectively. Two rightest plots F.3(c) and F.3(f) show the training BDT score for 3-prong τ_{had} (upper) and 2-prong τ_{had} (bottom).

Bibliography

[1] E. Bagnaschi et al., ‘Benchmark scenarios for low $\tan\beta$ in the MSSM’, tech. rep. LHCHXSWG-2015-002, CERN, 2015, URL: `http://cds.cern.ch/record/2039911`.

[2] E. Torassa, *The Standard Model and Higgs physics*, Progress in Particle and Nuclear Physics **100** (2018) 69 , ISSN: 0146-6410, URL: `http://www.sciencedirect.com/science/article/pii/S0146641018300036`.

[3] S. F. Novaes, *Standard model: An Introduction* (1999) 5, arXiv: `hep-ph/0001283 [hep-ph]`.

[4] S. L. Glashow, *Partial-symmetries of weak interactions*, Nuclear Physics **22** (1961) 579 , ISSN: 0029-5582, URL: `http://www.sciencedirect.com/science/article/pii/0029558261904692`.

[5] *Nobel Prize for Physics, 1979*, CERN Courier **19** (1979) 395, URL: `http://cds.cern.ch/record/1730492`.

[6] M. E. Peskin and D. V. Schroeder, *An Introduction to Quantum Field Theory; 1995 ed.* Includes exercises, Boulder, CO: Westview, 1995, URL: `https://cds.cern.ch/record/257493`.

[7] C. L. Bennett et al., *NINE-YEARWILKINSON MICROWAVE ANISOTROPY PROBE(WMAP) OBSERVATIONS: FINAL MAPS AND RESULTS*, **208** (2013) 20, URL: `https://doi.org/10.1088%2F0067-0049%2F208%2F2%2F20`.

[8] P. A. R. Ade et al., *Planck 2015 results. XIII. Cosmological parameters*, Astron. Astrophys. **594** (2016) A13, arXiv: `1502.01589 [astro-ph.CO]`.

[9] N. Aghanim et al., *Planck 2018 results. VI. Cosmological parameters* (2018), arXiv: `1807.06209 [astro-ph.CO]`.

[10] Y. Akrami et al., *Planck 2018 results. VII. Isotropy and Statistics of the CMB* (2019), arXiv: `1906.02552 [astro-ph.CO]`.

[11] G. Bertone et al., *Identifying WIMP dark matter from particle and astroparticle data*, JCAP **1803** (2018) 026, arXiv: `1712.04793 [hep-ph]`.

[12] L. Susskind, *Dynamics of Spontaneous Symmetry Breaking in the Weinberg-Salam Theory*, Phys. Rev. **D20** (1979) 2619.

[13] S. Weinberg, *Implications of Dynamical Symmetry Breaking*, Phys. Rev. **D13** (1976) 974, [Addendum: Phys. Rev.D19,1277(1979)].

[14] L. Susskind, *Dynamics of spontaneous symmetry breaking in the Weinberg-Salam theory*, Phys. Rev. D **20** (1979) 2619, URL: `https://cds.cern.ch/record/479553`.

[15] S. P. Martin, *A Supersymmetry primer* (1997), [Adv. Ser. Direct. High Energy Phys.18,1(1998)], arXiv: `hep-ph/9709356 [hep-ph]`.

[16] S. P. Martin, ‘A Supersymmetry Primer’, tech. rep. hep-ph/9709356, Comments: 160 pages. Version 7 (January 2016) contains many updates and improvements. Errata, source files, and a version with larger type (12 pt, 179 pages) can be found at http://www.niu.edu/spmartin/primer/, 1997, URL: `https://cds.cern.ch/record/334060`.

[17] J. Wess, ‘SUPERSYMMETRY AND SUPERGRAVITY’, *The Low-Energy Theorem for the Forward Compton Amplitude of a Stationary Composite System and the F-W Additive External Electromagnetic Interaction*, 1984 II.84.

[18] P. Fayet, *The Supersymmetric Standard Model*, Adv. Ser. Direct. High Energy Phys. **26** (2016) 397, arXiv: `1506.08277 [hep-ph]`.

[19] T. H. Hsieh, G. B. Halász and T. Grover, *All Majorana Models with Translation Symmetry are Supersymmetric*, Phys. Rev. Lett. **117** (2016) 166802, arXiv: `1604.08591 [cond-mat.str-el]`.

[20] P. Fayet, *Supersymmetry and Weak, Electromagnetic and Strong Interactions*, Phys. Lett. B **64** (1976) 159.

[21] P. Fayet, *Spontaneously Broken Supersymmetric Theories of Weak, Electromagnetic and Strong Interactions*, Phys. Lett. B **69** (1977) 489.

[22] R. Haag, J. T. Lopuszanski and M. Sohnius, *All Possible Generators of Supersymmetries of the s Matrix*, Nucl. Phys. **B88** (1975) 257.

[23] S. R. Coleman and J. E. Mandula, *All possible symmetries of the S Matrix*, Phys. Rev. **159** (1967) 1251, URL: `https://cds.cern.ch/record/405857`.

[24] R. N. Mohapatra, *Supersymmetry and R-parity: an Overview*, Phys. Scripta **90** (2015) 088004, arXiv: `1503.06478 [hep-ph]`.

[25] A. Djouadi, *The Anatomy of electro-weak symmetry breaking. II. The Higgs bosons in the minimal supersymmetric model*, Phys. Rept. **459** (2008) 1, arXiv: `hep-ph/0503173`.

[26] A. Djouadi, *The anatomy of electroweak symmetry breaking Tome II: The Higgs bosons in the Minimal Supersymmetric Model*, Phys. Rep. **459** (2008) 1, and references therein.

[27] H. P. Nilles, *Supersymmetry, supergravity and particle physics*, Phys. Rept. **110** (1984) 1.

[28] H. E. Haber and G. L. Kane, *The search for supersymmetry: Probing physics beyond the standard model*, Phys. Rept. **117** (1985) 75.

[29] D. de Florian et al., *Handbook of LHC Higgs Cross Sections: 4. Deciphering the Nature of the Higgs Sector* (2016), arXiv: `1610.07922 [hep-ph]`.

[30] G. C. Branco et al., *Theory and phenomenology of two-Higgs-doublet models*, Phys. Rept. **516** (2012) 1, arXiv: `1106.0034 [hep-ph]`.

[31] J. L. Feng, J.-F. Grivaz and J. Nachtman, *Searches for Supersymmetry at High-Energy Colliders*, Rev. Mod. Phys. **82** (2010) 699, [Reprint: Adv. Ser. Direct. High Energy Phys.21,351(2010)], arXiv: `0903.0046 [hep-ex]`.

[32] S. Dimopoulos and D. W. Sutter, *The Supersymmetric flavor problem*, Nucl. Phys. **B452** (1995) 496, arXiv: `hep-ph/9504415 [hep-ph]`.

[33] J. F. Gunion and H. E. Haber, *Errata for Higgs bosons in supersymmetric models: 1, 2 and 3* (1992), arXiv: `hep-ph/9301205 [hep-ph]`.

[34] A. Djouadi et al., *Fully covering the MSSM Higgs sector at the LHC*, JHEP **06** (2015) 168, arXiv: `1502.05653 [hep-ph]`.

[35] A. Djouadi et al., *The post-Higgs MSSM scenario: Habemus MSSM?,* Eur. Phys. J. C **73** (2013) 2650, arXiv: `1307.5205 [hep-ph]`.

[36] M. Carena et al., *MSSM Higgs Boson Searches at the LHC: Benchmark Scenarios after the Discovery of a Higgs-like Particle,* Eur. Phys. J. **C73** (2013) 2552, arXiv: `1302.7033 [hep-ph]`.

[37] S. Liebler et al., *The hMSSM approach for Higgs self-couplings revisited,* Eur. Phys. J. **C79** (2019) 65, arXiv: `1810.10979 [hep-ph]`.

[38] *Benchmark scenarios for low* $\tan\beta$ *in the MSSM* (2015), URL: `https://cds.cern.ch/record/2004747`.

[39] B. C. Allanach et al., *Precise determination of the neutral Higgs boson masses in the MSSM,* JHEP **09** (2004) 044, arXiv: `hep-ph/0406166 [hep-ph]`.

[40] R. V. Harlander, S. Liebler and H. Mantler, *SusHi: A program for the calculation of Higgs production in gluon fusion and bottom-quark annihilation in the Standard Model and the MSSM,* Comp. Phys. Commun. **184** (2013) 1605, arXiv: `1212.3249 [hep-ph]`.

[41] A. S. Kronfeld and C. Quigg, *Resource Letter: Quantum Chromodynamics,* Am. J. Phys. **78** (2010) 1081, arXiv: `1002.5032 [hep-ph]`.

[42] R. Harlander and W. B. Kilgore, *Higgs boson production in bottom quark fusion at next-to-next-to-leading order,* Phys. Rev. D **68** (2003) 013001, arXiv: `hep-ph/0304035`.

[43] M. Spira et al., *Higgs boson production at the LHC,* Nucl. Phys. B **453** (1995) 17, arXiv: `hep-ph/9504378`.

[44] S. Dittmaier, M. Krämer and M. Spira, *Higgs radiation off bottom quarks at the Fermilab Tevatron and the CERN LHC,* Phys. Rev. D **70** (7 2004) 074010, URL: `https://link.aps.org/doi/10.1103/PhysRevD.70.074010`.

[45] R. Harlander, M. Kramer and M. Schumacher, *Bottom-quark associated Higgs-boson production: reconciling the four- and five-flavour scheme approach* (2011), arXiv: `1112.3478 [hep-ph]`.

[46] M. R. Pahlavani and R Morad, 'Validity of Born Approximation for Nuclear Scattering in Path Integral Representation', tech. rep. arXiv:0907.0115, 2009, URL: `http://cds.cern.ch/record/1187440`.

[47] T. Gleisberg et al., *Event generation with SHERPA 1.1,* JHEP **02** (2009) 007, arXiv: `0811.4622 [hep-ph]`.

[48] S. Höche, 'Introduction to parton-shower event generators', *Proceedings, Theoretical Advanced Study Institute in Elementary Particle Physics: Journeys Through the Precision Frontier: Amplitudes for Colliders (TASI 2014): Boulder, Colorado, June 2-27, 2014*, 2015 235, arXiv: `1411.4085 [hep-ph]`.

[49] A. D. Martin et al., *Parton distributions for the LHC,* Eur. Phys. J. C **63** (2009) 189, arXiv: `0901.0002 [hep-ph]`.

[50] R. D. Ball et al., *Parton distributions for the LHC Run II,* JHEP **04** (2015) 040, arXiv: `1410.8849 [hep-ph]`.

[51] F. Maltoni et al., *Choosing the Factorization Scale in Perturbative QCD* (2007), arXiv: `hep-ph/0703156 [HEP-PH]`.

[52] J. Butterworth et al., *PDF4LHC recommendations for LHC Run II* (2015), arXiv: `1510.03865 [hep-ph]`.

[53] S. Dulat et al.,
New parton distribution functions from a global analysis of quantum chromodynamics,
Phys. Rev. D **93** (2016) 033006, arXiv: `1506.07443 [hep-ph]`.

[54] A. Martin et al.,
Heavy-quark mass dependence in global PDF analyses and 3- and 4-flavour parton distributions,
Eur. Phys. J. C **70** (2010) 51, arXiv: `1007.2624 [hep-ph]`.

[55] *Martin-Stirling-Thorne-Watt Parton Distribution Functions* (),
URL: `https://mstwpdf.hepforge.org/`.

[56] E Norrbin and T. Sjöstrand, *Production and Hadronization of Heavy Quarks*,
Eur. Phys. J. C **17** (2000) 137, URL: `https://cds.cern.ch/record/437604`.

[57] T. J. Humanic, *Extracting the hadronization timescale in $\sqrt{s} = 7$ TeV proton-proton collisions from pion and kaon femtoscopy*, J. Phys. **G41** (2014) 075105, arXiv: `1312.2303 [hep-ph]`.

[58] A. Buckley et al., *General-purpose event generators for LHC physics*,
Phys. Rept. **504** (2011) 145, arXiv: `1101.2599 [hep-ph]`.

[59] J.-C. Winter, F. Krauss and G. Soff, *A Modified cluster hadronization model*,
Eur. Phys. J. **C36** (2004) 381, arXiv: `hep-ph/0311085 [hep-ph]`.

[60] 'A study of the Pythia 8 description of ATLAS minimum bias measurements with the Donnachie-Landshoff diffractive model', tech. rep. ATL-PHYS-PUB-2016-017, CERN, 2016,
URL: `https://cds.cern.ch/record/2206965`.

[61] 'Summary of ATLAS Pythia 8 tunes', tech. rep. ATL-PHYS-PUB-2012-003, CERN, 2012,
URL: `https://cds.cern.ch/record/1474107`.

[62] S. Carrazza, S. Forte and J. Rojo, 'Parton Distributions and Event Generators',
Proceedings, 43rd International Symposium on Multiparticle Dynamics (ISMD 13), 2013 89,
arXiv: `1311.5887 [hep-ph]`.

[63] ALEPH, DELPHI, L3, and OPAL Collaborations, G. Abbiendi et al.,
Search for neutral MSSM Higgs bosons at LEP, Eur. Phys. J. C **47** (2006) 547,
arXiv: `hep-ex/0602042 [hep-ex]`.

[64] T. Aaltonen et al.,
Search for Neutral Higgs Bosons in Events with Multiple Bottom Quarks at the Tevatron,
Phys. Rev. **D86** (2012) 091101, arXiv: `1207.2757 [hep-ex]`.

[65] M. Aaboud et al., *Search for additional heavy neutral Higgs and gauge bosons in the ditau final state produced in 36 fb^{-1} of pp collisions at $\sqrt{s} = 13$ TeV with the ATLAS detector*,
JHEP **01** (2018) 055, arXiv: `1709.07242 [hep-ex]`.

[66] A. M. Sirunyan et al., *Search for additional neutral MSSM Higgs bosons in the $\tau\tau$ final state in proton-proton collisions at $\sqrt{s} = 13$ TeV*, JHEP **09** (2018) 007, arXiv: `1803.06553 [hep-ex]`.

[67] H. Bahl, S. Liebler and T. Stefaniak,
MSSM Higgs benchmark scenarios for Run 2 and beyond: the low $\tan\beta$ region,
Eur. Phys. J. **C79** (2019) 279, arXiv: `1901.05933 [hep-ph]`.

[68] *Summary plots from the ATLAS Higgs physics group* (),
URL: `https://atlas.web.cern.ch/Atlas/GROUPS/PHYSICS/CombinedSummaryPlots/HIGGS/`.

[69] ATLAS Collaboration, *The ATLAS experiment at the CERN Large Hadron Collider*,
JINST **3** (2008) S08003.

[70] L. Evans and P. Bryant, *LHC Machine*, JINST **3** (2008) S08001.

[71] O. S. Brüning et al., *LHC Design Report*, Geneva, 2004, URL: https://cds.cern.ch/record/782076.

[72] E. Mobs, *The CERN accelerator complex. Complexe des accélérateurs du CERN* (2016), General Photo, URL: https://cds.cern.ch/record/2197559.

[73] A. Ruiz-Martinez and A. Collaboration, 'The Run-2 ATLAS Trigger System', tech. rep. ATL-DAQ-PROC-2016-003, CERN, 2016, URL: https://cds.cern.ch/record/2133909.

[74] 'ATLAS Inner Detector Alignment Performance with February 2015 Cosmic Rays Data', tech. rep. ATL-PHYS-PUB-2015-009, CERN, 2015, URL: http://cds.cern.ch/record/2008724.

[75] J. Pequenao, 'Computer generated image of the whole ATLAS detector', 2008, URL: https://cds.cern.ch/record/1095924.

[76] L. Hauswald and A. Straessner, 'Systematic and Experimental Uncertainties in the Search for Neutral MSSM Higgs Bosons Decaying to Two Tau Leptons', Presented 2013, 2013, URL: http://cds.cern.ch/record/2280055.

[77] A Yamamoto et al., *Design and development of the ATLAS central solenoid magnet*, IEEE Trans. Appl. Supercond. **9** (1998) 852, URL: http://cds.cern.ch/record/404719.

[78] G. Aad et al., *The ATLAS Inner Detector commissioning and calibration*, Eur. Phys. J. **C70** (2010) 787, arXiv: 1004.5293 [physics.ins-det].

[79] A. Collaboration, 'Technical Design Report for the ATLAS Inner Tracker Pixel Detector', tech. rep. CERN-LHCC-2017-021. ATLAS-TDR-030, CERN, 2017, URL: https://cds.cern.ch/record/2285585.

[80] M Capeans et al., 'ATLAS Insertable B-Layer Technical Design Report', tech. rep. CERN-LHCC-2010-013. ATLAS-TDR-19, 2010, URL: https://cds.cern.ch/record/1291633.

[81] M. Capeans et al., *ATLAS Insertable B-Layer Technical Design Report* (2010).

[82] A Chilingarov, *Temperature dependence of the current generated in Si bulk*, Journal of Instrumentation **8** (2013) P10003, URL: https://doi.org/10.1088%2F1748-0221%2F8%2F10%2Fp10003.

[83] A Abdesselam and T Akimoto, 'The Barrel Modules of the ATLAS SemiConductor Tracker', tech. rep. ATL-INDET-PUB-2006-005. ATL-COM-INDET-2006-009. CERN-ATL-COM-INDET-2006-009, CERN, 2006, URL: https://cds.cern.ch/record/974073.

[84] A Vogel, 'ATLAS Transition Radiation Tracker (TRT): Straw Tube Gaseous Detectors at High Rates', tech. rep. ATL-INDET-PROC-2013-005, CERN, 2013, URL: https://cds.cern.ch/record/1537991.

[85] 'Particle Identification Performance of the ATLAS Transition Radiation Tracker', tech. rep. ATLAS-CONF-2011-128, CERN, 2011, URL: https://cds.cern.ch/record/1383793.

[86] *Performance of the ATLAS Transition Radiation Tracker in Run 1 of the LHC: tracker properties*, Journal of Instrumentation **12** (2017) P05002, URL: https://doi.org/10.1088%2F1748-0221%2F12%2F05%2Fp05002.

[87] G Parrour et al.,
'Performances of the ATLAS electromagnetic calorimeter filled with liqui Krypton: Higgs mass resolution in the Ho to gamma gamma and Ho to ZZ to 4e benchmark channels',
tech. rep. ATL-CAL-95-077. ATL-AC-PN-77, CERN, 1995,
URL: `https://cds.cern.ch/record/685696`.

[88] A. Collaboration,
'Technical Design Report for the Phase-II Upgrade of the ATLAS LAr Calorimeter',
tech. rep. CERN-LHCC-2017-018. ATLAS-TDR-027, CERN, 2017,
URL: `http://cds.cern.ch/record/2285582`.

[89] A Artamonov et al., *The ATLAS Forward Calorimeter*,
Journal of Instrumentation **3** (2008) P02010,
URL: `https://doi.org/10.1088%2F1748-0221%2F3%2F02%2Fp02010`.

[90] *ATLAS tile calorimeter: Technical Design Report*, Technical Design Report ATLAS,
Geneva: CERN, 1996, URL: `https://cds.cern.ch/record/331062`.

[91] S. Palestini, *The muon spectrometer of the ATLAS experiment*,
Nucl. Phys. Proc. Suppl. **125** (2003) 337, [,337(2003)].

[92] M Livan, 'Monitored drift tubes in ATLAS', tech. rep. ATL-M-PN-129, CERN, 1996,
URL: `https://cds.cern.ch/record/319197`.

[93] K. Nagai, *Thin gap chambers in ATLAS*,
Nuclear Instruments and Methods in Physics Research Section A: Accelerators, Spectrometers, Detectors and Associated Equipment **384** (1996) 219 , BEAUTY '96, ISSN: 0168-9002,
URL: `http://www.sciencedirect.com/science/article/pii/S0168900296010650`.

[94] *The ATLAS Experiment at the CERN Large Hadron Collider*, JINST **3** (2008) S08003.

[95] P. Hamal, *Physics prospects with the ALFA and AFP detectors* (2013),
URL: `https://cds.cern.ch/record/1548109`.

[96] S. Abdel Khalek et al., *The ALFA Roman Pot Detectors of ATLAS*, JINST **11** (2016) P11013,
arXiv: `1609.00249 [physics.ins-det]`.

[97] A. Collaboration, 'ATLAS Forward Detectors', General Photo, 2018,
URL: `https://cds.cern.ch/record/2627582`.

[98] A. Outreach,
'ATLAS Fact Sheet : To raise awareness of the ATLAS detector and collaboration on the LHC',
2010, URL: `https://cds.cern.ch/record/1457044`.

[99] J. Love, *The Evolution of the ATLAS Region of Interest Builder* (2018),
URL: `https://cds.cern.ch/record/2302393`.

[100] E. Simioni et al., *Upgrade of the ATLAS Level-1 Trigger with event topology information*,
Journal of Physics: Conference Series **664** (2015) 082052,
URL: `https://doi.org/10.1088%2F1742-6596%2F664%2F8%2F082052`.

[101] M Elsing et al., *The ATLAS Tier-0: Overview and operational experience*,
J. Phys.: Conf. Ser. **219** (2010) 072011, URL: `https://cds.cern.ch/record/1270548`.

[102] P. Jenni et al., *ATLAS high-level trigger, data-acquisition and controls: Technical Design Report*,
Technical Design Report ATLAS, Geneva: CERN, 2003,
URL: `https://cds.cern.ch/record/616089`.

[103] M. Aaboud et al., *Performance of the ATLAS Trigger System in 2015*,
Eur. Phys. J. **C77** (2017) 317, arXiv: `1611.09661 [hep-ex]`.

[104] J. Wenninger, *Operation and Configuration of the LHC in Run 2* (2019), URL: https://cds.cern.ch/record/2668326.

[105] O. Viazlo and A. L. Collaboration, 'ATLAS LUCID detector upgrade for LHC Run 2', tech. rep. ATL-FWD-PROC-2015-004, CERN, 2015, URL: https://cds.cern.ch/record/2062038.

[106] 'Luminosity determination in pp collisions at $\sqrt{s} = 13$ TeV using the ATLAS detector at the LHC', tech. rep. ATLAS-CONF-2019-021, CERN, 2019, URL: http://cds.cern.ch/record/2677054.

[107] Z Marshall, 'Simulation of Pile-up in the ATLAS Experiment', tech. rep. ATL-SOFT-PROC-2013-030, CERN, 2013, URL: https://cds.cern.ch/record/1616394.

[108] T. Novak, *New Techniques for Pile-up Simulation in ATLAS* (2018), URL: https://cds.cern.ch/record/2628404.

[109] O. Rifki, *The ATLAS Data Flow system in Run2: Design and Performance* (2016), URL: https://cds.cern.ch/record/2209354.

[110] J. Catmore et al., *A new petabyte-scale data derivation framework for ATLAS*, Journal of Physics: Conference Series **664** (2015) 072007, URL: https://doi.org/10.1088%2F1742-6596%2F664%2F7%2F072007.

[111] *Luminosity Public Results Run2* (), URL: https://twiki.cern.ch/twiki/bin/view/AtlasPublic/LuminosityPublicResultsRun2.

[112] 'The Optimization of ATLAS Track Reconstruction in Dense Environments', tech. rep. ATL-PHYS-PUB-2015-006, CERN, 2015, URL: https://cds.cern.ch/record/2002609.

[113] 'Performance of primary vertex reconstruction in proton-proton collisions at $\sqrt{s}$ =7 TeV in the ATLAS experiment', tech. rep. ATLAS-CONF-2010-069, CERN, 2010, URL: https://cds.cern.ch/record/1281344.

[114] B.-B. Chai, J. Vass and X. Zhuang, *Significance-linked connected component analysis for wavelet image coding*, IEEE transactions on image processing : a publication of the IEEE Signal Processing Society **8 6** (1999) 774.

[115] A Rosenfeld and J. Pfaltz, *Sequential operations in digital picture processing*, Journal of the ACM **13** (1996) 471.

[116] G. Aad et al., *A neural network clustering algorithm for the ATLAS silicon pixel detector*, JINST **9** (2014) P09009, arXiv: 1406.7690 [hep-ex].

[117] M. Aaboud et al., *Performance of the ATLAS Track Reconstruction Algorithms in Dense Environments in LHC Run 2*, Eur. Phys. J. **C77** (2017) 673, arXiv: 1704.07983 [hep-ex].

[118] F. Meloni, 'Primary vertex reconstruction with the ATLAS detector', tech. rep. ATL-PHYS-PROC-2016-163. 12, CERN, 2016, URL: https://cds.cern.ch/record/2222390.

[119] W. Waltenberger, R. Frühwirth and P. Vanlaer, *Adaptive vertex fitting*, Journal of Physics G: Nuclear and Particle Physics **34** (2007) N343, URL: https://doi.org/10.1088%2F0954-3899%2F34%2F12%2Fn01.

[120] S Pagan Griso et al., 'Vertex reconstruction plots: Collision performance plots for approval', tech. rep. ATL-COM-PHYS-2012-474, CERN, 2012, URL: https://cds.cern.ch/record/1445579.

[121] ATLAS Collaboration,
Topological cell clustering in the ATLAS calorimeters and its performance in LHC Run 1 (2016), arXiv: `1603.02934 [hep-ex]`.

[122] M. Cacciari, G. P. Salam and G. Soyez, *FastJet User Manual*, Eur. Phys. J. **C72** (2012) 1896, arXiv: `1111.6097 [hep-ph]`.

[123] G. P. Salam, *Towards Jetography*, Eur. Phys. J. **C67** (2010) 637, arXiv: `0906.1833 [hep-ph]`.

[124] M. Cacciari, G. P. Salam and G. Soyez, *The anti-k_t jet clustering algorithm*, JHEP **04** (2008) 063, arXiv: `0802.1189 [hep-ph]`.

[125] *Jet energy scale measurements and their systematic uncertainties in proton-proton collisions at $\sqrt{s} = 13$ TeV with the ATLAS detector. Jet energy scale measurements and their systematic uncertainties in proton-proton collisions at $\sqrt{s} = 13$ TeV with the ATLAS detector*, Phys. Rev. D **96** (2017) 072002. 36 p, URL: `https://cds.cern.ch/record/2257300`.

[126] 'Monte Carlo Calibration and Combination of In-situ Measurements of Jet Energy Scale, Jet Energy Resolution and Jet Mass in ATLAS', tech. rep. ATLAS-CONF-2015-037, CERN, 2015, URL: `https://cds.cern.ch/record/2044941`.

[127] M. Aaboud et al., *Jet energy scale measurements and their systematic uncertainties in proton-proton collisions at $\sqrt{s} = 13$ TeV with the ATLAS detector*, Phys. Rev. **D96** (2017) 072002, arXiv: `1703.09665 [hep-ex]`.

[128] 'Optimisation of the ATLAS b-tagging performance for the 2016 LHC Run', tech. rep. ATL-PHYS-PUB-2016-012, CERN, 2016, URL: `https://cds.cern.ch/record/2160731`.

[129] 'Optimisation and performance studies of the ATLAS b-tagging algorithms for the 2017-18 LHC run', tech. rep. ATL-PHYS-PUB-2017-013, CERN, 2017, URL: `http://cds.cern.ch/record/2273281`.

[130] 'Commissioning of the ATLAS high-performance b-tagging algorithms in the 7 TeV collision data', tech. rep. ATLAS-CONF-2011-102, CERN, 2011, URL: `https://cds.cern.ch/record/1369219`.

[131] 'Track Reconstruction Performance of the ATLAS Inner Detector at $\sqrt{s} = 13$ TeV', tech. rep. ATL-PHYS-PUB-2015-018, CERN, 2015, URL: `https://cds.cern.ch/record/2037683`.

[132] *Introduction to Heavy Flavour Jet Tagging with ATLAS* (), URL: `https://indico.cern.ch/event/655628/contributions/2670400/attachments/1518249/2370617/ASC_FTagHbbWS_BTagging.pdf`.

[133] D. Guest, K. Cranmer and D. Whiteson, *Deep Learning and its Application to LHC Physics*, Ann. Rev. Nucl. Part. Sci. **68** (2018) 161, arXiv: `1806.11484 [hep-ex]`.

[134] R. Fruhwirth, *Application of Kalman filtering to track and vertex fitting*, Nucl. Instrum. Meth. **A262** (1987) 444.

[135] ATLAS Collaboration, *Expected performance of the ATLAS b-tagging algorithms in Run-2*, ATL-PHYS-PUB-2015-022, 2015, URL: `http://cdsweb.cern.ch/record/2037697`.

[136] 'Pile-up subtraction and suppression for jets in ATLAS', tech. rep. ATLAS-CONF-2013-083, CERN, 2013, URL: `https://cds.cern.ch/record/1570994`.

[137] A. Hocker et al., *TMVA - Toolkit for Multivariate Data Analysis* (2007), arXiv: `physics/0703039 [physics.data-an]`.

[138] ATLAS Collaboration, *Electron efficiency measurements with the ATLAS detector using the 2015 LHC proton-proton collision data*, ATLAS-CONF-2016-024, 2016, URL: `http://cdsweb.cern.ch/record/2157687`.

[139] 'Electron reconstruction and identification in the ATLAS experiment using the 2015 and 2016 LHC proton-proton collision data at $\sqrt{s} = 13$ TeV', tech. rep. arXiv:1902.04655, * Temporary entry *: CERN, 2019, URL: `https://cds.cern.ch/record/2657964`.

[140] E. Haug and W. Nakel, *The elementary process of Bremsstrahlung*, World Scientific Lecture Notes in Physics, New Jersey, NJ: World Scientific, 2004, URL: `https://cds.cern.ch/record/789939`.

[141] T. G. Cornelissen et al., *The global 2track fitter in ATLAS*, Journal of Physics: Conference Series **119** (2008) 032013, URL: `https://doi.org/10.1088%2F1742-6596%2F119%2F3%2F032013`.

[142] 'Improved electron reconstruction in ATLAS using the Gaussian Sum Filter-based model for bremsstrahlung', tech. rep. ATLAS-CONF-2012-047, CERN, 2012, URL: `http://cds.cern.ch/record/1449796`.

[143] ATLAS Collaboration, *Electron and photon energy calibration with the ATLAS detector using LHC Run 1 data*, Eur. Phys. J. C **74** (2014) 3071, arXiv: `1407.5063 [hep-ex]`.

[144] G. Aad et al., *Readiness of the ATLAS Liquid Argon Calorimeter for LHC Collisions*, Eur. Phys. J. **C70** (2010) 723, arXiv: `0912.2642 [physics.ins-det]`.

[145] *Response uniformity of the ATLAS liquid argon electromagnetic calorimeter*, Nuclear Instruments and Methods in Physics Research Section A: Accelerators, Spectrometers, Detectors and Associated Equipment **582** (2007) 429 , ISSN: 0168-9002, URL: `http://www.sciencedirect.com/science/article/pii/S0168900207018591`.

[146] G. Aad et al., *Electron performance measurements with the ATLAS detector using the 2010 LHC proton-proton collision data*, Eur. Phys. J. **C72** (2012) 1909, arXiv: `1110.3174 [hep-ex]`.

[147] M. Aaboud et al., *Electron reconstruction and identification in the ATLAS experiment using the 2015 and 2016 LHC proton-proton collision data at $\sqrt{s} = 13$ TeV*, Submitted to: Eur. Phys. J. (2019), arXiv: `1902.04655 [physics.ins-det]`.

[148] *Muon reconstruction efficiency and momentum resolution of the ATLAS experiment in proton–proton collisions at 7 TeV in 2010*, The European Physical Journal C **74** (2014) 3034, ISSN: 1434-6052, URL: `https://doi.org/10.1140/epjc/s10052-014-3034-9`.

[149] ATLAS Collaboration, *Muon reconstruction performance of the ATLAS detector in proton–proton collision data at $\sqrt{s}$=13 TeV*, Eur. Phys. J. C **76** (2016) 292, arXiv: `1603.05598 [hep-ex]`.

[150] G. Aad et al., *Muon reconstruction performance of the ATLAS detector in proton–proton collision data at $\sqrt{s}$ =13 TeV*, Eur. Phys. J. **C76** (2016) 292, arXiv: `1603.05598 [hep-ex]`.

[151] G. Aad et al., *Measurements of Higgs boson production and couplings in the four-lepton channel in pp collisions at center-of-mass energies of 7 and 8 TeV with the ATLAS detector*, Phys. Rev. **D91** (2015) 012006, arXiv: `1408.5191 [hep-ex]`.

[152] M. Tanabashi et al., *Review of Particle Physics*, Phys. Rev. **D98** (2018) 030001.

[153] *Reconstruction, Energy Calibration, and Identification of Hadronically Decaying Tau Leptons in the ATLAS Experiment for Run-2 of the LHC* (), URL: `https://atlas.web.cern.ch/Atlas/GROUPS/PHYSICS/PUBNOTES/ATL-PHYS-PUB-2015-045/`.

[154] W Lampl et al., 'Calorimeter Clustering Algorithms: Description and Performance', tech. rep. ATL-LARG-PUB-2008-002. ATL-COM-LARG-2008-003, CERN, 2008, URL: `https://cds.cern.ch/record/1099735`.

[155] ATLAS Collaboration, *Tagging and suppression of pileup jets with the ATLAS detector*, ATLAS-CONF-2014-018, 2014, URL: `http://cdsweb.cern.ch/record/1700870`.

[156] C Limbach, *Reconstruction and Identification of Tau Leptons in ATLAS* (2014), URL: `https://cds.cern.ch/record/1951814`.

[157] M. Flechl, 'Identification and energy calibration of hadronic tau lepton decays at the LHC', *5th Large Hadron Collider Physics Conference (LHCP 2017) Shanghai, China, May 15-20, 2017*, 2017, arXiv: `1709.01351 [hep-ex]`.

[158] 'Measurement of the tau lepton reconstruction and identification performance in the ATLAS experiment using pp collisions at 13 TeV', tech. rep. ATLAS-CONF-2017-029, CERN, 2017, URL: `http://cds.cern.ch/record/2261772`.

[159] M. Huebner, 'Measurement of the tau lepton reconstruction and identification performance in the ATLAS experiment using pp collisions at $\sqrt(s)$=13 TeV', tech. rep. ATL-PHYS-PROC-2018-086, CERN, 2018, URL: `https://cds.cern.ch/record/2634998`.

[160] *Measurement of the tau lepton reconstruction and identification performance in the ATLAS experiment using pp collisions at 13TeV* (), URL: `https://atlas.web.cern.ch/Atlas/GROUPS/PHYSICS/CONFNOTES/ATLAS-CONF-2017-029/`.

[161] 'The ATLAS Tau Trigger in Run 2', tech. rep. ATLAS-CONF-2017-061, CERN, 2017, URL: `https://cds.cern.ch/record/2274201`.

[162] 'Measurement of the tau lepton reconstruction and identification performance in the ATLAS experiment using *pp* collisions at $\sqrt{s} = 13$ TeV', tech. rep. ATL-COM-PHYS-2016-929, CERN, 2016, URL: `https://cds.cern.ch/record/2199788`.

[163] B Lenzi, R Nicolaidou and S Hassani, *TrackInCaloTools: A package for measuring muon energy loss and calorimetric isolation in ATLAS*, Journal of Physics: Conference Series **219** (2010) 032049, URL: `https://doi.org/10.1088%2F1742-6596%2F219%2F3%2F032049`.

[164] '$E_{\mathrm{T}}^{\mathrm{miss}}$ performance in the ATLAS detector using 2015-2016 LHC p-p collisions', tech. rep. ATLAS-CONF-2018-023, CERN, 2018, URL: `https://cds.cern.ch/record/2625233`.

[165] ATLAS Collaboration, *Performance of missing transverse momentum reconstruction for the ATLAS detector in the first proton-proton collisions at $\sqrt{s}$= 13 TeV*, ATL-PHYS-PUB-2015-027, 2015, URL: `http://cdsweb.cern.ch/record/2037904`.

[166] G. Aad et al., *The ATLAS Simulation Infrastructure*, Eur. Phys. J. **C70** (2010) 823, arXiv: `1005.4568 [physics.ins-det]`.

[167] S. Agostinelli et al., *GEANT4: A Simulation toolkit*, Nucl. Instrum. Meth. **A506** (2003) 250.

[168] ATLAS Collaboration, *The simulation principle and performance of the ATLAS fast calorimeter simulation FastCaloSim*, ATL-PHYS-PUB-2010-013, 2010, URL: `http://cdsweb.cern.ch/record/1300517`.

[169] S. Heinemeyer, O. Stal and G. Weiglein, *Interpreting the LHC Higgs Search Results in the MSSM*, Phys. Lett. **B710** (2012) 201, arXiv: `1112.3026 [hep-ph]`.

[170] S. Chatrchyan et al., *Search for Neutral MSSM Higgs Bosons Decaying to Tau Pairs in pp Collisions at $\sqrt{s} = 7$ TeV*, Phys. Rev. Lett. **106** (2011) 231801, arXiv: `1104.1619 [hep-ex]`.

[171] *Search for neutral MSSM Higgs bosons decaying to $\tau^+\tau^-$ pairs in proton–proton collisions at s=7 TeV with the ATLAS detector*, Physics Letters B **705** (2011) 174 , ISSN: 0370-2693,
URL: `http://www.sciencedirect.com/science/article/pii/S0370269311012330`.

[172] S. Chatrchyan et al.,
Search for neutral Higgs bosons decaying to tau pairs in pp collisions at $\sqrt{s} = 7$ TeV,
Phys. Lett. **B713** (2012) 68, arXiv: `1202.4083 [hep-ex]`.

[173] E. Bagnaschi et al.,
Higgs production via gluon fusion in the POWHEG approach in the SM and in the MSSM,
JHEP **02** (2012) 088, arXiv: `1111.2854 [hep-ph]`.

[174] M. Wiesemann et al., *Higgs production in association with bottom quarks*,
Journal of High Energy Physics **2015** (2015) 132, ISSN: 1029-8479,
URL: `https://doi.org/10.1007/JHEP02(2015)132`.

[175] 'Multi-Boson Simulation for 13 TeV ATLAS Analyses', tech. rep. ATL-PHYS-PUB-2016-002, CERN, 2016, URL: `https://cds.cern.ch/record/2119986`.

[176] 'Monte Carlo Generators for the Production of a W or Z/γ^* Boson in Association with Jets at ATLAS in Run 2', tech. rep. ATL-PHYS-PUB-2016-003, CERN, 2016,
URL: `https://cds.cern.ch/record/2120133`.

[177] 'Simulation of top quark production for the ATLAS experiment at sqrt(s) = 13 TeV',
tech. rep. ATL-PHYS-PUB-2016-004, CERN, 2016,
URL: `https://cds.cern.ch/record/2120417`.

[178] ATLAS Collaboration, *Reconstruction, Energy Calibration, and Identification of Hadronically Decaying Tau Leptons in the ATLAS Experiment for Run-2 of the LHC*,
ATL-PHYS-PUB-2015-045, 2015, URL: `http://cdsweb.cern.ch/record/2064383`.

[179] *Jet energy scale measurements and their systematic uncertainties in proton-proton collisions at 13 TeV with the ATLAS detector*, Phys. Rev. D **96** (7 2017) 072002,
URL: `https://link.aps.org/doi/10.1103/PhysRevD.96.072002`.

[180] 'Calibration of the ATLAS b-tagging algorithm in $t\bar{t}$ semi-leptonic events',
tech. rep. ATLAS-CONF-2018-045, CERN, 2018, URL: `https://cds.cern.ch/record/2638455`.

[181] W. Buttinger, 'Using Event Weights to account for differences in Instantaneous Luminosity and Trigger Prescale in Monte Carlo and Data', tech. rep. ATL-COM-SOFT-2015-119, CERN, 2015,
URL: `https://cds.cern.ch/record/2014726`.

[182] L. Marchese, 'Muon reconstruction performance of the ATLAS detector in 2016',
tech. rep. ATL-PHYS-PROC-2017-246, CERN, 2017,
URL: `https://cds.cern.ch/record/2292925`.

[183] *Measurements of inclusive and differential fiducial cross-sections of tt production with additional heavy-flavour jets in proton-proton collisions at 13 TeV with the ATLAS detector*,
Journal of High Energy Physics **2019** (2019) 46, ISSN: 1029-8479,
URL: `https://doi.org/10.1007/JHEP04(2019)046`.

[184] J Butterworth et al.,
'Single Boson and Diboson Production Cross Sections in pp Collisions at sqrts=7 TeV',
tech. rep. ATL-COM-PHYS-2010-695, CERN, 2010,
URL: `https://cds.cern.ch/record/1287902`.

[185] M. Aaboud et al., *Search for high-mass new phenomena in the dilepton final state using proton-proton collisions at $\sqrt{s} = 13$ TeV with the ATLAS detector*, Phys. Lett. **B761** (2016) 372,
arXiv: `1607.03669 [hep-ex]`.

[186] W Davey et al.,
'Search for neutral MSSM Higgs bosons in the decay mode $H \to \tau^+\tau^- \to \tau_{\text{had}}\tau_{\text{had}}$ + 2 neutrinos in proton-proton collisions at $\sqrt{s}$=8 TeV with the ATLAS Experiment.',
tech. rep. ATL-COM-PHYS-2013-238, CERN, 2013,
URL: https://cds.cern.ch/record/1520112.

[187] 'Studies on top-quark Monte Carlo modelling for Top2016', tech. rep. ATL-PHYS-PUB-2016-020, CERN, 2016, URL: http://cds.cern.ch/record/2216168.

[188] N Besson et al., 'Measurement of the transverse momentum distribution of Z/gamma bosons in proton-proton collisions at roots = 7 TeV with the ATLAS detector: Update with 4.7 fb-1 of the previous measurement at this energy.', tech. rep. ATL-COM-PHYS-2013-117, CERN, 2013,
URL: https://cds.cern.ch/record/1513133.

[189] J. Neyman and E. S. Pearson,
On the Problem of the Most Efficient Tests of Statistical Hypotheses,
Philosophical Transactions of the Royal Society of London. Series A, Containing Papers of a Mathematical or Physical Character **231** (1933) 289, ISSN: 02643952,
URL: http://www.jstor.org/stable/91247.

[190] A. L. Read, *Presentation of search results: The CL(s) technique*,
J. Phys. **G28** (2002) 2693, [,11(2002)].

[191] G. Zech, *Upper limits in experiments with background or measurement errors*,
Nuclear Instruments and Methods in Physics Research Section A: Accelerators, Spectrometers, Detectors and Associated Equipment **277** (1989) 608 , ISSN: 0168-9002,
URL: http://www.sciencedirect.com/science/article/pii/016890028990795X.

[192] K. Cranmer et al.,
'HistFactory: A tool for creating statistical models for use with RooFit and RooStats',
tech. rep. CERN-OPEN-2012-016, New York U., 2012,
URL: https://cds.cern.ch/record/1456844.

[193] L. Moneta et al., *The RooStats Project*,
PoS **ACAT2010** (2010) 057, Comments: 11 pages, 3 figures, ACAT2010 Conference Proceedings,
URL: https://cds.cern.ch/record/1289965.

[194] W. Verkerke and D. P. Kirkby, *The RooFit toolkit for data modeling*,
eConf **C0303241** (2003) MOLT007, [,186(2003)], arXiv: physics/0306116 [physics].

[195] F. a. James, *MINUIT: Function Minimization and Error Analysis Reference Manual*
(1998), CERN Program Library Long Writeups, URL: https://cds.cern.ch/record/2296388.

[196] F. James and M. Roos, *Minuit: A System for Function Minimization and Analysis of the Parameter Errors and Correlations*, Comput. Phys. Commun. **10** (1975) 343.

[197] G. Cowan et al., *Asymptotic formulae for likelihood-based tests of new physics*,
Eur. Phys. J. C **71** (2011) 1554, [Erratum: Eur. Phys. J. C 73 (2013) 2501],
arXiv: 1007.1727 [physics.data-an].

[198] S. S. Wilks,
The Large-Sample Distribution of the Likelihood Ratio for Testing Composite Hypotheses,
Annals Math. Statist. **9** (1938) 60.

[199] A. Wald, *Tests of Statistical Hypotheses Concerning Several Parameters When the Number of Observations is Large*, Transactions of the American Mathematical Society **54** (1943) 426,
ISSN: 00029947, URL: http://www.jstor.org/stable/1990256.

[200] G. Cowan et al., *Asymptotic distribution for two-sided tests with lower and upper boundaries on the parameter of interest* (2012), arXiv: `1210.6948 [physics.data-an]`.

[201] E. Gross, *Practical Statistics for High Energy Physics*,
CERN Yellow Reports: School Proceedings **4** (2017) 165, ISSN: 2519-805X,
URL: `https://e-publishing.cern.ch/index.php/CYRSP/article/view/303`.

[202] A. Arbey, M. Battaglia, A. Djouadi and F. Mahmoudi,
The Higgs sector of the phenomenological MSSM in the light of the Higgs boson discovery,
JHEP **1209** (2012) 107, arXiv: `1207.1348 [hep-ph]`.

[203] A. Djouadi, *Implications of the Higgs discovery for the MSSM*, Eur. Phys. J. **C74** (2014) 2704,
arXiv: `1311.0720 [hep-ph]`.

[204] J. Baglio, A. Djouadi and J. Quevillon, *Prospects for Higgs physics at energies up to 100 TeV*,
Rept. Prog. Phys. **79** (2016) 116201, arXiv: `1511.07853 [hep-ph]`.

[205] C. Bernius, ‘HL-LHC prospects from ATLAS and CMS’, tech. rep. ATL-PHYS-PROC-2019-023,
CERN, 2019, URL: `https://cds.cern.ch/record/2666331`.

[206] M. Mangano and M. Mangano, *Physics at the FCC-hh, a 100 TeV pp collider*,
ed. by M. Mangano, vol. 3, CERN Yellow Reports: Monographs, 2017,
URL: `https://cds.cern.ch/record/2270978`.